

Towards Robust Monitoring of the Laser Powder Bed Fusion Process based on Acoustic Emission combined with Machine Learning Solutions

Présentée le 17 février 2023

Faculté des sciences et techniques de l'ingénieur
Laboratoire de métallurgie thermomécanique - Chaire PX Group
Programme doctoral en manufacturing

pour l'obtention du grade de Docteur ès Sciences

par

Rita DRISSI DAOUDI

Acceptée sur proposition du jury

Prof. V. Michaud, présidente du jury
Prof. R. Logé, Dr K. T. Wasmer, directeurs de thèse
Prof. V. K. Nadimpalli, rapporteur
Prof. S. Castagne, rapporteuse
Prof. Y. Bellouard, rapporteur

Acknowledgments

First, I would like to express my utmost gratitude to my thesis director, Prof Roland Logé. I could never thank you enough; you always supported me and believed in me. You were always available when I needed you and your knowledge. Your passion and your kindness made the accomplishment of this project possible. You are my mentor and the best guide I could hope for. I would always be grateful. I would as well acknowledge my co-thesis director Dr.Kilian Wasmer. Thank you for this very interesting project and for your supervision.

I am also thankful to all the members of my thesis jury, Prof. Yves Bellouard, Prof. Venkata Karthik Nadimpalli, Prof. Sylvie Castagne, and Prof. Véronique Michaud for their careful examination of my thesis, insightful comments, and fruitful discussion.

Thank you Dr. Jamasp Jhabvala for the numerous discussions and help during my experiments and thank you for your calm and kindness.

I would like to acknowledge the members involved in this project for their help and dedication. Mr. Siddartha Berns and Dr. Sylvain Hugon from HEIG-VD, Prof. Markus Strobl from PSI, Prof. Antonia Neels, Dr. Robert Zboray, Dr. Annapaola Parrilli, Prof. Patrik Hoffmann Dr Sergey Schevick, Dr. Vigneashwara Pandiyan, and Dr.Tri Le-Quang from Empa. I particularly thank Giulio Masinelli, for your guidance, your intelligence your countless help, this thesis work would not be what it is without you.

I would like to express my sincere gratitude to EPFL and the Advanced Manufacturing Doctoral School. I am grateful for my great colleagues, Eric, Toni, Céline, Cyril, Priscille, Mathijs, Joelle, Reza, Amir and Lucas.

Thank you to my “Neuchâtel family”: Gözden, Julien, Julie, Hossein, Shima, Navid, Mahtab and Claire; I am very grateful to have you all in my life. Margaux, I would never be able to thank you enough. My little sun, you helped me and enlightened everyday of this journey. Baptiste, thank you very much for all your support, the meaningful discussion and the continuous motivation. Thank you to my wonderful friends who always have been there for me: Sara, Janina, Luana, Seval, Alice and Simon.

I am profoundly thankful to my parents, Taoufiq and Nabila. I love you very much, I am grateful for your support during this thesis work and since the beginning. I am also very grateful to have the best sister someone can have, thank you Leila.

Finally, thank you to my darling Maxime. I could not have completed this milestone without your everyday support, care and love.

Abstract

Laser Powder Bed Fusion (LPBF) is an Additive Manufacturing (AM) process consolidating parts layer by layer, from a metallic powder bed. It allows no limitation in terms of geometry and is therefore of particular interest to various industries. Metallic LPBF samples can achieve near-full density and high resistance. However, to prevent defects from deteriorating the quality of the workpiece, process costly and time-consuming parameters optimization is required. The LPBF process lack of repeatability limits its applications. The Ph.D. thesis proposes an alternative solution to trial-and-error optimization, based upon real-time acoustic in-situ monitoring combined with state-of-the-art machine learning.

We first investigated the use of a low-cost microphone AM41 combined with machine learning (ML) algorithms. Three regimes (lack of fusion pores, conduction mode, and keyhole pores) and three alloys (316L stainless steel, bronze CuSn8, and Inconel 718) were selected. Three conventional ML algorithms and a Convolutional Neural Network (CNN) were chosen to perform the classification tasks. We proved that the acoustic emissions AE features are related to the laser-material interaction and do not originate from undesired machine or environmental noises. The regimes are classified with high accuracy ($> 87\%$) regardless of the algorithms and materials. The AE features used for the classifications are material and regime dependent. Finally, a CNN multi-label architecture for classifying the material and the process regimes simultaneously reached a very high classification accuracy (93%), which is of great interest for multi-materials LPBF systems. We also introduce alternative AI methods to reduce the amount of data needed to train the algorithms, as well as to transfer the knowledge from one material to another.

Saliency maps are used to determine the frequencies responsible for the ML algorithm classification. The analysis of saliency maps allows the quality of the trained model to be evaluated. A second microphone with a flat frequency response from 2 kHz to 200 kHz is compared with the AM41, whose response is restricted to bands around 10, 20, and 40 kHz. The information needed for the classification is scattered in the range 2 kHz-200 kHz, which allows both types of microphones to predict the regimes. Detailed investigation shows that most of the information is confined below 30 kHz, leading to an easier classification and a better model with the flat response microphone.

The need to have a robust ML database is highlighted, with the flat response microphone. Twelve different laser parameter sets are chosen for each processing regime, to construct a database for the training of a CNN, applied to stainless steel 316L. We prove the possibility of generalization, i.e. using the model for classifying the regimes with high confidence ($>96\%$), from AE signals recorded with unseen laser parameters. The influence of the “distance” in terms of power, speed, and enthalpy between the laser parameter sets included in the training database, and the unseen one, is studied. The position in the processing map is also investigated. At

least eight parameter sets should be included in the training database to predict the regime of any laser parameter set, Moreover, when a robust model is trained, a decrease in the classification accuracy can indicate the regimes domains frontiers. This monitoring solution can help construct processing maps for a given alloy.

Keywords

Additive Manufacturing, Laser Powder Bed Fusion, Acoustic Emission monitoring, Machine Learning

Résumé

La fusion laser sur lit de poudre (LPBF) est un procédé de fabrication additive consolidant des pièces couche par couche, à partir d'un lit de poudre métallique. Il permet la fabrication de géométrie complexe. Les pièces peuvent atteindre une densité et une résistance élevée. Il faut optimiser les paramètres du procédé, ce qui est long et coûteux. Le manque de répétabilité du procédé LPBF limite ses applications. Cette thèse propose une solution alternative à l'optimisation par essais et erreurs, basée sur la surveillance acoustique in-situ en temps réel combinée à un apprentissage automatique de pointe.

L'utilisation d'un microphone à faible coût AM41 a été combiné à des algorithmes d'apprentissage ML. Trois régimes (absence de pores de fusion, mode de conduction et pores keyhole) et trois alliages (acier inoxydable 316L, bronze CuSn8 et Inconel 718) ont été sélectionnés. Trois algorithmes et un réseau neuronal convolutif (CNN) ont été choisis pour la classification. Les émissions acoustiques AE sont liées à l'interaction laser-matière et ne proviennent pas de bruits indésirables de la machine ou de l'environnement. Les régimes sont classés avec une grande précision ($>87\%$) indépendamment des algorithmes et des matériaux. Les caractéristiques AE dépendent du matériau et du régime. Une architecture CNN multi-label pour la classification simultanée du matériau et des régimes a atteint une précision de classification élevée, 93%, ce qui est d'un grand intérêt pour les systèmes LPBF multi-matériaux. Nous présentons également des méthodes d'IA alternatives pour réduire la quantité de données nécessaires à l'entraînement des algorithmes, ainsi que pour transférer les connaissances d'un matériau à un autre.

Les cartes de saillance sont utilisées pour déterminer les fréquences responsables de la classification et permettent d'évaluer la qualité du modèle entraîné. Un second microphone avec une réponse en fréquence plate de 2 kHz à 200 kHz est comparé à l'AM41, dont la réponse est limitée autour de 10, 20 et 40 kHz. Les informations nécessaires à la classification sont dispersées dans la gamme 2 kHz-200 kHz, ce qui permet aux deux types de microphones de prédire les régimes. Une étude détaillée montre les informations sont confinées en dessous de 30 kHz, ce qui conduit à une classification plus facile et à un meilleur modèle avec le microphone à réponse plate.

La nécessité de disposer d'un model ML robuste est mise en évidence, avec le microphone à réponse plate. Douze ensembles de paramètres laser différents sont choisis pour chaque régime de, afin de construire une base de données pour l'apprentissage d'un CNN, appliqué à l'acier inoxydable 316L. Nous prouvons la possibilité de généralisation, c'est-à-dire l'utilisation du modèle pour classer les régimes avec une confiance élevée $>96\%$, à partir de signaux AE enregistrés avec des paramètres laser inconnus. L'influence de la "distance" et de la position en termes de puissance, de vitesse et d'enthalpie entre les ensembles de paramètres laser dans la

base de données d'entraînement et ceux qui n'ont pas été vus, est étudiée. Au moins huit ensembles de paramètres doivent être dans la base de données d'entraînement pour prédire le régime d'un ensemble non-vu. De plus, lorsqu'un modèle robuste est entraîné, une diminution de la précision de la classification peut indiquer les frontières des régimes. Cette solution de surveillance peut aider à construire des cartes de procédé pour un alliage donné.

Mots-clés

Fabrication additive, fusion laser en lit de poudre, surveillance par émission acoustique, apprentissage automatique.

Contents

Acknowledgments.....	i
Abstract.....	ii
Keywords.....	iii
Résumé	iv
Mots-clés.....	v
Acronyms	x
List of Figures	xii
Chapter 1 Introduction	1
1.1 Laser Powder Bed process	1
1.2 Analytical monitoring and defects formation	2
Chapter 2 State of the art.....	11
2.1 Machine Learning solutions.....	11
2.2 Optical monitoring	13
2.3 Acoustic monitoring.....	17
2.3.1 Acoustic monitoring in laser welding.....	18
2.3.2 Acoustic monitoring in Additive Manufacturing.....	22
References	29
Chapter 3 Scope of the thesis	42
3.1 Scope of the thesis	42
3.2 Thesis plan	45
Chapter 4 Differentiation of Materials and Laser Powder Bed Fusion Processing Regimes from Airborne Acoustic Emission Combined with Machine Learning	47
Abstract.....	48
4.1 Introduction.....	48
4.2 Experimental setup and data acquisition.....	52
4.3 Analysis of acoustic emission signature from LPBF process	58

4.3.1	Time-domain analysis.....	59
4.3.2	Frequency domain analysis.....	60
4.3.3	Time-frequency domain analysis.....	62
4.4	<i>t</i> -SNE visualisation	64
4.5	Classification results for different process regimes and materials.....	66
4.5.1	Origin of the acoustic emission features.....	68
4.5.2	One on one alloy classification.....	70
4.5.3	One on all alloy classification.....	72
4.5.4	Cross alloy classification- towards generalisation.....	73
4.5.5	Multi-label classification	74
4.5.6	Summary of the classification tasks	76
4.6	Conclusions.....	77
References		79
Learnings and following work:		86
Chapter 5	Deep Transfer Learning of Additive Manufacturing Mechanisms Across Materials in Metal-Based Laser Powder Bed Fusion Process	87
Abstract		88
5.1	Introduction.....	89
5.2	Theoretical basis	92
5.2.1	VGG-16 and ResNet-18	92
5.3	Transfer Learning.....	94
5.4	Experimental setup and methodology.....	95
5.4.1	Experimental setup	95
5.4.2	In situ sensing setup and data processing	98
5.4.3	Methodology.....	100
5.5	Transfer learning using VGG-16 and ResNet-18 architecture.....	101
5.5.1	Transfer learning using VGG -16 Architecture	103
5.5.2	Transfer learning using ResNet - 18 Architecture	106

5.5.3 Comparison of VGG-16 and ResNet - 18 without transfer learning.	109
5.6 Conclusion	110
References	112
Chapter 6 Semi- supervised Monitoring of Laser Powder Bed Fusion Process Based on Acoustic Emissions 117	
Abstract	118
6.1 Introduction.....	118
6.2 Theoretical basis	121
6.2.1 Variational Auto Encoder	121
6.2.2 Generative Adversarial Network	123
6.3 Experimental setup.....	124
6.3.1 Experimental setup and materials.....	124
6.3.2 Data acquisition and dataset preparation	126
6.3.3 Anomaly detection.....	127
6.3.4 VAE based anomaly detection.....	129
6.3.5 GANomaly based anomaly detection	132
6.3.6 Summary of the main results	136
6.4 Conclusions.....	136
References	138
Learnings and following work:	145
Chapter 7 On the importance of acoustic emission frequencies for in-situ monitoring of Laser Powder Bed Fusion	146
Abstract	147
7.1 Introduction.....	147
7.2 Methodology and experimental plan.....	152
7.3 Results.....	158
7.3.1 AM41 microphone.....	159
7.3.2 CM16 microphone	162

7.4	Discussion	169
7.5	Conclusions.....	171
References		172
Chapter 8 Acoutics emission for the prediction of processing regimes in Laser Powder Bed Fusion, and the generation of processing maps.....		
		180
Abstract		181
8.1	Introduction.....	182
8.2	LPBF Experiments.....	184
8.2.1	Experimental setup and data acquisition	184
8.2.2	Experimental plan.....	186
8.3	Data processing.....	189
8.4	Results and discussion	191
8.4.1	Toward the generalization of the ML model over the entire processing map	191
8.4.2	Influence of the position, number of parameter sets and choice of process parameters on the classification accuracy	191
8.5	Conclusions.....	200
References		202
Chapter 9 Conclusions and future work.....		
		209
9.1	Conclusions.....	209
9.2	Future work.....	210
Curriculum Vitae.....		212

Acronyms

ABAE	Air Borne Acoustic Emission
AE	Acoustic Emission
AI	Artificial Intelligence
AM	Additive Manufacturing
ANN	Artificial Neural Network
BP	Band Power
CNN	Convolution Neural Network
DT	Decision Tree
FBG	Fiber Bragg grating
FFT	Fast Fourier Transform
GB	Gradient Boost
IR	Infra-Red
KNN	k-Nearest Neighbor
LE	Light Emission
LPBF	Laser Powder Bed Fusion
LR	Logistic Regression
LSTM	Long Short Time Memory
ML	Machine Learning
MLP	Multilayer perceptron
NN	Neural Network
RF	Random Forest
RNN	Recurrent Neural Network
SBAE	Structure Borne Acoustic Emission

Acronyms

SCNN	Spectral Convolution Neural Network
SPD	Sound Pressure Deviation
STFT	Short Time Fourier Transform
SVM	Support Vector Machine

List of Figures

Figure 1. Laser powder bed fusion process steps schematic representation [13]	1
Figure 2. Schematic of the LPBF laser-mater interaction with the main process parameters [13]	2
Figure 3. Schematic trend of porosity and cracks density with changes of the energy density. The red circle indicates the optimum processing conditions.[R.Drissi-Daoudi, PhD thesis]	3
Figure 4. Examples of microstructure of 316L LPBF work pieces: From left to right, keyhole mode, conduction mode, conduction mode with cracks, LoF mode. [R.Drissi-Daoudi, PhD thesis]	3
Figure 5. Schematic representation of LoF pores formation. [R.Drissi-Daoudi, PhD thesis]	3
Figure 6 . Cross-sectional of balling effect agglomerates of different sizes for high velocity (750 mm/s) and increasing power until high power 1430W [27]	4
Figure 7. Bubble formation due to keyhole collapsing [32]	4
Figure 8. Slice from neutron tomography of a SS316 L sample (P=200 W, v=400 mm/s, t=20 μ m, h=100 μ m) with the associated scanning strategy forming keyhole in the T shape. [R.Drissi-Daoudi, PhD thesis]5	
Figure 9. Slice from neutron tomography of a SS316L sample (P=120 W, v=600 mm/s, t=40 μ m, h=100 μ m) with the associated scanning strategy forming the LoF line. [R.Drissi-Daoudi, PhD thesis]	6
Figure 10. The translation rule applied to the normalized enthalpy of bronze samples versus the normalized melt pool of red gold (in green) and 316L (in orange). [42]	7
Figure 11. Formation mechanisms of different types of spatter: morphology of spherical splashing (type-I splashing); of coarse spherical morphology (type-II splashing); of irregular splashing (type-III splashing) [43]	7
Figure 12. Schematic illustration of a powder layer with a portion (in yellow) under the laser beam that melts and form the track N with a big LOF, considering the presence of a spatter [23]	8
Figure 13. Simulation of a denudation zone apparition. [25]	9
Figure 14. Architecture of the designed sequential decision analysis neural network taking into account pyrometer measurement in the first ANN echelon and high speed camera images for the 2 next ANN echelons as well as the outcome of the first ANN echelon. [91]	14
Figure 15. Schematic methodology of supervised classification of defect formation from the extracting of melt pool characteristics from thermal images. [93]	15

List of Figures

Figure 16. Heatmap for a delamination defect. A. the thermal image b. the heatmap with areas of high importance for the classification highlighted.[100]	17
Figure 17. Schematic model for ABAE and SBAE during laser welding. The upper panel shows a typical trend for ABAE with respect to the laser power, the middle panel presents the trend for SBAE, and the lower panel a schematic representation of the soundwaves for each step of the welding penetration. [123]19	
Figure 18. Schematic architecture of the ANN used by Huang and Kocacevic [130]	21
Figure 19. Cross section of the weld with different power inputs leading to conduction weld, keyhole weld, or keyhole with porosity formation weld in a Titanium plate [134].....	21
Figure 20. The ANN architecture used by Lee et al using frequency level to classify different weld type.[136].....	22
Figure 21. Cross section of a LPBF single line with keyhole and cracks formation with the acoustic signal associated [137]	23
Figure 22. Example of a spectrogram of one scanning layer extracted from the AE signals acquired with a high sensitivity Xarion microphone [138]	24
Figure 23. The schematic representation of the build plate with the four piezoceramic transducers attached below. [139].....	24
Figure 24. Level of complexity below the printed and recorded layers.[140].....	25
Figure 25. Porosity density of the printed cubes divided in three classes.[140].....	25
Figure 26. The ANN achitecture used by Eschner et al.[140]	25
Figure 27. The three LPBF regimes classified in [121] b.medium quality (keyhole pores), c. high quality (conduction mode) and d. poor quality (LoF porosity)	26
Figure 28. The double running window methodology for localization purpose [122]	26
Figure 29. Five categories are considered- balling, slight balling, normal, slight overheating, and overheating of single tracks studied in [141].....	27
Figure 30. Experimental plan used for the segmentation between keyhole formation and non-pores segments in [142].....	28
Figure 31. Thesis outline and chapters structure schematically represented.....	44
Figure 32. Experimental setup of the LPBF process with the PAC AM41 acoustic sensor installed.	53
Figure 33. Processing map showing the normalised melt pool depth (i.e. depth divided by the laser spot size) as a function of the normalised enthalpy (as defined in (Ghasemi-Tabasi et al. 2020)) for the printed	

List of Figures

stainless steel, Inconel and bronze samples. The optimal processing condition is around a normalised enthalpy of 25 for all alloys (Ghasemi-Tabasi et al. 2020). Lower normalised enthalpies lead to LoF pores, while larger values lead to keyhole pores. Experimental setup of the LPBF process with the PAC AM41 acoustic sensor installed.	56
Figure 34. Keyhole porosity formation along one laser track, in stainless steel (316L), and its corresponding acoustic emission signal; a) 3D reconstruction of the <i>keyhole pores</i> formed in one line; b) 2D section of region shown in (a); c) acoustic emission signal corresponding to the selected laser track.	57
Figure 35. Typical micrographs of the three regimes (<i>LoF pores</i> , <i>conduction mode</i> and <i>keyhole pores</i>) for stainless steel (316L), bronze (CuSn ₈), and Inconel (Inconel 718).	57
Figure 36. Raw AE signals correspond to the three different regimes: <i>LoF pores</i> , <i>conduction mode</i> , and <i>keyhole pores</i> for stainless steel, bronze and Inconel (Note: Signal corresponding to <i>LoF pores</i> and <i>Keyhole pores</i> regimes for the three alloys are using same process parameter).	59
Figure 37. Distribution of AE _{RMS} features for the three regimes occurring in stainless steel, bronze and Inconel.	60
Figure 38. Typical FFT plots for stainless steel, bronze and Inconel depicting discrete frequency distributions among the alloys and across the three regimes.	61
Figure 39. Comparison of cumulative energy content between five frequency bands for three regimes in stainless steel, bronze and Inconel.	62
Figure 40. 3D wavelet representation of the AE signal for three laser regimes occurring in stainless steel, bronze and Inconel depicting the absolute intensities in temporal frequency distribution among the alloys.	63
Figure 41. A comprehensive list of statistical features extracted for training the ML model in this work.	64
Figure 42. Low-dimension feature space representation using <i>t</i> -SNE with perplexity =10 for three different regimes in the LPBF processing of stainless steel, bronze, and Inconel. Subscripts 1 and 2 indicate the number of process parameters considered to define a regime.	65
Figure 43. Schematic flow of the monitoring methodology in the LPBF process for the three ML models. The acoustic signals are divided into fixed-width sliding windows of 5 ms, then 304 features are extracted and feeded to the 3 ML algorithms. 70% of the data are used for training, and 30% are kept for testing. The objective is to classify the different regimes (<i>LoF pores</i> , <i>conduction mode</i> , <i>keyhole pores</i>).	67
Figure 44. An illustration of the CNN architecture used in this work with five convolutional layers and fully connected layers.	68
Figure 45. A illustration of the multi-label CNN architecture used in this work with five convolutional layers and two branches of fully connected layers.	75

List of Figures

Figure 46. Accuracy curves confirming that CNN models trained for classifying regimes on individual materials and multi-materials learn with training epochs.....	75
Figure 47. Schematics of the VGG-16 block	93
Figure 48. Schematics of the ResNet -18 architecture.	94
Figure 49. Different strategies in transfer learning based on the problem complexity.....	95
Figure 50. Experimental setup involving LPBF process	96
Figure 51. Normalized enthalpy of the printed stainless steel samples of different build qualities versus the normalized melt pool depth (Pandiyan et al., 2020).....	98
Figure 52. Normalized enthalpy of the printed bronze samples of different build qualities versus the normalized melt pool depth.	98
Figure 53. Workflow to build the spectrogram dataset from line track experiments.	99
Figure 54. Workflow of the proposed methodology.	100
Figure 55. Accuracy and training loss plots during the training of the VGG-16 model on stainless-steel spectrogram dataset.	103
Figure 56. Freezing weights of the pretrained VGG-16 for transfer learning.	104
Figure 57. Accuracy and training loss plots during transfer learning of pretrained VGG-16 model on bronze spectrogram dataset.	105
Figure 58. Accuracy and training loss plots during the training of ResNet-18 model on stainless-steel spectrogram dataset.	106
Figure 59. Freezing weights of pretrained ResNet-18 for transfer learning.....	108
Figure 60. Accuracy and training loss plots during transfer learning of pretrained ResNet-18 model on bronze spectrogram dataset.	108
Figure 61. Illustration of (a) an autoencoder and (b) variational autoencoder architecture depicting latent space with and without regularisation.	122
Figure 62. Illustration of a GAN architecture with generator network G and a discriminator network D .	123
Figure 63. Comparisons of the distribution generated by the generator with training iteration with the actual distribution.....	124
Figure 64. Customized LPBF experimental setup with the embedded acoustic sensor setup for anomaly detection.	125

List of Figures

Figure 65. Optical pictures of different regimes such as <i>balling</i> , <i>LoF pores</i> , <i>conduction mode</i> , and <i>keyhole pores</i> occurring during LPBF of Inconel 718.....	126
Figure 66. Schematic of the data acquisition pipeline with PAC AM4I acoustic sensor and photodiode trigger.	127
Figure 67. Normalized AE signals acquired of the four investigated process regimes, namely <i>balling</i> , <i>LoF pores</i> , <i>conduction mode</i> , and <i>keyhole pores</i>	127
Figure 68. The architecture of the proposed variational autoencoder network.	129
Figure 69. Training loss plot of VAE model on acoustic signals corresponding to <i>conduction mode</i> regime.	130
Figure 70. Distribution plots of reconstruction losses for normal and abnormal conditions.....	131
Figure 71. Reconstructions of the VAE model on (a) the "normal" and (b) the anomaly conditions.	132
Figure 72. The architecture of the proposed GANomaly network comprising the generator and discriminator.....	133
Figure 73. Training loss plot (a) Encoder loss, (b) Generator loss and (c) Construction loss of GANomaly model on acoustic signals corresponding to <i>conduction mode</i> regime.....	134
Figure 74. Distribution plots of reconstruction losses for normal and abnormal conditions.....	135
Figure 75. Box plots of reconstruction losses for normal and abnormal conditions confirm that the AE signal corresponding to anomaly regimes is greater than the threshold of 0.22.	136
Figure 76. Experimental set-up of the custom-built LPBF with the CM16 and the AM41 microphones.....	152
Figure 77. Typical example of microstructure of the three regimes, a. Keyhole pores, b. Conduction mode, c. LoF pores.	153
Figure 78. Process parameter map with thirteen parameter sets for each category, in yellow for the keyhole domain, in green for the conduction mode, and in blue for LoF pores. The parameter sets are numbered from 1 to thirteen for the keyhole pores domain. The same numbering strategy can be transferred to the two other domains. The “central point” (i.e. the set unseen by the ML training) is depicted in black. The dotted line represents the limits of each process regime domain.	154
Figure 79. Signal of an LPBF scan line with keyhole pores generation parameters. In black the signal recorded with the CM16 microphone, in yellow with the AM41 microphone and in orange the laser voltage signal used as trigger for data acquisition.	155
Figure 80. FFT responses of the averaged AE signals for each category, recorded by the CM16 flat frequency response microphone	155

List of Figures

Figure 81. FFT responses of the averaged AE signals for each category, recorded by the AM41 microphone.	155
Figure 82. The position in the base plate of the 13 samples (see Table 24 for the corresponding process parameters). The positions are the same for the three printed metallurgical regimes (keyhole pores, conduction mode and LoF pores).	156
Figure 83. RMS for different low pass filter frequencies (from 20 kHz to 130 kHz), for the keyhole pores category.	156
Figure 84. RMS for the three regimes categories (keyhole pores, conduction mode and LoF pores) when all the samples are filtered with a low pass filter at 60 kHz, compared to the raw signal of the keyhole pores category	156
Figure 85. Scheme of the double line experiments. Two adjacent LPBF lines with different laser parameters are recorded as one line. The first line in red in c. is built with the parameters of the central black point, in Figure 3, of the keyhole pores category (251 W and 350mm/s). The second line in orange in c. is built with the parameters of the central black point of the conduction mode (89 W and 450 mm/s). a. Micrograph of the keyhole part of the line, b. micrograph of the conduction mode part of the same line and c. raw acoustic signal acquired with the CM16 microphone for one of these double-lines .No evident differences can be noticed between the two half of the signal.	157
Figure 86. Scheme of the CNN architecture with two max pooled convolution layers, followed with one convolution layer and 2 fully connected layers.	159
Figure 87. Validation and training losses in function of the epochs for the model Figure 86 trained for 200 epochs.	160
Figure 88. Example of a spectrogram of one signal of each category (keyhole pores, conduction mode, and LoF pores) of the unseen parameter tested set with averaged the saliencies of the 1100 signals in each category of the unseen parameter tested set (central black point) as well as its standard deviation for the CNN model (Figure 86) trained with the AM41 signals.	161
Figure 89. An example of the spectrogram of one double-line AE signal, the averaged saliency maps of the 547 recorded double-lines assuming the conduction mode, and their standard deviation.....	162
Figure 90. Scheme of the CNN architecture with one max pooled convolution layer, followed with one convolution layer and 3 fully connected layers.	163
Figure 91. Validation and training losses in function of the epochs for the model Figure 90 trained for 50 epochs.	163
Figure 92. Example of a spectrogram of one signal of each category (keyhole pores, conduction mode, and LoF pores) of the unseen parameter tested se (black central point Figure 78) with the averaged saliency	

List of Figures

values of the 1100 signals in each category of the unseen parameter tested set (black central point Figure 78), as well as their standard deviation, for the CNN model in Figure 90 trained with the CM16 raw signals.	164
Figure 93. a. A example of a spectrogram of a. AE signal filtered with a low pass filter at 60 kHz of the tested set. b The average saliency maps of the tested category keyhole pores, c. The average saliency maps of the tested category conduction mode, d. The average saliency maps of the tested category LoF pores, e. The average saliency maps of the tested category noise.	166
Figure 94. Scheme of the CNN architecture with four convolution layer folowed by 3 fully connected layers.	167
Figure 95. Validation and training losses in function of the epochs for the model of Figure 94 trained for 15 epochs.	167
Figure 96. Example of a spectrogram of one signal of each category (keyhole pores, conduction mode, and LoF pores) of the unseen parameter tested set (black central point Figure 78 with saliencies averaged over the 1100 signals in each category, and the corresponding standard deviations for the CNN model described in Figure 94, trained with the CM16 signals, filtered with a low-pass filter at 60 kHz, downsampled 4 times and normalized.	168
Figure 97. An example of the spectrogram of one double-line AE signal, the averaged saliency maps of the 547 recorded double-lines assuming the conduction mode, and their standard deviation.....	169
Figure 98. Experimental set-up of the custom-built LPBF with the CM16 microphone	185
Figure 99. Typical example of microstructure of the three regimes, a. Keyhole pores, b. Conduction mode, c. LoF pores. The dotted red line delimits the recorded lines from the printed cube.	186
Figure 100. Process parameter map with the thirteen parameter sets for each category, in green for the keyhole domain, in orange for the conduction mode, and in blue for Lof pores. The parameter sets are numbered from 1 to 13 for the keyhole pores domain. The same numbering strategy can be transferred to the two other domains. The “central point” is depicted in black. Three iso-normalized enthalpies at 80, 25 and 17 are plotted. The full markers are the six parameter sets closest to each central points, and the six empty markers are the six parameter sets the furthest away from the central points.	188
Figure 101. Example of a spectrogram for the three regime related categories.	190
Figure 102. Scheme of the CNN architecture with two convolutional layers and two fully connected layers	190
Figure 103. Micrograph of a cross section of the sample. a) n°4 in the conduction mode domain and b) of the n°1 in the LoF pores domain. The parameter sets used for these samples are at the boundary between the conduction and LoF domains.	193

List of Figures

Figure 104. Average classification accuracy of the processing regime of the unseen parameter set, as a function of the relative normalized distance in terms of speed d_s for different numbers of parameter sets included in the training database (from 2 to 12).....	198
Figure 105. Average classification accuracy of the processing regime of the unseen parameter set, as a function of the relative normalized distance in terms of power d_p for different numbers of parameter sets included in the training database (from 2 to 12).....	198
Figure 106. Linear regressions of the average classification accuracy when predicting the process regime of an unseen parameter set, as a function of the distance d_s (speed) and d_p (power).	199

Chapter 1 Introduction

1.1 Laser Powder Bed process

Laser powder bed fusion (LPBF), also called Selective Laser Melting, has received the most focus among the different additive manufacturing methods for metals and alloys [1], [2]. It consolidates layer-by-layer metallic parts of a given alloy powder with a laser beam. Near full density and mechanical properties competing with those obtained by conventional manufacturing routes, can now be achieved due to recent progress [3]. Complex geometries can be manufactured with minimal feedstock waste [4]. It is of great interest to various industries. For example, aerospace applications contain complex geometries that require the assembling of different parts with different alloys or with a gradient of alloy compositions, using AM technologies results in lightweight structures with significant cost savings [5], [6]. With AM technologies for the medical industry, the patient's own imaging data could be used as CAD input to process implants or devices [7]–[10]. Many other industries such as automotive [11] or jewelry [12] are as well more and more interested in AM technologies' capabilities. Figure 1 presents schematically the different steps of the LPBF process and Figure 2 presents the interaction between the laser and the powder bed and the main process parameters [13].

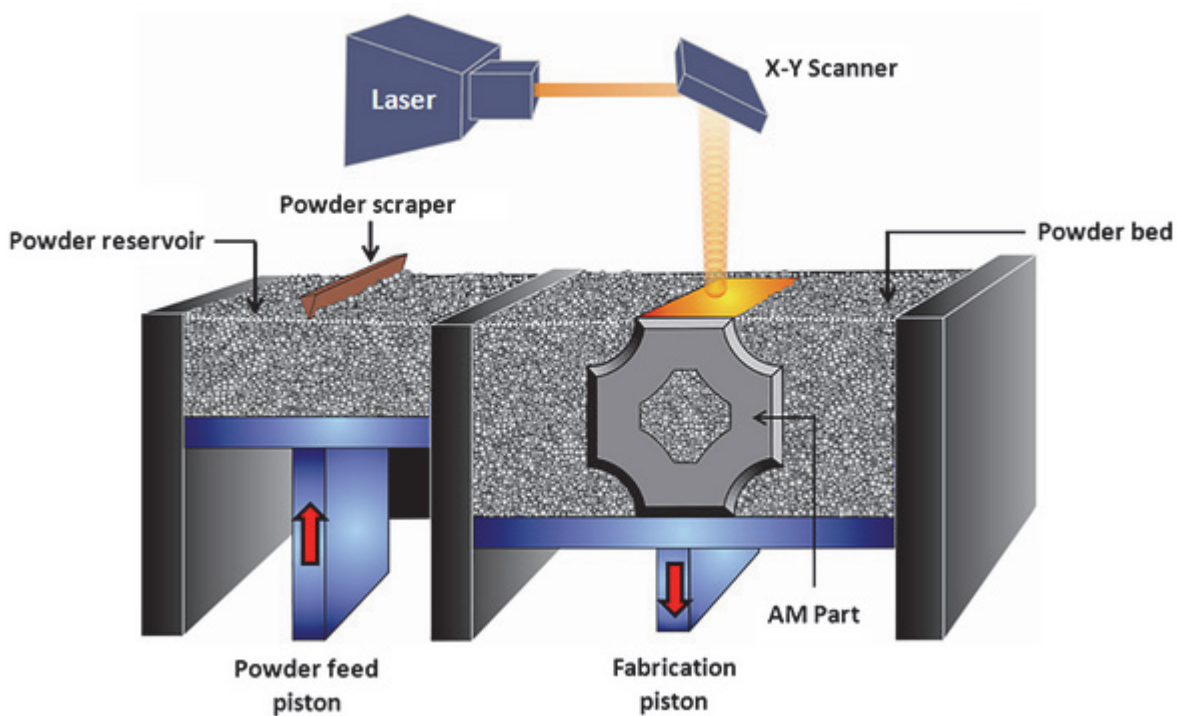


Figure 1. Laser powder bed fusion process steps schematic representation [13]

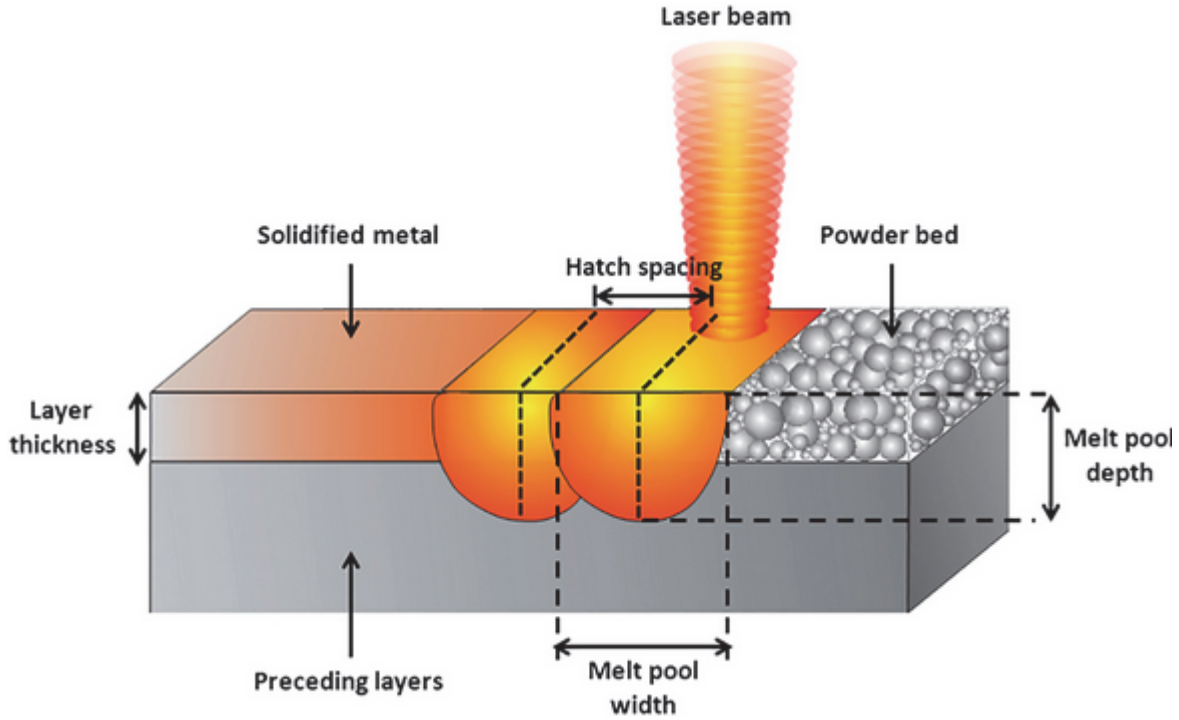


Figure 2. Schematic of the LPBF laser-mater interaction with the main process parameters [13]

1.2 Analytical monitoring and defects formation

The LPBF process involves an important number of parameters, Yadroitsev [14] has identified 130 of them. Any change in any of them has a direct impact on the workpiece quality, leading to a lack of repeatability [15]. Most of the authors, however, agree on four significant process parameters: the laser speed v , laser power P , layer thickness t , and hatching distance h , i.e the distance between two laser paths. The energy density, E , equation 1, is occasionally used to monitor the process [16], [17].

$$E = \frac{P}{vth} \left[\frac{W \cdot s}{mm^3} \right] \quad (1)$$

Two main types of defect can decrease the quality part: porosities and cracks [18]–[20]. The porosity and crack content related to the energy density is often reported or understood as illustrated in Figure 3 for the majority of alloys. The porosity content decreases as the laser energy increases, until reaching a short plateau and then increases again. The cracking behavior is alloy-dependent, nevertheless generally the trend is opposite. Three modes or process regimes can be distinguished in Figure 3 for increasing energy density E : Lack of Fusion (LoF) mode, conduction mode, and keyhole mode. An example of the melt-pool shape for each mode for a given alloy -stainless steel 316L- is shown in Figure 4.

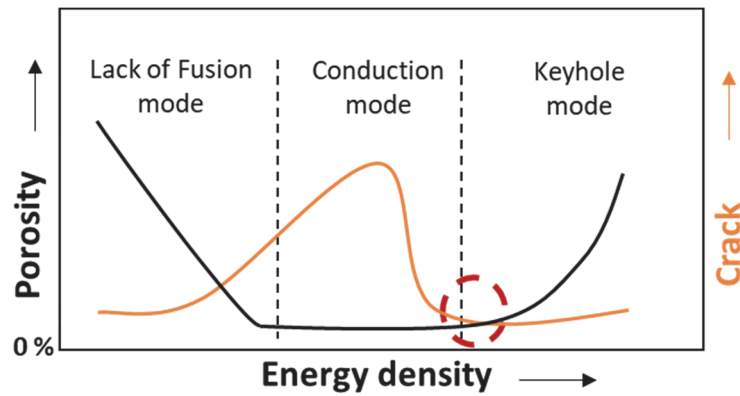


Figure 3. Schematic trend of porosity and cracks density with changes of the energy density. The red circle indicates the optimum processing conditions.[R.Drissi-Daoudi, PhD thesis]

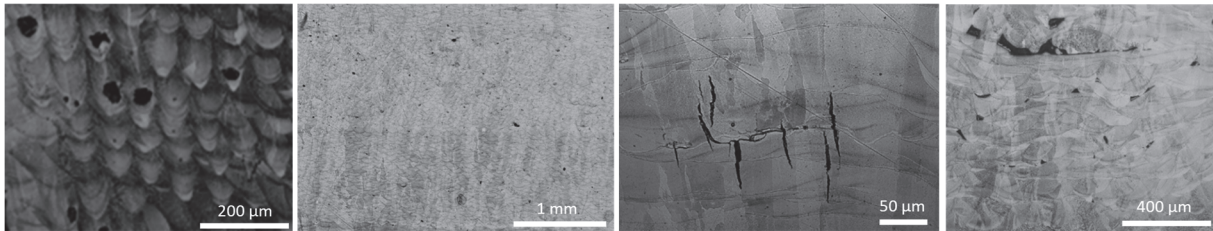


Figure 4. Examples of microstructure of 316L LPBF work pieces: From left to right, keyhole mode, conduction mode, conduction mode with cracks, LoF mode. [R.Drissi-Daoudi, PhD thesis]

In the LoF mode, LoF pores are created. Lack of fusion (LoF) porosities formation originates from the lack of bonding between two layers resulting from incomplete fused spots, incomplete fusion, or incomplete penetration [21]–[24] (Figure 5). The laser parameters and the powder distribution influence the LoF formation. When the energy input is very low in the LoF domain the balling phenomenon occurs. Under these conditions, only the top layer is melted and the layers below act as a substrate. The upper layer incomplete wetting, therefore, results in a weak anchor and the surface tension tendency to minimize the surfaces induces a solidification of the molten powder into a ball shape [25]–[27] (Figure 6). LOF can also occur with limited balling when insufficient hatch overlap is present.

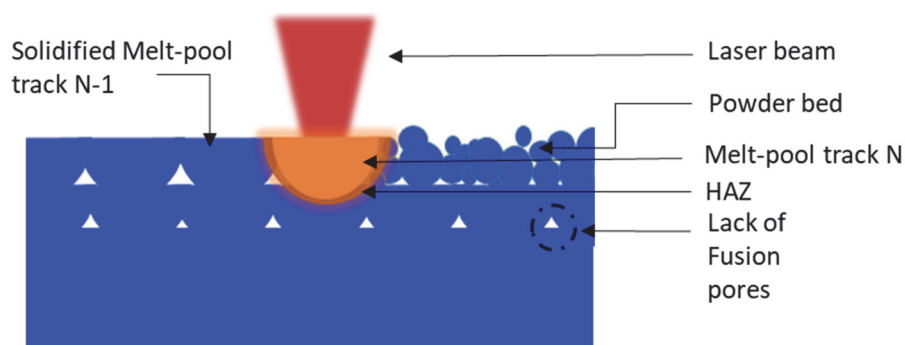


Figure 5. Schematic representation of LoF pores formation. [R.Drissi-Daoudi, PhD thesis]

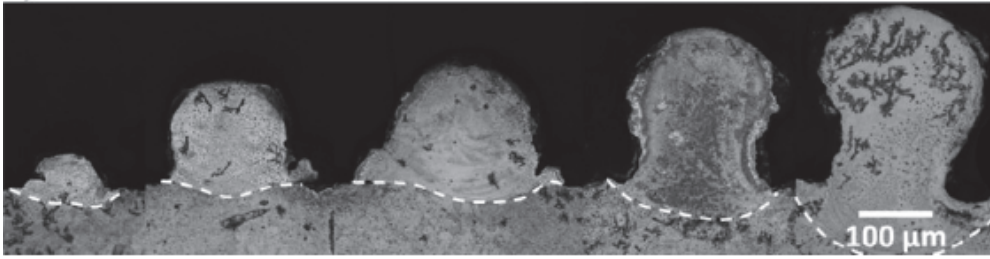


Figure 6 . Cross-sectional of balling effect agglomerates of different sizes for high velocity (750 mm/s) and increasing power until high power 1430W [27]

The keyhole mode can be stable with no formation of pores and when it becomes unstable, it may lead to entrap a gas bubble in the molten metal creating a porosity. The characteristic keyhole well is first created by the melt reaching the evaporation state [28], [29]. The keyhole is then filled with metal vapor at high temperature which is partially or totally ionized and exercises a pressure – called recoil pressure – on the inner surface of the keyhole [30], [31]. The addition of the effects of gravity and surface tension creates the characteristic keyhole shape. A bubble is formed due to the well collapsing than an acoustic waves is generated driving pores near the keyhole tip far enough away from the large thermal gradient field around the keyhole that they can be trapped through solidification [143]. A second mechanism is the Marangoni effect whose driving force is the surface tension. It is a convection effect explained by the local variations in density and temperature. The bubble is brought into the molten pool behind the keyhole and is captured by the solidification front. The second mechanism is shown in the simulation in Figure 7 [32]. The formation of keyholes is a dynamic defect; the porosity follows the laser movement, thus one or multiple keyholes may be created in one laser line scan.

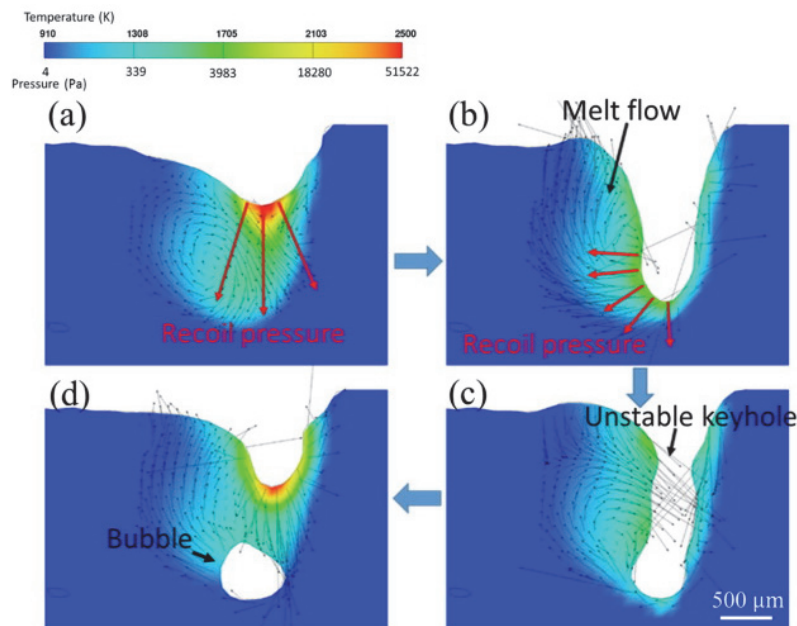


Figure 7. Bubble formation due to keyhole collapsing [32]

The conduction mode is defined as the regime where the energy input is just enough to melt about 1.5 layer with depth divided by $\frac{1}{2}$ the width and not create LoF pores, but where the energy input is not high enough to initiate keyholes. A conduction melt shape can be seen Figure 4. However, the conduction mode is the regime where the residual stresses are the highest, and is therefore prone to cracks formation. Large residual stresses are induced by the Thermal Gradient Mechanism (TGM) and the cool-down mechanism of the molten top layers. It implies a high degree of tensile residual stresses (TRS), producing distorted shape and reducing the mechanical properties and fatigue life. TRS is also always the driving force for the formation of cracks [33]. The cracking behavior is metal-dependent, but different types of cracks can be identified. The lack of fusion pores induce a stress concentration around their tip. The same phenomenon can occur at the grains or the melt-pools boundaries. Cracking can also be driven by micro-segregation creating weakened and brittle phases. Solidification cracks arise between the solidified and the melt-pool areas. Solidification induced shrinkage entraps the remaining liquid in the interdendritic regions which then act as crack initiation sites. Finally, liquation cracks, unlike solidification cracks, take place in the heat-affected zone (HAZ) and do not reveal the dendritic morphology. The material is typically heated rapidly to a temperature lower than the overall liquidus of the material, but high enough to cause the melting of certain grain boundaries, leading to crack initiation [34]–[37].

The scanning strategy is often optimized to reduce residual stresses. However when the laser stops, depending on the energy of the laser, it creates a LoF or a keyhole pore. At this point, the velocity is very low, even zero for a short time-period, the energy input is therefore high, which can lead to keyholing (Figure 8). LoF are created if the energy is low, at the boundaries from LoF mode and conduction mode. At the end of the line some powder is ablated, and when the laser stops, the amount of powder do not have the time to melt completely (Figure 9).

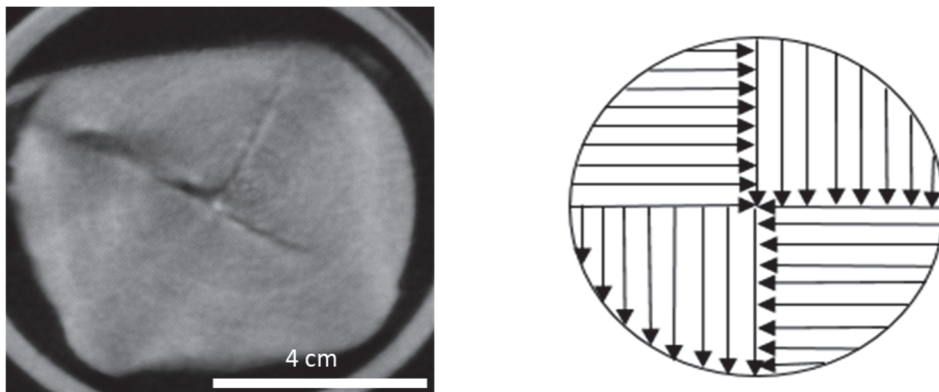


Figure 8. Slice from neutron tomography of a SS316 L sample ($P=200$ W, $v=400$ mm/s, $t=20$ μ m, $h=100$ μ m) with the associated scanning strategy forming keyhole in the T shape. [R.Drissi-Daoudi, PhD thesis]

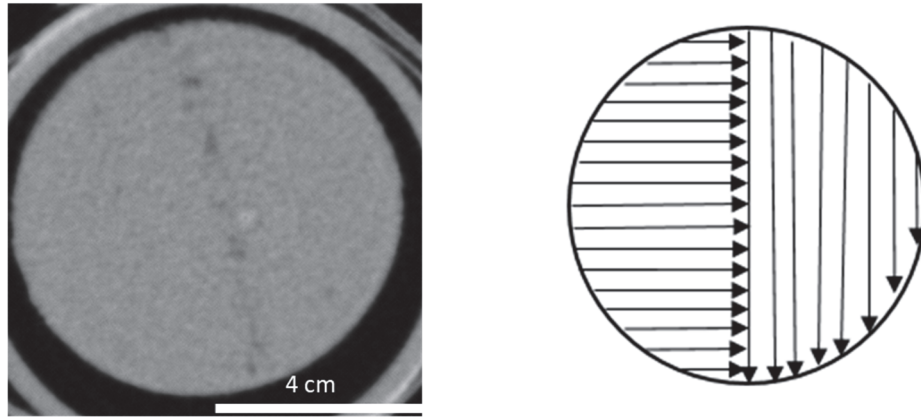


Figure 9. Slice from neutron tomography of a SS316L sample ($P=120$ W, $v=600$ mm/s, $t=40$ μm , $h=100$ μm with the associated scanning strategy forming the LoF line. [R.Drissi-Daoudi, PhD thesis]

In Figure 2 it can be seen that the range of laser parameters for defect-free parts is narrow, near the keyhole mode threshold, whereas the range of all possible parameters is very large. Obviously, the trial-error method is very costly and time-consuming. The relevance of equation (1) is often questioned [38], [39] since, for the same E , very different microstructures can be found [40]. Another equation taking into account the optical and thermal properties of the alloy has been developed to monitor the process and find conditions corresponding to the keyhole threshold. The normalized enthalpy (equation 2) considers an energy balance between the input and the dissipated energy, it is linked to the melt pool depth \bar{d} normalized by the laser spot size [41].

$$\overline{\Delta H} = \frac{\alpha P}{\rho(C\Delta T + L_m)\sqrt{\pi\omega^3 v D}} \quad (2)$$

$$\bar{d} = \frac{d}{\omega} \quad (3)$$

Where α is the absorptivity of the bulk material, P is the laser power (W), ρ the density (kg/m^3), C the specific heat ($\text{J}/\text{kg}\cdot\text{K}$), ΔT the difference between the melting and initial temperature (K), L_m the latent heat of melting (kJ/kg), ω the laser spot radius (m), v the laser speed (m/s), D the thermal diffusivity (m^2/s).

The equation accounts for the heat diffusion mechanism in the sample (as opposed to equation (1)). Ghasemi et al. [42] developed a translation rule based on the powder absorptivity parameters, to be able to transfer optimal process parameters from one alloy to the other, using the normalized enthalpy (Figure 10).

Introduction

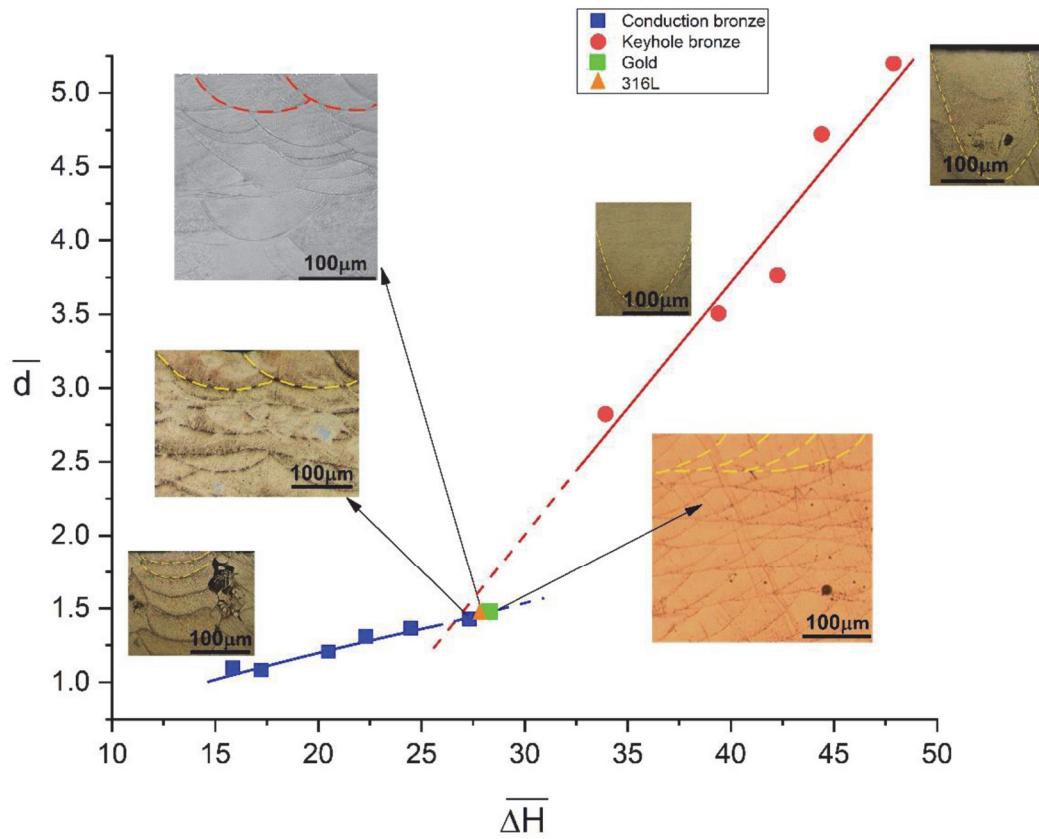


Figure 10. The translation rule applied to the normalized enthalpy of bronze samples versus the normalized melt pool of red gold (in green) and 316L (in orange). [42]

However, the laser-mater interaction still remains highly nonlinear and complex other phenomena such as spattering or denudation leading to defect creation remain stochastic and highly unpredictable.

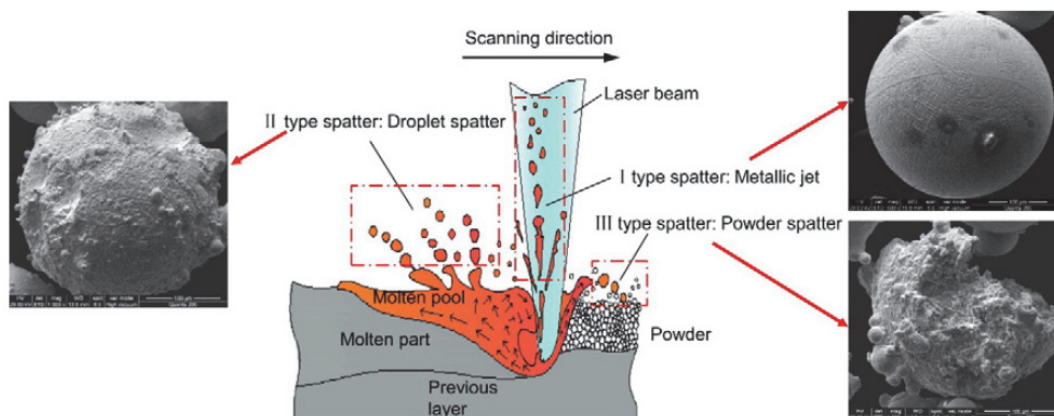


Figure 11. Formation mechanisms of different types of spatter: morphology of spherical splashing (type-I splashing); of coarse spherical morphology (type-II splashing); of irregular splashing (type-III splashing) [43]

Spattering can occur at low or high energy usually for high laser velocity. Three types of spatters are depicted in Figure 11. Type I: metallic jet is characterized by the recoil pressure coming from the evaporated pressure creating a depression below the laser. The high vapor surface flux exercises a pressure force that ejects the liquid metal. Type II: Droplet spatters are explained by surface tension temperature dependency, creating Marangoni effects and Plateau-Rayleigh instability which eject, from the surface liquid, metal with low viscosity [43]. Type III: Non-melted powder spatters at the front of the melt-pool are described by Matthews et al [25] who claim that the non-uniform heating of the particle, as the laser radius is on the order of particle diameter, leads to a strong lateral thermal gradient. Hence, one side of the particle reaches boiling and the extracted vapor's highly localized recoil pressure is strong enough to propel the particle. The momentum transfer with the neighboring particles explains the powder spattering. When spatters lie on the powder bed, it will create large LoF defects in the next line scans, as illustrated Figure 12 [23].

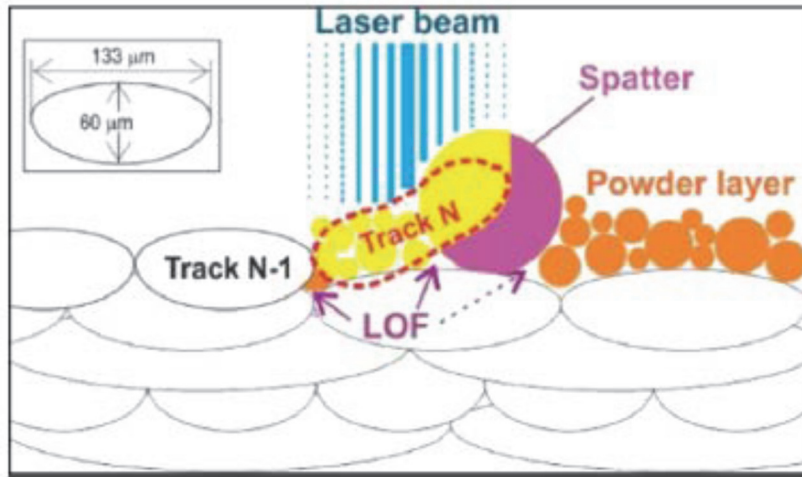


Figure 12. Schematic illustration of a powder layer with a portion (in yellow) under the laser beam that melts and form the track N with a big LOF, considering the presence of a spatter [23]

Denudation zones (Figure 13) appear when the strong flow due to the Marangoni effects makes the collapsing of a wall: the surface tension is then pulling adjacent particles and creates side pores close to the partially melted particles. It will also create pores in the next layer [25].

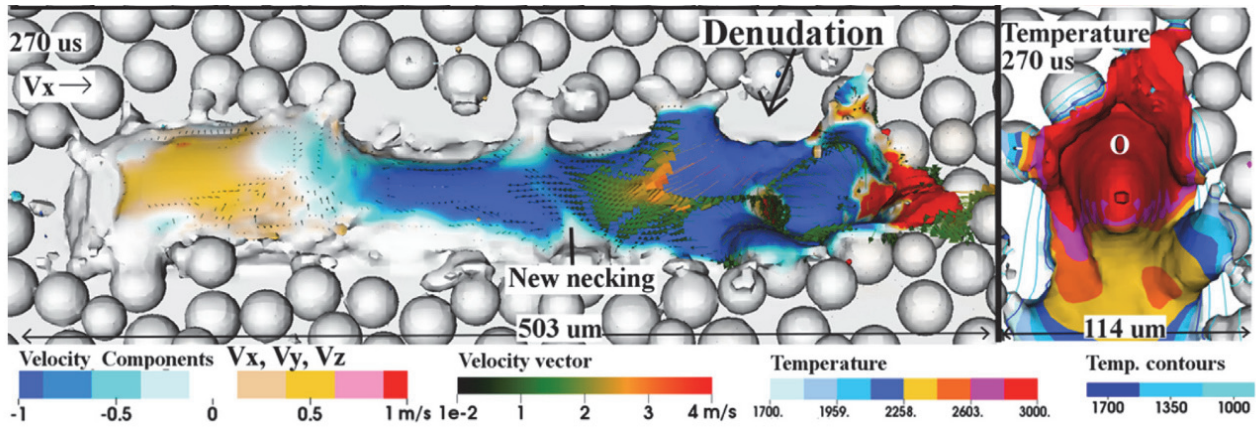


Figure 13. Simulation of a denudation zone apparition. [25]

This introduction to the defects formation in the LPBF process shows how difficult it is to monitor the process, from analytical approaches or through laser parameters optimization. LPBF remains a process with reproducibility issues. The need for a robust monitoring system to broaden the industrialization of this manufacturing process is the motivation for this thesis. The next sections will propose a literature review on the monitoring methods of laser processes, and contextualize the thesis objectives.

Chapter 2 State of the art

During a laser process, the laser beam hits the powder surface and it is absorbed, reflected, refracted, scattered, and transmitted. These phenomena result in heating, melting, vaporization, or plasma formation [44], which emit radiation, acoustic, and electromagnetic waves that can be monitored. The monitoring possibilities are here restricted to two categories: optical and acoustic methods. For both categories, the monitoring approach can be combined with Machine Learning solutions.

2.1 Machine Learning solutions

The learning algorithm can be categorized as supervised, semi-supervised or unsupervised. If the classes - input categories - are all or partially predicted and known examples, it is a supervised or semi supervised ML. In these cases, an expert has to previously label each class. A model is determined from the labelled data and then the label of a new piece of data is predicted knowing the previously learned model. When the system does not know the label or the nature and number of classes, it is called unsupervised. The system must target the data according to their available attributes, and classify them into homogeneous groups of examples. The similarity is usually calculated according to a distance function. It is then up to the operator to associate the meaning of each group and patterns in a group. The most used classification algorithms are briefly defined below.

Logistic regression (LR) algorithm is a supervised ML algorithm, analysing the relation between one or more independent variables to classify data into discrete classes. LR uses a sigmoid function to map the predictions and their probabilities. This S-shaped function converts real value into a value ranged between 0 and 1. If its output is greater than a predefined threshold the model will predict that the instance belongs to that class, if it is lower it will predict that it does not. The classification is based on the maximum likelihood, assessing concordance [45], [46].

K-Nearest Neighbour (KNN) algorithm is a non-parametric instance based supervised classifier. It uses the proximity to predict the class of a data point. The main assumption is that the points that are similar are found near one another. A class is assigned on the basis of a majority vote of the data point near the tested point [47], [48].

Support Vector Machine (SVM) algorithm have to find a hyperplanes with the maximum margin (the maximum distance between data points of the classes) in an N-dimensional space to distinctly classify the data points. Support vectors are data points closer to the hyperplanes that influence its position and orientation. The support vectors maximizes the margin of the classifier. The larger the margin the more confidence the classifier will have to predict a class. A class is predicted when the tested data is detected in the correspondent side of the hyperplane and its margin. [49]

Decision tree (DT) starts with a root nodes that expands on decision nodes and leaf nodes. Leaf nodes represent class labels (output of the decisions) and branches represent conjunctions of features that lead to those class labels. Each decision nodes is based on features of the dataset [50].

Random Forest (RF) algorithm consists of an ensemble of Decision Trees so that the decision about a new data sample is determined by majority voting. It is a nonparametric framework, and it is robust to the presence of outliers, noise, feature value transformations, and overfitting [51].

Gradient boost (GB) algorithm as the RF algorithm is based on the concept of ensemble learning. It combines multiple of weak classifiers to build a strong one. Several gradient descent procedures are combined to minimize some global loss. Different loss function can be chosen and optimized for a specific classification task [52], [53].

All the algorithms described above rely on the labelling of the classes as well as on the features chosen to feed the supervised algorithm. The choice of the features have a great influence on the accuracy of the classifier. The features in laser processes can usually be extracted from the time domain, the spatial-temporal domain, the frequency domain or the time-frequency domain of the data.

On the other hand, clustering in machine learning is a technique to group unlabelled datasets into different clusters of similar data points. Similar patterns are identified to group the data. It is an unsupervised learning method. The clustered can as well be fed as input to a supervised algorithm. A popular algorithm is the K-Means clustering Algorithm. K defines the number of pre-defined clusters that need to be found. It is a centroid-based technique. The aim is to minimize the sum of distance between the data point and their clusters [54].

Neural networks (NNs) also known as artificial neural networks (ANN) is based on nodes layers. Each node is called artificial neurons and model the neurons in the biological brain. ANNs contain an input layer, one or more hidden layers, and an output layer. Each artificial neuron, connects to another and has an associated weight, transfer function and a threshold. The node is activated and sends data to the next layer trough the transfer function if the output is above a specified threshold [55], [56]. An ANN model has to be trained and the difference between the processed output and the target output. The model adjusts its weights accordingly. After successive adjustments (epochs) the NN produce an output similar to the target and reaches a specified level of accuracy. This method of learning is called back-propagation rule [57]. The information from inputs is fed forward. Multilayer perceptron (MLP) is a fully connected class of ANN using the backpropagation training. Each node is one layer connects to every node in the following layer with a certain weight.

Convolution neural network (CNN) are fed forwards ANNs where convolution layers are used in the hidden layers. It has attracted a lot of attention and research due to high performance for supervised or unsupervised classification tasks of complex or noisy datasets. CNNs have a lot of hyperparameter to optimize in order to

reach proper accuracy for a specific application (kernel size, number of layer, type of layer etc.). Some architectures have been developed and proven efficient for a range of application [58]. More information on deep learning CNN can be found in [55], [59].

Spectral CNN are as well developed reaching high performance. They combine deep learning capabilities, inherited from conventional CNNs, and spectral graph theory [60]. In CNN the spatial is recovered from the input data using kernels while in SCNN a weighted graph G is used. [61], [62].

Another class of deep neural network found in the literature is a deep belief network (DBN). Its specification is that it is composed by multiple hidden units with connections between the layers but not between units within each layer. It is a composition of restricted Boltzmann machines (RBMs) [63].

Finally, recurrent neural network (RNN) are designed for times series or data involving sequences. Indeed, unlike feedforward NNs they allow previous outputs to be used as inputs. They have feedback connections. Each recurrent layer has an input weights set and a second one for the hidden unit [64], [65]. A popular RNN algorithm is the long short term memory (LSTM) capable of handling long-term dependencies. [66]

2.2 Optical monitoring

Optical monitoring methods can be differentiated as spatially resolved, when a camera (optical or IR) is used, spatially integrated when photodiodes or pyrometers are involved, and spectrally resolved when spectrometers are employed [44].

IR cameras measures melt pool size and temperature, while high-speed cameras monitor the powder bed / laser interaction. These methods are the most reported in the literature [39], [67]–[76]. The monitored length scale is typically about 10-100 μm , and the laser speed is usually in the range of 100-1000 mm/s. Thus, the cameras should have a high degree of spatial resolution and fast time response, increasing the cost as well as the amount of data to manage. Furthermore, these methods can only monitor the top surface layer.

Photodiodes [77]–[79] and pyrometers [80] convert the light emission (LE) into a single voltage value, decreasing the amount of data to manage but also the accuracy. The surface temperature is measured. The wavelength range that the semiconductor photodiode perceives is limited by optical filtering. More than one photodiode can be combined to extend the possible output data monitoring [79]. They are fast sensors and sensitive even at low cost. Light Emission (LE) is measured by spectrometers. The intensity can be a function of wavelength or frequency. Spectrometers cover a wide frequency range from gamma rays to microwaves [81], [82].

Combining different methods is a solution that benefits from the advantages of several techniques. High-speed camera and temperature control techniques are often coupled. Melt-pool temperature monitoring, with a pyrometer/camera combination, has been proven to be able to determine balling of the powder [83] and spattering behavior [68], [84]. A coaxial CMOS camera and a photodiode system to monitor the melt-pool have been associated and could dynamically adjust the laser power according to varying thermal conductivity regions

within the build [69], [85]. Spectrometers are coupled with interferometers to benefit from both methods of reflection in the process [86]–[90]

Gaikwad et al. [91] combined pyrometer, optical sensing and a machine learning algorithm. They studied the effect of varying common LPBF process parameters, i.e. laser power (P) and laser velocity (V), on the quality of single laser tracks. Four categories have been identified: keyholing, conduction, lack-of-fusion, and balling. A designed sequential decision analysis neural network is used for the classification task. Its architecture is presented in Figure 14. The physical reasoning is included, facilitating interpretability and outperforming the other tested methods (CNN, LSTM and RNN). 121 laser power and laser velocity combinations were printed. Between 6 and 10 lines of each combinations were deposited for a total of 1009 single tracks. 60% of those lines are randomly chosen for the trained, 20% for the validation and 20% for the testing.

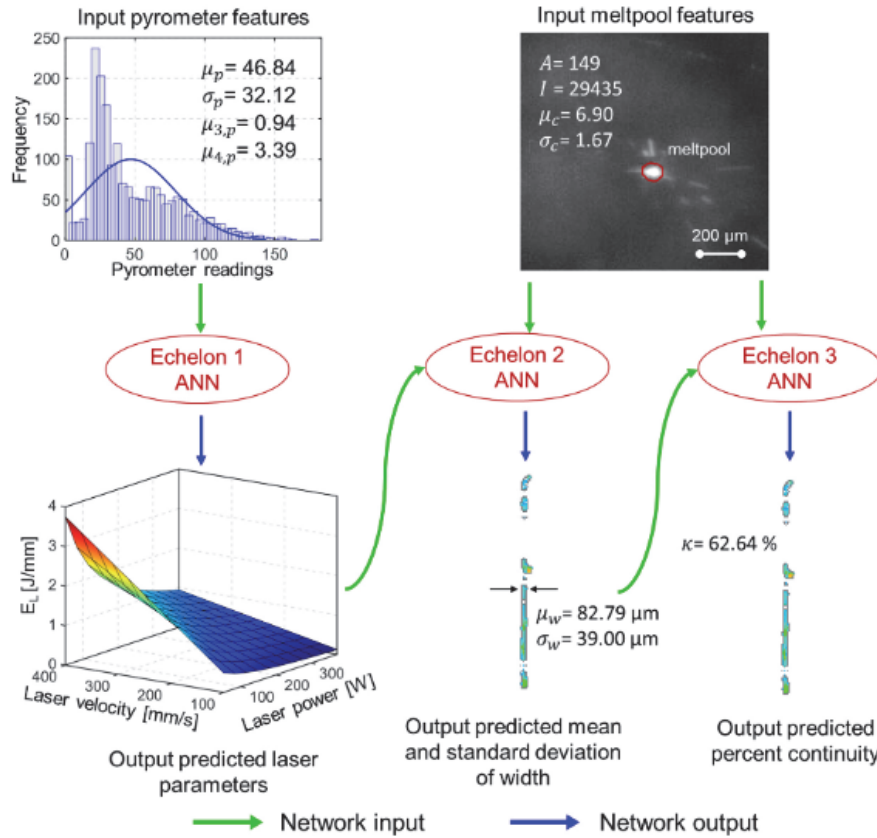


Figure 14. Architecture of the designed sequential decision analysis neural network taking into account pyrometer measurement in the first ANN echelon and high speed camera images for the 2 next ANN echelons as well as the outcome of the first ANN echelon. [91]

Thermal imaging is often combined with ML algorithms to monitor the LPBF process. Mahmoudi et al. [92] used thermal images from a two-wavelength imaging pyrometer, in LPBF fabrication of 300 layers of 17-4

PH stainless steel with artificially induced defects. Multiple classification techniques were investigated to distinguish good conditions from anomalies. LR, KNN, SVM and RF were tested and achieved over 90% classification accuracy. The algorithms were trained on 3 layers (225 ROIs) including faulty and faultless region and tested on 1 layer (75 ROIs) also including both categories. Khanzadeh et al. [75], [93] present thermal monitoring based on dual-wavelength pyrometer measurements as well. They captured time-varying melt pool signals of a Ti-6Al-V thin wall fabricated by LPBF. The categories are labeled as either pores or normal melt pools, according to X-ray tomography measurements. They used melt pool characteristics (e.g. length, width, longest axis) as input for several supervised classification techniques (KNN, SVM, DT); they all achieved over 95% accuracy. One parameter for a thin wall is processed and the algorithms were trained on 80% of the dataset randomly chosen and tested on the remaining 20%. The methodology is described Figure 15. Similar methodologies can be found in Mitchell et al. [94].

Supervised ML algorithms such as SVM, or RF have been used to classify normal building and undesired flaw occurrence from high resolution single lens cameras, with an accuracy of 80% [95]. Colosimo and Grasso studied the temporal domain and the spatiotemporal domain in order to identify both the time and location of defect occurrences, the used a k-mean clustering algorithm for defect detection [96].

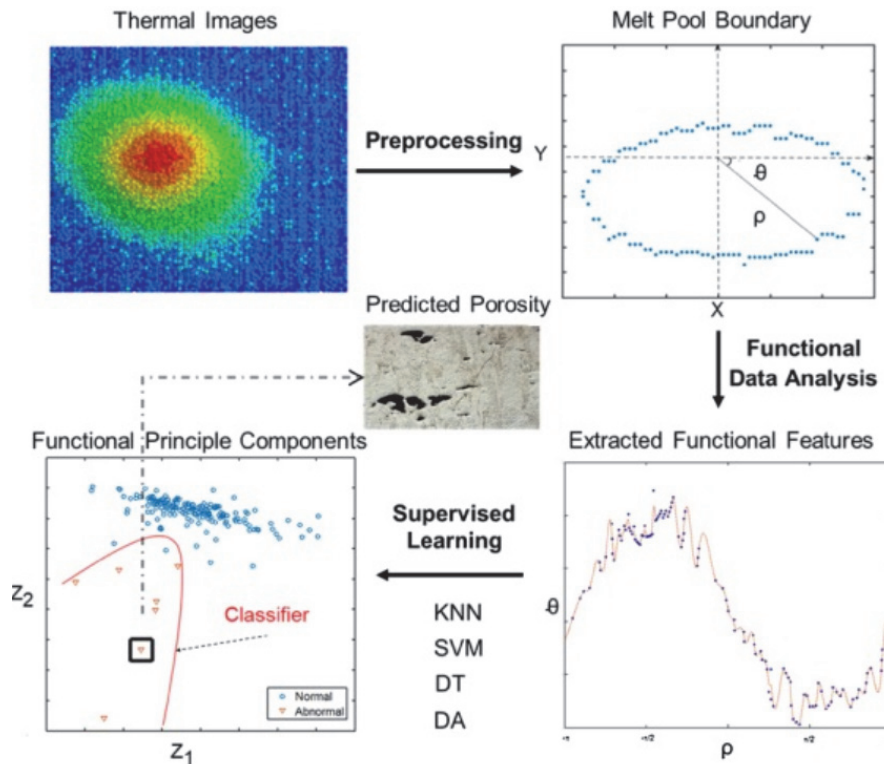


Figure 15. Schematic methodology of supervised classification of defect formation from the extracting of melt pool characteristics from thermal images. [93]

Several studies proved that CNN was a performant classifier for thermal imaging, while avoiding the features extraction step [97]–[100]. Kwon et al [99] classified seven levels of laser power conditions of a stainless steel

workpiece. The algorithm is trained of 88% of the dataset of each power conditions and tested on the 12% remaining of each power condition. The effect of hyperparameters of the CNN network was studied; they achieved a classification accuracy of 98.9 % Baumgartl et al. [100] used thermographic off axis images to classify delamination and metal splatter in the LPBF process of H13 steel. A CNN network was used for the classification task and achieved 96.80% of confidence. The dataset was split for the training and the validation. The model was evaluated with computing class activation gradient-weighted heatmaps. The heatmap indicated what part of the piece is used for the classification. It indicated that the temperature difference between the delaminated part and a non-delaminated part was determinant for the classification decision. The heatmap with the part responsible for the final decision is shown Figure 16.

CNN has proven effective for detecting and classifying anomalies from optimal conditions from high-speed camera images as well [73], [101]–[105]. Yazdi et al. [102] fed wavelet transforms extracted from raw optical images and reached a better classification with their hybrid deep learning model then with the classical machine learning method (SVM, KNN, LR, classical CNN) tested. Caggiano et al. reached as well 99.4% classification accuracy with a bi-stream CNN. Scime and Beuth [104], [105] worked on the detection of layer delamination and geometric deformation in the fabrication of Ti-6Al-4V and stainless steel 316L. A multi-scale CNN analyzed the images at two scales. The same group also examined [106] melt pool optical imaging anomaly detection of In718 LPBF pieces. The features extractions was unsupervised, by the use of histogram of gradients clustering, then followed by a supervised classification with SVM. Three categories (balling, under-melting, keyholing porosity) are classified, reaching 85.1% accuracy.

Larsen et al. [107] used two high speed cameras images to classify four categories (optimal, stable, marginal and unstable) in 316L LPBF pieces. One set of parameters per category is chosen. However, one build is kept for training, a second build for validation, and one for testing purpose. A CNN-based semi supervised algorithm is trained and reaches at least 93% classification accuracy.

Ye et al. as well as Grasso et al. [108], [109] used an IR camera to monitor the plume and spatter generation, to differentiate melting regimes and defects. Ye et al. classified five melting modes (from over-melted to under-melted) with 5 different parameter sets, leading to 5 different densities in 304 L stainless steel, with a deep belief network (DBN). They achieved over 80% classification accuracy. Grasso et al. [109] used an SVM to classify defects generation from good conditions and reached over 90 % of classification accuracy.

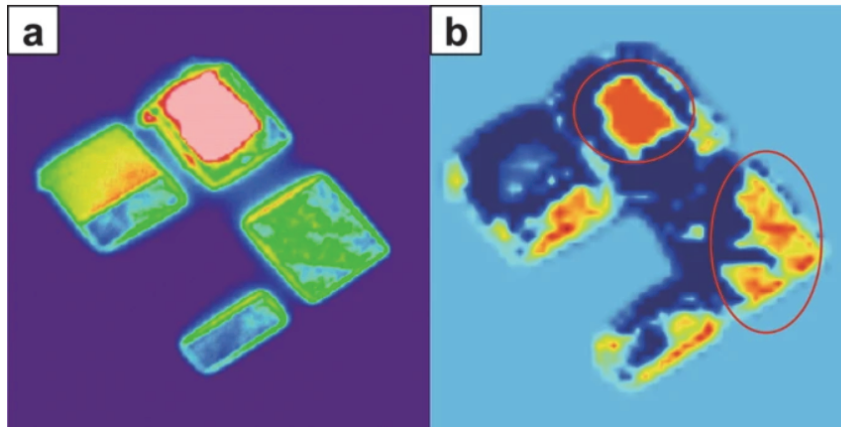


Figure 16. Heatmap for a delamination defect. A. the thermal image b. the heatmap with areas of high importance for the classification highlighted.[100]

Zhang et al. [110] used optical images to extract not only characteristics of the 316L melt pool, but also plume and spatters from single tracks of LPBF. Three qualities of line were achieved with three different powers. SVM and CNN were compared for the classification task. They both reached good classification accuracies, but CNN outperformed SVM with an average accuracy of 92%. Another study by Repossini et al. [111] considered the inclusion of spatter characteristics for the classification from optical images. Three qualities (under-melted, normal-melted and over-melted) of 18Ni pieces were processed. It was confirmed that including spatter features improves the accuracy of classification. The presented studies split the datasets for the training and the testing of the algorithm.

2.3 Acoustic monitoring

Acoustic Emission (AE) is often used as non-destructive method to monitor laser processing. The advantages of AE are the easier management of one dimensional data, and the high sensitivity of accurate fast and relatively cheap sensors. The most important feature is the possibility to detect any defect not only at the surface but also in the bulk during LPBF processing [112]–[114]. The cracks initiation, propagation, and 3D reconstruction can also be studied with AE [115], [116].

Two types of acoustic methods can be distinguished. Ultrasonic waves can be focused into the process zone: it is then possible to identify the presence of defects and to estimate their dimensions by inspecting the scattering pattern of the waves propagating in the material. It is, however, often desirable to have precise information about the nature of the defects [117]–[120]. The second type is a direct measurement of the signals emitted by the process and defect formation. Three sensor types are described in the literature: structure-borne AE (SBAE), mostly piezoelectric sensors which need to be in direct contact with the process zone; air-borne AE (ABAE), mostly condenser microphones; and optical Fiber Bragg gratings (FBGs). ABAE sensors are reported to have a limited frequency range and be less accurate, but the coupling of SBAE with the process piece or build plate is not straightforward and their use is still restricted. FBG is an interferometric structure,

imprinted inside the core of an optical fiber with unique spectral characteristics of reflectivity. The acoustic waves created during the AM process result in periodical extensions/compressions of the optical fiber core. These deformations affect the reflectivity properties of the FBG that follow the behavior of the upcoming pressure waves. The high sensitivity and time resolution of those sensors make them very versatile for acoustic applications but their utilization necessitates expensive tunable lasers [121], [122]. They are placed in the atmosphere near the process, but their functioning mode is closer to SBAE. They record information related to the distortion and the mass density related to the atmosphere near the melt pool.

2.3.1 Acoustic monitoring in laser welding

Acoustic monitoring was widely investigated for laser welding applications. It was deduced that different welds lead to different AE due to differences of pressure generated by the molten pool, plasma generation, thermal stress, metal vapor, or keyhole oscillation.

Bastuck et al. [123] compared ABAE and SBAE sensitivities at high frequencies (ABAE: 700 – 1200 kHz, SBAE: 400 1000 kHz). Short-Time Fourier Transform (STFT) spectrograms were extracted from the acquired signal during laser welding of three steel alloys with one zinc coating. The power of the laser was linearly increased in the range from 80 W to 2000 W to achieve different weld depths. Both sensor signals could be correlated to the penetration depth. The signal of the SBAE vanished when the weld reached complete penetration. Moreover, the presence of zinc coating was only detected by the ABAE sensor. Figure 17 presents these results schematically.

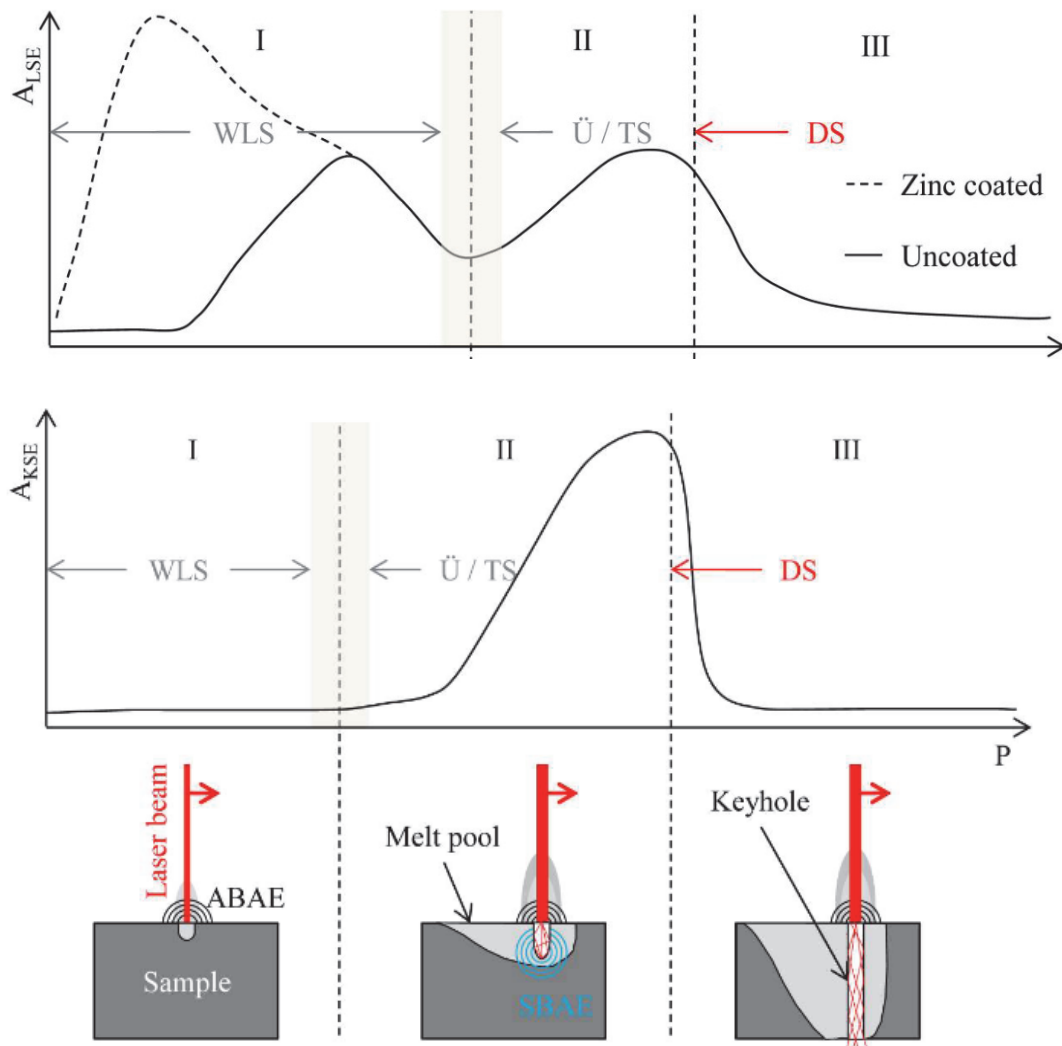


Figure 17. Schematic model for ABAE and SBAE during laser welding. The upper panel shows a typical trend for ABAE with respect to the laser power, the middle panel presents the trend for SBAE, and the lower panel a schematic representation of the soundwaves for each step of the welding penetration. [123]

Most studies were first focused on the use of ABAE with a frequency range up to 50 kHz [124]–[131]. Mao et al. [132] compared frequency bands amplitudes for several laser powers, leading to different weld conditions in Al 1100 sheets. They detected keyhole welding between 3 kHz and 9 kHz. The microphone had a flat response from 1 kHz to 17 kHz. The amplitude of acoustic emission increased, at these frequencies, with penetration depth. These frequencies appeared to be associated with the hydro-dynamical instabilities leading to the transient closure of the keyhole. Lee et al. [131] ranged the information of interest in the frequencies from 500 to 2000 Hz for welding of steel AH36. Nava-Rüdiger et al. [127] studied the influence of the change of laser power in the frequency domain of the AE signals acquired. The amplitude of the frequencies around 400-600 Hz increased when the laser power increased, leading to an increase in penetration depth.

In 1994 Farson et al [126], [133], combined ABAE with a classifier to discriminate the good welds and the welds with insufficient penetration. Spectrograms of acoustic signals acquired with an ABAE sensor, with a

frequency spectrum from 50 Hz to 20 kHz, were recorded from laser lap welds of 304 stainless steel. The amplitude difference in the range of [1-2] kHz could determine if the weld was penetrating enough. The reliability of the classifier was found to be above 90 %.

Gu and Duley [125] in 1996 used an ABAE flat response from 0 to 20 kHz frequency spectrum.[125] Normalized acoustic spectra emitted during laser welding of 1 mm thick mild steel were investigated. They claimed that the AE in the 12–17 kHz frequency range is related to instabilities in the keyhole, and that changes can be measured when a phenomenon such as insufficient penetration or formation of porosities occurs. They used a linear discrimination algorithm from spectrum components to classify overheated, fully penetrated and partially penetrated welds. The accuracy ranged from 67% to 83%.

Luo et al. [129] used an electrets microphone with a frequency spectrum from 0 to 20 kHz to record AE from the laser welding of an undefined alloy. They used a designed ANN to classify a good weld from a defective one, with an accuracy up to 85%. With an FFT and a wavelet transform analysis, they highlighted that a good weld was mostly detectable from 10 to 20 kHz. The sound intensity from 10 to 20 kHz was however much higher in keyhole laser welding than that in conduction mode laser welding, as the pressure was directly related to the density and temperature of the electrons in the plasma. Moreover, they detected a decrease of amplitude around 781 Hz and 1562 Hz, which as associated to defect formation.

Huang and Kovacevic [130] employed acoustic signals from an ABAE of frequency sensitivity from 20Hz to 20 kHz to monitor the laser welding of steel DP980 plates. 28 different welding parameters were used to achieve different weld depths, and the corresponding acoustic signals were acquired. A noise reduction method was applied to the AE signals. Measurement of the depth of each weld was performed with optical microscope images of sample cross-sections. Sound pressure deviation (SPD) and band power (BP) ranged the information of interest from 500 to 2000 Hz. The different features were fed to a NN (Figure 18) and the trained model was applied on 14 other welds: the quality of the prediction of depth was dependent on the chosen 14 training parameter sets. If the power of a weld was not present in the training dataset the error was higher. Proving that the algorithm was detecting changes of parameters and not the laser-matter interaction. The mean error between the depth and the prediction could vary from 6% to 23%. A multiple regression analysis indicated that the relationship between the acoustic signatures, the welding parameters, and the depth of weld penetration is linear.

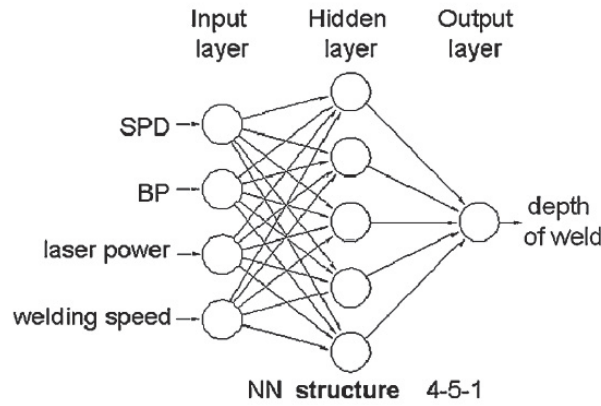


Figure 18. Schematic architecture of the ANN used by Huang and Kocacevic [130]

Two main studies were carried out for laser welding, combining SBAE with ML solutions. Shevchik and Wasmer [114], [134], [135] used a piezoceramic transducer with a frequency spectrum up to 1850 kHz to monitor the laser welding of Titanium plates. They used a RF and a GB ML algorithm to distinguish with good accuracy (from 74% to 95%) between stable keyhole weld, unstable keyhole weld, conduction welding and spatter generation (Figure 19).

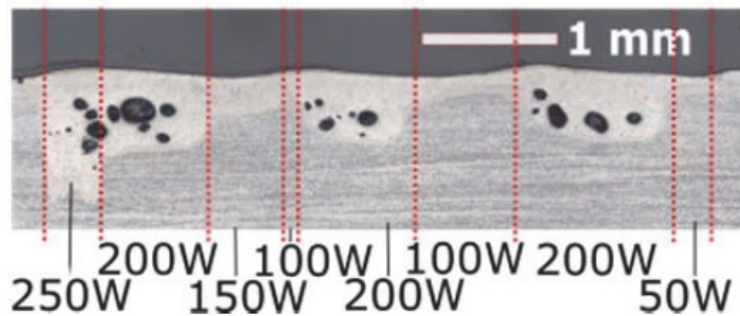


Figure 19. Cross section of the weld with different power inputs leading to conduction weld, keyhole weld, or keyhole with porosity formation weld in a Titanium plate [134]

Lee et al [136] used a back-propagation ANN (presented Figure 20) to classify three qualities of the weld (good weld, unsuccessful, and with defect) from the frequency range extracted from SBAE signals during the welding process of stainless steel 304 plates. They reached a classification accuracy of 88%. 15 different process conditions were considered, and the labeling was performed by optical measurements. The frequencies of interest were from 100 kHz to 500 kHz, resulting from the fluctuation of the inert gas rather than from the welding process.

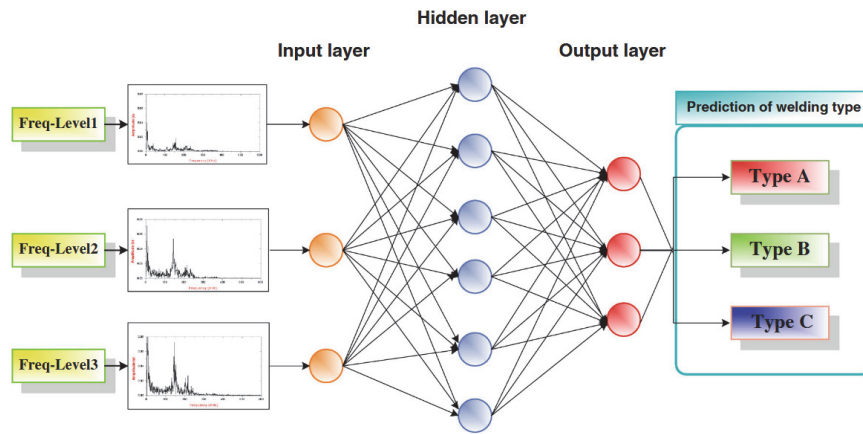


Figure 20. The ANN architecture used by Lee et al using frequency level to classify different weld type.[136]

However, it has to be noted that the presented studies investigate different alloys with or without coating, and the presence of a coating could change the frequencies of interest.

2.3.2 Acoustic monitoring in Additive Manufacturing

Less research has been performed on AE monitoring of additive manufacturing. The laser-matter interaction due to the powder and the controlled atmosphere is more complicated and is noisier. However, especially with the coupling to machine learning (ML) solutions, the method is gaining weight and progressively shows great capabilities.

2.2.2.1 Without Machine Learning

Ito et al. [137] acquired AE signals from a wireless piezoelectric sensor for the monitoring of LPBF single laser tracks, or full layers. The analysis of the amplitude of the raw signal allowed to localize keyholes and cracks in a nickel-based alloy with an error of a few millimeters. The analysis was carried out on 3 different singles track conditions and on 6 different multitrack conditions. An example of the correlation of the defects with the acoustic signals is presented in Figure 21. The authors explain the delay between the occurrence of the defect and the change of amplitude to the time needed for the sound waves to travel until the sensor. The more distant the sensor from the printed piece, the higher the delay. The chosen SBAE has a flat response and high sensitivity between 150 and 600 kHz, except at the resonance frequency of 250 kHz. Two piezoelectric sensors were glued on top of the substrate as only one layer was printed.

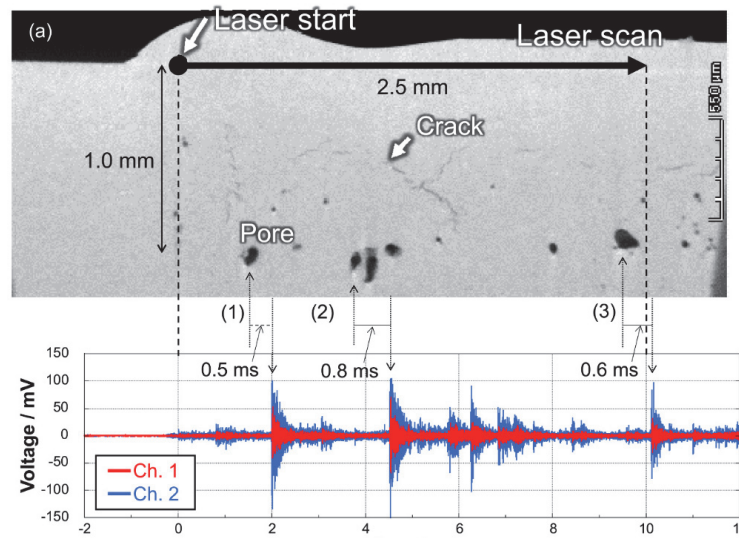


Figure 21. Cross section of a LPBF single line with keyhole and cracks formation with the acoustic signal associated [137]

Gutknecht et al. [138] compared a microphone, an on-axis two-color pyrometer, and an off-axis thermography camera for the monitoring of the LPBF process for 316L stainless steel. They measured the difference in the temporal resolution as well as the influence of the distance, the location, different scanning directions, and the laser speed. They used twelve different process conditions. For all sensors, they recorded process deviations such as lack-of-fusion, defocusing, and spatter. The distance and inclination of the microphone show a frequency-dependent dissipation, especially critical above 300 kHz. The microphone chosen was a very sensitive ABAE, a membrane-free XARION Eta250. It is an optical microphone using the principle of interferometry to measure sound in a frequency range of 10 Hz to 1 MHz. Its sensitivity is 40 times higher than the camera and 15 times higher than the pyrometer. The frequencies below 40 kHz were filtered and considered as noise and machine-related. The ABAE high temporal resolution (about 80 μ s) is applicable only from 100 kHz because of reverberation in the build chamber. A spectrogram of one scanning layer extracted from the AE signals is presented in Figure 22. The authors detected millisecond phenomena at higher frequency bands. They highlighted the advantages to have several different monitoring methods simultaneously.

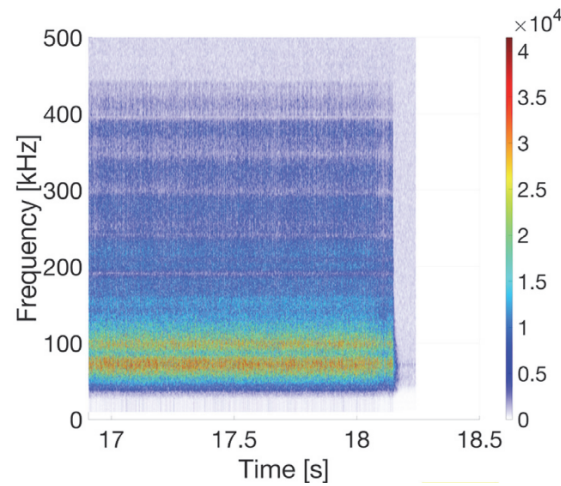


Figure 22. Example of a spectrogram of one scanning layer extracted from the AE signals acquired with a high sensitivity Xarion microphone [138]

2.2.2.2 Combined with Machine Learning

Taheri et al. [139] used the frequency spectrum features of AE signals to classify with a K-means Algorithm clustering the Directed energy deposition (DED) process conditions. Spectral features were used for the clustering in two bands of frequencies (below and above 800 kHz). Three conditions - optimal, low laser power and low powder feed- were classified with 87% accuracy confidence. One parameter set per condition was used. The AE signals were acquired by four piezoceramic transducers attached below the build plate (Figure 23). Their frequency range is 100-2000 kHz. They obtained a better clustering and a better classification accuracy when the features were extracted in the higher frequency band. The alloy investigated was Ti64.

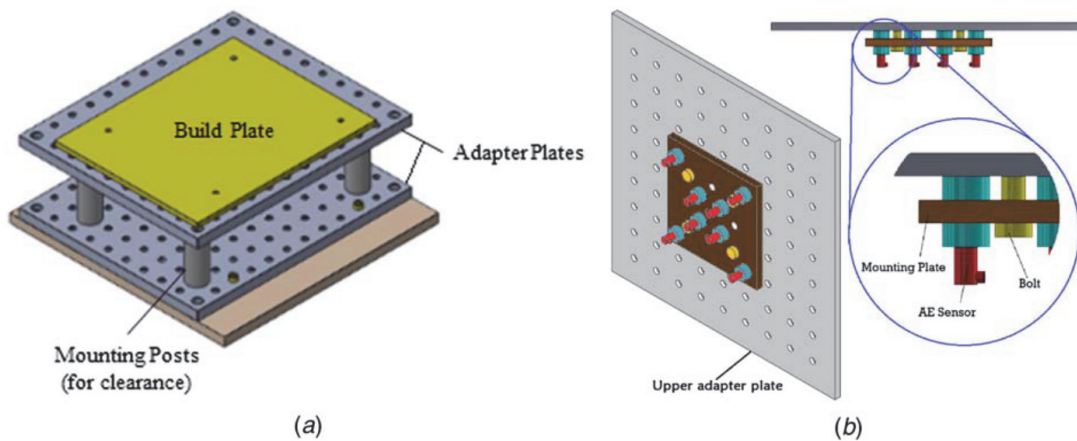


Figure 23. The schematic representation of the build plate with the four piezoceramic transducers attached below. [139]

Eschner et al. [140] studied the use of a mass less piezoceramic sensor for the monitoring of stainless steel in LPBF. 54 cubes were printed with 3 levels of laser power, 3 levels of scan speed, 2 levels of hatching distance, 3 levels of complexity. The level of complexity is illustrated Figure 24. The SBAE sensor is placed below the substrate and the different levels of complexity are printed to study the influence of the recorded AE signals. The difference in laser power, scan speed, and hatching distance resulted in different densities. Three density classes were discriminated (Figure 25) and used as a measure of quality. Short-Time Fourier Transform (STFT) are computed, dividing a long time into short time period and applies a Fourier transform in order to extract spectrograms from the AE signals. The spectrograms are then fed to a designed ANN. The ANN is illustrated Figure 26. 70% of the data are randomly used for the training and 30% are kept for the validation. A classification accuracy of 88% was obtained. No significant difference between the complexity levels was highlighted.

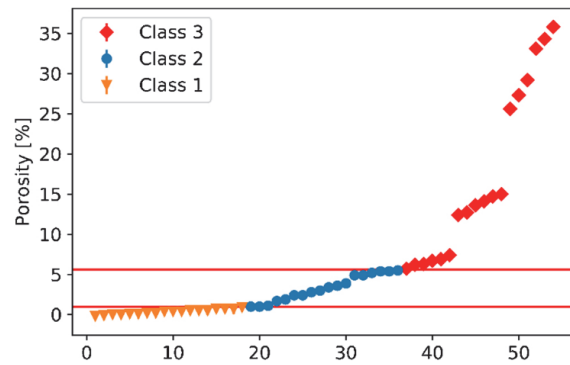
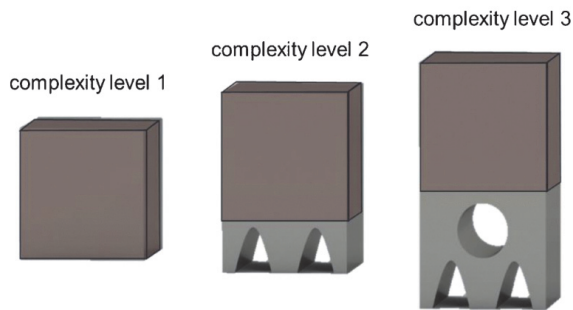


Figure 24. Level of complexity below the printed and recorded layers.[140]

Figure 25. Porosity density of the printed cubes divided in three classes.[140]

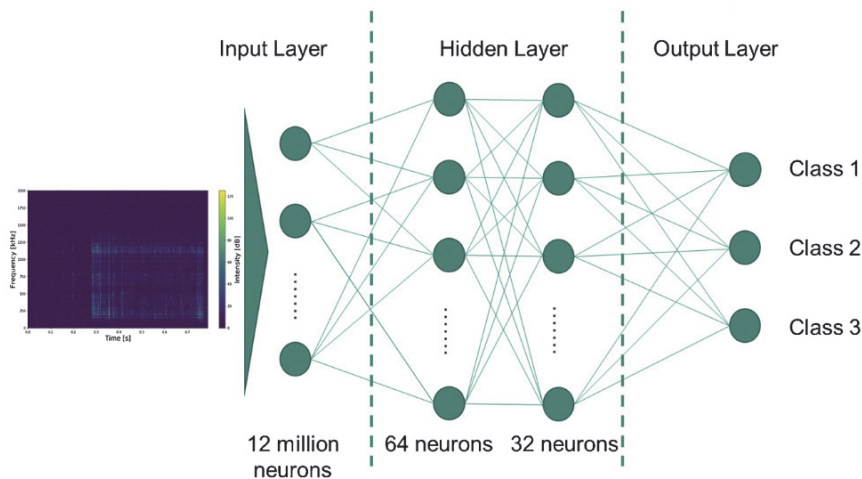


Figure 26. The ANN achitecture used by Eschner et al.[140]

In Shechnik et al. [121], AE signals were collected during LPBF of stainless steel CL20ES with a Fiber Bragg Grating (FBG). Three LPBF regimes were studied: poor quality (LoF porosity), medium quality (keyhole

pores) and high quality (conduction mode), with one set of laser parameters associated to each regime. Figure 27 presents the corresponding micrographs. The study was performed in the time-frequency domain with the use of wavelet transforms. The spectrogram goes until 200 kHz and the information seems to be scattered below 100 kHz. The authors compared the classification results of a classic CNN and a Spectral CNN, and classified successfully with more than 83% confidence the three classes. The SCNN performance was better than a classical CNN. In a following work [122], they used two running windows (as illustrated in Figure 28) with various time spans as input to a SCNN to address the localization of defects. The classification accuracies varied between 73 and 91%, depending on the time span of the running window and the process quality. A localization of 2.2–5.8 mm² was achieved for a given layer. The authors achieved a compromise for classification accuracy and localization precision with a running window of 80 ms.

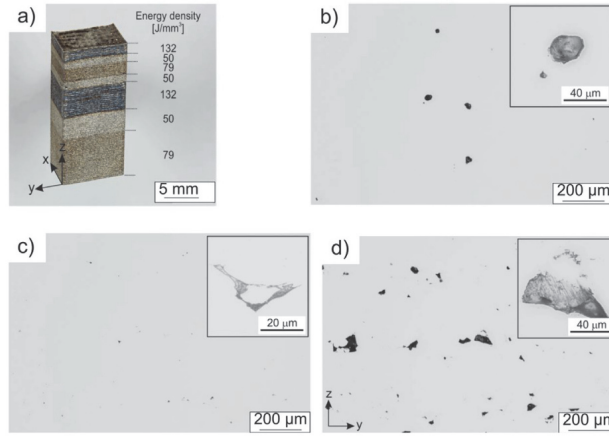


Figure 27. The three LPBF regimes classified in [121] b. medium quality (keyhole pores), c. high quality (conduction mode) and d. poor quality (LoF porosity)

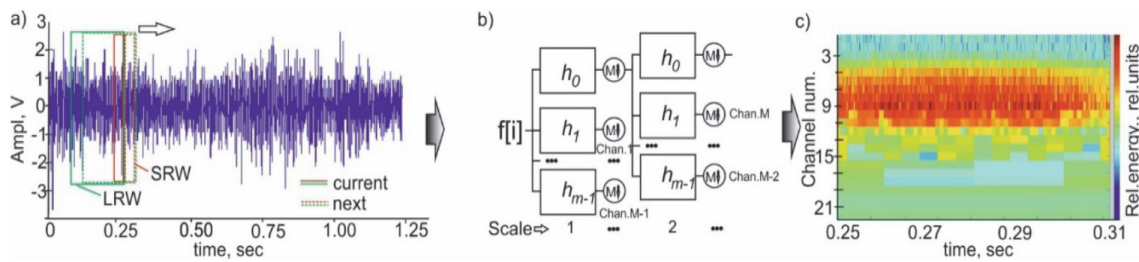


Figure 28. The double running window methodology for localization purpose [122]

Ye et al. [141] studied the monitoring with ABAE signals from single LPBF lines of 304 stainless steel, using a pulsed laser. A microphone with a frequency response from 0 to 100 kHz was used to acquire the AE signals. Five categories were considered: balling, slight balling, normal, slight overheating, and overheating (presented Figure 29). First, with one parameter set per condition, the classification results are compared according to the data treatment: raw data, after FFT, or after FFT and noising. Three ML algorithm classification results are

compared as well: DBN, MLP, and SVM. 60% of the data are taken for training and 40% are kept for testing and validating. For the three algorithms, the classification was more than 20% better with FFT or FFT and denoising data treatment. However no significant difference was highlighted between the FFT and FFT + denoising treatments. The DBN and SVM have comparable classification result ($> 95\%$) but are 13% better than the MLP results. A DBN is then trained with two sets of parameters per category where random parameter combinations were employed for testing and validating. A classification accuracy of 93% is found. The FFT analysis narrowed the range of frequencies of interest below 65 kHz.

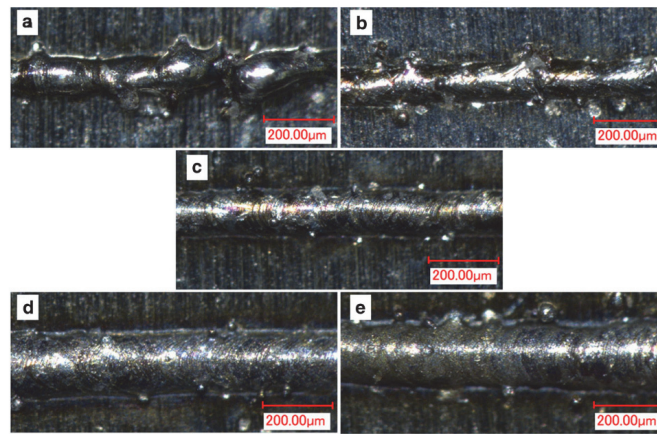


Figure 29. Five categories are considered- balling, slight balling, normal, slight overheating, and overheating of single tracks studied in [141]

The experimental plan of Tempelman et al.[142] is presented in Figure 30. Several lines are processed in one LPBF layer of 316L stainless steel powder. A low-frequency range microphone (the authors do not specify the frequency range of sensitivity) placed on one side of the build chamber, above the build surface, approximately 25–30 cm from the center of the build area, records the emitted AE signals. The chosen laser parameters are scattered in the 2D power/speed processing maps. This results in keyhole porosity formation at certain positions. X-ray radiography segments confirmed the presence of keyhole pores or the absence of pores. A SVM algorithm is then used to classify the two categories, 75% of the data were randomly selected for the training and 25% for the testing. Different window sizes (2.5 ms, 3.5 ms, 5 ms and 7.5 ms) are compared as well as different features fed to the algorithm. Ensemble empirical mode decomposition (EEMD) features and FFT features led to high accuracy classification (92%) for all considered window sizes. Classification with basic statistical features had low performance (around 65%). For the shorter window size, EEMD performed (94%) a bit better than FFT features (92%) and for 7.5 ms window size, FFT features delivered 97% classification accuracy. However, FFT features were computationally cheaper to extract. Moreover, a trade-off had to be found between classification accuracy and spatial resolution. The authors confirmed the results of Shechnik et al. The content at signal frequencies from 10 to 50 kHz was found to be the most important for detecting pore formations. The reproducibility was evaluated by testing the trained SVM on 4 others plates processed with the same parameters.

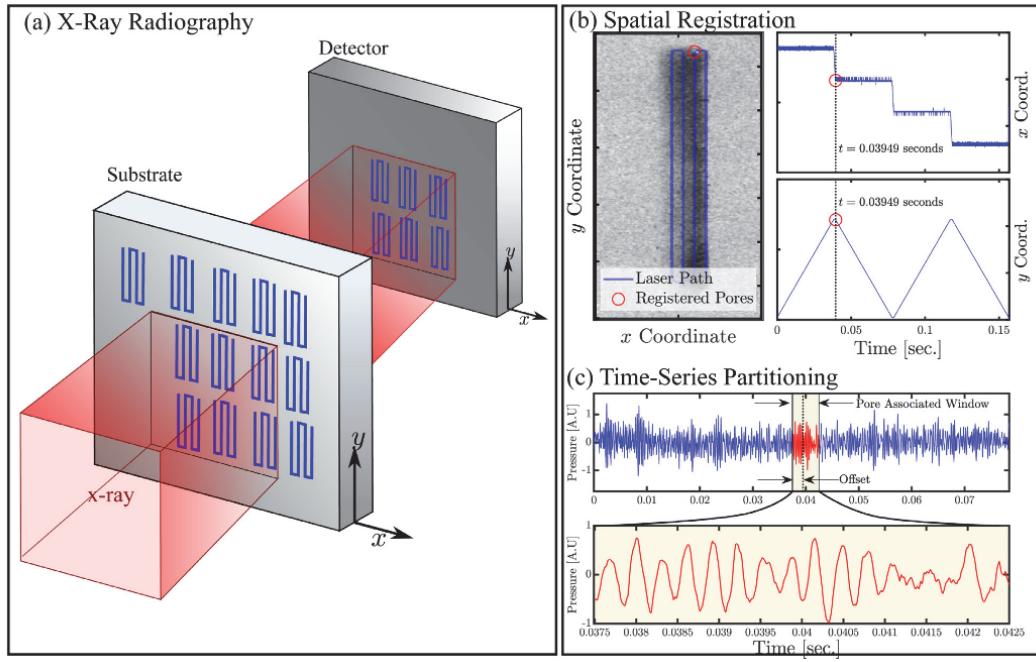


Figure 30. Experimental plan used for the segmentation between keyhole formation and non-pores segments in [142]

A reliable monitoring model in which the LPBF process parameters are controlled in real-time, using ML with AE, and that differentiates defects in the whole sample volume, is still lacking in the literature. A major drawback in the existing work is the lack of generalization and reproducibility of the monitoring methodologies. By generalization, we mean that the algorithm should be able to identify process regimes (categories) from AE signals recorded with laser parameters that were not used for the training of the algorithm. The development of such a model is possible only if a significant part of the learning relates to laser-material interaction and the related physical phenomena.

References

- [1] G. N. Levy, R. Schindel, and J. P. Kruth, "RAPID MANUFACTURING AND RAPID TOOLING WITH LAYER MANUFACTURING (LM) TECHNOLOGIES, STATE OF THE ART AND FUTURE PERSPECTIVES," *CIRP Annals*, vol. 52, no. 2, pp. 589–609, Jan. 2003, doi: 10.1016/S0007-8506(07)60206-6.
- [2] "Wohlers Report 2021," *Wohlers Associates*. <https://wohlersassociates.com/product/wohlers-report-2021/> (accessed Sep. 19, 2022).
- [3] T. DebRoy *et al.*, "Additive manufacturing of metallic components – Process, structure and properties," *Progress in Materials Science*, vol. 92, pp. 112–224, Mar. 2018, doi: 10.1016/j.pmatsci.2017.10.001.
- [4] C. Y. Yap *et al.*, "Review of selective laser melting: Materials and applications," *Applied Physics Reviews*, vol. 2, no. 4, p. 041101, Dec. 2015, doi: 10.1063/1.4935926.
- [5] R. Liu, Z. Wang, T. Sparks, F. Liou, and J. Newkirk, "Aerospace Applications of Laser Additive Manufacturing," *Laser Additive Manufacturing: Materials, Design, Technologies, and Applications*, pp. 351–371, Sep. 2016, doi: 10.1016/B978-0-08-100433-3.00013-0.
- [6] N. K. Dey, "Additive manufacturing laser deposition of Ti-6Al-4V for aerospace repair application," p. 70.
- [7] F. Rengier *et al.*, "3D printing based on imaging data: review of medical applications," *Int J Comput Assist Radiol Surg*, vol. 5, no. 4, pp. 335–341, Jul. 2010, doi: 10.1007/s11548-010-0476-x.
- [8] J. M. Williams *et al.*, "Bone tissue engineering using polycaprolactone scaffolds fabricated via selective laser sintering," *Biomaterials*, vol. 26, no. 23, pp. 4817–4827, Aug. 2005, doi: 10.1016/j.biomaterials.2004.11.057.
- [9] C. L. Ventola, "Medical Applications for 3D Printing: Current and Projected Uses," *P T*, vol. 39, no. 10, pp. 704–711, Oct. 2014.
- [10] B. Vandenbroucke and J. Kruth, "Selective laser melting of biocompatible metals for rapid manufacturing of medical parts," *Rapid Prototyping Journal*, vol. 13, no. 4, pp. 196–203, Jan. 2007, doi: 10.1108/13552540710776142.
- [11] S. N. Reddy, V. Maranan, T. W. Simpson, T. Palmer, and C. J. Dickman, "Application of topology optimization and design for additive manufacturing guidelines on an automotive component: ASME 2016 International Design Engineering Technical Conferences and Computers and Information in Engineering Conference, IDETC/CIE 2016," *42nd Design Automation Conference*, 2016, doi: 10.1115/DETC2016-59719.

- [12] U. E. Klotz, D. Tiberto, and F. Held, "Optimization of 18-karat yellow gold alloys for the additive manufacturing of jewelry and watch parts," *Gold Bull*, vol. 50, no. 2, pp. 111–121, Jun. 2017, doi: 10.1007/s13404-017-0201-4.
- [13] A. Sola and A. Nouri, "Microstructural porosity in additive manufacturing: The formation and detection of pores in metal parts fabricated by powder bed fusion," *Journal of Advanced Manufacturing and Processing*, vol. 1, no. 3, p. e10021, 2019, doi: 10.1002/amp.2.10021.
- [14] I. Yadroitsau, "Direct manufacturing of 3D objects by selective laser melting of metal powders," These de doctorat, Saint-Etienne, 2008. Accessed: Aug. 26, 2022. [Online]. Available: <https://www.theses.fr/2008STET4006>
- [15] P. Hanzl, M. Zetek, T. Bakša, and T. Kroupa, "The Influence of Processing Parameters on the Mechanical Properties of SLM Parts," *Procedia Engineering*, vol. 100, pp. 1405–1413, Jan. 2015, doi: 10.1016/j.proeng.2015.01.510.
- [16] Y. H. Zhou *et al.*, "Selective laser melting of typical metallic materials: An effective process prediction model developed by energy absorption and consumption analysis," *Additive Manufacturing*, vol. 25, pp. 204–217, Jan. 2019, doi: 10.1016/j.addma.2018.10.046.
- [17] I. Koutiri, E. Pessard, P. Peyre, O. Amlou, and T. De Terris, "Influence of SLM process parameters on the surface finish, porosity rate and fatigue behavior of as-built Inconel 625 parts," *Journal of Materials Processing Technology*, vol. 255, pp. 536–546, May 2018, doi: 10.1016/j.jmatprotec.2017.12.043.
- [18] A. Mostafaei *et al.*, "Defects and anomalies in powder bed fusion metal additive manufacturing," *Current Opinion in Solid State and Materials Science*, vol. 26, no. 2, Jan. 2022, doi: 10.1016/j.cossms.2021.100974.
- [19] W. King *et al.*, "Laser powder bed fusion additive manufacturing of metals; physics, computational, and materials challenges," *Applied Physics Reviews*, vol. 2, p. 041304, Dec. 2015, doi: 10.1063/1.4937809.
- [20] E. O. Olakanmi, R. F. Cochrane, and K. W. Dalgarno, "A review on selective laser sintering/melting (SLS/SLM) of aluminium alloy powders: Processing, microstructure, and properties," *Progress in Materials Science*, vol. 74, pp. 401–477, Oct. 2015, doi: 10.1016/j.pmatsci.2015.03.002.
- [21] T. Mukherjee and T. DebRoy, "Mitigation of lack of fusion defects in powder bed fusion additive manufacturing," *Journal of Manufacturing Processes*, vol. 36, pp. 442–449, Dec. 2018, doi: 10.1016/j.jmapro.2018.10.028.
- [22] M. Tang, P. C. Pistorius, and J. L. Beuth, "Prediction of lack-of-fusion porosity for powder bed fusion," *Additive Manufacturing*, vol. 14, pp. 39–48, Mar. 2017, doi: 10.1016/j.addma.2016.12.001.

- [23] K. Darvish, Z. W. Chen, and T. Pasang, "Reducing lack of fusion during selective laser melting of CoCrMo alloy: Effect of laser power on geometrical features of tracks," *Materials & Design*, vol. 112, pp. 357–366, Dec. 2016, doi: 10.1016/j.matdes.2016.09.086.
- [24] M. Laleh *et al.*, "Two and three-dimensional characterisation of localised corrosion affected by lack-of-fusion pores in 316L stainless steel produced by selective laser melting," *Corrosion Science*, vol. 165, p. 108394, Apr. 2020, doi: 10.1016/j.corsci.2019.108394.
- [25] M. J. Matthews, G. Guss, S. A. Khairallah, A. M. Rubenchik, P. J. Depond, and W. E. King, "Denu-
dation of metal powder layers in laser powder bed fusion processes," *Acta Materialia*, vol. 114, pp. 33–42, Aug. 2016, doi: 10.1016/j.actamat.2016.05.017.
- [26] V. Gunenthiram *et al.*, "Experimental analysis of spatter generation and melt-pool behavior during the powder bed laser beam melting process," *Journal of Materials Processing Technology*, vol. 251, pp. 376–386, Jan. 2018, doi: 10.1016/j.jmatprotec.2017.08.012.
- [27] V. Gunenthiram, P. Peyre, M. Schneider, M. Dal, C. Frederic, and R. Fabbro, "Analysis of laser–melt pool–powder bed interaction during the selective laser melting of a stainless steel," *Journal of Laser Applications*, vol. 29, p. 022303, May 2017, doi: 10.2351/1.4983259.
- [28] A. Kaplan, "A model of deep penetration laser welding based on calculation of the keyhole profile," *J. Phys. D: Appl. Phys.*, vol. 27, no. 9, pp. 1805–1814, Sep. 1994, doi: 10.1088/0022-3727/27/9/002.
- [29] J. Dowden, N. Postacioglu, M. Davis, and P. Kapadia, "A keyhole model in penetration welding with a laser," *J. Phys. D: Appl. Phys.*, vol. 20, no. 1, pp. 36–44, Jan. 1987, doi: 10.1088/0022-3727/20/1/006.
- [30] S. Pang, X. Chen, J. Zhou, X. Shao, and C. Wang, "3D transient multiphase model for keyhole, vapor plume, and weld pool dynamics in laser welding including the ambient pressure effect," *Optics and Lasers in Engineering*, vol. 74, pp. 47–58, Nov. 2015, doi: 10.1016/j.optlaseng.2015.05.003.
- [31] S. Pang, X. Chen, W. Li, X. Shao, and S. Gong, "Efficient multiple time scale method for modeling compressible vapor plume dynamics inside transient keyhole during fiber laser welding," *Optics & Laser Technology*, vol. 77, pp. 203–214, Mar. 2016, doi: 10.1016/j.optlastec.2015.09.024.
- [32] R. Lin, H. Wang, F. Lu, J. Solomon, and B. E. Carlson, "Numerical study of keyhole dynamics and keyhole-induced porosity formation in remote laser welding of Al alloys," *International Journal of Heat and Mass Transfer*, vol. 108, pp. 244–256, May 2017, doi: 10.1016/j.ijheatmasstransfer.2016.12.019.
- [33] C. Teng *et al.*, "A review of defect modeling in laser material processing," *Additive Manufacturing*, vol. 14, pp. 137–147, Mar. 2017, doi: 10.1016/j.addma.2016.10.009.

- [34] B. Cheng, S. Shrestha, and K. Chou, "Stress and deformation evaluations of scanning strategy effect in selective laser melting," *Additive Manufacturing*, vol. 12, pp. 240–251, Oct. 2016, doi: 10.1016/j.addma.2016.05.007.
- [35] M. Cloots, P. J. Uggowitzer, and K. Wegener, "Investigations on the microstructure and crack formation of IN738LC samples processed by selective laser melting using Gaussian and doughnut profiles," *Materials & Design*, vol. 89, pp. 770–784, Jan. 2016, doi: 10.1016/j.matdes.2015.10.027.
- [36] L. N. Carter, C. Martin, P. J. Withers, and M. M. Attallah, "The influence of the laser scan strategy on grain structure and cracking behaviour in SLM powder-bed fabricated nickel superalloy," *Journal of Alloys and Compounds*, vol. 615, pp. 338–347, Dec. 2014, doi: 10.1016/j.jallcom.2014.06.172.
- [37] L. Carter, M. Attallah, and R. Reed, "Laser Powder Bed Fabrication of Nickel-base Superalloys: Influence of Parameters; Characterisation, Quantification and Mitigation of Cracking," p. 10.
- [38] A. M. Rubenchik, W. E. King, and S. S. Wu, "Scaling laws for the additive manufacturing," *Journal of Materials Processing Technology*, vol. 257, pp. 234–243, Jul. 2018, doi: 10.1016/j.jmatprotec.2018.02.034.
- [39] U. Scipioni Bertoli, G. Guss, S. Wu, M. J. Matthews, and J. M. Schoenung, "In-situ characterization of laser-powder interaction and cooling rates through high-speed imaging of powder bed fusion additive manufacturing," *Materials & Design*, vol. 135, no. C, Art. no. LLNL-JRNL-738525, Sep. 2017, doi: 10.1016/j.matdes.2017.09.044.
- [40] W. M. Tucho, V. H. Lysne, H. Austbø, A. Sjolyst-Kverneland, and V. Hansen, "Investigation of effects of process parameters on microstructure and hardness of SLM manufactured SS316L," *Journal of Alloys and Compounds*, vol. 740, pp. 910–925, Apr. 2018, doi: 10.1016/j.jallcom.2018.01.098.
- [41] D. B. Hann, J. Iammi, and J. Folkes, "A simple methodology for predicting laser-weld properties from material and laser parameters," *J. Phys. D: Appl. Phys.*, vol. 44, no. 44, p. 445401, Oct. 2011, doi: 10.1088/0022-3727/44/44/445401.
- [42] H. Ghasemi-Tabasi, J. Jhabvala, E. Boillat, T. Ivas, R. Drissi-Daoudi, and R. E. Logé, "An effective rule for translating optimal selective laser melting processing parameters from one material to another," *Additive Manufacturing*, vol. 36, p. 101496, Dec. 2020, doi: 10.1016/j.addma.2020.101496.
- [43] D. Wang *et al.*, "Mechanisms and characteristics of spatter generation in SLM processing and its effect on the properties," *Materials & Design*, vol. 117, pp. 121–130, Mar. 2017, doi: 10.1016/j.matdes.2016.12.060.
- [44] T. Purtonen, A. Kalliosaari, and A. Salminen, "Monitoring and Adaptive Control of Laser Processes," *Physics Procedia*, vol. 56, pp. 1218–1231, Jan. 2014, doi: 10.1016/j.phpro.2014.08.038.

- [45] D. G. Kleinbaum and M. Klein, *Logistic Regression*. New York, NY: Springer New York, 2010. doi: 10.1007/978-1-4419-1742-3.
- [46] D. W. H. Jr, S. Lemeshow, and R. X. Sturdivant, *Applied Logistic Regression*. John Wiley & Sons, 2013.
- [47] D. W. Aha, D. Kibler, and M. K. Albert, "Instance-based learning algorithms," *Mach Learn*, vol. 6, no. 1, pp. 37–66, Jan. 1991, doi: 10.1007/BF00153759.
- [48] B. Sun, J. Du, and T. Gao, "Study on the Improvement of K-Nearest-Neighbor Algorithm," in *2009 International Conference on Artificial Intelligence and Computational Intelligence*, Nov. 2009, vol. 4, pp. 390–393. doi: 10.1109/AICI.2009.312.
- [49] C. Cortes and V. Vapnik, "Support-vector networks," *Mach Learn*, vol. 20, no. 3, pp. 273–297, Sep. 1995, doi: 10.1007/BF00994018.
- [50] J. R. Quinlan, "Learning decision tree classifiers," *ACM Comput. Surv.*, vol. 28, no. 1, pp. 71–72, Mar. 1996, doi: 10.1145/234313.234346.
- [51] L. Breiman, "Random Forests," *Machine Learning*, vol. 45, no. 1, pp. 5–32, Oct. 2001, doi: 10.1023/A:1010933404324.
- [52] L. Mason, J. Baxter, P. L. Bartlett, and M. R. Frean, "Boosting Algorithms as Gradient Descent," p. 7.
- [53] Z. Xu, G. Huang, K. Q. Weinberger, and A. X. Zheng, "Gradient boosted feature selection," in *Proceedings of the 20th ACM SIGKDD international conference on Knowledge discovery and data mining*, New York, NY, USA, Aug. 2014, pp. 522–531. doi: 10.1145/2623330.2623635.
- [54] J. A. Hartigan and M. A. Wong, "Algorithm AS 136: A K-Means Clustering Algorithm," *Journal of the Royal Statistical Society. Series C (Applied Statistics)*, vol. 28, no. 1, pp. 100–108, 1979, doi: 10.2307/2346830.
- [55] J. Schmidhuber, "Deep Learning in Neural Networks: An Overview," *Neural Networks*, vol. 61, pp. 85–117, Jan. 2015, doi: 10.1016/j.neunet.2014.09.003.
- [56] S. S. Haykin, *Neural Networks and Learning Machines*. Prentice Hall, 2009.
- [57] D. E. Rumelhart, G. E. Hinton, and R. J. Williams, "Learning representations by back-propagating errors," *Nature*, vol. 323, no. 6088, Art. no. 6088, Oct. 1986, doi: 10.1038/323533a0.

- [58] N. Aloysius and M. Geetha, "A review on deep convolutional neural networks," in *2017 International Conference on Communication and Signal Processing (ICCSP)*, Apr. 2017, pp. 0588–0592. doi: 10.1109/ICCSP.2017.8286426.
- [59] S. Albawi, T. A. Mohammed, and S. Al-Zawi, "Understanding of a convolutional neural network," in *2017 International Conference on Engineering and Technology (ICET)*, Aug. 2017, pp. 1–6. doi: 10.1109/ICEngTechnol.2017.8308186.
- [60] M. Mathieu, M. Henaff, and Y. LeCun, "Fast Training of Convolutional Networks through FFTs," Dec. 2013, Accessed: Sep. 24, 2022. [Online]. Available: https://openreview.net/forum?id=3RMnfrH_Fi8eU
- [61] M. Edwards and X. Xie, "Graph Based Convolutional Neural Network." arXiv, Sep. 28, 2016. doi: 10.48550/arXiv.1609.08965.
- [62] M. Defferrard, X. Bresson, and P. Vandergheynst, "Convolutional Neural Networks on Graphs with Fast Localized Spectral Filtering." arXiv, Feb. 05, 2017. doi: 10.48550/arXiv.1606.09375.
- [63] G. E. Hinton, "Deep belief networks," *Scholarpedia*, vol. 4, no. 5, p. 5947, May 2009, doi: 10.4249/scholarpedia.5947.
- [64] T. Mikolov, "Recurrent neural network based language model," p. 24.
- [65] A. C. Tsoi, "Recurrent neural network architectures: An overview," in *Adaptive Processing of Sequences and Data Structures: International Summer School on Neural Networks "E.R. Caianiello" Vietri sul Mare, Salerno, Italy September 6–13, 1997 Tutorial Lectures*, C. L. Giles and M. Gori, Eds. Berlin, Heidelberg: Springer, 1998, pp. 1–26. doi: 10.1007/BFb0053993.
- [66] S. Hochreiter and J. Schmidhuber, "Long Short-term Memory," *Neural computation*, vol. 9, pp. 1735–80, Dec. 1997, doi: 10.1162/neco.1997.9.8.1735.
- [67] S. K. Everton, M. Hirsch, P. Stravroulakis, R. K. Leach, and A. T. Clare, "Review of in-situ process monitoring and in-situ metrology for metal additive manufacturing," *Materials & Design*, vol. 95, pp. 431–445, Apr. 2016, doi: 10.1016/j.matdes.2016.01.099.
- [68] T. Furumoto, K. Egashira, K. Munekage, and S. Abe, "Experimental investigation of melt pool behaviour during selective laser melting by high speed imaging," *CIRP Annals*, vol. 67, no. 1, pp. 253–256, Jan. 2018, doi: 10.1016/j.cirp.2018.04.097.
- [69] P. Lott, H. Schleifenbaum, W. Meiners, K. Wissenbach, C. Hinke, and J. Bültmann, "Design of an Optical system for the In Situ Process Monitoring of Selective Laser Melting (SLM)," *Physics Procedia*, vol. 12, pp. 683–690, Jan. 2011, doi: 10.1016/j.phpro.2011.03.085.

- [70] P. Bidare, I. Bitharas, R. M. Ward, M. M. Attallah, and A. J. Moore, “Fluid and particle dynamics in laser powder bed fusion,” *Acta Materialia*, vol. 142, pp. 107–120, Jan. 2018, doi: 10.1016/j.actamat.2017.09.051.
- [71] C. Bruna-Rosso, A. G. Demir, and B. Previtali, “Selective laser melting finite element modeling: Validation with high-speed imaging and lack of fusion defects prediction,” *Materials & Design*, vol. 156, pp. 143–153, Oct. 2018, doi: 10.1016/j.matdes.2018.06.037.
- [72] F. Caltanissetta, M. Grasso, S. Petró, and B. M. Colosimo, “Characterization of in-situ measurements based on layerwise imaging in laser powder bed fusion,” *Additive Manufacturing*, vol. 24, pp. 183–199, Dec. 2018, doi: 10.1016/j.addma.2018.09.017.
- [73] Y. Zhang, J. Y. H. Fuh, D. Ye, and G. S. Hong, “In-situ monitoring of laser-based PBF via off-axis vision and image processing approaches,” *Additive Manufacturing*, vol. 25, pp. 263–274, Jan. 2019, doi: 10.1016/j.addma.2018.10.020.
- [74] J. L. Bartlett, F. M. Heim, Y. V. Murty, and X. Li, “In situ defect detection in selective laser melting via full-field infrared thermography,” *Additive Manufacturing*, vol. 24, pp. 595–605, Dec. 2018, doi: 10.1016/j.addma.2018.10.045.
- [75] M. Khanzadeh, W. Tian, A. Yadollahi, H. R. Doude, M. A. Tschopp, and L. Bian, “Dual process monitoring of metal-based additive manufacturing using tensor decomposition of thermal image streams,” *Additive Manufacturing*, vol. 23, pp. 443–456, Oct. 2018, doi: 10.1016/j.addma.2018.08.014.
- [76] H. Krauss, T. Zeugner, and M. F. Zaeh, “Layerwise Monitoring of the Selective Laser Melting Process by Thermography,” *Physics Procedia*, vol. 56, pp. 64–71, Jan. 2014, doi: 10.1016/j.phpro.2014.08.097.
- [77] S. Coeck, M. Bisht, J. Plas, and F. Verbist, “Prediction of lack of fusion porosity in selective laser melting based on melt pool monitoring data,” *Additive Manufacturing*, vol. 25, pp. 347–356, Jan. 2019, doi: 10.1016/j.addma.2018.11.015.
- [78] T. Craeghs, F. Bechmann, S. Berumen, and J.-P. Kruth, “Feedback control of Layerwise Laser Melting using optical sensors,” *Physics Procedia*, vol. 5, pp. 505–514, Jan. 2010, doi: 10.1016/j.phpro.2010.08.078.
- [79] F. Vakili-Farahani, J. Lungershausen, and K. Wasmer, “Wavelet analysis of light emission signals in laser beam welding,” *Journal of Laser Applications*, p. 022424 (7 pp.), 2017, doi: 10.2351/1.4983507.
- [80] M. Pavlov, M. Doubenskaia, and I. Smurov, “Pyrometric analysis of thermal processes in SLM technology,” *Physics Procedia*, vol. 5, pp. 523–531, Jan. 2010, doi: 10.1016/j.phpro.2010.08.080.

- [81] J. Trapp, A. M. Rubenchik, G. Guss, and M. J. Matthews, "In situ absorptivity measurements of metallic powders during laser powder-bed fusion additive manufacturing," *Applied Materials Today*, vol. 9, pp. 341–349, Dec. 2017, doi: 10.1016/j.apmt.2017.08.006.
- [82] V. N. Lednev *et al.*, "In situ multi-elemental analysis by laser induced breakdown spectroscopy in additive manufacturing," *Additive Manufacturing*, vol. 25, pp. 64–70, Jan. 2019, doi: 10.1016/j.addma.2018.10.043.
- [83] M. Islam, T. Purtonen, H. Piili, A. Salminen, and O. Nyrhilä, "Temperature Profile and Imaging Analysis of Laser Additive Manufacturing of Stainless Steel," *Physics Procedia*, vol. 41, pp. 835–842, Jan. 2013, doi: 10.1016/j.phpro.2013.03.156.
- [84] T. Furumoto, T. Ueda, M. R. Alkahari, and A. Hosokawa, "Investigation of laser consolidation process for metal powder by two-color pyrometer and high-speed video camera," *CIRP Annals*, vol. 62, no. 1, pp. 223–226, Jan. 2013, doi: 10.1016/j.cirp.2013.03.032.
- [85] J.-P. Kruth, J. Dufloy, P. Mercelis, J. Van Vaerenbergh, T. Craeghs, and J. De Keuster, "On-line monitoring and process control in selective laser melting and laser cutting," in *Proceedings of the 5th Lane Conference, Laser Assisted Net Shape Engineering*, 20070901, vol. 1, pp. 23–37. Accessed: Aug. 29, 2022. [Online]. Available: <https://lirias.kuleuven.be/retrieve/118273>
- [86] P. J. DePond *et al.*, "In situ measurements of layer roughness during laser powder bed fusion additive manufacturing using low coherence scanning interferometry," *Materials & Design*, vol. 154, pp. 347–359, Sep. 2018, doi: 10.1016/j.matdes.2018.05.050.
- [87] G. Guan *et al.*, "Evaluation of selective laser sintering processes by optical coherence tomography," *Materials & Design*, vol. 88, pp. 837–846, Dec. 2015, doi: 10.1016/j.matdes.2015.09.084.
- [88] D. Hertle and M. Sieben, "Process Monitoring using the Principle of Reflection Diagnosis," *Physics Procedia*, vol. 12, pp. 771–778, Jan. 2011, doi: 10.1016/j.phpro.2011.03.096.
- [89] J. A. Kanko, A. P. Sibley, and J. M. Fraser, "In situ morphology-based defect detection of selective laser melting through inline coherent imaging," *Journal of Materials Processing Technology*, vol. 231, pp. 488–500, May 2016, doi: 10.1016/j.jmatprotec.2015.12.024.
- [90] A. Neef, V. Seyda, D. Herzog, C. Emmelmann, M. Schönleber, and M. Kogel-Hollacher, "Low Coherence Interferometry in Selective Laser Melting," *Physics Procedia*, vol. 56, pp. 82–89, Jan. 2014, doi: 10.1016/j.phpro.2014.08.100.

- [91] A. Gaikwad, B. Giera, G. M. Guss, J.-B. Forien, M. J. Matthews, and P. Rao, “Heterogeneous sensing and scientific machine learning for quality assurance in laser powder bed fusion – A single-track study,” *Additive Manufacturing*, vol. 36, p. 101659, Dec. 2020, doi: 10.1016/j.addma.2020.101659.
- [92] M. Mahmoudi, A. A. Ezzat, and A. Elwany, “Layerwise Anomaly Detection in Laser Powder-Bed Fusion Metal Additive Manufacturing,” *Journal of Manufacturing Science and Engineering*, vol. 141, no. 3, Jan. 2019, doi: 10.1115/1.4042108.
- [93] M. Khanzadeh, S. Chowdhury, M. Marufuzzaman, M. A. Tschopp, and L. Bian, “Porosity prediction: Supervised-learning of thermal history for direct laser deposition,” *Journal of Manufacturing Systems*, vol. 47, pp. 69–82, Apr. 2018, doi: 10.1016/j.jmsy.2018.04.001.
- [94] J. A. Mitchell, T. A. Ivanoff, D. Dagel, J. D. Madison, and B. Jared, “Linking pyrometry to porosity in additively manufactured metals,” *Additive Manufacturing*, vol. 31, p. 100946, Jan. 2020, doi: 10.1016/j.addma.2019.100946.
- [95] C. Gobert, E. W. Reutzel, J. Petrich, A. R. Nassar, and S. Phoha, “Application of supervised machine learning for defect detection during metallic powder bed fusion additive manufacturing using high resolution imaging,” *Additive Manufacturing*, vol. 21, pp. 517–528, May 2018, doi: 10.1016/j.addma.2018.04.005.
- [96] M. Grasso, V. Laguzza, Q. Semeraro, and B. M. Colosimo, “In-Process Monitoring of Selective Laser Melting: Spatial Detection of Defects Via Image Data Analysis,” *Journal of Manufacturing Science and Engineering*, vol. 139, no. 5, Nov. 2016, doi: 10.1115/1.4034715.
- [97] M. H. Kunkel, A. Gebhardt, K. Mpofu, and S. Kallweit, “Quality assurance in metal powder bed fusion via deep-learning-based image classification,” *Rapid Prototyping Journal*, vol. 26, no. 2, pp. 259–266, Jan. 2019, doi: 10.1108/RPJ-03-2019-0066.
- [98] H. Elwarfalli, D. Papazoglou, D. Erdahl, A. Doll, and J. Speltz, “In Situ Process Monitoring for Laser-Powder Bed Fusion using Convolutional Neural Networks and Infrared Tomography,” in *2019 IEEE National Aerospace and Electronics Conference (NAECON)*, Jul. 2019, pp. 323–327. doi: 10.1109/NAECON46414.2019.9058251.
- [99] O. Kwon *et al.*, “A deep neural network for classification of melt-pool images in metal additive manufacturing,” *J Intell Manuf*, vol. 31, no. 2, pp. 375–386, Feb. 2020, doi: 10.1007/s10845-018-1451-6.
- [100] H. Baumgartl, J. Tomas, R. Buettner, and M. Merkel, “A deep learning-based model for defect detection in laser-powder bed fusion using in-situ thermographic monitoring,” *Prog Addit Manuf*, vol. 5, no. 3, pp. 277–285, Sep. 2020, doi: 10.1007/s40964-019-00108-3.

- [101] Z. Snow, B. Diehl, E. W. Reutzel, and A. Nassar, "Toward in-situ flaw detection in laser powder bed fusion additive manufacturing through layerwise imagery and machine learning," *Journal of Manufacturing Systems*, vol. 59, pp. 12–26, Apr. 2021, doi: 10.1016/j.jmsy.2021.01.008.
- [102] R. Mojahed Yazdi, F. Imani, and H. Yang, "A hybrid deep learning model of process-build interactions in additive manufacturing," *Journal of Manufacturing Systems*, vol. 57, pp. 460–468, Oct. 2020, doi: 10.1016/j.jmsy.2020.11.001.
- [103] A. Caggiano, J. Zhang, V. Alfieri, F. Caiazzo, R. Gao, and R. Teti, "Machine learning-based image processing for on-line defect recognition in additive manufacturing," *CIRP Annals*, vol. 68, no. 1, pp. 451–454, Jan. 2019, doi: 10.1016/j.cirp.2019.03.021.
- [104] L. Scime and J. Beuth, "Anomaly detection and classification in a laser powder bed additive manufacturing process using a trained computer vision algorithm," *Additive Manufacturing*, vol. 19, pp. 114–126, Jan. 2018, doi: 10.1016/j.addma.2017.11.009.
- [105] L. Scime and J. Beuth, "A multi-scale convolutional neural network for autonomous anomaly detection and classification in a laser powder bed fusion additive manufacturing process," *Additive Manufacturing*, vol. 24, pp. 273–286, Dec. 2018, doi: 10.1016/j.addma.2018.09.034.
- [106] L. Scime and J. Beuth, "Using machine learning to identify in-situ melt pool signatures indicative of flaw formation in a laser powder bed fusion additive manufacturing process," *Additive Manufacturing*, vol. 25, pp. 151–165, Jan. 2019, doi: 10.1016/j.addma.2018.11.010.
- [107] S. Larsen and P. A. Hooper, "Deep semi-supervised learning of dynamics for anomaly detection in laser powder bed fusion," *J Intell Manuf*, vol. 33, no. 2, pp. 457–471, Feb. 2022, doi: 10.1007/s10845-021-01842-8.
- [108] D. Ye, J. Y. Hsi Fuh, Y. Zhang, G. S. Hong, and K. Zhu, "In situ monitoring of selective laser melting using plume and spatter signatures by deep belief networks," *ISA Transactions*, vol. 81, pp. 96–104, Oct. 2018, doi: 10.1016/j.isatra.2018.07.021.
- [109] M. Grasso and B. M. Colosimo, "A statistical learning method for image-based monitoring of the plume signature in laser powder bed fusion," *Robotics and Computer-Integrated Manufacturing*, vol. 57, pp. 103–115, Jun. 2019, doi: 10.1016/j.rcim.2018.11.007.
- [110] Y. Zhang, G. S. Hong, D. Ye, K. Zhu, and J. Y. H. Fuh, "Extraction and evaluation of melt pool, plume and spatter information for powder-bed fusion AM process monitoring," *Materials & Design*, vol. 156, pp. 458–469, Oct. 2018, doi: 10.1016/j.matdes.2018.07.002.

- [111] G. Repossini, V. Laguzza, M. Grasso, and B. M. Colosimo, “On the use of spatter signature for in-situ monitoring of Laser Powder Bed Fusion,” *Additive Manufacturing*, vol. 16, pp. 35–48, Aug. 2017, doi: 10.1016/j.addma.2017.05.004.
- [112] H. Wu, Z. Yu, and Y. Wang, *A New Approach for Online Monitoring of Additive Manufacturing Based on Acoustic Emission*. 2016. doi: 10.1115/MSEC2016-8551.
- [113] K. Wasmer, F. Saeidi, B. Meylan, F. Vakili-Farahani, and S. A. Shevchik, “When AE (Acoustic Emission) meets AI (Artificial Intelligence),” p. 8.
- [114] K. Wasmer *et al.*, “Laser processing quality monitoring by combining acoustic emission and machine learning: a high-speed X-ray imaging approach,” *Procedia CIRP*, vol. 74, pp. 654–658, Jan. 2018, doi: 10.1016/j.procir.2018.08.054.
- [115] S. A. Shevchik, B. Meylan, G. Violakis, and K. Wasmer, “3D reconstruction of cracks propagation in mechanical workpieces analyzing non-stationary acoustic mixtures,” *Mechanical Systems and Signal Processing*, vol. 119, pp. 55–64, Mar. 2019, doi: 10.1016/j.ymssp.2018.09.022.
- [116] M. Strantzà, D. Van Hemelrijck, P. Guillaume, and D. G. Aggelis, “Acoustic emission monitoring of crack propagation in additively manufactured and conventional titanium components,” *Mechanics Research Communications*, vol. 84, pp. 8–13, Sep. 2017, doi: 10.1016/j.mechrescom.2017.05.009.
- [117] A. Vieira, E. Moura, L. Gonçalves, and J. Rebello, “Characterization of welding defects by fractal analysis of ultrasonic signals,” *Chaos Solitons & Fractals*, vol. 38, Jan. 2007, doi: 10.1016/j.chaos.2007.01.012.
- [118] V. K. Nadimpalli, L. Yang, and P. B. Nagy, “In-situ interfacial quality assessment of Ultrasonic Additive Manufacturing components using ultrasonic NDE,” *NDT & E International*, vol. 93, pp. 117–130, Jan. 2018, doi: 10.1016/j.ndteint.2017.10.004.
- [119] D. Cerniglia and N. Montinaro, “Defect Detection in Additively Manufactured Components: Laser Ultrasound and Laser Thermography Comparison,” *Procedia Structural Integrity*, vol. 8, pp. 154–162, 2018, doi: 10.1016/j.prostr.2017.12.016.
- [120] D. Cerniglia, M. Scafidi, A. Pantano, and J. Rudlin, “Inspection of additive-manufactured layered components,” *Ultrasonics*, vol. 62, pp. 292–298, Sep. 2015, doi: 10.1016/j.ultras.2015.06.001.
- [121] S. A. Shevchik, C. Kenel, C. Leinenbach, and K. Wasmer, “Acoustic emission for in situ quality monitoring in additive manufacturing using spectral convolutional neural networks,” *Additive Manufacturing*, vol. 21, pp. 598–604, May 2018, doi: 10.1016/j.addma.2017.11.012.

- [122] S. A. Shevchik, G. Masinelli, C. Kenel, C. Leinenbach, and K. Wasmer, "Deep Learning for In Situ and Real-Time Quality Monitoring in Additive Manufacturing Using Acoustic Emission," *IEEE Transactions on Industrial Informatics*, vol. 15, no. 9, pp. 5194–5203, Sep. 2019, doi: 10.1109/TII.2019.2910524.
- [123] M. Bastuck, H.-G. Herrmann, B. Wolter, D. Böttger, and P.-C. Zinn, "AkuProLas: Acoustic Inline Process Monitoring for Laser Welding Applications," p. 10.
- [124] W. W. Duley and Y. L. Mao, "The effect of surface condition on acoustic emission during welding of aluminium with CO₂ laser radiation," *J. Phys. D: Appl. Phys.*, vol. 27, no. 7, pp. 1379–1383, Jul. 1994, doi: 10.1088/0022-3727/27/7/007.
- [125] H. Gu and W. W. Duley, "A statistical approach to acoustic monitoring of laser welding," *J. Phys. D: Appl. Phys.*, vol. 29, no. 3, pp. 556–560, Mar. 1996, doi: 10.1088/0022-3727/29/3/011.
- [126] D. Farson, Y. Sang, and A. Ali, "Relationship between airborne acoustic and optical emissions during laser welding," *Journal of Laser Applications*, vol. 9, no. 2, pp. 87–94, Apr. 1997, doi: 10.2351/1.4745448.
- [127] E. Nava-Rüdiger and M. Houlot, "Integration of real time quality control systems in a welding process," *Journal of Laser Applications*, vol. 9, no. 2, pp. 95–102, Apr. 1997, doi: 10.2351/1.4745449.
- [128] H. Zeng, Z. Zhou, Y. Chen, H. Luo, and L. Hu, "Wavelet analysis of acoustic emission signals and quality control in laser welding," *Journal of Laser Applications*, vol. 13, no. 4, pp. 167–173, Aug. 2001, doi: 10.2351/1.1386799.
- [129] H. Luo, H. Zeng, L. Hu, X. Hu, and Z. Zhou, "Application of artificial neural network in laser welding defect diagnosis," *Journal of Materials Processing Technology*, vol. 170, no. 1, pp. 403–411, Dec. 2005, doi: 10.1016/j.jmatprotec.2005.06.008.
- [130] W. Huang and R. Kovacevic, "A neural network and multiple regression method for the characterization of the depth of weld penetration in laser welding based on acoustic signatures," *J Intell Manuf*, vol. 22, no. 2, pp. 131–143, Apr. 2011, doi: 10.1007/s10845-009-0267-9.
- [131] C.-J. Lee, J.-D. Kim, and Y.-C. Kim, "Study on monitoring of plasma emission signal in lap welding of Zn coated steel sheet using CO₂ laser," *Int. J. Precis. Eng. Manuf.*, vol. 16, no. 3, pp. 495–500, Mar. 2015, doi: 10.1007/s12541-015-0067-4.
- [132] Y. Mao, G. Kinsman, and W. W. Duley, "Real-Time Fast Fourier Transform Analysis of Acoustic Emission during CO₂ Laser Welding of Materials," *Journal of Laser Applications*, vol. 5, no. 2, pp. 17–22, Oct. 1993, doi: 10.2351/1.4745326.

- [133] D. Farson, K. Hillsley, J. Sames, and R. Young, "Frequency-time characteristics of air-borne signals from laser welds," *ICALEO*, vol. 1994, no. 1, pp. 86–94, Oct. 1994, doi: 10.2351/1.5058875.
- [134] S. Shevchik, "Acoustic emission for in situ monitoring of laser processing," p. 9.
- [135] T. Le-Quang *et al.*, "Why is in situ quality control of laser keyhole welding a real challenge?," *Procedia CIRP*, vol. 74, pp. 649–653, Jan. 2018, doi: 10.1016/j.procir.2018.08.055.
- [136] S. Lee, S. Ahn, and C. Park, "Analysis of Acoustic Emission Signals During Laser Spot Welding of SS304 Stainless Steel," *J. of Materi Eng and Perform*, vol. 23, no. 3, pp. 700–707, Mar. 2014, doi: 10.1007/s11665-013-0791-9.
- [137] K. Ito, M. Kusano, M. Demura, and M. Watanabe, "Detection and location of microdefects during selective laser melting by wireless acoustic emission measurement," *Additive Manufacturing*, vol. 40, p. 101915, Apr. 2021, doi: 10.1016/j.addma.2021.101915.
- [138] K. Gutknecht, M. Cloots, R. Sommerhuber, and K. Wegener, "Mutual comparison of acoustic, pyrometric and thermographic laser powder bed fusion monitoring," *Materials & Design*, vol. 210, p. 110036, Nov. 2021, doi: 10.1016/j.matdes.2021.110036.
- [139] H. Taheri, L. W. Koester, T. A. Bigelow, E. J. Faierson, and L. J. Bond, "In Situ Additive Manufacturing Process Monitoring With an Acoustic Technique: Clustering Performance Evaluation Using K-Means Algorithm," *Journal of Manufacturing Science and Engineering*, vol. 141, no. 4, Feb. 2019, doi: 10.1115/1.4042786.
- [140] N. Eschner, L. Weiser, B. Häfner, and G. Lanza, "Classification of specimen density in Laser Powder Bed Fusion (L-PBF) using in-process structure-borne acoustic process emissions," *Additive Manufacturing*, vol. 34, p. 101324, Aug. 2020, doi: 10.1016/j.addma.2020.101324.
- [141] D. Ye, G. S. Hong, Y. Zhang, K. Zhu, and J. Y. H. Fuh, "Defect detection in selective laser melting technology by acoustic signals with deep belief networks," *Int J Adv Manuf Technol*, vol. 96, no. 5, pp. 2791–2801, May 2018, doi: 10.1007/s00170-018-1728-0.
- [142] J. R. Tempelman *et al.*, "Detection of keyhole pore formations in laser powder-bed fusion using acoustic process monitoring measurements," *Additive Manufacturing*, vol. 55, p. 102735, Jul. 2022, doi: 10.1016/j.addma.2022.102735.
- [143] C. Zhao *et al.*, "Critical instability at moving keyhole tip generates porosity in laser melting," *Science*, vol. 370, no. 6520, pp. 1080–1086, Nov. 2020, doi: 10.1126/science.abd1587

Chapter 3 Scope of the thesis

In this chapter, we present the main objectives of the thesis, as well as the methodology followed to reach them.

3.1 Scope of the thesis

This thesis studies the possibility and the limits of acoustic emission monitoring of the LPBF process, when coupled with machine learning. The final goal is to design a robust in situ and real-time control of the LPBF process using acoustic emission. To reach this goal it is important to understand the process, how to acoustically monitor it correctly and how to construct a robust ML learning algorithm for this application. The scope of this thesis is, therefore, threefold (Figure 31).

First, the LPBF process is studied in order to understand the thermal history associated to distinct types of laser-matter interactions and mechanisms of defects formation for three alloys: stainless steel 316L, bronze CuSn8, and Inconel 718. This knowledge, with the help of 2D and 3D characterization, will allow the possibility to create intentionally the different process regimes studied in this thesis: keyhole mode, conduction mode, and LoF pores. An appropriate choice of laser parameters demonstrates that the ML algorithms classification is significantly related to laser-matter interaction. Moreover, effective processing maps are constructed, such that they can lead to the development of a robust database for ML algorithms, and therefore to robust LPBF monitoring.

Second, we propose the implementation of an acoustic emission-based solution to effectively monitor the regimes leading to creation of porosity in the LPBF process. Based on the literature and some preliminary tests, the choice of an airborne sensor is made for the monitoring of pores formation. The installation of the microphones inside the build chamber as well as the right triggering to synchronize the recording is studied. The AE features in time, frequencies, and time-frequencies domains are investigated. The classification results and the saliency maps of two microphones with different frequency responses are detailed, highlighting the important frequency ranges involved in the classification of the LPBF process regimes.

Different machine learning methods are compared to classify the three main LPBF processing regimes. Moreover, alternative ML techniques to reduce the amount of data needed to train the AI algorithms and to transfer the knowledge from one material to another are investigated. The quality of CNN models are

evaluated thanks to saliency maps, and criteria are determined for constructing a robust database that can generalize the use of algorithms to conditions unseen by the training.

The knowledge acquired in this thesis helps the fast construction of processing maps and a better understanding of laser-matter interaction phenomena in porosity related process regimes. It could also lead, in the future, to the spatial localization of porosities.

The thesis contains 9 chapters and is constructed in a cumulative manner, from five distinct paper manuscripts, which have been published, submitted, or are about to be submitted to international peer-reviewed journals.

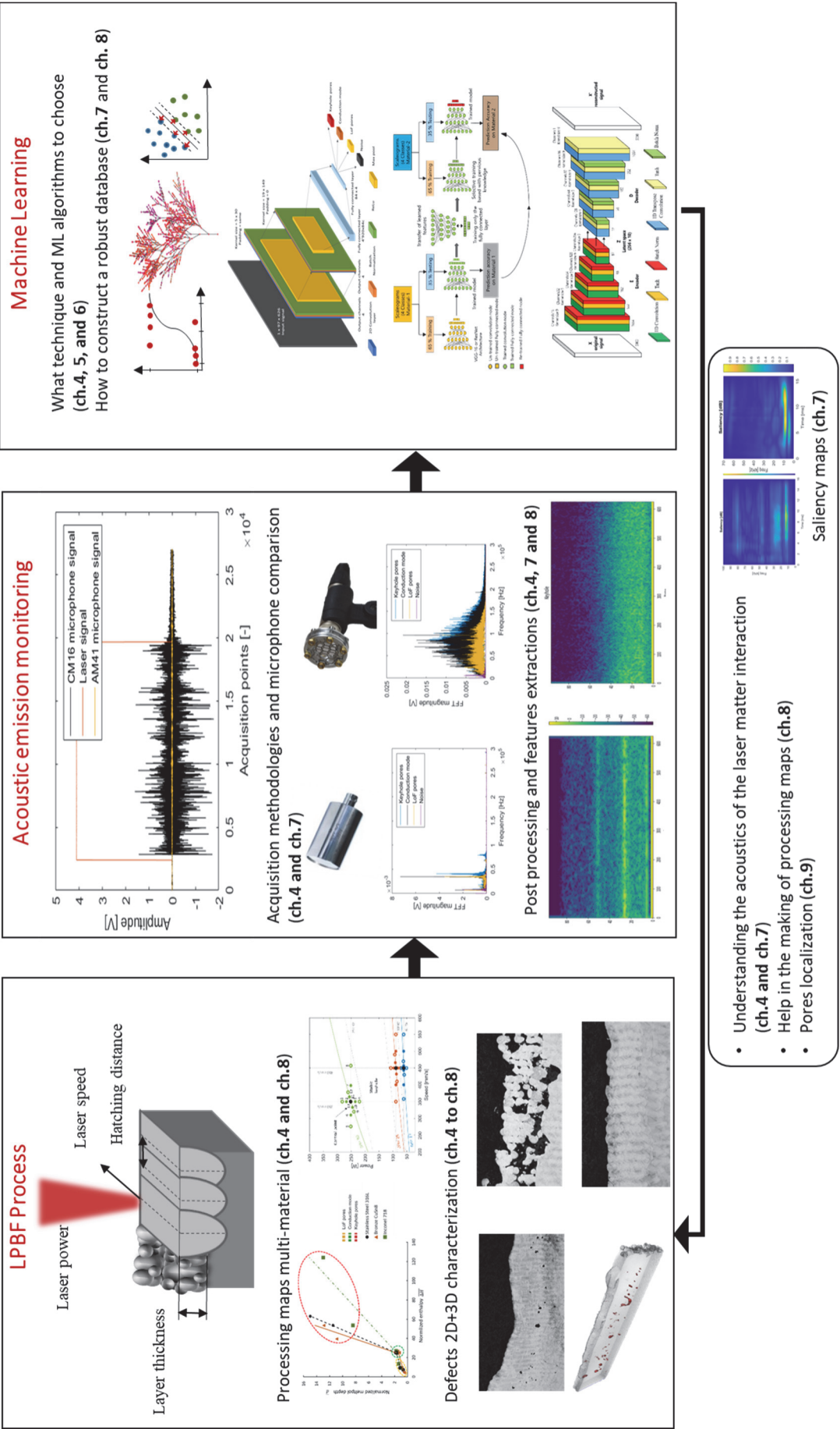


Figure 31. Thesis outline and chapters structure schematically represented

3.2 Thesis plan

Chapter 1 – Introduction.

This chapter presents a short introduction to AM techniques and especially the LPBF process, its main applications, and drawbacks.

Chapter 2 – State of the art.

This chapter provides a literature review of the understanding of the defects formation in the LPBF process, as well as the different monitoring solutions. The different acoustic monitoring techniques are detailed, together with the machine learning algorithms developed for this purpose. The objective is to contextualize the different papers presented in the thesis.

Chapter 3 - Scope of the thesis.

Chapter 3 presents the thesis objectives and structure with the help of a schematic illustration of the general goals.

Chapter 4 - Differentiation of Materials and Laser Powder Bed Fusion Processing Regimes from Airborne Acoustic Emission Combined with Machine Learning.

This chapter presents an analysis of the AE signals acquired during LPBF processing of three metallic alloys: stainless steel (316L), bronze (CuSn₈), and Inconel (Inconel 718). Three metallurgical states are studied: key-hole pores, conduction mode, and LoF pores. First, we show that the frequency distribution of AE signals for the three materials shows that a significant energy concentration between 1 and 60 kHz. Three ML algorithms LR, RF, and SVM, as well as a CNN, were trained, and high classification accuracy was obtained for all algorithms. We also showed that generalization of the classification of LPBF defects between alloys seems not to be possible. Finally, a multi-label CNN is shown to classify the alloy AND the process regime at the same time, with high confidence.

Chapter 5 - Deep Transfer Learning of Additive Manufacturing Mechanisms Across Materials in Metal-Based Laser Powder Bed Fusion Process.

This chapter presents a deep transfer learning method using the experiments and the data collected in chapter 4. It demonstrates the possibility to use a trained model on acoustic data from one material (stainless steel) and classify with high accuracy (above 80%) four metallurgical states (*balling*, *LoF pores*, *conduction mode* and *key-hole pores*) in another bronze alloy, without retraining from scratch.

Chapter 6 - Semi-supervised Monitoring of Laser Powder Bed Fusion Process Based on Acoustic Emissions.

This chapter presents a semi-supervised method as an alternative to the fully supervised one in chapter 4, applied to Inconel 718 AE classification. The undesirable regimes, namely, *balling*, *LoF pores*, and *keyhole pores* could be differentiated from the reference (desired) regime of *conduction mode*.

Chapter 7 - On the importance of acoustic emission frequencies for in-situ monitoring of Laser Powder Bed Fusion.

This chapter compares the classification accuracies of a CNN model as well as the saliency maps, based on acoustic data obtained with two microphones with different frequency responses. It highlights the importance of frequency information in acoustic emission-based monitoring and shows how saliency maps of a trained CNN can be effective in determining the frequency footprints associated with three LPBF regimes: keyhole pores, conduction mode and LoF pores.

Chapter 8 – Acoustic emission for the prediction of processing regimes in Laser Powder Bed Fusion, and the generation of processing maps.

This chapter presents the results of a CNN model applied to spectrograms extracted from measurements of an air-borne acoustic sensor for the classification of LPBF processing regimes. The aim of this work is to establish a methodology for the construction of a robust training database from which the algorithm can predict the process regime (among the three categories: keyhole pores, conduction mode, or LoF pores) at any point within the conventional LPBF processing map, i.e. in new regions that were not considered in the training database.

Chapter 9.-. Conclusions and perspectives.

This last chapter summarizes the main results of the thesis and provides an outlook for future work in the domain.

Chapter 4

Differentiation of Materials and Laser Powder Bed Fusion Processing Regimes from Airborne Acoustic Emission Combined with Machine Learning.

Rita Drissi-Daoudi ^a, Vigneashwara Pandiyan ^b, Roland Logé ^a, Sergey Shevchik ^b, Giulio Masinelli ^b, Hossein Ghasemi-Tabasi ^a, Annapaola Parrilli ^c, Kilian Wasmer ^b

^a *Thermomechanical Metallurgy Laboratory – PX Group Chair, Ecole Polytechnique Fédérale de Lausanne (EPFL), CH-2002 Neuchâtel, Switzerland*

^b *Laboratory for Advanced Materials Processing (LAMP), Swiss Federal Laboratories for Materials Science and Technology (Empa) - CH-3602 Thun, Switzerland*

^c *Centre for X-ray Analytics, Swiss Federal Laboratories for Materials Science and Technology (EMPA), CH-8600 Dübendorf, Switzerland.*

Rita Drissi-Daoudi, Vigneashwara Pandiyan, Roland Logé, Sergey Shevchik, Giulio Masinelli, Hossein Ghasemi-Tabasi, Annapaola Parrilli & Kilian Wasmer (2022) **Differentiation of materials and laser powder bed fusion processing regimes from airborne acoustic emission combined with machine learning**, Virtual and Physical Prototyping, 17:2, 181-204, DOI: [10.1080/17452759.2022.2028380](https://doi.org/10.1080/17452759.2022.2028380)

Contribution: Rita Drissi-Daoudi developed the experimental plan and printed the samples. She wrote parts of the manuscript.

Abstract

This study investigates the use of a low cost microphone combined with state-of-the-art machine learning algorithms as online process monitoring able to differentiate various materials and process conditions of Laser-Powder Bed Fusion (LPBF). Three processing regimes (*lack of fusion pores*, *conduction mode* and *keyhole pores*) and three alloys (316L stainless steel, bronze (CuSn8), and Inconel 718) were selected. It was found, by analysing the acoustic signatures resolved in the time, frequency, and time-frequency domains, that the regimes are statistically distinct, which was also confirmed by the *t*-distributed stochastic neighbour embedding (*t*-SNE) visualisation. Three conventional machine learning algorithms and a Convolutional Neural Network (CNN) were chosen to perform the classification tasks resulting in five main findings. First, for the first time, it was proven that the AE features are related to the laser-material interaction and not from undesired machine or environmental noise. Second, it was found that the process regimes are classified with high accuracy (> 87%) regardless of the algorithms and materials. Third, it was demonstrated that it is possible to build a single model from the three materials and still reach high classification accuracy (>86%) of the different regimes. Forth, we proved that the AE features used for the classifications are material and regime dependent. Hence, it seems not possible to have a universal or generalised model for most metals. Finally, with LPBF processing of multi-materials on the rise, a strategy for classifying the material and the process regimes simultaneously using a CNN multi-label architecture reached a very high classification accuracy ($\approx 93\%$). The results demonstrate the potential of our approaches for online LPBF process monitoring of different materials and regimes.

Keywords: Acoustic emission; Additive manufacturing; In situ monitoring; Machine learning; Artificial Intelligence; Laser material processing;

4.1 Introduction

Laser-Powder Bed Fusion (LPBF) is the most studied laser-based three-dimensional (3D) printing process, which consolidates parts, layer-by-layer, from powders (King et al. 2015). Metallic 3D printed workpieces via LPBF can achieve near full-density, and the resulting mechanical properties are comparable with (or even exceed) those obtained by conventional processing routes (Yap et al. 2015; DebRoy et al. 2018). Though the process looks conceptually simple, the underlying dynamics of rapid melting and cooling of the melt pool, the powder stock material properties, and the surrounding environments make it complicated and prone to defects such as balling, LoF pores, and keyhole pores. The formation of such defects limits technology applications (King et al. 2015; Dowling et al. 2020; Khairallah et al. 2016; du Plessis, Yadroitsava, and Yadroitsev 2020).

It is well known that the quality of the produced part during LPBF is directly dependent on the process window parameters such as laser energy density, the composition of the powder alloy, scanning speed, layer thickness, strategy for scanning, environment, etc. (Chua, Ahn, and Moon 2017; Van Elsen 2007; Spears and Gold 2016; Gu et al. 2006; Kurzynowski et al. 2012). The range of process parameters to achieve near full-density characteristics is limited to a narrow window, called the keyhole threshold (Qi et al. 2017; King et al. 2014; Cunningham et al. 2019; Ghasemi-Tabasi et al. 2020). Identifying the optimal processing window is tremendously time-consuming and expensive as it requires a trial and error approach (Aboulkhair et al. 2014), sometimes coupled with numerical simulations (King et al. 2015; Heeling, Cloots, and Wegener 2017; Mukherjee and DebRoy 2018). During the LPBF process, lack of energy input causes incomplete overlap of the melt pool with the adjacent layer resulting in porosity formation called Lack of Fusion (LoF) pores (Gong et al. 2014). LoF pores appear in two forms: weak bonding or incompletely melted metal particles (Zhang, Li, and Bai 2017). LoF pores are irregularly shaped and can be larger than 500 μm , resulting in an epicentre of crack propagation during cyclic loading when the part is operational (Coeck et al. 2019). An increase in energy density produces melt pools with shallow depths known as conduction mode, where the ratio between the melting depth (D) and laser beam diameter (ϕ_{laser}) is $D/\phi_{\text{laser}} \leq 1$. In LPBF, the conduction mode refers to processing conditions with a density higher than 99.9%. A further increase in energy density leads to deeper melt pools depths, eventually resulting in the intense evaporation of the material, which causes the formation of a vapor channel called a keyhole. The stability of the keyhole mechanism is known to be rather unstable (Le-Quang et al. 2018). Its collapse during the process leaves behind trails of voids (King et al. 2014). Actually, this porosity occurs mainly when the volumetric energy density is too high; such pores are called keyhole pores (Thanki et al. 2019). Apart from porosities occurring due to suboptimal laser parameters, porosities can also occur based on the powder composition's physical property. Indeed, the physical property of the powder alloys influences heat absorption and heat transfer during the process. The high solidification rate traps the gas bubbles before it rises and escapes, resulting in defect inclusions in the shape of spherical pores (Zhang, Li, and Bai 2017). Even when the parameters have been well defined, the defect formation due to laser-material interaction is known to be highly non-linear and stochastic by nature, making it significantly non-reproducible (Dowling et al. 2020; du Plessis, Yadroitsava, and Yadroitsev 2020; Nassar et al. 2019). One solution to this drawback is developing an in situ and real-time process regime monitoring technique, which is the main aim of this contribution. Monitoring the process and interpretation of the sensor data helps to understand and mitigate the numerous unfavourable events happening in the process zone (Shevchik et al. 2018; Everton et al. 2016).

In recent years, process monitoring and control of metal-based LPBF processes have been the main focus of several investigations. It helps in a broader adaptation as a mainstream manufacturing technique in industries (Masinelli et al. 2020). Based on the reviews of Tapia and Elwany (Tapia and Elwany 2014), Everton *et al.* (Everton et al. 2016), Grasso and Colosimo (Grasso et al. 2018), and Yan *et al.* (Yan et al. 2018), the most

popular monitoring method is by in situ optical inspections of the process zone using photodiodes and high-speed cameras. For the former method, which also includes pyrometers, the optical radiations emitted and reflected from the process zone are sensed by photodiodes. Information regarding the temperature, laser energy coupling inside the workpiece, and process stability can be derived using photodiodes (Shevchik et al. 2020a; Shevchik, Le-Quang, et al. 2019; Forien et al. 2020; Yan et al. 2018). The advantage of this method is that it is cost-efficient and has outstanding temporal resolutions. Commercial photodiodes detect bandwidths of several megahertz up to gigahertz, making them capable of following highly dynamic processes such as laser-material interaction (Le-Quang et al. 2018; Zhao et al. 2017). Nevertheless, as the signals are averaged over the photodiode field-of-view, this method lacks spatial resolution. The use of high-speed cameras can overcome this issue. With a suitable camera and optical setup, information regarding the melt pool's geometry, temperature distribution on the workpiece's surface, evolution and fluctuation of the vapour plume, and even the ejections of liquid droplets (spatters) can be obtained (Grasso et al. 2018; Hooper 2018; Yan et al. 2018). High-speed cameras are significantly advantageous for the physical understanding of the process. However, its industrial implementation for process monitoring suffers from the very high cost of the system. Another common disadvantage of optical detection methods is that they are limited to the process zone's surface region. Consequently, the detection of defects, such as porosity and cracks, is challenging. An alternative to optical methods is the acoustic emission (AE) technique. Acoustic sensors can detect sound waves generated by an additive manufacturing machine. It includes the laser-material interaction, propagating inside the workpiece (structure-borne) and atmosphere (airborne). Therefore, they are very sensitive to the process zone's volumetric behaviours and can detect better the process instabilities that lead to porosity and cracks (Shevchik et al. 2020b; Shevchik, Masinelli, et al. 2019; Shevchik et al. 2018; Shevchik, Le-Quang, et al. 2019). Obviously, the origin of AE source in metal-based LPBF processes are manifolds such as laser-material interaction (rapid melting and cooling, defect formation and related process regime) as well as undesired environment and machine noises and finally even from the process parameters themselves. Like photodiodes, acoustic sensors are also cost-efficient and have been successfully implemented to monitor other industrial dynamic processes (Pandiyana, Shevchik, et al. 2020; Pandiyana and Tjahjowidodo 2019, 2017). The acoustic emission combined with machine learning methods has a proven track record in carrying information of the process zone when a thermal source (Chen, Kovacevic, and Jandgric 2003; Wu, Wang, and Yu 2016; Wu, Yu, and Wang 2017) or laser (Gu and Duley 1996; Wasmer et al. 2017; Shevchik, Masinelli, et al. 2019) interacts with a material and more details are given below.

The accomplishment of real-time monitoring in any dynamic process requires the computers to learn and model the patterns in the sensor data. The perspectives of using Machine Learning (ML) in metal-based LPBF has been written by Sing *et al.* (Sing et al. 2021) and the one in 3D bioprinting by Yu and Jiang (Yu and Jiang 2020). Scime and Beuth (Scime and Beuth 2018a, 2018b, 2019; Scime et al. 2020) published several approaches using cameras and Machine Learning (ML) to identify process footprints leading to defect creation.

They used computer vision algorithms (Scime and Beuth 2018a) and Convolutional Neural Network (CNN) (Scime and Beuth 2018b) during the powder spreading stage of the process to detect and classify anomalies automatically. They used a similar approach (computer vision algorithms) and unsupervised ML to differentiate between observed melt pools Scime and Beuth (2019). Digital camera images were combined with a deep residual neural network and region proposal network to detect the powder bed defects, namely, the warpage, part shifting, and short feed (Xiao, Lu, and Huang 2020). Alessandra Caggiano *et al.* (Caggiano et al. 2019) have combined the powder bed and process zone images with a Bi-stream CNN to detect the process quality. Apart from optical methods, thermal sensor data have been used along with ML algorithms such as *K*-Nearest Neighbor (KNN) and Decision Tree (DT) to predict part quality (Khanzadeh, Chowdhury, et al. 2018). Khanzadeh *et al.* (Khanzadeh, Tian, et al. 2018) have also proposed a multilinear principal component analysis (MPCA) approach for extraction of low dimensional features from thermal maps to monitor AM process. In the literature, AE has been combined with Spectral CNN (Shevchik et al. 2018; Shevchik, Masinelli, et al. 2019; Wasmer et al. 2017), deep belief networks (Ye, Hong, et al. 2018), reinforcement learning (Wasmer et al. 2019), and Support Vector Machine (SVM) (Ye, Fuh, et al. 2018) for real-time monitoring of the LPBF processes, but always for a single material and one process condition per regime. In recent years, in addition to online monitoring, ML algorithms have been either applied in other fields of AM such as developing process model or are combined with physics based-models such as Finite Element (FE) simulations to overcome the problem of data-driven approach. Jiang et al. (Jiang et al. 2020) exploited deep neural networks to predict the connection status between printed lines taking into account four process parameters; filament extrusion speed, print speed, line distance and layer height. Ren *et al.* (Ren et al. 2021) published a work where they used a Temperature-Pattern Recurrent Neural Networks (TP-RNN) model to predict the temperature field for multi-layer cube deposition planning. Finally, a comprehensive review of ML algorithms used in the context of additive manufacturing has been reported by Goh *et al.* (Goh, Sing, and Yeong 2020).

While literature reports monitoring the LPBF process dealing with one material, artificial intelligence (AI) techniques in monitoring different materials are seldom mentioned. When analysing AE signals with ML, the identification of different types of porosities in 316L stainless steel was demonstrated successfully (Shevchik, Masinelli, et al. 2019; Shevchik et al. 2018). Moving to another material or generalisation among materials would require the building of a new database, which leads to the following questions:

- (i) Are the acoustic signatures material dependent, or instead, can it be generalised for broader scenarios? In other words, a distinct database for materials having different mechanical, optical and thermal properties are needed? or can a single database be used? This question was not examined so far in the literature.

- (ii) Can a single ML model monitor the process regimes when dealing with different materials be built if the acoustic signatures are material-dependent?
- (iii) Can we distinguish both the material and the regime when dealing with different materials? If so, it would provide precious information on the material(s) in which defects are formed without the need for time-consuming microscopy analysis.

The reported work investigates the AE features recorded during LPBF, resolved in time, frequency, and time-frequency domains, and statistically correlates them with the occurrence of three process regimes: *LoF pores*, *keyhole pores*, or with the absence of pores (*conduction mode*). As mentioned earlier, the conduction mode refers to processing conditions with a density higher than 99.9%. The analysis is performed on three different material alloys, stainless steel (316L), bronze (CuSn₈), and Inconel (Inconel 718), that have distinct optical, mechanical and thermal properties. Four ML models based on Logistic regression (LR), Random Forest (RF), Support Vector Machines (SVM), and a CNN were selected for classification tasks of the process regimes. The rising attention for producing different materials part using the LPBF techniques brings new process monitoring challenges. To address them, a new approach by developing a CNN architecture able to classify the process regimes and the processed alloy is proposed. The ability to analyse AE features of different alloys provides key information for answering questions (i) and (ii) related to the generalisation of ML algorithms and to the possibility of distinguishing the different alloys using a single model. Finally, a CNN-based multi-label classification model addresses question (iii) on distinguishing regimes and materials.

The paper is organised into 6 Sections. Experimental considerations are presented in Section 4.2. The analysis of the acoustic signal emitted during the LPBF process in time, frequency, and time-frequency domains for the three alloys is summarised in Section 4.3. The representations and visualisation of the acoustic features in low dimensional space using *t*-distributed Stochastic Neighbour Embedding (*t*-SNE) is discussed in Section 4.4. Section 4.5 starts by determining the origin of AE features used for classification. Then, it presents the results of the developed online monitoring systems for the different materials and process regimes using traditional ML and CNN architectures; focusing on the universality and material identification aspects. Finally, this paper's findings and future works on in situ and real-time monitoring for the LPBF process are discussed in Section 4.6.

4.2 Experimental setup and data acquisition

In this work, the experiments were performed on an in-house LPBF system shown in Figure 32. The customised LPBF system can have a scan speed up to 20 m·s⁻¹. The enclosed chamber of the LPBF system has a Continuous-Wave (CW) modulated Ytterbium fibre laser for melting the powder and a recoater mechanism for creating a new powder layer. The fibre laser operates in continuous mode with a 1070 ± 10 nm wavelength,

and the beam is around 82 microns ($1/e^2$) at the focal plane with an $M^2 < 1.1$. The recoater mechanism spreads the metal powder to a thickness of around 40 μm . The chamber's atmosphere is controlled under a laminar flowing closed loop of argon and a monitored maximum oxygen level of 200 ppm. The LPBF system is equipped with a PAC AM4I (Physical Instrument, Germany) airborne acoustic sensor, hereafter referred to as microphone, and an Advantech Data Acquisition (DAQ) card (Advantech, Taiwan) to get feedback from the process zone.

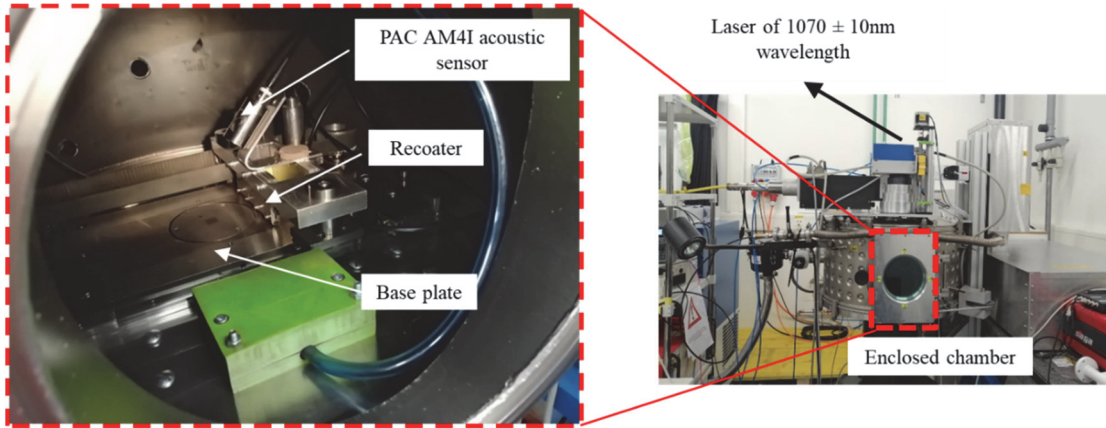


Figure 32. Experimental setup of the LPBF process with the PAC AM4I acoustic sensor installed.

All experiments were performed with the in-house LPBF system. To start with, we built some transition layers of a selected material on the base plate. These transition layers have two main purposes. First, it will act as a transition material from the base plate to the one processed. Second, it must be thick enough to ensure that our experiments will have the same heat flow as processing a single material. As these transition layers do not require to be of high quality, faster processing parameters were selected layers to save preparation time. On top of these transition layers, high-density layers were built to guarantee the same initial condition for the experiments with chosen proves parameters. Finally, a series of overlapping line tracks were produced during which the AE signals were recorded with the PAC AM4I microphone. The transition layers, the high-density layers and the overlapping line tracks can be seen in Figure 35. To simplify the design space, the scanning strategy selected is one-directional and parallel, with a hatch distance of 0.1 mm. The experiments were performed with three different alloys, stainless steel (316L), bronze (CuSn_8) and Inconel (Inconel 718), and their corresponding chemical composition are summarised in Table 1. The Stainless Steel 316L micro powder, MetcoAdd 316L, was bought from Oerlikon Metco with a particle size distribution between 45 and 15 μm . The bronze (CuSn_8) powder having an average particle size of 30 μm was purchased from Heraeus Materials SA. The nickel-based super-alloy Inconel 718 powder was purchased from Oerlikon Metco, exhibiting a bi-modal particle size distribution with peak values at 45 and 15 μm .

Differentiation of Materials and Laser Powder Bed Fusion Processing Regimes from Airborne Acoustic Emission Combined with Machine Learning

Table 1. Chemical composition of the powders of Nickel-based super-alloy (Inconel 718)), bronze (CuSn8), and stainless steel (316L),

Chemical composition of stainless steel (316L) powder					
Fe	Cr	Ni	Mo	Other	C
Balance	18	12	2	< 1.00	< 0.03

Chemical composition of Bronze (CuSn8) powder						
Cu	P	S	Fe	Ni	Zn	As
Balance	0.06 ± 0.02	≤ 0.05	≤ 0.05	< 0.03	≤ 0.2	≤ 0.05

Chemical composition of Inconel (718) powder						
Ni	Fe	Cr	Nb+Ta	Mo	Ti	Al
Balance	18	18	5	3	1	0.60

The microphone was positioned at a distance of approximately 10 cm from the build plate, as shown in Figure 32. It has a frequency response in the range of 0-100 kHz. The AE signals were acquired at a rate of 1 MHz and stored locally for further processing with a custom-built C# code on the Advantech DAQ card. The data acquisition rate was chosen to ensure that the Nyquist Shannon theorem (Jerri 1977) is satisfied. The captured signal was triggered by a photodiode using a beam splitter setup. This configuration ensures that the process and the data obtained are synchronised. Once the laser interacts with the powder bed, the photodiode's minimum amplitude threshold is surpassed, which triggers the acquisition of the acoustic signals and the data recording. Prior to analysing the signal features in time, frequency, and time-frequency domains, they were filtered with a low-pass Butterworth filter to remove frequency contents higher than 100 kHz as they do not fall inside the sensitivity range of the AE sensor.

In this contribution, the three most common process regimes known in LPBF are investigated; they are *LoF pores*, *conduction mode* (or absence of pores), and *keyhole pores* (Qi et al. 2017; King et al. 2014; Cunningham et al. 2019; Ghasemi-Tabasi et al. 2020). The conduction mode regime is considered the normal regime since it results in the highest material density in conjunction with adequate material properties. In contrast, *LoF pores* and *keyhole pores* are considered as abnormal regimes and must be avoided. In addition, two process parameters were selected per regime. The reasons lying behind the selection of process regimes and parameters are fourfold. First, selecting two sets of parameters for each regime was motivated by the fact that, in the literature, most studies used a single process parameter per regime, such as in Shevchik *et al.* (Shevchik et al. 2018), and this limits the sampling of the process space. Adding a second process parameter for each regime will increase the process space and demonstrate that our approach is valid for multi-process parameters. Second, to ensure that AE features selected for the classification task are solely related to the process regimes and not from the undesired environment, the machine noises, or machine parameters; one set of laser parameters (**bold red** values in Table 2) were identical for all three alloys for the regimes, *LoF pores* and *keyhole pores*. Having the same process parameter for a specific regime across the material guarantees that the undesired environment, the machine noises, and the machine parameters are identical. Hence, under such circumstances,

Differentiation of Materials and Laser Powder Bed Fusion Processing Regimes from Airborne Acoustic Emission Combined with Machine Learning

being able to differentiate the material will prove that AE features are exclusively correlated to the laser-material interaction and so the process regime. Third, rather than selecting the second set of parameters randomly within both regimes, it was decided to have them based on a physical basis. Consequently, they were chosen to have the same normalised enthalpy (Qi et al. 2017; King et al. 2014; Cunningham et al. 2019; Ghasemi-Tabasi et al. 2020) across all alloys (*blue* values in Table 2 and also shown in Figure 33). Finally, as it is not possible to achieve the regime *conduction mode* with the same laser parameters sets due to the differences in material properties, we selected the process parameters having a normalised enthalpy around 25, which was proven to be an optimised value for high-density conduction mode in three materials, including 316L stainless steel and bronze (Ghasemi-Tabasi et al. 2020) (*green* values in Table 2, and circled points in Figure 33). Based on these considerations, the selected laser parameters for inducing or avoiding defects are listed in Table 2 for the three selected alloys. A total of 100 line track experiments were performed for each set of process parameters on each alloy. The analysis of the corresponding acoustic signatures is reviewed in Section 3.

Table 2: Two set of laser parameters for stainless steel, bronze and Inconel to induce the process regimes (regimes) *LoF pores*, *conduction mode* and *keyhole pores*. In bold, the first set of parameters for *LoF pores*, and *keyhole pores* is kept constant for the three alloys.

Regimes	Stainless steel			Bronze			Inconel		
	Laser power (W)	Scan speed (mm/s)	Normal-ized en-thalpy	Laser power (W)	Scan speed (mm/s)	Normal-ized en-thalpy	Laser power (W)	Scan speed (mm/s)	Normal-ized en-thalpy
<i>LoF pores</i>	50	350	7	50	350	4.4	50	350	13.4
	70	400	<i>9.2</i>	110	400	<i>9.2</i>	36	400	<i>9.2</i>
<i>Conduction mode</i>	180	350	25	300	350	26.5	100	350	27
	135	200	25	215	200	25	69	200	25
<i>Keyhole pores</i>	450	350	63	450	350	39.4	450	350	124
	250	150	<i>53.5</i>	396	150	<i>53.5</i>	127	150	<i>53.5</i>

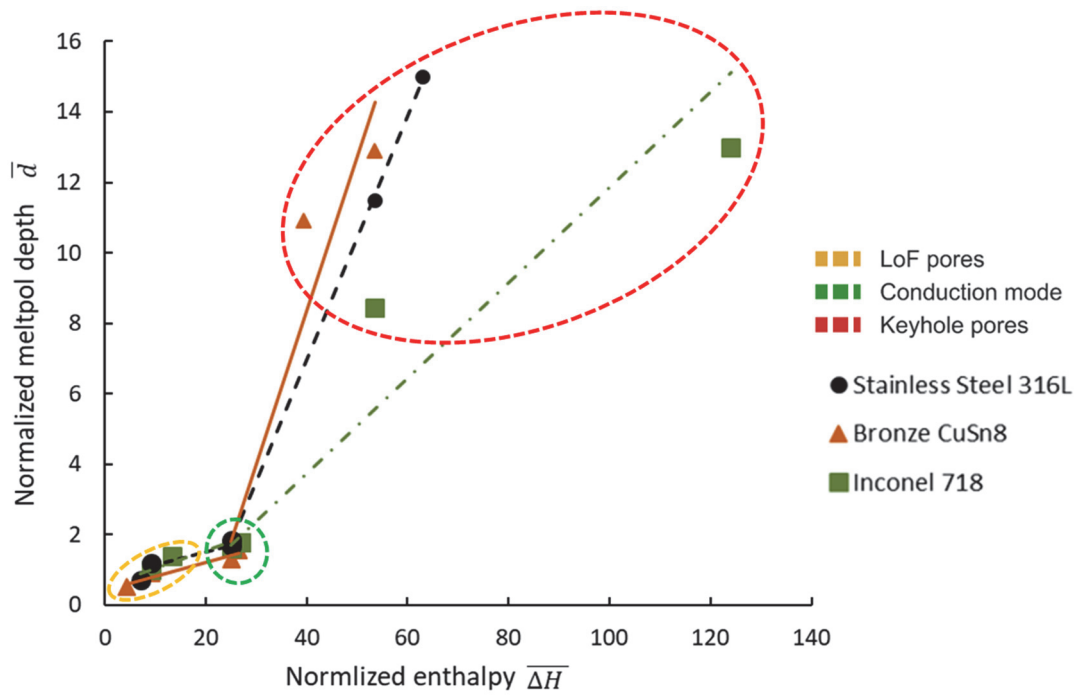


Figure 33. Processing map showing the normalised melt pool depth (i.e. depth divided by the laser spot size) as a function of the normalised enthalpy (as defined in (Ghasemi-Tabasi et al. 2020)) for the printed stainless steel, Inconel and bronze samples. The optimal processing condition is around a normalised enthalpy of 25 for all alloys (Ghasemi-Tabasi et al. 2020). Lower normalised enthalpies lead to LoF pores, while larger values lead to keyhole pores. Experimental setup of the LPBF process with the PAC AM41 acoustic sensor installed.

The diagnostic on the type of defect regimes (regime) for data labelling was obtained and confirmed via X-ray tomography (Figure 34) and cross-sectioning of selected lines (Figure 35). Based on this analysis and experience, the same process regime was assumed for each of the 100 lines using the same process parameters. Typical micrographs, representative of the three labelled regimes for the three materials, are shown in Figure 35. In this figure, the three process zones are visible. At the bottom of the figure, the preparation cube is characterised by a large melt zone and high defect content. It is followed by a high-density layer, which for the conduction mode are identical to the top layer. The latter is made of overlapping line tracks during which the AE signals are recorded. The samples were etched to reveal the melt pools, whose depths are reported in Figure 33. The stainless steel, bronze and Inconel samples were etched with (i) Aqua regia diluted (100 mL HNO_3 , 100 mL HCl , 100 mL H_2O) for 30 seconds, (ii) ASTM No.30 (5 mL H_2O_2 , 25 mL NH_3 , 25 mL H_2O) for 5 to 10 seconds, and (iii) Kalling's No.2 Reagent (5 g CuCl , HCl 100 mL, $\text{C}_2\text{H}_6\text{O}$ 100 mL, H_2O 100 mL) for 10 to 20 seconds, respectively. Micrographs were taken with a Leica DM6000M light optical microscope in bright field mode.

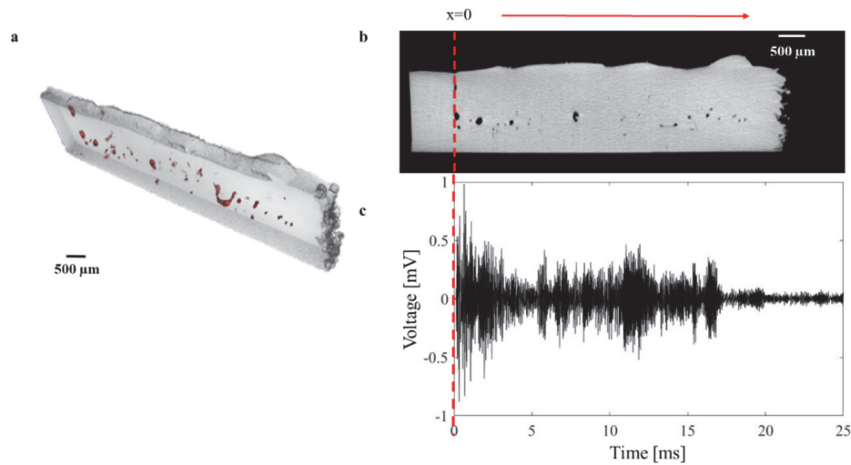


Figure 34. Keyhole porosity formation along one laser track, in stainless steel (316L), and its corresponding acoustic emission signal; a) 3D reconstruction of the *keyhole pores* formed in one line; b) 2D section of region shown in (a); c) acoustic emission signal corresponding to the selected laser track.

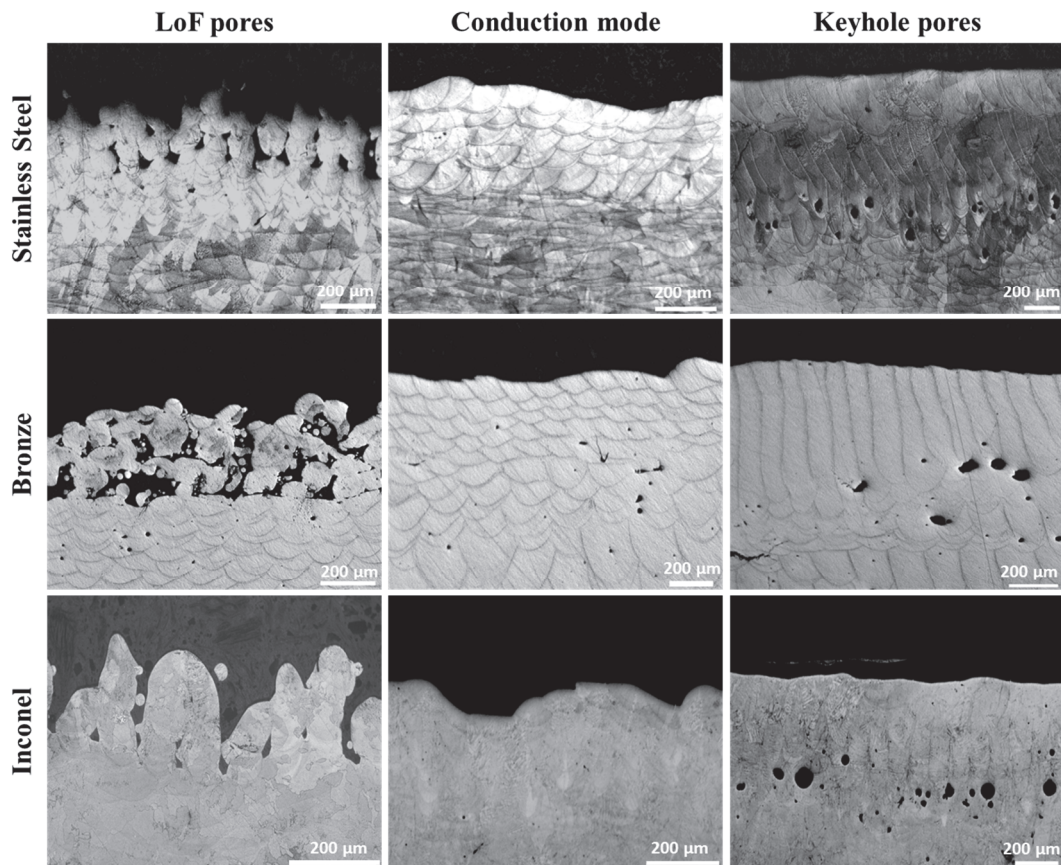


Figure 35. Typical micrographs of the three regimes (*LoF pores*, *conduction mode* and *keyhole pores*) for stainless steel (316L), bronze (CuSn₈), and Inconel (Inconel 718).

4.3 Analysis of acoustic emission signature from LPBF process

As already mentioned, the LPBF process suffers from a lack of repeatability due to defect formation's stochastic nature. This inconvenience results in the occurrence of defects such as *LoF pores* and *keyhole pores*. For real-time identification of these defects, it is imperative to have information about the changes taking place in the process zone over time. In Pandiyan *et al.* (Pandiyan, Drissi-Daoudi, et al. 2020), such analysis was performed for 316L for the three regimes investigated in this study, along with *balling* (another type of lack-of-fusion mechanism). The study's outcomes proved features in time, frequency, and time-frequency domains are specific for different regimes. A similar analysis on the three selected alloys is performed to determine whether the conclusion can be generalised for other alloys too. Besides, we will investigate whether the features in the three domains are specific to each alloy. To perform the feature analysis, similar to Pandiyan *et al.* (Pandiyan, Drissi-Daoudi, et al. 2020), a window of 5 ms is used to split the sensor's signals to extract several features in the three domains. It was selected after an exhaustive search to reach the best compromise between time resolution and classification accuracy. A short running window increases defect detection time and spatial resolution but are also sensitive to limited information and noise. The period must be minimum enough to cover a defect formed with the chosen parameters. The choice of the window size for features analysis is the same as the one chosen for the classification which will be discussed later.

Figure 36 compares typical raw AE signals (peak-to-peak) corresponding to the three regimes from the three alloys. Specifically, it indicates that irrespective of the alloy, the AE signals' amplitude increases from *LoF pores* to *keyhole pores*.

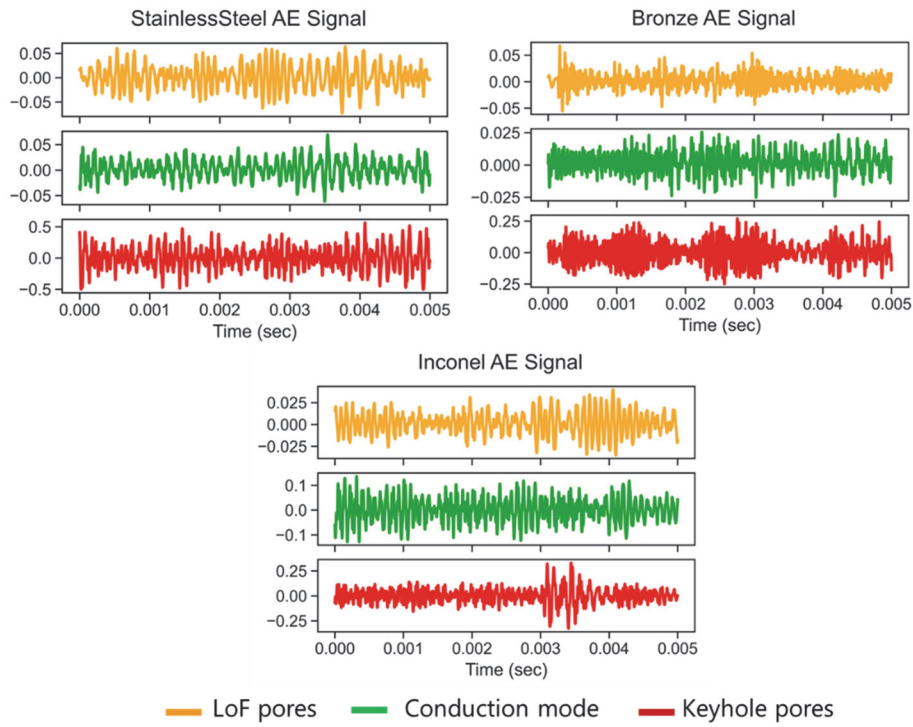


Figure 36. Raw AE signals correspond to the three different regimes: *LoF pores*, *conduction mode*, and *keyhole pores* for stainless steel, bronze and Inconel (Note: Signal corresponding to *LoF pores* and *Keyhole pores* regimes for the three alloys are using same process parameter).

4.3.1 Time-domain analysis

The time-domain analysis gives the features as a function of amplitude changing over time. The statistical distribution of the features based on time-domain such as Root Mean Square (AE_{RMS}), mean, crest-power, standard deviation, skewness, variance, kurtosis, median, etc., were analysed to correlate with the three selected regimes. As the conclusions are similar for all features distributions, only the AE_{RMS} distribution for the three regimes in the three alloys is shown in the form of a ridge plot in Figure 37. The range of AE_{RMS} distribution values in *LoF pores* for stainless steel and Inconel are higher less than for bronze. This may be related to the absorptivity at the laser Near-Infrared Red (NIR) wavelength, lower in bronze than the two other alloys. Therefore, the required input energy to reach the conduction mode for the bronze alloy needs to be higher, even though the bronze melting point is lower (Ghasemi-Tabasi et al. 2020). The distribution of AE_{RMS} starts to spread as the regime moves from *LoF pores* to *conduction mode*, while *keyhole pores* have a much larger deviation. This may be due to the highly unstable behaviour of the keyhole (Shevchik et al. 2020b). The examination of time-domain features such as skewness, crest-power, median, kurtosis, etc., also exhibited distinct distributions amongst the regimes for all three alloys. Such a distinct distribution of statistical time-domain features motivates the use of ML algorithms to perform real-time monitoring.

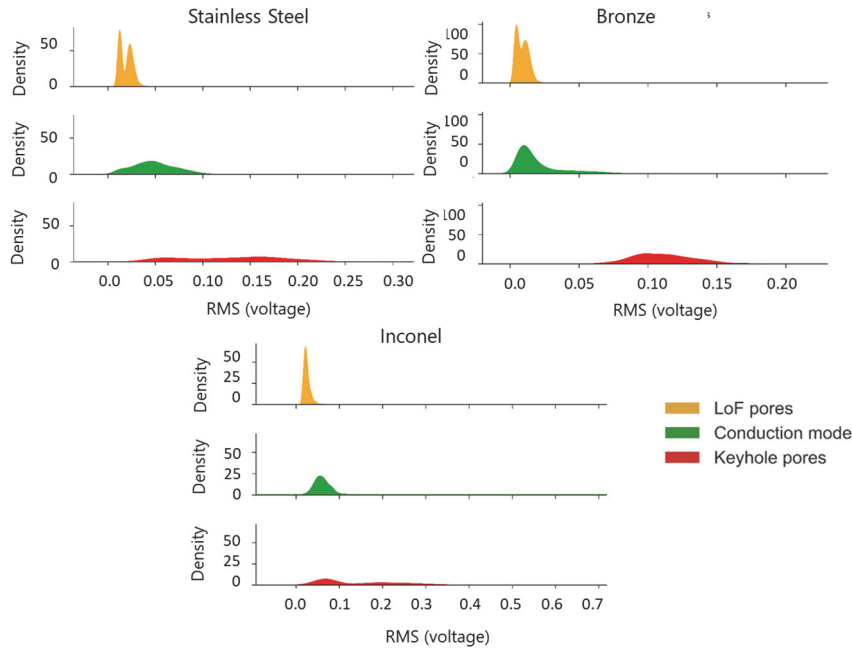


Figure 37. Distribution of AE_{RMS} features for the three regimes occurring in stainless steel, bronze and Inconel.

4.3.2 Frequency domain analysis

The periodic components of a signal can be identified when the signal is resolved in the frequency domain. To be specific, decomposing a signal with Fast Fourier Transforms (FFT) analysis reveals these periodic components'. The representation of AE in the frequency domain for all three regimes provided additional interesting insights compared to the time domain. Figure 38 presents the Power Spectral Density (PSD) distribution in the FFT plots, which was calculated using the Welch method (Welch 1967) for a window of 5 ms. Irrespective of the alloys, distinct peaks are visible at more or less 10 and 40 kHz, as evident from Figure 38 across the three regimes. Most peaks were found around these frequency bands, as the PAC AM4I acoustic sensor's response was also higher in this region. Besides, for the regime *keyhole porosity* of bronze, it can be inferred that the magnitude of the frequency content in the vicinity of 10 kHz is higher than at 40 kHz.

In contrast, the PSD distribution values corresponding to LoF pores were much lower than for other alloys for bronze. This decrease may again be related to the lower absorptivity of bronze at the NIR wavelength. When processing Inconel, the frequency peaks were found at more or less 10 and 40 kHz for all regimes except for the *conduction mode*. For Inconel, a surge in frequency peaks around 10 kHz compared to other frequency ranges seems to be correlated to a high-density conduction mode process. It is also to be noted that regimes across alloys showed some degree of resemblance, for example, as indicated by arrows in Figure 38 on *LoF pores* between stainless steel and Inconel.

Differentiation of Materials and Laser Powder Bed Fusion Processing Regimes from Airborne Acoustic Emission Combined with Machine Learning

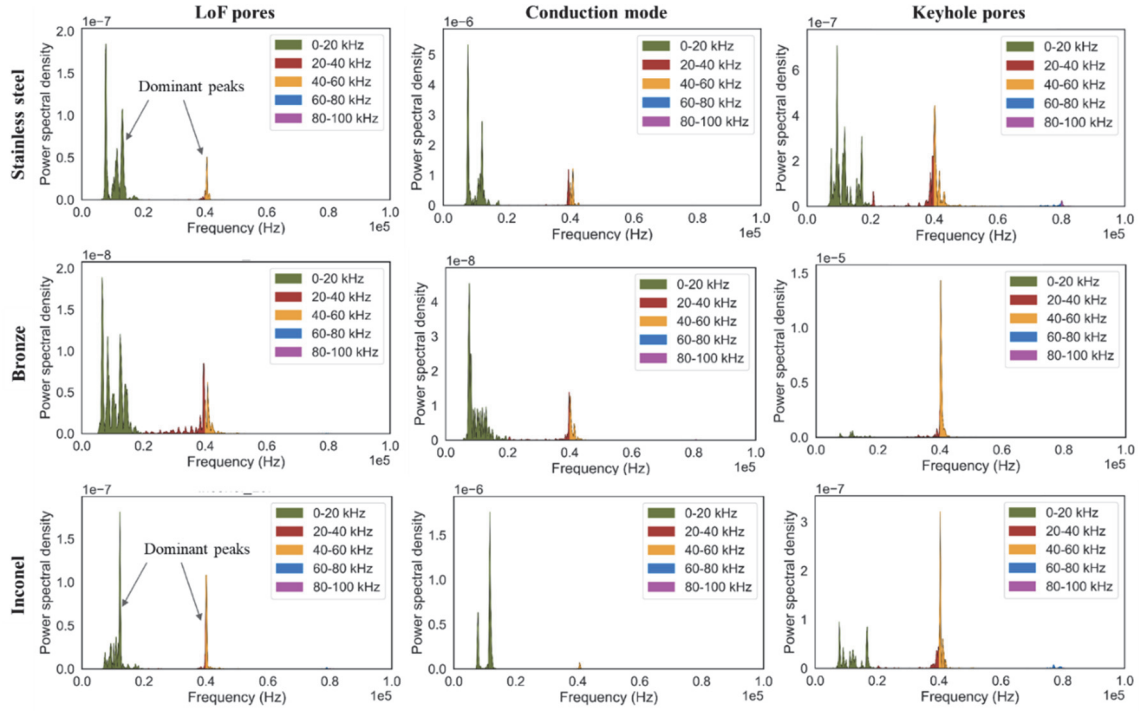


Figure 38. Typical FFT plots for stainless steel, bronze and Inconel depicting discrete frequency distributions among the alloys and across the three regimes.

One of the most critical aspects of the frequency domain analysis is understanding the correlation between signal power densities in different frequency bands for each regime. The microphone's operating range of 1–100 kHz was divided into five frequency bands, namely 0–20 kHz, 20–40 kHz, 40–60 kHz, 60–80 kHz, and 80–100 kHz for such an analysis. All results, in terms of cumulative energy density values for a window size of 5 ms calculated by the periodogram method (Babtle 1948), are presented in Figure 39. This figure is important since the energy density distribution plots between the five bands were calculated on the whole dataset. Therefore, it gives an overall sparse representation between the alloys and regimes. For bronze, stainless steel, and Inconel, the energy contents were concentrated within the frequency range of 0–60 kHz.

In contrast, the frequency bands below 40 kHz have more significant contributions for stainless steel, especially in the *conduction mode*. As shown in Figure 39, the energy level concentration of the regimes *LoF pores* was prevalent in the frequency band of 0–20 kHz for all alloys. However, for the regime *conduction mode* of Inconel (Figure 39 (a)), there is a decrease in the energy density value of the frequency band 40–60 kHz as compared to the other alloys. From the energy density distribution plots, it can be concluded that laser interaction with the molten pool causes AE signals to carry more energy at 0–20kHz than other frequency bands. The discrete frequency and energy density distribution plots of the AE signals between the different bands motivate the use of these frequency domain features as input to ML algorithms to classify the regimes and the different alloys.

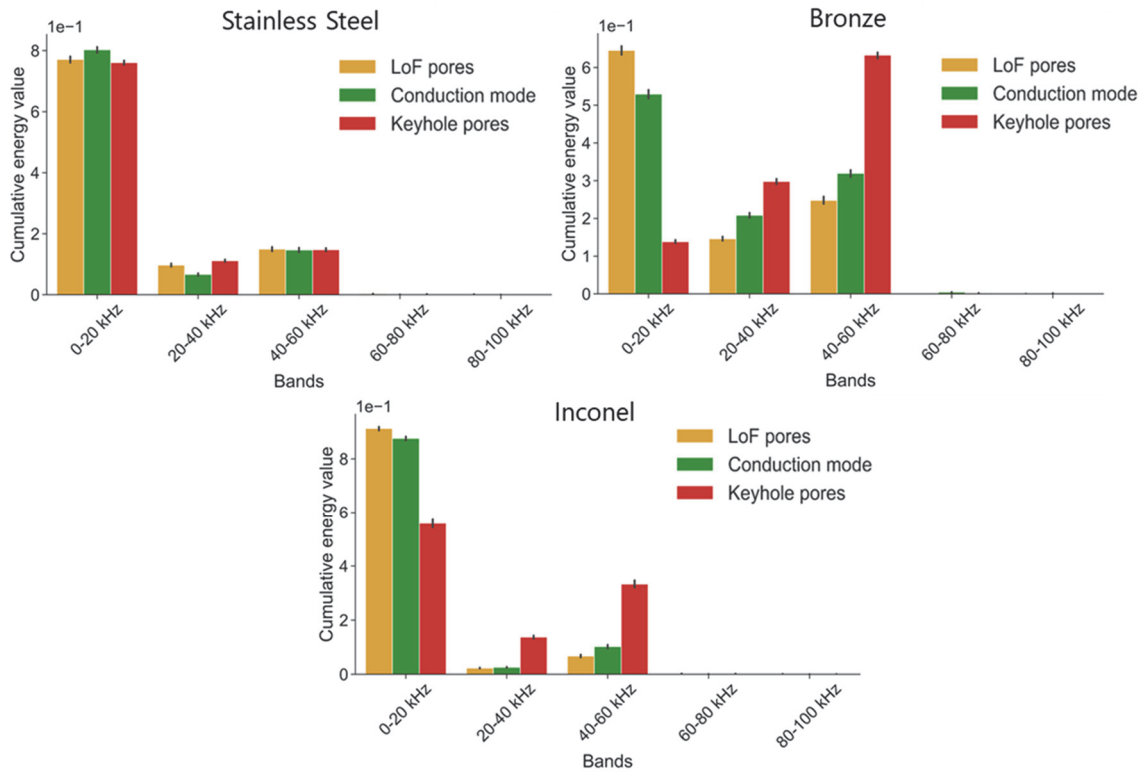


Figure 39. Comparison of cumulative energy content between five frequency bands for three regimes in stainless steel, bronze and Inconel.

4.3.3 Time-frequency domain analysis

Though the frequency domain analysis gives the frequency components in a signal, it lacks the time localisation of frequencies. The analysis of the AE signals in the frequency domains with time localisation via Wavelet transformation (WT) (Mallat 1999) is presented in this section. The Continuous Wavelet Transformation (CWT) was carried on the filtered AE signals on window sizes of 5 ms. The CWT was calculated on the acoustic signals with the mother wavelet as Morlet (Lin and Qu 2000), as it has a very good approximation error compared to other mother wavelets (Cohen 2018). The wavelet transforms are represented in a 3-dimensional (3D) plot in Figure 40. In this figure, in order to have the distinct peaks visible, the scale of each figure had to be adapted. As for the frequency domain, the wavelet coefficient values were also found to be in the range of around 0–60 kHz for all regimes and alloys. This figure has been depicted with absolute values to show how the intensity of temporal frequency components corresponding to acoustic signals originates during the laser's interaction on different alloys in the process zone. These results also corroborate with the study results made in the frequency domain analysis in Section 4.3.2. Figure 40 indicates that the values were not continuous with the time scale, and plots appeared in the form of distinct peaks as indicated in the figure by arrows. Also, the wavelet coefficient values were dominant at around 10 kHz for *LoF pores* in Inconel and stainless steel. In contrast, the wavelet coefficient values for bronze were greater at around 40 kHz for *keyhole*

Differentiation of Materials and Laser Powder Bed Fusion Processing Regimes from Airborne Acoustic Emission Combined with Machine Learning

pores, still to be correlated with a higher energy density. For Inconel, similar to the results of frequency domain analysis of the regime *conduction mode*, the wavelet coefficient values were observed to be around 10 kHz, whereas they were much higher than the other two regimes. As the resonant sensor was used in this study, the peaks across different regimes for the three materials were populated around 20 kHz and 40 kHz. But it should be noted that irrespective of similarity in the population of the peaks, they carry different intensity values, which is a statistical indicator that laser-material interaction across material and within regimes are different. Based on the distribution and intensity of the wavelet energy coefficients, it can be concluded that the time-resolved frequency features computed using WT will allow the classification of regimes and alloys during real-time monitoring.

It is important to state that the statistical study in Section 4.3 primarily focuses on understanding and correlating acoustic emissions when laser interacts with a material causing different regimes. Hence, we have not tried to monitor or localise defects that form due to different process regimes inside the process zone.

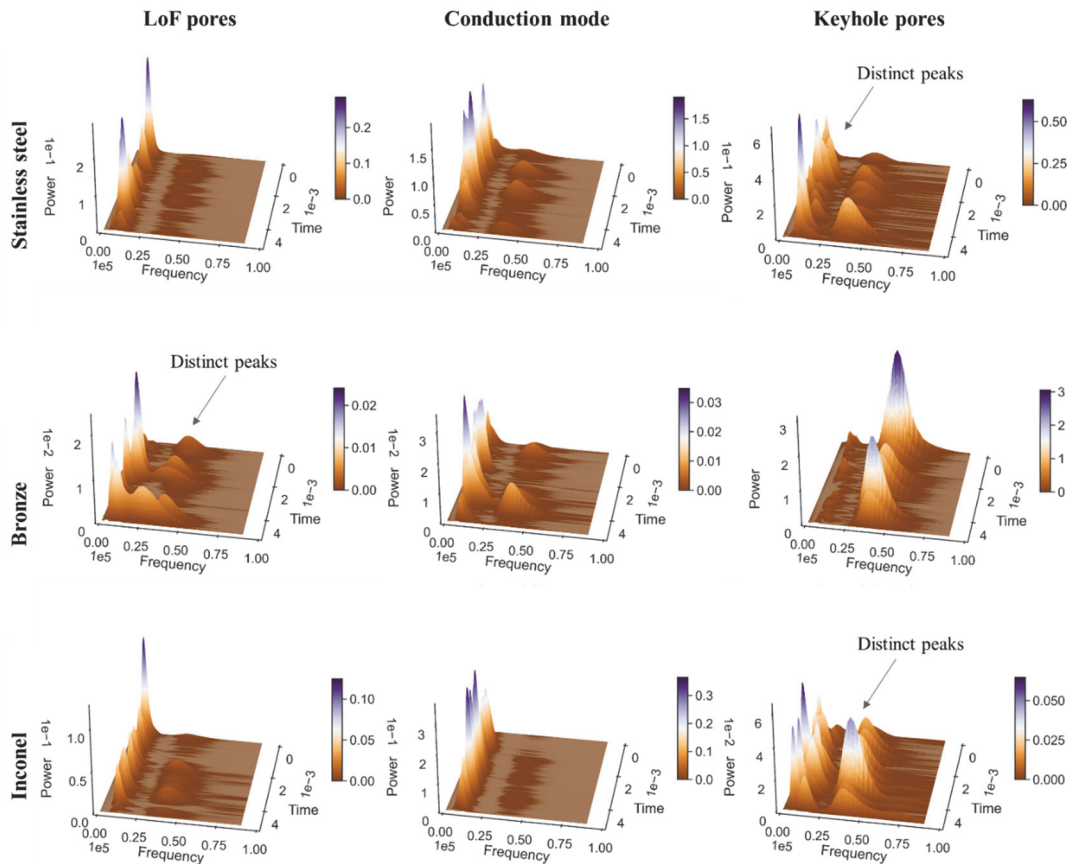


Figure 40. 3D wavelet representation of the AE signal for three laser regimes occurring in stainless steel, bronze and Inconel depicting the absolute intensities in temporal frequency distribution among the alloys.

4.4 *t*-SNE visualisation

The visualisation of the plots corresponding to the three regimes in Section 4.3 motivates extracting statistical features from each one to be used as inputs for ML models. A total of 304 features, as listed in Figure 41, were calculated based on a few works focused on classification in material processing (Pandiyani, Shevchik, et al. 2020; Pandiyani et al. 2018) using standard python libraries such as NumPy, Scipy, etc. (Lee et al. 2019; Harris et al. 2020) with 23 features from the time domain, 18 features from the frequency domain, and 263 features from the time-frequency domain.

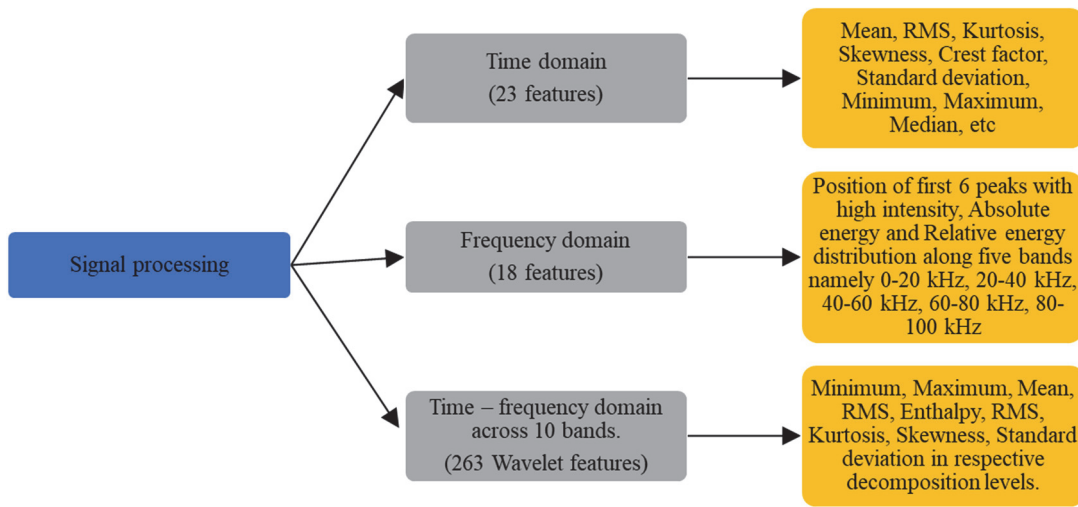


Figure 41. A comprehensive list of statistical features extracted for training the ML model in this work.

Prior to feeding them into the ML models for classification, finding correlations between them will help choose ML model complexity. With the numerous statistical features calculated from the three domains, the search for recognisable correlations becomes problematic. Dimensional reduction techniques such as *t*-SNE enable the visualisation of high-dimensional datasets by their projection into the lower-dimensional space, from which they can be easily recognised. *t*-SNE is a dimensionality reduction technique that non-linearly models the neighbour's probability distribution around each point for mapping the input multi-dimensional data into a lower-dimensional space. In this context, compared to other non-linear dimensionality techniques, *t*-SNE can retain both the local and global structure of the data simultaneously, enabling data exploration and cluster visualisation in a low-dimensional space (Maaten and Hinton 2008). Since it is a dimensionality reduction technique, the input features after computation is no longer identifiable. In our case, the acoustic features (304 features for a window of 5 ms) from the time, frequency, and time-frequency domains, that were previously discussed were the inputs to perform the *t*-SNE computation. The motivation to use *t*-SNE is to interpret and

visualise a lower dimension representation to ensure that selected statistical features can form distinct clusters in the lower dimension space.

The perplexity is a hyper-parameter, which gives a ratio of preserving the data's local structure (number of neighbours) and global structure (overall shape). For the perplexity parameter, a value of 10 was chosen after an exhaustive search to visualise the low feature space representation on the AE data acquired during the experiments, and the results are presented in Figure 42. In this figure, the features for each regime are plotted in two shades of colour depending on whether the set of parameters 1 or 2 in Table 2 for a given regime was used. In Figure 42, the *t*-SNE plots show that the three regimes (*LoF pores*, *conduction mode*, and *keyhole pores*) appear as distinctive clusters independently of the alloy. There is no drastic change when changing the number of process parameters from 1 to 2 to define a regime. The primary objective of *t*-SNE was to check the presence of clusters and also to visualise them. Nevertheless, a slight overlap among the three regimes exists for stainless steel (see Figure 42 (a)).

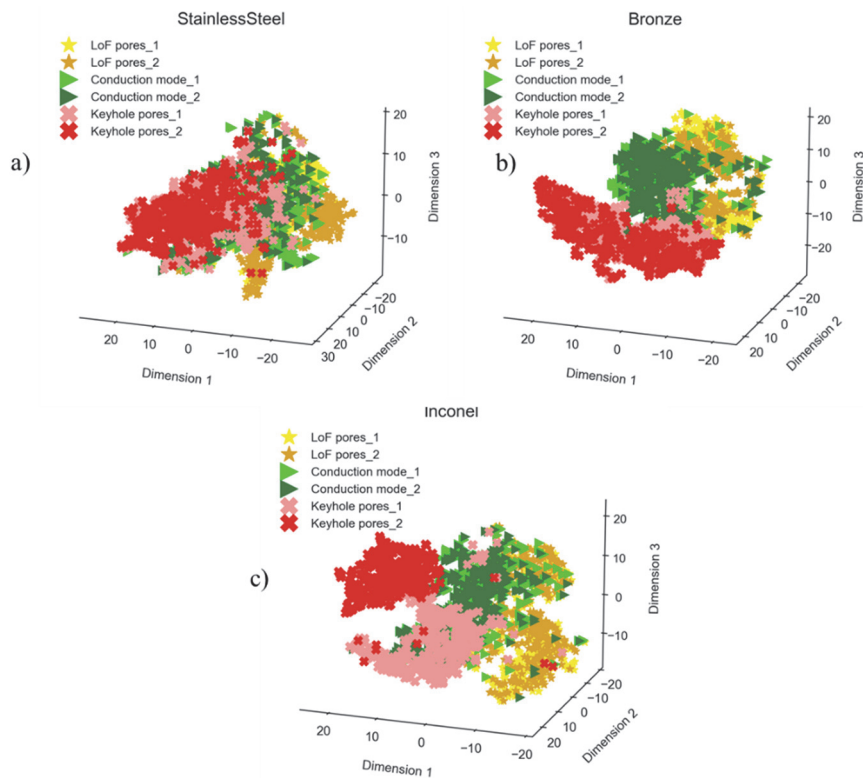


Figure 42. Low-dimension feature space representation using *t*-SNE with perplexity = 10 for three different regimes in the LPBF processing of stainless steel, bronze, and Inconel. Subscripts 1 and 2 indicate the number of process parameters considered to define a regime.

4.5 Classification results for different process regimes and materials

In 2018, Shevchik *et al.* (Shevchik et al. 2018) demonstrated that they could classify AE signals for the categories *LoF pores*, *conduction mode*, and *keyhole pores* with an accuracy ranging from 83 to 89% for 316L. To achieve these results, they acquired the AE data with a highly sensitive optoacoustic sensor (Fiber Bragg Grating (FBG)). The acoustic features were the relative energies of the WT's narrow frequency bands extracted from all signals. The window size was 160 ms. This section aims to generalise the findings for other metals but using a simple, low-cost microphone, multi-process parameters, and with a window size reduced by a factor of 32 (5 ms). Having two process parameters per category is important to extend the process phase space. The latter is of high importance as it allows a more precise location when the process changes from a "defect-free regime to a defect regime (e.g. from *conduction mode* to *keyhole pores*).

In this section, the extracted time, frequency, and time-frequency domain features from windows of 5 ms are concatenated to form a vector made out of 304 features. These features will be the input of the selected ML algorithms for classifying the three categories. For each of the three categories —*LoF pores*, *conduction mode*, and *keyhole pores* from the LPBF process — a discrete label was assigned for each alloy. The schematic flow of the monitoring methodology is illustrated in Figure 43. A dataset consisted of 3000 rows of features (3000 X 304) and their corresponding ground truth classifier labels for each alloy. The dataset prepared for all three alloys was balanced, with 1000 rows corresponding to each category. The dataset was stochastically split into two subsets, with 70% for training and 30% for testing. This approach simulated real-life conditions where the trained system has to operate with new input data (the test subset). The ML classification models were trained in a supervised manner on the training dataset with the help of the Scikit-learn ML library (Pedregosa et al. 2011). The robustness of the trained model was evaluated by comparing the model's predictions on the test set with the ground truth.

Differentiation of Materials and Laser Powder Bed Fusion Processing Regimes from Airborne Acoustic Emission Combined with Machine Learning

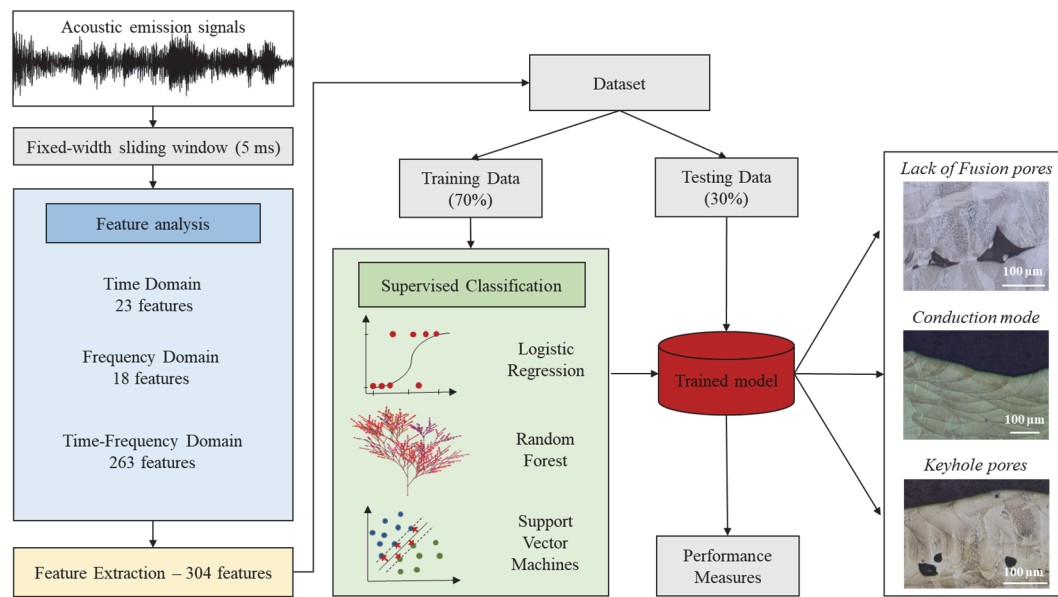


Figure 43. Schematic flow of the monitoring methodology in the LPBF process for the three ML models. The acoustic signals are divided into fixed-width sliding windows of 5 ms, then 304 features are extracted and fed to the 3 ML algorithms. 70% of the data are used for training, and 30% are kept for testing. The objective is to classify the different regimes (*LoF pores*, *conduction mode*, *keyhole pores*).

Three ML algorithms based on different complexities are used to perform the three alloys' classification task for comparison. The three ML algorithms selected for the classification tasks are Logistic Regression (LR), Random Forest (RF), and Support Vector Machines (SVM). The logistic regression model combines linear regression and the sigmoid function to return probability values, which can then be mapped to the three discrete categories. The Random forest algorithm used in this work for the classification task had 100 decision trees, and the splits were based on entropy (Pedregosa et al. 2011). Finally, the SVM algorithm used radial basis function (RBF) kernel during training for performing classification.

As an alternative to the use of the extracted features for the classification task, a CNN fed by the raw acoustic signals for the individual alloys is also used in this study. The CNN was preferred over other neural network architectures such as recurrent networks to better compare with ML algorithms, using a vector input. The CNN architecture used to classify the mechanisms for all the individual alloys is illustrated in Figure 44. This architecture design was inspired based on the VGG-16 model (Simonyan and Zisserman 2014) and included five layers with a kernel size of 16. The total number of kernels for the first layer was four and was doubled across each layer, eventually leading to a total number of kernels to 64 in the fifth convolutional layer. A stride of 1 and a padding of 0 was applied across all five convolutional layers. Each layer, except the final fully connected layer, after 1D convolution, was batch normalised before applying the Rectified Linear Units (ReLU) activation function.

As stated, the CNN network's input was the raw acoustic signal with windows of 5 ms, which is a time-series signal consisting of 5,000 data points. During the network training for the individual alloys, the weight was updated by back-propagating the cross-entropy loss. The model's training for 300 epochs, with a batch size of 100 and a learning rate of 0.01 lasted for two hours. Out of the 3,000 rows of raw signals (1,000 rows for each category), 70% of the rows were stochastically picked for training with equal weight to the categories, and the remaining 30% was used for testing the model performance. The training of the network was done using the PyTorch library and a Titan RTX Nvidia GPU. To avoid overfitting, batch normalisation was applied across layers in the CNN model. Additionally, it was also ensured that the datasets were shuffled across epochs.

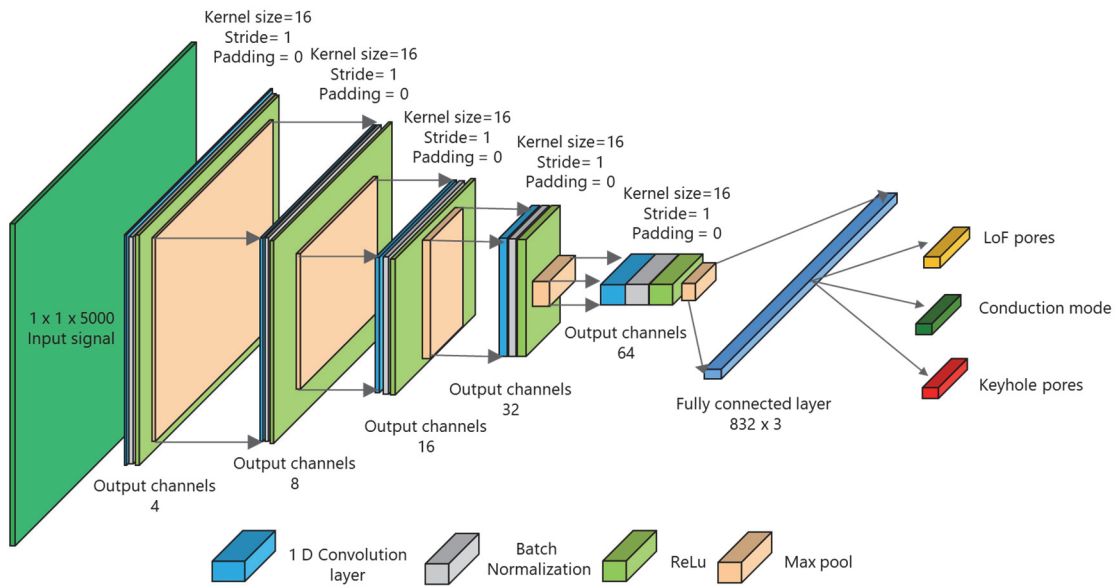


Figure 44. An illustration of the CNN architecture used in this work with five convolutional layers and fully connected layers.

4.5.1 Origin of the acoustic emission features

In this work, a microphone PAC AM4I (Physical Instrument, Germany) was used, which is a high sensitivity airborne sensor. Obviously, such a non-contact sensor captures any acoustic signals (or sounds) reaching it. Their origins are multiple, and the main ones can be summarised as workplace environment, machine and laser noises, and laser-material interactions. The latter is directly related to the process regimes and so the selected categories (*LoF pores*, *conduction mode*, *keyhole pores*). Under such circumstances and for this study, it is imperative to demonstrate that the features used for the classification task come solely from the categories; this is the core objective of this sub-section.

To address this issue, experiments with the same process parameters for all three alloys for the categories *LoF pores* and *keyhole pores* (**bold red** values) in Table 2 were performed. It was not possible for the category *conduction mode* due to the distinct properties of the selected alloys (stainless steel, bronze and Inconel). When

the same process parameter leads to a single process regime for all three alloys, only the laser-material interaction is not identical, caused by the differences in the optical, mechanical, and thermal properties. Consequently, if the features extracted from the microphone are related to this laser-material interaction, it will be possible to classify with high accuracy the alloys using the categories *LoF pores* and *keyhole pores* (**bold red** values) separately in Table 2. In contrast, the classification results being poor would have implied that the features originated from either the workplace environment, machine or laser noises, or process parameters.

The 3 by 3 confusion matrix for the classification of three alloys for the categories *LoF pores* and *keyhole pores* using the four algorithms (LR, SVM, RF and CNN) are shown in Table 3, giving the categories (*stainless steel*, *bronze*, *Inconel*) (in rows) versus the ground truth (in columns). The accuracy for the classification in Table 3 is defined based on the number of true positives divided by the total number of tests in each category. These values are given in the diagonal cells of Table 3 (dark grey cells). The misclassifications or the classification errors are computed as the sum of the false positives and false negatives divided by the total number of the tests for each category. These corresponding values are filled in off-diagonal row cells. For example, the classification accuracy of the category *stainless steel* using the RF model for *LoF pores*, in **violet** in Table 3, is 98%. The classification error is 1% with the categories *bronze* and *Inconel*. From this table, it is observed that most classification results are higher than 95% independently of the category, alloy and algorithm used. With these results, the obvious conclusion is that the features extracted from the microphone indeed represent the laser-material interaction and the associated process regime.

Table 3: Confusion matrices of the LR, SVM, RF and CNN models trained on the laser regimes across three alloys. Tables for the classification accuracy results in the three alloys. The classification results in each cell are organised in the following descending order: LR (**Bold**), SVM (Normal), RF (*Italics*), and CNN (**Bold Italics**). All values are in %.

<i>LoF pores</i>				<i>Keyhole pores</i>			
Ground truth \ Classification accuracy [%]	<i>Stainless steel</i>	<i>Bronze</i>	<i>Inconel</i>		<i>Stainless steel</i>	<i>Bronze</i>	<i>Inconel</i>
<i>Stainless steel</i>	99 98 100 100	1 1 0 0	0 1 0 0		95 96 97 97	0 0 0 3	5 4 3 0
<i>Bronze</i>	0 0 1 1.5	98 96 99 97	2 4 0 1.5		0 0 0 5	100 100 100 95	0 0 0 0
<i>Inconel</i>	1 1.5 1 0	0 1.5 1 1	99 97 98 99		5 9 11 1	1 1 1 0	94 90 88 99

4.5.2 One on one alloy classification

The previous sub- section demonstrated that the AE features are related to the laser-material interaction and associated process regimes (categories *LoF pores*, *conduction mode*, and *keyhole pores*). As already mentioned, in 2018, Shevchik *et al.* (Shevchik et al. 2018) classified the AE signals for one of the selected alloy (*stainless steel* - 316L) and for the same categories using an FBG as an airborne opto-acoustic sensor. However, they used only one process parameter per category, which restrains the process phase space. It was decided here to add a second process parameter for each category to increase the process phase space and to demonstrate that our approach is valid for multi-process parameters.

The 3 by 3 confusion matrix for the classification of three mechanisms and three alloys using the three ML models using the extracted features (LR, SVM, and RF) are shown in Table 4. As for Section 4.5.1, although the ML algorithms vary in terms of complexity and implementation, they all had excellent accuracy. Performance measure experiment with 30% test dataset and 304 features on the LR model had an average classification accuracy of 90.3% for stainless steel, 98.6% for bronze, 98% for Inconel. From the confusion matrices,

we can interpret that only a minimum fraction of samples is misclassified. Consequently, three main conclusions can be drawn. First, the classification accuracy is not sensitive to the ML algorithms. Second, the classification accuracy results demonstrate that not only the *conduction mode* mechanism can be distinguished from defective regimes, but it is possible to differentiate the pore formation regime (*LoF pores* and *keyhole pores*). Finally, considering the wide range of metals used, the proposed approach is robust for an extensive range of materials for classification on the explicit condition that the acoustic features corresponding to the materials of interest are part of the training database.

Table 4 also shows the 3 by 3 confusion matrices using the proposed CNN architecture. Although the base CNN architecture used for the classification task was the same as in Section 4.5.1, their performance was different. The average CNN prediction accuracy in bronze was higher at 98.2%, followed by Inconel (98%) and stainless steel (92.8%). The CNN network's prediction accuracy suggests that raw signals can also be used directly instead of extracting the features independently. Scrutinising Table 4, it is seen that the classification accuracy of stainless steel is lower than in bronze or Inconel. The nature of these results is unknown, but it is due to the non-distinct acoustic patterns inside the signals from the different categories of stainless steel that affect the classification performance.

Table 4: Confusion matrix (results of the classification accuracy) of the LR, SVM, RF, and CNN models trained on each individual alloy dataset. The classification results in each cell are organised in the following descending order: LR (**Bold**), SVM (Normal), RF (*Italics*), and CNN (**Bold Italics**). All values are in %.

Ground truth \ Classification accuracy [%]	Stainless steel			Bronze			Inconel		
	<i>LoF pores</i>	<i>Conduction mode</i>	<i>Keyhole pores</i>	<i>LoF pores</i>	<i>Conduction mode</i>	<i>Keyhole pores</i>	<i>LoF pores</i>	<i>Conduction mode</i>	<i>Keyhole pores</i>
<i>LoF pores</i>	92 87 93 93	0 0 1 7	8 13 6 0	100 100 98 98	0 0 0 2	0 0 2 0	99 99 98 99	0 2 0 1	1 1 2 0
<i>Conduction mode</i>	0 0 0 5.5	91 93 97 89	9 7 3 5.5	0 0 0 3.5	99 100 99 96.5	1 0 1 0	2 0.5 2 0	98 99 98 99	0 0.5 0 1
<i>Keyhole pores</i>	5 3.5 6 0	7 9.5 6 3.5	88 87 88 96.5	1 1 0 0	2 3 1 3	97 96 99 100	1 2 3 1.5	2 3 4 2.5	97 95 93 96

4.5.3 One on all alloy classification

The previous section demonstrated that our approach is valid for monitoring while processing single alloy workpieces. Still, the major drawback of industrial application is twofold. First, a classification model has to be built for any material used. Second, the correct material-dependent model has to be "loaded" prior to the processing. Any mistakes at this stage will result in the loss of raw material, machining time, and human resources. Thus, instead of developing one individual classification model for each material, a single classification model was also trained to classify the regimes irrespective of the material by grouping the three alloy datasets according to the ground-truth labels. This approach will answer question (ii) in the introduction.

Similarly to Table 4, Table 5 shows the 3 by 3 confusion matrices for the three regimes on the combined dataset for all ML algorithms. The average classification accuracy is slightly lower than the individual models but remains very high, ranging from 90 to 94.6%, depending on the regime and ML algorithm. The CNN model prediction accuracy suggests that raw acoustic signals can also be used for classifying the three process regimes irrespective of the alloy. We can infer that real-time monitoring of multi-materials using a single ML model will be feasible.

Table 5: Confusion matrices of the LR, RF and SVM model trained on the combined alloy dataset and tested for each alloy and process regimes. The classification results in each cell are organised in the following descending order: LR (**Bold**), SVM (Normal), RF (*Italics*), and CNN (**Bold Italics**). All values are in %.

Ground truth Classification accuracy [%]	<i>LoF pores</i>	<i>Conduction mode</i>	<i>Keyhole pores</i>
<i>LoF pores</i>	97 93 95 90	3 1 1 9.5	0 6 4 0.5
<i>Conduction mode</i>	3 0 0 8	92 93 97 87	5 7 3 5
<i>Keyhole pores</i>	2 7 3 0	5 7 5 4	93 86 92 96

4.5.4 Cross alloy classification- towards generalisation

In Sections 4.5.2 and **Error! Reference source not found.**, we have proven that ML algorithms can classify the categories of the alloys they have been trained for — either in separate or combined models. However, a question remains whether the same models to classify a new, unseen material (See question (i) in the introduction) can be used. To address this question, several classification tasks were performed on alloys that were not part of the training dataset to understand this hypothesis, using three combinations: one on one (e.g., Inconel on stainless steel) and combinations of two alloys on one (e.g., bronze and Inconel on stainless steel). For this study, RF was selected as the significance of the features for classification can be extracted. Out of the 9 possible combinations among the three alloys, 3 cases had poor average classification accuracy (below 50%), 5 had average accuracies around 70%, and 1 had an average accuracy above 80%. To illustrate these results, one case with good classification and another with poor classification are discussed in this section.

As an example of a good classification case, Table 6 (left) shows the 3 by 3 confusion matrix for a classification RF model built from stainless steel and bronze and tested on Inconel for the three different categories. We can interpret that only a minimum fraction of samples between *keyhole pores* and *conduction mode* are misclassified. As an example of a poor classification case, the RF model built from stainless steel and Inconel and tested on bronze, also shown in Table 6 (right), was chosen. Scrutinising the different classification results, no trend could be found between alloys' choice to train the RF model and the alloy on which the model was tested. In other words, it seems not possible to have a universal or generalised model for most metals. Further investigation on identifying the similarity of features distributions between the alloys, with Kullback–Leibler (KL) divergence, will enable us to understand these results. This analysis will be performed in future work.

Table 6: Confusion matrix of the RF model trained on two alloys and tested on a new alloy. *Left table* is a good case: Bronze and Stainless steel on Inconel, *Right table* is a bad case: Inconel and Stainless steel on bronze. All values in %.

Stainless steel + Bronze on Inconel Good case (80%)				Stainless steel + Inconel on Bronze Poor case (35%)			
<div> <div>Ground truth</div> <div>Classification accuracy [%]</div> </div>							
	<i>LoF pores</i>	<i>Conduction mode</i>	<i>Keyhole pores</i>	<i>LoF pores</i>	<i>Conduction mode</i>	<i>Keyhole pores</i>	
	<i>LoF pores</i>	61	0	39	100	0	0
	<i>Conduction mode</i>	0	93	7	0	42	58
	<i>Keyhole pores</i>	6	6	88	14	24	62

4.5.5 Multi-label classification

In Sections 4.5.2 and **Error! Reference source not found.**, most of the ML models discussed were able to classify regimes with high confidence on models trained with single material models or different material. In contrast, in Section 4.5.4, it was shown that features are material dependent and the possibility to have a universal model is low. Considering these facts, it seems possible to classify the regimes and the alloys (See question (iii) in the introduction). Such classification task can be performed via a multi-label classification. If successful, it will bring three significant advantages to the AM community for the LPBF process of different materials. First, using various materials on the same machine to build single material parts, our methodology could be used for automatic process parameters selection. Second, in the case of defect regime detection, it will determine in which of the materials the defect is created. If most defects are localised within one particular material, the machine operator will know that this specific material's process parameters must be enhanced. Finally, the knowledge of the material and regimes could be used as feedback information to adapt the process parameters if regular deviations in quality are detected.

We propose a multi-label classification CNN architecture to classify the regime and the material simultaneously on a given signal window, as illustrated in Figure 45. The architecture used included five layers with a kernel size of 16, followed by three fully connected layers. The flattened fully connected layer is split into two linear layers, out of which one predicts the regime, and the other one predicts the material. The CNN architecture for multi-label classification, as depicted in Figure 45, is an improvised architecture from the CNN architecture used for classifying regimes in mono-materials in Figure 44. The CNN network input was the raw acoustic signal with a window length of 5 ms with two ground truth labels corresponding to the regime and the material. During the network training, weights were updated by back-propagating the summation of the two cross-entropy losses corresponding to the two branches of the output layer. During the network training, weights were updated by back-propagating the summation of the two cross-entropy losses corresponding to the two branches of the linear layer, as shown in Equation (1).

$$Loss = Cross\ entropy\ Loss\ 1_{mechanism} + Cross\ entropy\ Loss\ 2_{material} \quad (1)$$

Differentiation of Materials and Laser Powder Bed Fusion Processing Regimes from Airborne Acoustic Emission Combined with Machine Learning

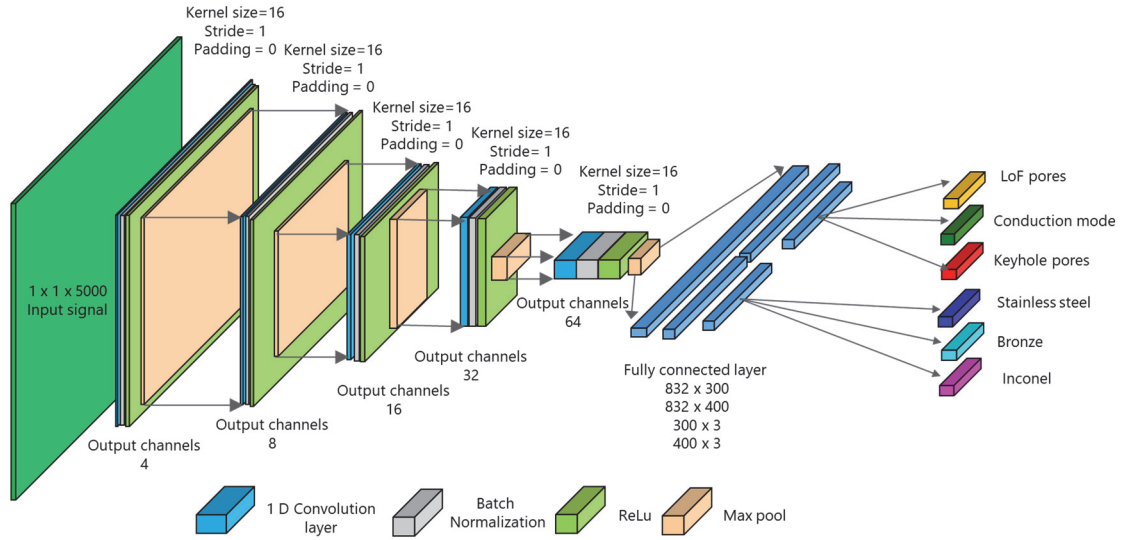


Figure 45. A illustration of the multi-label CNN architecture used in this work with five convolutional layers and two branches of fully connected layers.

The network was trained for 300 epochs, with a batch size of 100 and a learning rate of 0.01 lasted for two hours. Figure 46 confirms the network's accuracy in classifying regimes and alloys increases with training and update of the weights.

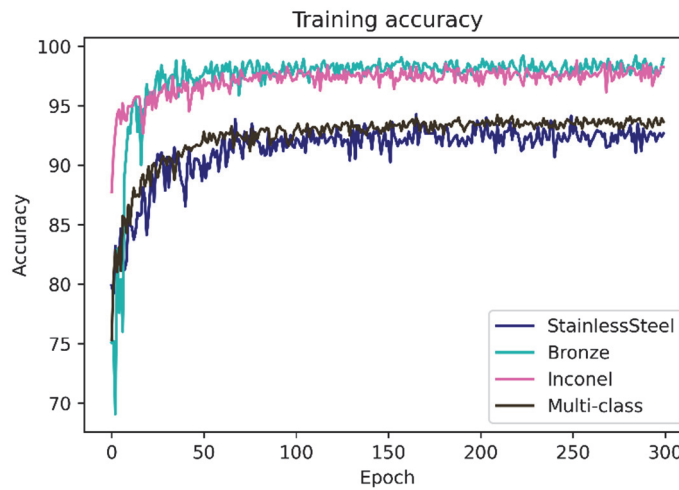


Figure 46. Accuracy curves confirming that CNN models trained for classifying regimes on individual materials and multi-materials learn with training epochs.

The newly configured CNN network for multi-label had the AE raw signals as inputs data. The multi-label classification of the mechanism and the alloy was performed simultaneously, and their accuracy is shown in Table 7. From this table, the overall classification accuracies were 93.3% for the process regimes and 94% for the alloys. Considering the selected process parameters for the process regimes and alloys (See Table 2), these

results are of utmost importance for two reasons. First, it establishes that our approach can be successfully applied as a robust and low-cost in situ and real-time process monitoring of multi-material LPBF processes. Second, it confirms the results of Section 4.5.1; the features used for the classification task originated from the laser-material interaction and the associated process regime. Had it been the process parameters, the classification accuracies for the materials in Table 7 would not exceed 77.6%. As a reminder, for the process regimes, *LoF pores* and *keyhole pores*, one set of process parameters was identical for all alloys (**bold red** values in Table 1), and so it would have equal probability to be classified for any of the three alloys. In other words, these two common process parameters would classify the material correctly with a maximum probability of 33.3%. In contrast, it would be 100% for the other four process parameters, giving the 77.6% (466 out of 600).

Table 7: Confusion matrices of the multi-label CNN model trained on two ground-truth labels.

Left table: classification accuracy on the regimes. *Right table:* classification accuracy on the materials. All values are in %.

Process regimes (93.3%)

Ground truth \ Classification accuracy [%]	<i>LoF pores</i>	<i>Conduction mode</i>	<i>Keyhole pores</i>
<i>LoF pores</i>	93.0	6.5	0.5
<i>Conduction mode</i>	6.0	91.0	3.0
<i>Keyhole pores</i>	0.5	3.5	96.0

Materials (94.0%)

Ground truth \ Classification accuracy [%]	<i>Stainless steel</i>	<i>Bronze</i>	<i>Inconel</i>
<i>Stainless steel</i>	97.0	2.0	1.0
<i>Bronze</i>	2.0	91.0	7.0
<i>Inconel</i>	0.5	5.5	94.0

4.5.6 Summary of the classification tasks

The results of the classification tasks in this section can be summarised as follows.

- We demonstrated that the AE signatures used for the classification task are strongly related to the laser-material interaction and are unique for each material.

- When coupled with ML algorithms, the features from low-cost airborne acoustic sensors can classify the type of defect regimes (regimes) with very high confidence irrespective of the materials considered.
- The classification of defect regimes irrespective of the material based on a single ML model is feasible by combining the dataset from different alloys.
- The generalisation of the classification of LPBF defects to other (untrained) alloys cannot be made, as the acoustic signals representing the defect formation mechanisms are material-dependent. Failure of generalisations have the positive outcome of successful classification of alloys and regimes simultaneously.
- The multi-label CNN model proposed in this work can simultaneously identify the processing regime and the alloy, with excellent accuracy.

4.6 Conclusions

This contribution presents an analysis of the AE signals acquired during LPBF processing of three metallic alloys: stainless steel (316L), bronze (CuSn₈), and Inconel (Inconel 718). The experiments were conducted in a custom-designed LPBF machine equipped with an acoustic sensor. The AE sensor used is the PAC AM4I sensor, an airborne sensor with a frequency response in the range of 1–100 kHz. Data acquisitions are made with an Advantech DAQ system at a sampling rate of 1 MHz to record the AE during the experiments. Different laser powers and laser velocities were used to produce overlapping line tracks to simulate three major material qualities (regimes) in LPBF: *LoF pores*, *conduction mode*, and *keyhole pores*. This main contribution objective focuses on the correlation of the three regimes with their corresponding AE signals. The acoustic data resolved in three different domains (time, frequency, and time-frequency) were statistically quantified and visualised to characterise the three regimes for all three alloys. The following generalised conclusions based on the experimental results are summarised below.

Airborne AE is a potential contender for real-time monitoring when processing different materials. They can capture discrete AE signatures corresponding to different laser-material interaction regimes across different alloys. The statistical distribution of different time-domain features among the regimes for all three alloys appear to be different, suggesting that they can be used as an input feature to ML algorithms for in situ and real-time monitoring. The frequency distribution of AE signals for the three materials shows that a significant energy concentration is located between 1 and 60 kHz. The frequency peaks were dominant at around 10 and 40 kHz, as the PAC AM4I acoustic sensor's sensitivity is higher in this region. The comparison of the energy

concentration in five energy bands divided equally between 1 Hz to 100 kHz showed that these three regimes under study exhibit discrete energy levels for all three alloys. The distinct energy levels corresponding to the different regimes can also be used as a feature input to any ML algorithm for classification. The visualisation of wavelet plots for a time scale of 5 ms suggests that the energy coefficient distributions are almost synonymous with the frequency-domain results. Discrete peaks from the wavelet plot during the line scan experiments assert that the regimes are distinct, and a proper selection of the window size is vital for real-time defect localisation. The feature reduction based on the *t*-SNE technique hinted that the regimes features are clustered in the feature space irrespective of the three alloys. The visualisation of the clustered feature space suggests that the LPBF process involving Inconel, bronze, and stainless steel is highly dynamic, and only algorithms capable of classifying data in non-linear spaces would be able to identify them.

Traditional ML algorithms such as LR, RF, and SVM were trained on selected features for classification. Apart from these conventional models, CNN was also trained to classify the raw acoustic signals corresponding to the 3 regimes. Very high classification accuracy was obtained from the ML models such as LR (> 90%), RF (> 92%), SVM (> 89%), and CNN (> 92.5%) on the individual alloys. To address the challenge of the LPBF process of different materials, an ML model built from the three materials showed that the acoustic features prove promising for real-time monitoring, as the classification accuracy was higher than 86%. The study also showed that generalisation of the classification of LPBF defects between alloys is not possible in most cases as the acoustic signals representing the regimes are material dependent. Finally, the multi-label CNN results suggest that — apart from classifying the regimes in different materials with good accuracy — it can also be used to classify the alloy and the regime at the same time. This is of great interest for the LPBF process of multiple materials.

In general, these research outcomes confirm that the extraction of acoustic signals and their features in time, frequency, and time-frequency domains — combined with ML — is a promising technique for in situ and real-time quality monitoring for most metals. We also propose data acquisition strategies, data pre-processing, and ML algorithms to build a complete monitoring system for the LPBF process. The study of the phenomena at frequencies higher than 100 kHz requires a contact AE sensor, a work under investigation. Out of the many events in the laser-material interaction zone, only three processing regimes are correlated to acoustic signals in this research work. The feasibility of understanding the acoustic features corresponding to the early detection of other phenomena such as the evolution of microstructure, propagation of cracks, and delamination are also part of our future work. Also, ML models used in this work are discriminative models, which means they draw boundaries in the data space. As the dataspace changes, they are susceptible to error. And as we move from one machine to another, there is a high probability that this data space will change owing to the geometry of the chamber, machine parameters, the initial condition of the powder spread, location of the airborne acoustic sensor etc. Therefore, for the purpose of universality across machines, developments can be foreseen in generative models or techniques like domain adaptation or transfer learning.

References

- Aboulkhair, Nesma T, Nicola M Everitt, Ian Ashcroft, and Chris Tuck. 2014. "Reducing porosity in AlSi10Mg parts processed by selective laser melting." *Additive Manufacturing* 1:77-86.
- Babtle, MS. 1948. "Smoothing periodograms from time-series with continuous spectra." *Nature* 161 (4096):686-7.
- Caggiano, Alessandra, Jianjing Zhang, Vittorio Alfieri, Fabrizia Caiazzo, Robert Gao, and Roberto Teti. 2019. "Machine learning-based image processing for on-line defect recognition in additive manufacturing." *CIRP annals* 68 (1):451-4.
- Chen, Changming, Radovan Kovacevic, and Dragana Jandgric. 2003. "Wavelet transform analysis of acoustic emission in monitoring friction stir welding of 6061 aluminum." *International Journal of Machine Tools and Manufacture* 43 (13):1383-90.
- Chua, Zhong Yang, Il Hyuk Ahn, and Seung Ki Moon. 2017. "Process monitoring and inspection systems in metal additive manufacturing: Status and applications." *International Journal of Precision Engineering and Manufacturing-Green Technology* 4 (2):235-45.
- Coeck, Sam, Manisha Bisht, Jan Plas, and Frederik Verbist. 2019. "Prediction of lack of fusion porosity in selective laser melting based on melt pool monitoring data." *Additive Manufacturing* 25:347-56.
- Cohen, MX. 2018. "A better way to define and describe Morlet wavelets for time-frequency analysis. bioRxiv: 14."
- Cunningham, Ross, Cang Zhao, Niranjana Parab, Christopher Kantzos, Joseph Pauza, Kamel Fezzaa, Tao Sun, and Anthony D Rollett. 2019. "Keyhole threshold and morphology in laser melting revealed by ultrahigh-speed x-ray imaging." *Science* 363 (6429):849-52.
- DebRoy, Tarasankar, HL Wei, JS Zuback, T Mukherjee, JW Elmer, JO Milewski, Allison Michelle Beese, A de Wilson-Heid, A De, and W Zhang. 2018. "Additive manufacturing of metallic components—process, structure and properties." *Progress in Materials Science* 92:112-224.
- Dowling, L, J Kennedy, S O'Shaughnessy, and D Trimble. 2020. "A review of critical repeatability and reproducibility issues in powder bed fusion." *Materials & Design* 186:108346.
- du Plessis, Anton, Ina Yadroitsava, and Igor Yadroitsev. 2020. "Effects of defects on mechanical properties in metal additive manufacturing: A review focusing on X-ray tomography insights." *Materials & Design* 187:108385.

- Everton, Sarah K, Matthias Hirsch, Petros Stravroulakis, Richard K Leach, and Adam T Clare. 2016. "Review of in-situ process monitoring and in-situ metrology for metal additive manufacturing." *Materials & Design* 95:431-45.
- Forien, Jean-Baptiste, Nicholas P Calta, Philip J DePond, Gabe M Guss, Tien T Roehling, and Manyalibo J Matthews. 2020. "Detecting keyhole pore defects and monitoring process signatures during laser powder bed fusion: a correlation between in situ pyrometry and ex situ X-ray radiography." *Additive Manufacturing*:101336.
- Ghasemi-Tabasi, Hossein, Jamasp Jhabvala, Eric Boillat, Toni Ivas, Rita Drissi-Daoudi, and Roland E Logé. 2020. "An effective rule for translating optimal selective laser melting processing parameters from one material to another." *Additive Manufacturing* 36:101496.
- Goh, Guo Dong, Swee Leong Sing, and Wai Yee Yeong. 2020. "A review on machine learning in 3D printing: applications, potential, and challenges." *Artificial Intelligence Review*:1-32.
- Gong, Haijun, Khalid Rafi, Hengfeng Gu, Thomas Starr, and Brent Stucker. 2014. "Analysis of defect generation in Ti-6Al-4V parts made using powder bed fusion additive manufacturing processes." *Additive Manufacturing* 1:87-98.
- Grasso, M, AG Demir, B Previtali, and BM Colosimo. 2018. "In situ monitoring of selective laser melting of zinc powder via infrared imaging of the process plume." *Robotics and Computer-Integrated Manufacturing* 49:229-39.
- Gu, DD, YF Shen, JL Yang, and Y Wang. 2006. "Effects of processing parameters on direct laser sintering of multicomponent Cu based metal powder." *Materials science and technology* 22 (12):1449-55.
- Gu, Hongping, and Walt W Duley. 1996. "Resonant acoustic emission during laser welding of metals." *Journal of Physics D: Applied Physics* 29 (3):550.
- Harris, Charles R, K Jarrod Millman, Stéfan J van der Walt, Ralf Gommers, Pauli Virtanen, David Cournapeau, Eric Wieser, Julian Taylor, Sebastian Berg, and Nathaniel J Smith. 2020. "Array programming with NumPy." *Nature* 585 (7825):357-62.
- Heeling, Thorsten, Michael Cloots, and Konrad Wegener. 2017. "Melt pool simulation for the evaluation of process parameters in selective laser melting." *Additive Manufacturing* 14:116-25.
- Hooper, Paul A. 2018. "Melt pool temperature and cooling rates in laser powder bed fusion." *Additive Manufacturing* 22:548-59.

- Jerri, A. J. 1977. "The Shannon sampling theorem—Its various extensions and applications: A tutorial review." *Proceedings of the IEEE* 65 (11):1565-96. doi: 10.1109/PROC.1977.10771.
- Jiang, Jingchao, Chunling Yu, Xun Xu, Yongsheng Ma, and Jikai Liu. 2020. "Achieving better connections between deposited lines in additive manufacturing via machine learning." *Math. Biosci. Eng* 17 (4).
- Khairallah, Saad A, Andrew T Anderson, Alexander Rubenchik, and Wayne E King. 2016. "Laser powder-bed fusion additive manufacturing: Physics of complex melt flow and formation mechanisms of pores, spatter, and denudation zones." *Acta Materialia* 108:36-45.
- Khanzadeh, Mojtaba, Sudipta Chowdhury, Mohammad Marufuzzaman, Mark A Tschopp, and Linkan Bian. 2018. "Porosity prediction: Supervised-learning of thermal history for direct laser deposition." *Journal of manufacturing systems* 47:69-82.
- Khanzadeh, Mojtaba, Wenmeng Tian, Aref Yadollahi, Haley R Doude, Mark A Tschopp, and Linkan Bian. 2018. "Dual process monitoring of metal-based additive manufacturing using tensor decomposition of thermal image streams." *Additive Manufacturing* 23:443-56.
- King, Wayne E, Andrew T Anderson, Robert M Ferencz, Neil E Hodge, Chandrika Kamath, Saad A Khairallah, and Alexander M Rubenchik. 2015. "Laser powder bed fusion additive manufacturing of metals; physics, computational, and materials challenges." *Applied Physics Reviews* 2 (4):041304.
- King, Wayne E, Holly D Barth, Victor M Castillo, Gilbert F Gallegos, John W Gibbs, Douglas E Hahn, Chandrika Kamath, and Alexander M Rubenchik. 2014. "Observation of keyhole-mode laser melting in laser powder-bed fusion additive manufacturing." *Journal of materials processing technology* 214 (12):2915-25.
- Kurzynowski, Tomasz, Edward Chlebus, Bogumiła Kuźnicka, and Jacek Reiner. 2012. Parameters in selective laser melting for processing metallic powders. Paper presented at the High Power Laser Materials Processing: Lasers, Beam Delivery, Diagnostics, and Applications.
- Le-Quang, T, SA Shevchik, B Meylan, F Vakili-Farahani, MP Olbinado, A Rack, and K Wasmer. 2018. "Why is in situ quality control of laser keyhole welding a real challenge?" *Procedia CIRP* 74:649-53.
- Lee, Gregory R, Ralf Gommers, Filip Waselewski, Kai Wohlfahrt, and Aaron O'Leary. 2019. "PyWavelets: A Python package for wavelet analysis." *Journal of Open Source Software* 4 (36):1237.
- Lin, Jing, and Liangsheng Qu. 2000. "Feature extraction based on Morlet wavelet and its application for mechanical fault diagnosis." *Journal of sound and vibration* 234 (1):135-48.
- Maaten, Laurens van der, and Geoffrey Hinton. 2008. "Visualizing data using t-SNE." *Journal of machine learning research* 9 (Nov):2579-605.

Mallat, Stéphane. 1999. *A wavelet tour of signal processing*: Elsevier.

Masinelli, Giulio, Sergey A Shevchik, Vigneashwara Pandiyan, Tri Quang-Le, and Kilian Wasmer. 2020. Artificial Intelligence for Monitoring and Control of Metal Additive Manufacturing. Paper presented at the International Conference on Additive Manufacturing in Products and Applications.

Mukherjee, T, and Tarasankar DebRoy. 2018. "Mitigation of lack of fusion defects in powder bed fusion additive manufacturing." *Journal of Manufacturing Processes* 36:442-9.

Nassar, Abdalla R, Molly A Gundermann, Edward W Reutzel, Paul Guerrier, Michael H Krane, and Matthew J Weldon. 2019. "Formation processes for large ejecta and interactions with melt pool formation in powder bed fusion additive manufacturing." *Scientific reports* 9 (1):1-11.

Pandiyan, Vigneashwara, Wahyu Caesarendra, Tegoeh Tjahjowidodo, and Hock Hao Tan. 2018. "In-process tool condition monitoring in compliant abrasive belt grinding process using support vector machine and genetic algorithm." *Journal of Manufacturing Processes* 31:199-213.

Pandiyan, Vigneashwara, Rita Drissi-Daoudi, Sergey Shevchik, Giulio Masinelli, Roland Logé, and Kilian Wasmer. 2020. "Analysis of time, frequency and time-frequency domain features from acoustic emissions during Laser Powder-Bed fusion process." *Procedia CIRP* 94:392-7.

Pandiyan, Vigneashwara, Sergey Shevchik, Kilian Wasmer, Sylvie Castagne, and Tegoeh Tjahjowidodo. 2020. "Modelling and monitoring of abrasive finishing processes using artificial intelligence techniques: A review." *Journal of Manufacturing Processes* 57:114-35.

Pandiyan, Vigneashwara, and Tegoeh Tjahjowidodo. 2017. "In-process endpoint detection of weld seam removal in robotic abrasive belt grinding process." *The International Journal of Advanced Manufacturing Technology* 93 (5-8):1699-714.

———. 2019. "Use of Acoustic Emissions to detect change in contact mechanisms caused by tool wear in abrasive belt grinding process." *Wear* 436:203047.

Pedregosa, Fabian, Gaël Varoquaux, Alexandre Gramfort, Vincent Michel, Bertrand Thirion, Olivier Grisel, Mathieu Blondel, Peter Prettenhofer, Ron Weiss, and Vincent Dubourg. 2011. "Scikit-learn: Machine learning in Python." *the Journal of machine Learning research* 12:2825-30.

Qi, Ting, Haihong Zhu, Hu Zhang, Jie Yin, Linda Ke, and Xiaoyan Zeng. 2017. "Selective laser melting of Al7050 powder: Melting mode transition and comparison of the characteristics between the keyhole and conduction mode." *Materials & Design* 135:257-66.

Ren, K, Y Chew, N Liu, YF Zhang, JYH Fuh, and GJ Bi. 2021. "Integrated numerical modelling and deep learning for multi-layer cube deposition planning in laser aided additive manufacturing." *Virtual and physical prototyping*:1-15.

Scime, Luke, and Jack Beuth. 2018a. "Anomaly detection and classification in a laser powder bed additive manufacturing process using a trained computer vision algorithm." *Additive Manufacturing* 19:114-26.

———. 2018b. "A multi-scale convolutional neural network for autonomous anomaly detection and classification in a laser powder bed fusion additive manufacturing process." *Additive Manufacturing* 24:273-86.

———. 2019. "Using machine learning to identify in-situ melt pool signatures indicative of flaw formation in a laser powder bed fusion additive manufacturing process." *Additive Manufacturing* 25:151-65.

Scime, Luke, Derek Siddel, Seth Baird, and Vincent Paquit. 2020. "Layer-wise anomaly detection and classification for powder bed additive manufacturing processes: A machine-agnostic algorithm for real-time pixel-wise semantic segmentation." *Additive Manufacturing* 36:101453.

Shevchik, Sergey A, Christoph Kenel, Christian Leinenbach, and Kilian Wasmer. 2018. "Acoustic emission for in situ quality monitoring in additive manufacturing using spectral convolutional neural networks." *Additive Manufacturing* 21:598-604.

Shevchik, Sergey A, Tri Le-Quang, Farzad Vakili Farahani, Neige Faivre, Bastian Meylan, Silvio Zanolli, and Kilian Wasmer. 2019. "Laser welding quality monitoring via graph support vector machine with data adaptive kernel." *IEEE Access* 7:93108-22.

Shevchik, Sergey A, Giulio Masinelli, Christoph Kenel, Christian Leinenbach, and Kilian Wasmer. 2019. "Deep learning for in situ and real-time quality monitoring in additive manufacturing using acoustic emission." *IEEE Transactions on Industrial Informatics* 15 (9):5194-203.

Shevchik, Sergey, Tri Le-Quang, Bastian Meylan, Farzad Vakili Farahani, Margie P Olbinado, Alexander Rack, Giulio Masinelli, Christian Leinenbach, and Kilian Wasmer. 2020a. "Author correction: Supervised deep learning for real-time quality monitoring of laser welding with X-ray radiographic guidance." *Scientific reports* 10 (1):1-2.

———. 2020b. "Supervised deep learning for real-time quality monitoring of laser welding with X-ray radiographic guidance." *Scientific reports* 10 (1):1-12.

Simonyan, Karen, and Andrew Zisserman. 2014. "Very deep convolutional networks for large-scale image recognition." *arXiv preprint arXiv:1409.1556*.

- Sing, SL, CN Kuo, CT Shih, CC Ho, and CK Chua. 2021. "Perspectives of using machine learning in laser powder bed fusion for metal additive manufacturing." *Virtual and physical prototyping* 16 (3):372-86.
- Spears, Thomas G, and Scott A Gold. 2016. "In-process sensing in selective laser melting (SLM) additive manufacturing." *Integrating Materials and Manufacturing Innovation* 5 (1):16-40.
- Tapia, Gustavo, and Alaa Elwany. 2014. "A review on process monitoring and control in metal-based additive manufacturing." *Journal of Manufacturing Science and Engineering* 136 (6).
- Thanki, Aditi, Louca Goossens, Raya Mertens, Gabriel Probst, Wim Dewulf, Ann Witvrouw, and Shofeng Yang. 2019. "Study of keyhole-porosities in selective laser melting using X-ray computed tomography." *Proceedings of iCT 2019*:1-7.
- Van Elsen, Maarten. 2007. "Complexity of Selective Laser Melting: a new optimisation approach."
- Wasmer, K, C Kenel, C Leinenbach, and SA Shevchik. 2017. In situ and real-time monitoring of powder-bed AM by combining acoustic emission and artificial intelligence. Paper presented at the International Conference on Additive Manufacturing in Products and Applications.
- Wasmer, K, T Le-Quang, B Meylan, and SA Shevchik. 2019. "In situ quality monitoring in AM using acoustic emission: A reinforcement learning approach." *Journal of Materials Engineering and Performance* 28 (2):666-72.
- Welch, Peter. 1967. "The use of fast Fourier transform for the estimation of power spectra: a method based on time averaging over short, modified periodograms." *IEEE Transactions on audio and electroacoustics* 15 (2):70-3.
- Wu, Haixi, Yan Wang, and Zhonghua Yu. 2016. "In situ monitoring of FDM machine condition via acoustic emission." *The International Journal of Advanced Manufacturing Technology* 84 (5-8):1483-95.
- Wu, Haixi, Zhonghua Yu, and Yan Wang. 2017. "Real-time FDM machine condition monitoring and diagnosis based on acoustic emission and hidden semi-Markov model." *The International Journal of Advanced Manufacturing Technology* 90 (5-8):2027-36.
- Xiao, Ling, Mingyuan Lu, and Han Huang. 2020. "Detection of powder bed defects in selective laser sintering using convolutional neural network." *The International Journal of Advanced Manufacturing Technology*:1-12.
- Yan, Zhaorui, Weiwei Liu, Zijue Tang, Xuyang Liu, Nan Zhang, Mingzheng Li, and Hongchao Zhang. 2018. "Review on thermal analysis in laser-based additive manufacturing." *Optics & Laser Technology* 106:427-41.

- Yap, Chor Yen, Chee Kai Chua, Zhi Li Dong, Zhong Hong Liu, Dan Qing Zhang, Loong Ee Loh, and Swee Leong Sing. 2015. "Review of selective laser melting: Materials and applications." *Applied Physics Reviews* 2 (4):041101.
- Ye, Dongsan, Geok Soon Hong, Yingjie Zhang, Kunpeng Zhu, and Jerry Ying Hsi Fuh. 2018. "Defect detection in selective laser melting technology by acoustic signals with deep belief networks." *The International Journal of Advanced Manufacturing Technology* 96 (5-8):2791-801.
- Ye, DS, YHJ Fuh, YJ Zhang, GS Hong, and KP Zhu. 2018. "Defects Recognition in Selective Laser Melting with Acoustic Signals by SVM Based on Feature Reduction." *MS&E* 436 (1):012020.
- Yu, Chunling, and Jingchao Jiang. 2020. "A perspective on using machine learning in 3D bioprinting." *International Journal of Bioprinting* 6 (1).
- Zhang, Bi, Yongtao Li, and Qian Bai. 2017. "Defect formation mechanisms in selective laser melting: a review." *Chinese Journal of Mechanical Engineering* 30 (3):515-27.
- Zhao, Cang, Kamel Fezzaa, Ross W Cunningham, Haidan Wen, Francesco De Carlo, Lianyi Chen, Anthony D Rollett, and Tao Sun. 2017. "Real-time monitoring of laser powder bed fusion process using high-speed X-ray imaging and diffraction." *Scientific reports* 7 (1):1-11.

Learnings and following work:

The design of experiment of the chapter four proved that the classification is mainly performed on the laser-matter information of the AE signals. This is a sine qua non condition to the use of AE based monitoring. It is also the foundation to the generalization to condition outside of the training conditions, i.e other alloy, parameters or machine AE signals. The chapter four proved that, with the chosen sensor, the generalization from one alloy to another is not possible. The features on the studied frequencies are material dependent. To reach a more robust monitoring approach, two methodologies are investigated. The first one consists in developing ML solutions based on transfer learning (chapter five) or semi-supervised (chapter 6) algorithms, and the second one is to optimize the choice of the microphone, considering a flat frequency response (chapters 7 and 8).

The chapter five investigated a deep learning network transferring knowledge from stainless steel (316L) to bronze (CuSn8), considering four LPBF process regimes such as *balling*, *LoF pores*, *conduction mode*, and *keyhole pores*, reducing the computational need and the amount of data required for a reliable classification.

The chapter six investigates a semi-supervised approach where the defect categories are differentiated from the conduction mode regime. This method reduced the amount of data needed for the classification as well as computational needs and the requirement of a balanced dataset.

These two following chapters take into consideration the balling defect as an independent category, the other chapters considers balling as a sub-category of the LoF domain.

Chapter 5

Deep Transfer Learning of Additive Manufacturing Mechanisms Across Materials in Metal-Based Laser Powder Bed Fusion Process

Vigneashwara Pandiyan ^{a, *}, Rita Drissi-Daoudi ^b, Sergey Shevchik ^a, Giulio Masinelli ^a, Tri Le-Quang ^a, Roland Logé^b, Kilian Wasmer ^a

^a *Laboratory for Advanced Materials Processing (LAMP), Swiss Federal Laboratories for Materials Science and Technology (Empa)-CH-3602 Thun, Switzerland*

^b *Thermomechanical Metallurgy Laboratory – PX Group Chair, Ecole Polytechnique Fédérale de Lausanne (EPFL), CH-2002 Neuchâtel, Switzerland*

Vigneashwara Pandiyan, Rita Drissi-Daoudi, Sergey Shevchik, Giulio Masinelli, Tri Le-Quang, Roland Logé, Kilian Wasmer, **Deep transfer learning of additive manufacturing mechanisms across materials in metal-based laser powder bed fusion process**, Journal of Materials Processing Technology, Volume 303, 2022, 117531, ISSN 0924-0136, <https://doi.org/10.1016/j.jmatprotec.2022.117531>

Contribution: Rita Drissi-Daoudi developed the experimental plan and printed the samples. She reviewed the manuscript.

Abstract

The defective regimes in metal-based Laser Powder Bed Fusion (LPBF) processes can be minimized by deploying in-situ monitoring strategies comprising Machine learning (ML) algorithms and sensing techniques. So far, algorithms trained for monitoring a particular material type cannot be re-used to monitor another material in Additive Manufacturing (AM). This is a topic rarely researched in AM. Inspired by the idea of transfer learning in ML, we demonstrate the knowledge learned by the two native Deep Learning (DL) networks, namely VGG and ResNets, on four LPBF process mechanisms such as *balling*, *Lack of Fusion (LoF) pores*, *conduction mode*, and *keyhole pores* in stainless steel (316L) can be transferred to bronze (CuSn8). In this work, the spectrograms computed using Wavelet Transforms (WT) on Acoustic Emissions (AE) during the LPBF process of stainless steel and bronze are used for training the two DL networks. Either network is first trained for classification by spectrograms representing four mechanisms during the processing of stainless steel. The trained model is then re-trained using transfer learning with spectrograms from bronze data for a similar classification task. The accuracy of the two networks during transfer learning shows that it is effectively possible to learn transferable features from one material to another with minimum network training time and dataset collection.

Keywords: Powder bed fusion; *In-situ* monitoring; Wavelet Transform; Convolutional neural network; Transfer learning.

5.1 Introduction

Additive manufacturing (AM) has become a prominent method in fabricating complicated and intricate shapes in leading industrial sectors compared to the traditional manufacturing techniques (Tapia and Elwany, 2014). AM offers advantages such as minimum wastage of material and a cleaner production environment compared to subtractive machining techniques that were traditionally practiced. Laser Powder Bed Fusion (LPBF) is a variant among metal additive manufacturing techniques that have been quite well known for a while and are the most investigated. In LPBF, the parts are built-in sequential layers. A laser beam moves around a powder bed of thickness ranging from 20-60 μm prepared by a re-coater mechanism. The laser irradiation melts and fuses the particles in a powder bed with their neighboring layers as well as with adjacent particles in the same layer. The laser irradiation scans are performed selectively by moving optical elements in the laser head based on the original 3D computer-aided design (CAD). The process of irradiating and refilling the powder bed continues until the whole part is built, typically going up to thousands of layers.

Building parts without defects in processing a specific material involves choosing optimum parameter levels to achieve desired properties. Numerous parameters such as laser power (Spears and Gold, 2016), scanning speed (Esmailizadeh et al., 2020), scanning pattern (Liu et al., 2021), the material composition of the powder (Knieps et al., 2021), surrounding environment (Ch et al., 2019), laser beam size (Gerstgrasser et al., 2021), etc., affect the LPBF process quality. During the process, any deviation from the optimum window parameters for any material causes significant changes in the laser-material interaction affecting the melt pool's depth, width, and length. The resulting melt pool geometry influences the quality of the built part. Conversely, unfavourable melt pool geometries lead to the formation of defect mechanisms such as *balling*, porosity, *LoF pores*, delamination, cracks and deviation from the desired microstructure. Some effects of the parameters on laser-material interaction and the corresponding defect mechanism are listed in Table 8.

Deep Transfer Learning of Additive Manufacturing Mechanisms Across Materials in Metal-Based Laser Powder Bed Fusion Process

Table 8. Effect of parameter level on laser-material interaction in LPBF process.

Parameter	Parameter level	Mechanism evolved	Remarks on laser-material interaction	Reference
Laser power	High	Cracks, Distortion and <i>keyhole pore</i> formation	<ul style="list-style-type: none"> Evaporation of material, the occurrence of residual stresses 	(Simson et al., 2017)
	Low	Balling	<ul style="list-style-type: none"> Weak flowability of the melt pool resulting in a small contact area to the substrate 	(Li et al., 2012)
		LoF pores	<ul style="list-style-type: none"> Less likelihood of powder ablation and plasma formation resulting in low absorptivity Neighbouring scan tracks are not connected sufficiently 	(Li et al., 2012)
Beam quality, intensity profile, spot size	-	Microstructure	<ul style="list-style-type: none"> Affects the spatial distribution of energy delivered and the cooling rate 	(McLouth et al., 2018)
Scanning speed	High	Balling	<ul style="list-style-type: none"> Higher scan speeds cause more shear stress in the liquid phase resulting in higher surface tension inside the melt pool 	(Gu et al., 2013)
		Thermal-induced cracks	<ul style="list-style-type: none"> Extremely high cooling rates caused by very high scan speeds 	(Gu et al., 2013)
	Low	Porosity	<ul style="list-style-type: none"> Increase of the energy density 	(Aboulkhair et al., 2014)
Scan pattern/strategy	-	Delamination, Microstructure, Thermal induced cracks	<ul style="list-style-type: none"> Influences the heat transfer with the environment in the vicinity of the melt pool and also energy absorption due to modified surface morphology from previous scans 	(Parry et al., 2016)
Scan spacing	Overlapping distance	Microstructure, Thermal induced cracks, Porosity	<ul style="list-style-type: none"> Optimum overlaps ensure the material is sufficiently dense, achieves full strength and also affects energy absorption. 	(Aboulkhair et al., 2014)
Powder particle shape	-	Porosity	<ul style="list-style-type: none"> These impact light absorption and the heat transfer between the particles Flowability of the powder during the recoat affecting packing density and uniformity 	(Brika et al., 2020)

At present, the industrial standard for non-destructive examination of the build quality regarding the defect mechanisms listed in Table 8 is carried out via off-line quality control methods such as X-ray tomography (Maskery et al., 2016), ultrasonic inspection (Rieder et al., 2016), etc. The major disadvantage of off-line methods is that it does not allow taking corrective actions on the occurrence of the defect, resulting in wastage of the material and valuable manpower and machine time. Though LPBF techniques have made some progress concerning building parts out of different materials, production speed, machine construction, etc., the technology still lacks repeatability. Hence, there is a need for robust and cost-effective *in-situ* quality monitoring

systems, but their development is in the early stages. Understanding the defect mechanism formation is crucial for such development, followed by strategies to suppress these defect formations. The defect mechanisms can be understood with the help of suitable sensing (Everton et al., 2016) and signal processing techniques (Pandiyani et al., 2020). With mechanisms happening in the order of microseconds, sensors should have good sensitivity along with high spatial and temporal resolution. Sensors such as pyrometer (Artzt et al., 2020), infrared imaging (Grasso et al., 2018), cameras (Scime et al., 2020), optoacoustic (Gutknecht et al., 2021), acoustics (Shevchik et al., 2018), etc., have been reported in the literature for monitoring the melt pool dynamics and the defect mechanisms. One promising approach for automatic detection of defects is using a Machine Learning (ML) algorithm capable enough to recognize patterns from the sensor signature.

Craeghs et al. (2010) demonstrated that based on the response of the photodiode sensor, the laser power can be altered by a feedback control loop in real-time. Craeghs et al. (2012) have also mapped the melt pool and thermal behaviour with a high-speed camera and a photodiode for monitoring the build. Photodiodes and semiconductor (CMOS) cameras have also been used to detect process failures based on the interpretation of the melt pool dynamics (Clijsters et al., 2014). Berumen et al. (2010) showed that coaxially mounted cameras can be used to monitor the shape and size of the melt pool. Solidification mechanisms of the melt pool have been studied by correlating the surface temperature with the pyrometer (Furumoto et al., 2013). Detection of unstable behaviors in the process has been demonstrated by infrared imaging of the melt pool (Grasso et al., 2018). The plume properties for challenging materials like zinc and its alloys have been imaged using infra-red sensors for in-process sensing (Grasso et al., 2018).

The dimensions of the melt pools in the LPBF process range between 50 to 250 μm and appear for a few microseconds. Monitoring systems based on visual and optical sensors require high spatial and temporal resolution to capture these phenomenon, making them very expensive. Additionally, the cost for processing the data from these sensors are also high as they require heavy computational resource. Alternatively, AE air-borne and structure-borne sensors with the reliable temporal resolution are proposed as an economical solution for monitoring the additive manufacturing process (Shevchik et al., 2019). Pandiyani et al. (2020) have demonstrated that air-borne acoustics captured across four different LPBF regimes exhibited different characteristics in time, frequency and time-frequency domains. Gutknecht et al. (2021) presented that AE has 40 times higher sensitivity than the camera and 15 times more sensitive than the pyrometer in detecting flaws. Furthermore, AE events have been correlated with the location of the micro defects that occur in the LPBF process (Ito et al., 2021). A defect detection system based on a deep belief network (DBN) and microphone data have been successfully developed to classify *balling* and other mechanisms (Ye et al., 2018). Shevchik et al. (2019) developed a spectral convolutional neural network classifier to distinguish the acoustic features for different mechanisms occurring in the LPBF process. Generative models such as Variational Autoencoders (VAEs) and Generative Adversarial Networks (GANs) has been applied on acoustic signatures corresponding to different laser regime in LPBF to distinguish defect-free regimes from anomalies (Pandiyani et al., 2021). A bi-stream

Deep Convolutional Neural Network (DCNN) trained with images acquired during the LPBF layering process was able to identify defective conditions (Caggiano et al., 2019). Unsupervised machine learning algorithms have also been implemented to detect and classify anomalies in the LPBF process (Scime and Beuth, 2018). A few review works have extensively reported the application of ML techniques for monitoring 3D printing. Yu and Jiang (2020) focused their review on 3D bioprinting; Meng et al. (2020) wrote their review from the perspective of the ML algorithms; whereas Goh et al. (2021) concentrated not only on the application but also challenges and potential of ML in AM processes

The *in-situ* monitoring techniques based on ML have been successfully demonstrated for various base materials such as Stainless-steel (Eschner et al., 2018), Bronze (Scime et al., 2020), Inconel (Pandiyan et al., 2021) and Titanium (Kouprianoff et al., 2021). Owing to the significant differences in optical and thermal physical properties of the base powder particles, the experimental parameters listed in Table 8 vary considerably for the occurrence of defect mechanisms among the different materials. It is well-known that the melt pools formed are mainly a function of the powder material and thermodynamic properties. As a result, there would be a change in the distribution of process signatures captured by the sensors, which would make any algorithm developed for *in-situ* monitoring for a particular material non-reusable for another material with confidence. The present work is a feasibility study that focuses on using the idea of Transfer Learning (TL) in Convolutional Neural Networks (CNN). This work aims to demonstrate that the knowledge learned by a CNN from the sensor signatures corresponding to the four mechanisms; *balling*, *LoF pores*, *conduction mode* and *keyhole pores* during the processing of stainless steel can be transferred to bronze. In this work, wavelet transforms are used to extract spectrograms which were subsequently used as input to two architectures, namely VGG-16 and ResNets-18.

The paper is organized into five sections: a brief outline of the LPBF process, the mechanisms in the process and the research gaps in-process monitoring are discussed in Section 0. Section 5.2 gives a brief theoretical basis on the VGG-16, ResNet-18 architecture and Transfer Learning. Section 5.4 presents the experimental conditions and methodology proposed. Section 5.5 discusses the transfer learning results on VGG-16 and ResNet-18. Finally, the main contribution of this paper and future works for further optimization of the proposed methodology is discussed in Section 4.5.

5.2 Theoretical basis

5.2.1 VGG-16 and ResNet-18

VGG-16 is one of the state-of-the-art CNN architectures built for object recognition by Oxford's renowned Visual Geometry Group (VGG) (Simonyan and Zisserman, 2014). The number 16, in this case, indicates the total number of layers involved in building this architecture, as shown schematically in Figure 47. VGG-16 was one of the first architectures to demonstrate the benefit of increasing the depth of neural nets for better

classification accuracy. VGG16 network architecture's uniqueness is that all convolution layers have only a 3X3 filter with a stride one and always use a 2X2 filter of stride 2 for max-pooling layers. Even though it was designed for classifying 1000 categories, it can be used to classify a smaller number of categories (Pandiyan et al., 2019) and sometimes a higher number of categories (Grm et al., 2018). However, due to its numerous fully connected nodes, it is a rather large network, with approximately 138 million parameter weights compared to other networks. The network's size is the main drawback in terms of its deployment (Alippi et al., 2018) as well as the time required for its training (Qassim et al., 2017). To date, it is still considered to be an excellent pretrained vision model for solving image recognition and segmentation problems (Long et al., 2015). However, Canziani et al. (2016) indicated it could be replaced by more recent advanced and lighter networks such as Inception and Residual Networks (ResNets).

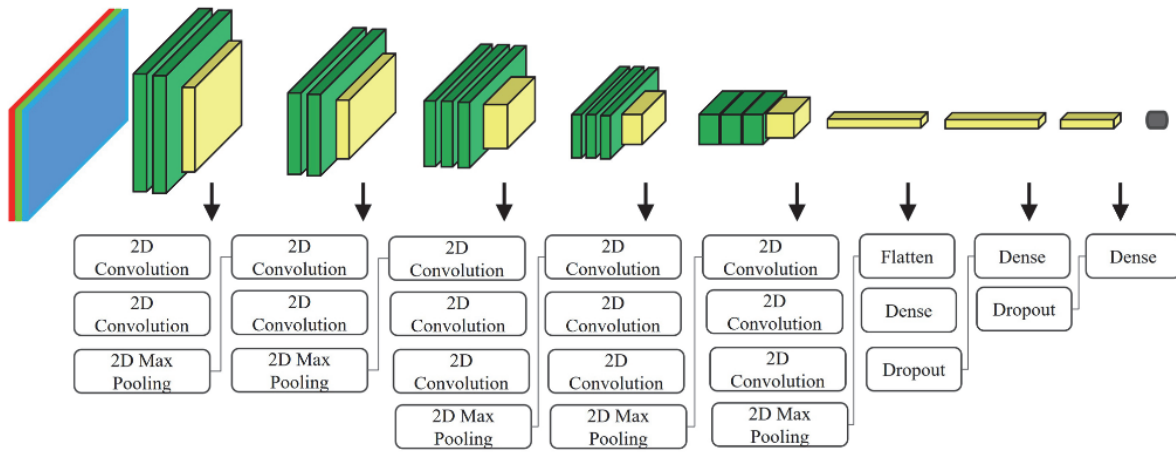


Figure 47. Schematics of the VGG-16 block

The accuracy of any neural network architecture would saturate, or in worst scenarios, would potentially decrease with the increase in the number of layers. The training of very deep networks is complicated due to the vanishing gradient problem. Indeed, the gradients' repeated multiplication during the backpropagation results in making the gradient significantly small, which was presented by Huang et al. (2016). To address this issue, He et al. (2015) developed a newer type of architecture to overcome this vanishing gradient problem, namely ResNets. The ResNets employs a shortcut connection skipping the layers to ease the flow of gradients, and it is schematically represented in Figure 48. The identity skip connection enables the deep networks to go deeper to learn representations with a higher level of abstractions. Canziani et al. (2016) showed that skip connections enable the network to converge faster than plain counterparts such as VGG-16. There are different variants of Resnets; typically, ResNet-18, 34, 50, 101, corresponding to the depth of the layers. Apart from the depth of the layers, the significant difference between these architectures is that, as the layer depth increases beyond 50, the expensive 3X3 convolution is replaced by 1X1 convolutions to reduce computation.

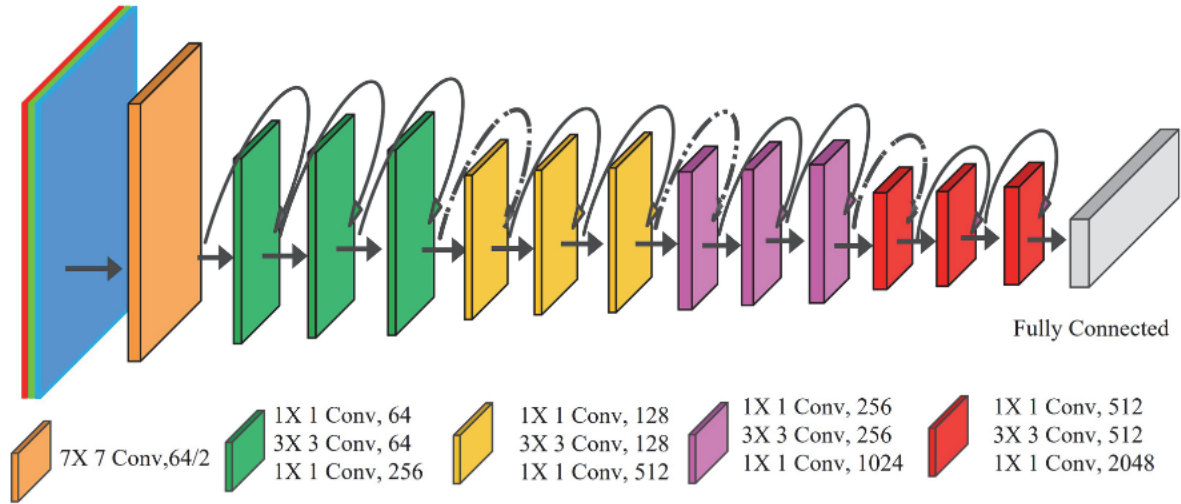


Figure 48. Schematics of the ResNet -18 architecture.

5.3 Transfer Learning

Traditional machine learning algorithms are trained based on a particular feature space to solve specific tasks. With a change in feature distribution or with the introduction of a new task, the algorithm might fail to adapt. In this case, the algorithm has to be re-trained from scratch. Transfer learning is a paradigm where a model already trained on a similar task is re-used with minimum training to accomplish the second task. With neural architectures built with deep layers, the pretrained weights in them can be re-used with minimum training and usage of computing resources. But, it is also to be noted that transfer learning is handy in deep learning if the features learned by the pre-trained model from the first task are general. Figure 49 presents different strategies adapted based on the complexity of the second task. In the case of tasks with higher complexity, the whole network is trained from the saved weights, as shown in Figure 49(a). For a similar task, the few convolution layers or classification layers are trained, as illustrated in Figure 49(b) and(c). The training time is directly proportional to the number of learnable parameters to be updated during training. Apart from image recognition and segmentation applications, the transfer learning paradigm has also been applied to fault diagnosis in locomotive bearings (Yang et al., 2019), to identifying useful life prediction of the tool in manufacturing processes (Sun et al., 2018), which prompted us to exploit this technique towards AM.

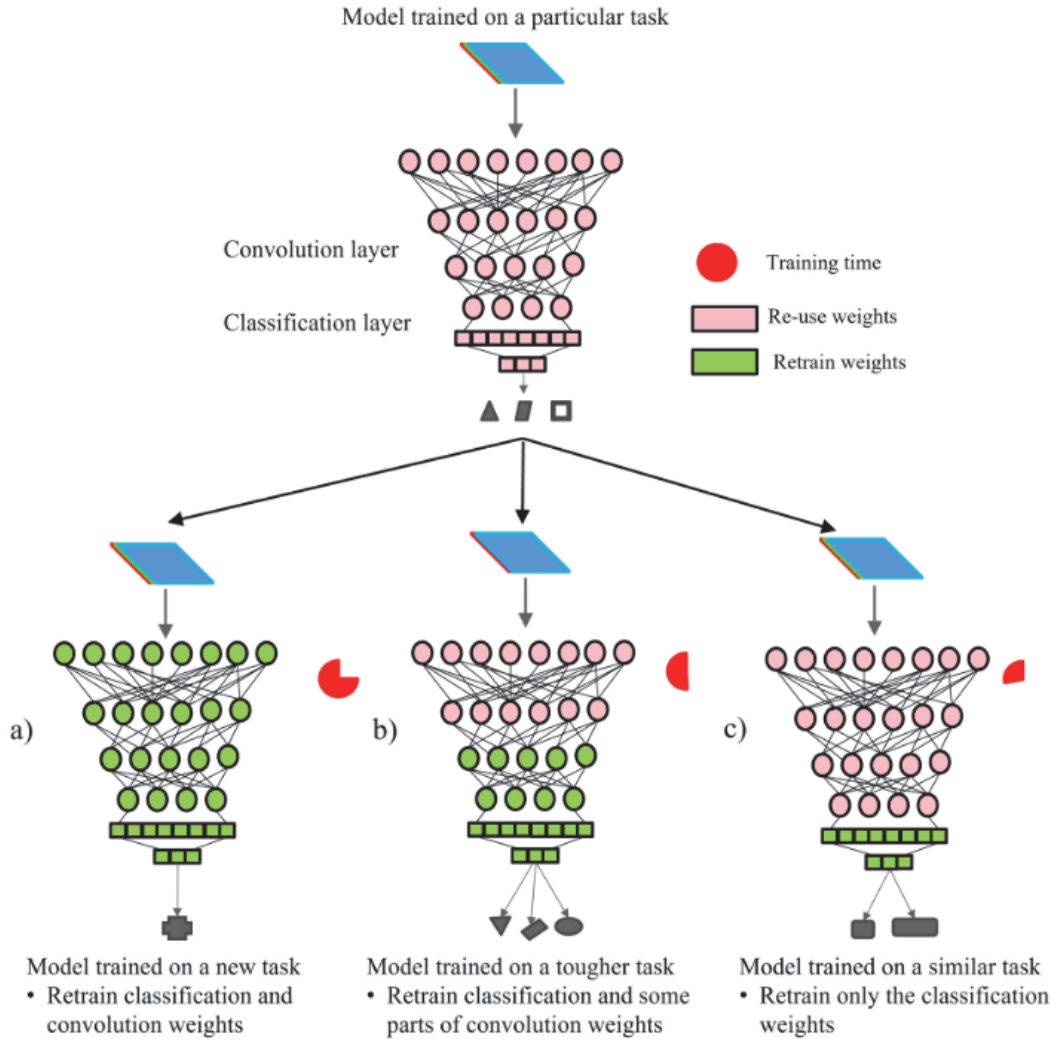


Figure 49. Different strategies in transfer learning based on the problem complexity.

5.4 Experimental setup and methodology

5.4.1 Experimental setup

A series of LPBF line tracks were produced for two different materials using a customized setup shown in Figure 50. In this study, two materials with significant differences in mechanical, optical and thermal properties. The first powder is a 316L stainless steel (MetcoAdd 316L) from Oerlikon Metco, whereas the second material was a bronze (CuSn8) purchased from Heraeus Materials SA (Ghasemi-Tabasi et al., 2020). The chemical composition of the stainless steel and bronze powders are listed in Table 9 and Table 10. The spherical powder particle size distributions and their relative densities are listed in Table 11. The process parameters inducing the four build qualities; *balling*, *LoF pores*, *conduction mode* and *keyhole pores*, are listed in Table 12. From this table, it is seen that two process parameters per condition have been used. The single-line tracks were performed on a defect-free cube built previously having a 40 μm thickness over the build plate using a

Deep Transfer Learning of Additive Manufacturing Mechanisms Across Materials in Metal-Based Laser Powder Bed Fusion Process

reciprocating recoating mechanism, as depicted in Figure 50. The line tracks were of length 13 mm were produced with a parallel uni-directional scan strategy with a spacing of 0.1mm between them. A continuous-wave fiber laser with a $1070 \pm 10\text{nm}$ wavelength with a spot size of $82 \mu\text{m}$ ($1/e^2$) at the focal plane with an $M^2 < 1.1$ was used. The enclosed process chamber prevented the powder bed from being contaminated during the experiments, and nitrogen was used as the inert gas with a flow rate of 1m/s. Additionally it was ensured that the oxygen content inside the chamber was below 200 ppm, which corresponds to 0.01%.

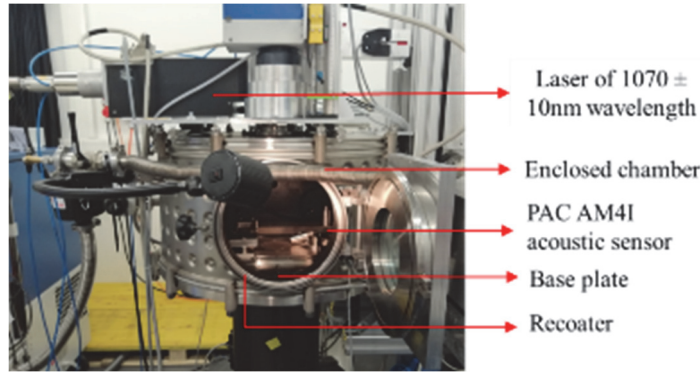


Figure 50. Experimental setup involving LPBF process

Table 9. The alloy composition of austenitic steel 316L powder given in weight percent (nominal)

Fe (Iron)	Ni (Nickel)	Cr	Mo	C (Carbon)	Other
Balance	122	18	2	< 0.03	< 1.00

Table 10. Composition of Bronze CuSn₈ powder given in weight percent (nominal)

Cu	P	S	Fe	Ni	Zn	As	Zr	Sn	Other
Balance	0.06 ± 0.02	≤ 0.05	≤ 0.05	< 0.03	≤ 0.2	≤ 0.05	≤ 0.05	7.80 ± 0.8	< 1.00

Table 11. Powders particles details

	D_{10} (μm)	D_{50} (μm)	D_{90} (μm)	Relative density %
316 L	18.24	30.04	45.65	55.3
Bronze	20.11	31.11	44.25	59.7

Table 12. Scanning parameters for single line tracks experiments.

Mechanism	Stainless steel		Bronze	
	Laser power (W)	Scan speed (mm/s)	Laser power (W)	Scan speed (mm/s)
<i>Balling</i>	25	500	25	300
	90	800	50	300
<i>LoF pores</i>	50	500	100	300
	150	525	150	300
<i>Conduction mode</i>	150	300	170	150
	170	400	250	300
<i>Keyhole pores</i>	200	250	350	300
	450	300	450	300

The four build qualities were simulated on both powders based on the normalized enthalpy calculations as plotted in Figure 51 and Figure 52. The normalized enthalpy over the normalized melt pool depth was calculated (Ghasemi-Tabasi et al., 2020) based on Equations (2) and (3), where ρ is the density $\left(\frac{kg}{m^3}\right)$, α is the absorptivity of the bulk material, P is the laser power (W), C the specific heat $\left(\frac{J}{kg.K}\right)$, ΔT the difference between the melting and initial temperature (K), L_m the latent heat of melting $\left(\frac{kJ}{kg}\right)$, ω the laser spot radius (m), V the laser speed $\left(\frac{m}{s}\right)$, D the thermal diffusivity $\left(\frac{m^2}{s}\right)$, and d the melt pool depth (m).

$$\bar{d} = \frac{\Delta H}{\Delta h} = \frac{\alpha P}{\rho(C \Delta T L_m) \sqrt{\pi \omega^3 V D}} \quad (2)$$

$$\bar{d} = \frac{d}{\omega} \quad (3)$$

The work's primary focus was to evaluate whether the proposed transfer learning strategy can be applied for a larger process space and independent of the process parameters across the materials. As confirmed from Figure 51 and Figure 52 we can see that two sets of parameters were chosen across mechanisms with different normalized enthalpies covering a larger process space. Again comparing between Figure 51 and Figure 52, the enthalpies of the mechanisms across stainless steel and bronze are different, confirming that if transfer learning works, it might be independent of the process parameters across materials. Also, to make the classification and transfer learning task a bit trickier, the dataset was prepared by including data corresponding to *balling* and *LoF pores* for the two alloys. Laser energy density is considered a critical factor affecting the properties of as-built parts (Gu et al., 2013). Out of the four build qualities studied in this work, three of them, namely *balling*, *LoF pores* and *keyhole*, are unfavourable. The occurrence of *balling* and *LoF pores* is the result of a deficit in laser power. On the other hand, porosity caused by keyholes is due to excessive laser power absorbed. However, due to the two materials' optical reflectivity, the energy required for the same mechanism is higher for bronze than for stainless steel. Lastly, cross-sections perpendicular to the line track is investigated by a light microscope to confirm either the occurrence or absence of defects. Typical optical microscopic images of the different build qualities for stainless steel and bronze are shown in Figure 51 (stainless steel) and Figure 52 (bronze).

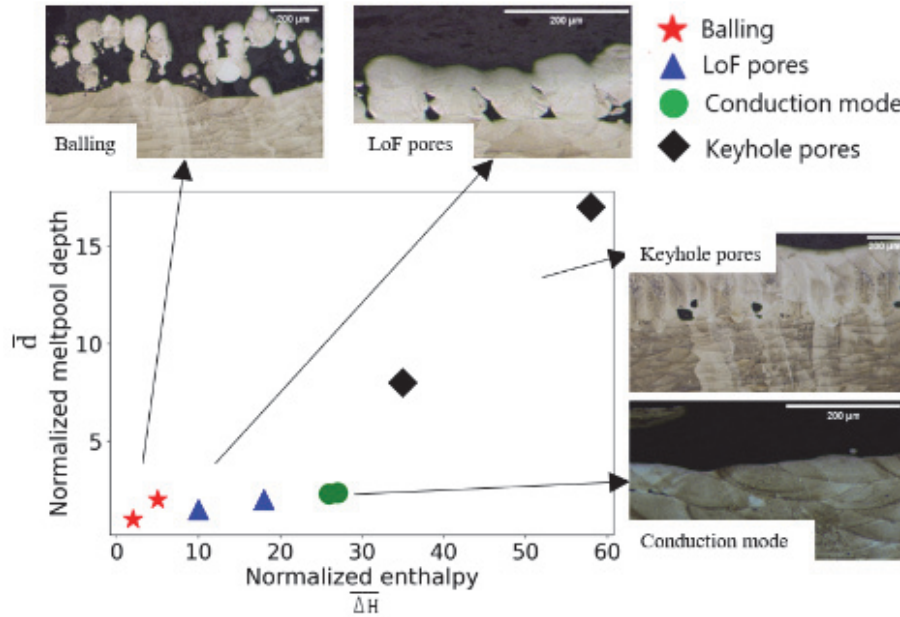


Figure 51. Normalized enthalpy of the printed stainless steel samples of different build qualities versus the normalized melt pool depth (Pandiyan et al., 2020).

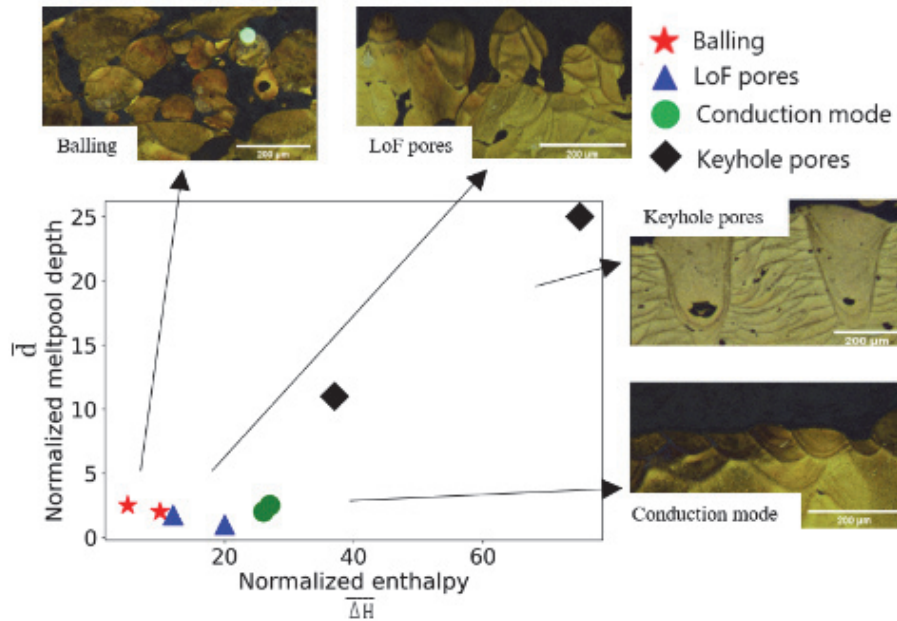


Figure 52. Normalized enthalpy of the printed bronze samples of different build qualities versus the normalized melt pool depth.

5.4.2 In situ sensing setup and data processing

An air-borne acoustic emission (AE) sensor PAC AM4I with a working range of 0 – 100 kHz was used to capture the process signatures emitted during line track trials for both materials. The acoustic sensor is a resonant sensor with peak frequencies around 40 and 80kHz. It is kept in proximity to the build plate at 10 cm, as

shown in Figure 50. The sensor location was fixed for all experiments to ensure repeatability and consistency. The AE signals were captured at a rate of 1 MHz, satisfying the Nyquist Shannon theorem using an Advantech Data Acquisition (DAQ) card. The acquisition of the DAQ card was triggered once the laser hits the powder based on thresholding. The data captured are locally stored for further processing. In this work, 200 line tracks were performed for each material, and the four build qualities resulted in 1600 lines.

The acquired AE signals were sequentially processed, as illustrated in Figure 53, to obtain spectrograms which were subsequently used as input to the VGG and ResNet architectures. For each set of process parameters, the signals were split into window sizes of 2500 μ s. Based on the operating range of the acoustic PAC AM4I sensor, frequencies higher than 100 kHz was removed using a low pass Butterworth filter. Next, the filtered signal was convoluted with a scaled and translated version of the wavelet to compute the Continuous Wavelet Transform (CWT) coefficients. After an exhaustive search, the Morlet was used as the mother wavelet with a scaling value of 500. The application of Morlet wavelet for feature extraction and analysis has been well established for fault diagnosis in ball bearings (Kankar et al., 2011) and gear-box (Lin and Qu, 2000). The coefficients computed after the transform are converted into a 2D spectrogram of size 512 X 512 pixels. The maximum and minimum limits were computed from the CWT coefficients of all build quality to scale all the spectrogram images. For each material and build quality, 2000 spectrogram images were produced per mechanism. This database is balanced in order to avoid biasing during the CNN training.

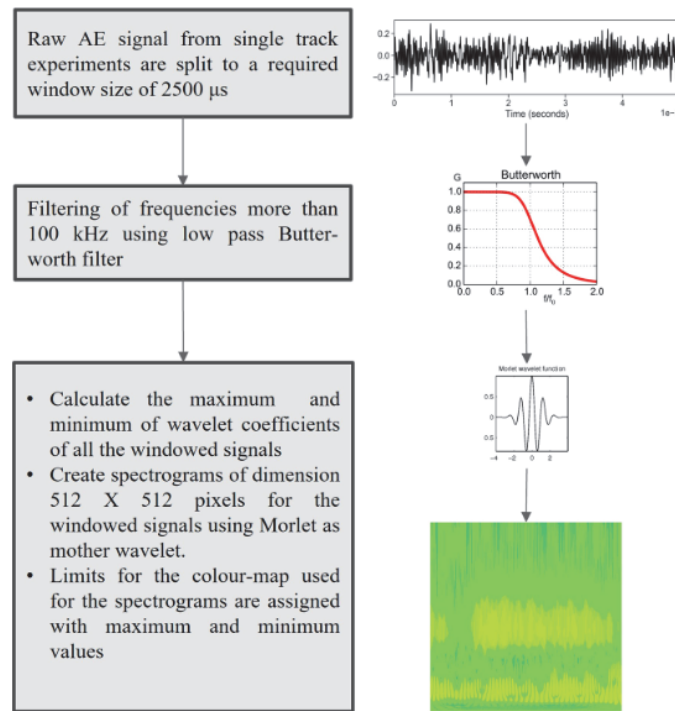


Figure 53. Workflow to build the spectrogram dataset from line track experiments.

5.4.3 Methodology

The proposed methodology for transferring knowledge acquired about different build qualities by a convolutional network from one material to another material is depicted in Figure 54. First, the network is supervisedly trained with labelled spectrogram images from stainless steel for each build condition. It is important to note that the network weights are initially randomized during training. The performance of the network is assessed by comparing the prediction of the network and the corresponding ground truth. Once a reliable accuracy is achieved, indicated by the training accuracy and loss curves reaching a plateau, the training is stopped. Second, the pre-trained model is used as the base model to train the build quality found in another material, in this case, bronze. However, during the training with the second material, the network is not trained from the beginning. Actually, only a part of the network weights is re-trained, as shown in Figure 54. A part of the knowledge learned by the network from the first material (stainless steel) is preserved, and the new knowledge of the second material (bronze) is augmented. Once a reasonable accuracy is achieved on the second material, the training is stopped. This work trains deep networks such as VGG -16 and ResNet -18 on spectrogram images corresponding to four different build qualities. The trained VGG-16 and ResNet-18 architecture weights are frozen until the last layer, thereby restoring the learned knowledge. Only the last layer weights are allowed to be updated during training with spectrogram images corresponding to bronze. The transfer learning was performed in two modes. In the first mode, the freezed network was trained on the bronze spectrogram dataset with a size similar to the stainless steel training dataset. In the second mode, the bronze dataset was reduced to half (50%) the size of the stainless steel dataset during re-training of the freezed network.

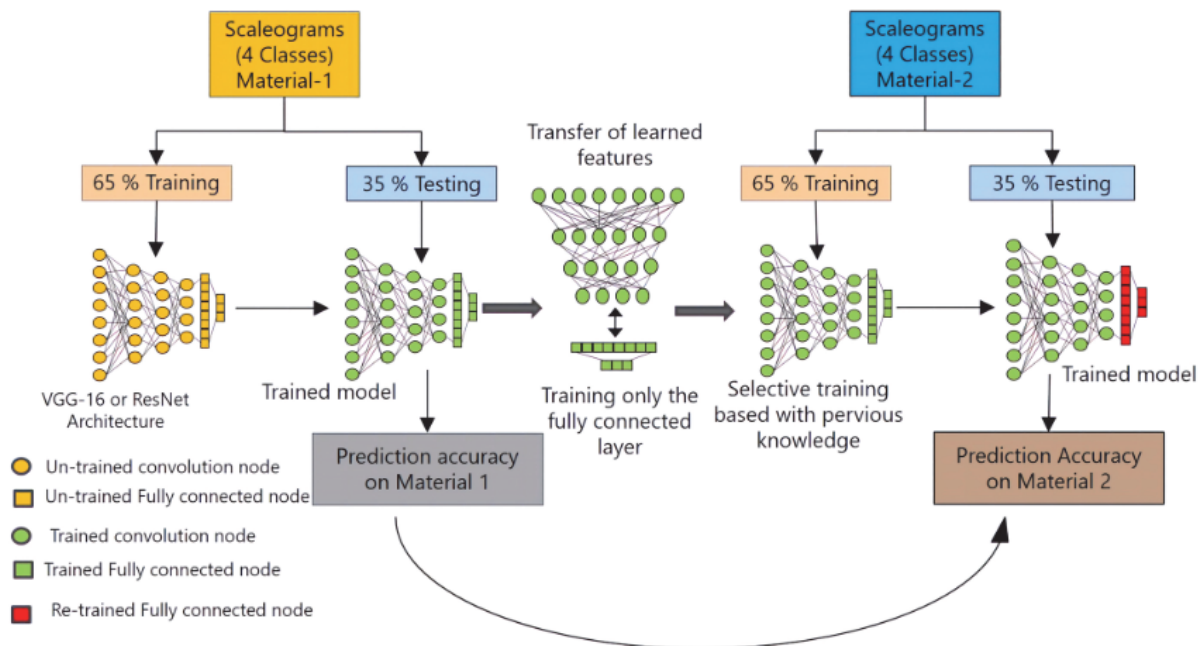


Figure 54. Workflow of the proposed methodology.

5.5 Transfer learning using VGG-16 and ResNet-18 architecture

The spectrogram images created, as discussed in section 5.4.2, with a resolution of 512 X 512 pixels, is given as input to two types of CNN architectures, namely VGG-16 and ResNet-18. From a dataset of 8000 spectrogram images for each material, 5200 images were stochastical selected for the training and the remaining 2800 images were used for testing. We ensured that the weightage, i.e. the number of spectrogram images of all four build qualities in the train and test datasets, is balanced during this stochastical selection. The VGG-16 and ResNet-18 CNN architectures are trained with a GeForce RTX 2080 Ti Graphical Processing Unit (GPU). The training process of the two CNN architectures was implemented in Pytorch (Paszke et al., 2019). The training parameters for both VGG-16 and ResNet-18 architectures are listed in Table 13. The 200 epochs for training was chosen over an exhaustive search to have a fair comparison across two different architectures and the respective accuracy of the two models. Furthermore, batch normalization was applied across layers in the respective model to ensure that overfitting does not occur. It was also ensured that the datasets were shuffled across epochs, and a dropout of 0.5 was applied during training. Additionally, we have stabilized the training by reducing the learning rate to half after every 25 epochs.

Deep Transfer Learning of Additive Manufacturing Mechanisms Across Materials in Metal-Based Laser Powder Bed Fusion Process

Table 13. Parameters used in VGG and ResNet Architectures for training.

Training parameters	VGG-16	VGG-16-Transfer learning	ResNet - 18	ResNet - 18 Transfer learning
Type of analysis	Classification	Classification	Classification	Classification
Solver name	'sgdm'	'sgdm'	'sgdm'	'sgdm'
Learn rate	0.001	0.001	0.001	0.001
Rate of change in learning rate	50% every 25 epoch	50% every 25 epoch	50% every 25 epoch	50% every 25 epoch
Momentum	0.9	0.9	0.9	0.9
Total Epochs	200	200	200	200
BatchSize	10	10	40	40
Shuffle	Every-epoch	Every-epoch	Every-epoch	Every-epoch
Batch normalization	True	True	True	True
Training set	65% / 5200 stainless steel spectrograms	Mode 1: 5200 bronze spectrograms Mode 2: 2600 bronze spectrograms	65% / 5200 stainless steel spectrograms	Mode 1: 5200 bronze spectrograms Mode 2: 2600 bronze spectrograms
Testing set	35% / 2800 stainless steel spectrograms	Mode 1: 2800 bronze spectrograms Mode 2: 1400 bronze spectrograms	35% / 2800 stainless steel spectrograms	Mode 1: 2800 bronze spectrograms Mode 2: 1400 bronze spectrograms
Input image size	512 x 512 pixels	512 x 512 pixels	512 x 512 pixels	512 x 512 pixels
Loss function	Cross-entropy	Cross-entropy	Cross-entropy	Cross-entropy
GPU training	GeForce RTX 2080 Ti	GeForce RTX 2080 Ti	GeForce RTX 2080 Ti	GeForce RTX 2080 Ti
Dropout	0.5	0.5	0.5	0.5
Library	Pytorch	Pytorch	Pytorch	Pytorch

5.5.1 Transfer learning using VGG -16 Architecture

The Fully Connected (FC) classification layer of the VGG-16 architecture, which typically classify 1000 classes, is modified based on our objective for classifying four build qualities, i.e. *balling*, *LoF pores*, *conduction mode* and *keyhole pores*. During training with the stainless steel data, the cross-entropy was the loss function on a batch size of 10 for 200 epochs. After every epoch, the model with updated weights is tested against the test dataset consisting of 2800 images. During the entire training process of the VGG-16 network, the ≈ 134 million parameter weights were updated. The learning rate was initialized at 0.001 and halved after every 25 epochs. Figure 55 shows the accuracy and loss curves for the VGG-16 model trained on the spectrogram images. It is seen that the accuracy increases and the loss decrease with every epoch, confirming that the network learns patterns during the training process. The classification accuracy of the trained VGG-16 on the test dataset is shown in the confusion matrix in Table 14. In this table, trained VGG-16 model prediction of built qualities (balling, LoF pores, conduction mode and keyhole pores) (in rows) versus the ground truth (in columns) using the parameters listed in Table 13 after 200 epochs are given. The classification accuracies in the table are defined as the number of true positives divided by the total number of tests for each category. These values are given in the diagonal cells of the table (dark grey cells). The classification errors are computed as the number of the true negatives divided by the total number of the tests for each category. These corresponding values are filled in non-diagonal row cells. After 200 epochs, using the training parameters listed in Table 13, the trained VGG-16 model achieves an accuracy of $\approx 96\%$ for classifying the four build qualities. The model training on the GPU listed in lasted for 18 hours.

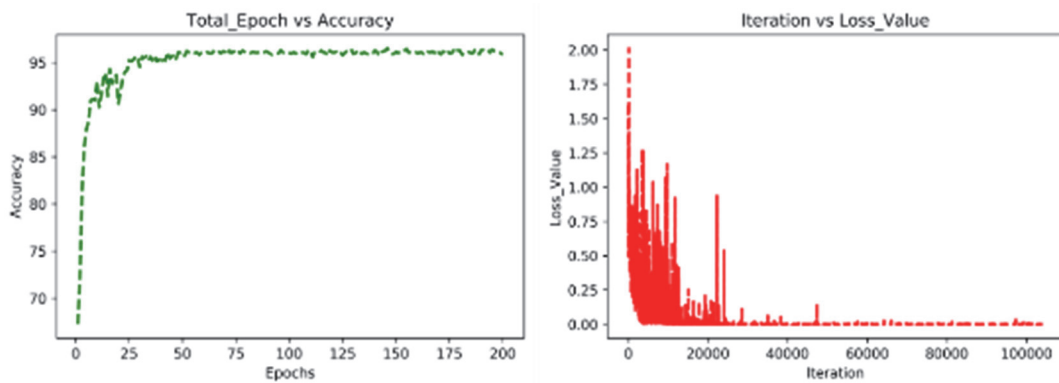


Figure 55. Accuracy and training loss plots during the training of the VGG-16 model on stainless-steel spectrogram dataset.

Table 14. Confusion matrix depicting the accuracy of trained VGG-16 network on stainless-steel mechanisms in the test set.

Classification accuracy [%] \ Ground truth	<i>Balling</i>	<i>LoF pores</i>	<i>Conduction mode</i>	<i>Keyhole pores</i>
<i>Balling</i>	97.75	0	1.75	0.5
<i>LoF pores</i>	3.0	95	1.50	0.50
<i>Conduction mode</i>	0.75	0.25	96.75	2.25
<i>Keyhole pores</i>	0.75	0.25	4.25	94.75

For the transfer learning, the weights of the VGG-16 model trained on classifying the stainless steel build qualities are frozen except the FC layer, as shown in

Figure 56. The weights in the FC layer get updated during the transfer learning of the pre-trained VGG-16 network with the bronze spectrogram dataset. During the transfer learning of the pre-trained VGG-16 network with the bronze dataset, about ≈ 119 million weight parameters get updated, whereas ≈ 15 million weight parameters from the convolutions layers have learned the patterns are frozen. The transfer learning was executed in two modes. First, training the freezed network with the bronze spectrogram dataset with a size similar to the stainless steel training dataset (8000 images). Second, by reducing the bronze dataset to half (4000 images).

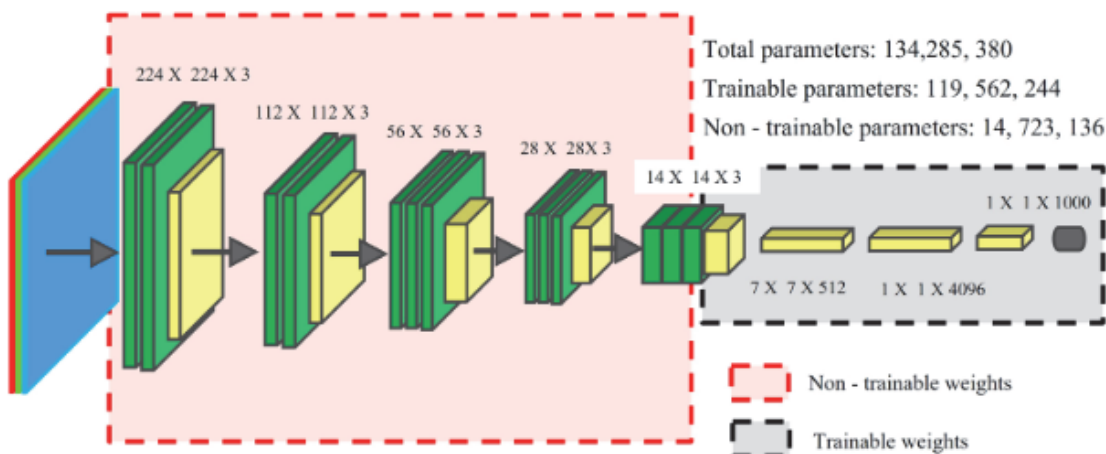


Figure 56. Freezing weights of the pretrained VGG-16 for transfer learning.

The training parameters used during the transfer learning of the pre-trained VGG-16 are listed in Table 13. Figure 57 shows the accuracy and loss curves during transfer learning on the full bronze dataset. Comparing

loss curves between Figure 55 and Figure 57, it is evident that the loss values are more stable during the base VGG-16 network training process than during the transfer learning.

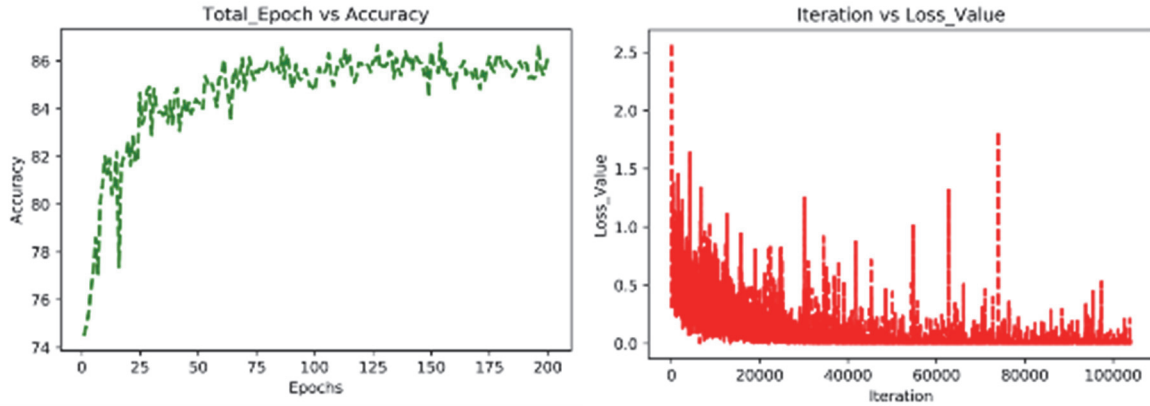


Figure 57. Accuracy and training loss plots during transfer learning of pretrained VGG-16 model on bronze spectrogram dataset.

The classification accuracy of the VGG-16 model from the transfer learning on the full bronze test dataset is given in the confusion matrix in Table 15 (a). After 200 epochs computed in 9 hours, the VGG-16 model from the transfer learning reached an average accuracy of $\approx 85\%$. Missclassification was found between two mechanisms, such as *LoF pores* and *conduction mode*. For transfer learning in the second mode, where the frozen VGG-16 network is trained with the bronze dataset, which is 50% in size of the stainless steel dataset, an accuracy of $\approx 82\%$ was achieved, and evidence of this is in Table 15 (b). The transfer learning in the second mode lasted for 6 hours for 200 epochs. The training times were considerably reduced two-fold during the transfer learning of the VGG-16 model in the first mode and threefold in the second mode.

Table 15. Classification accuracy of the VGG-16 model via transfer leaning for mechanisms occurring during the LPBF process of bronze a) Full dataset b) 50% of the dataset.

a) Full dataset (Mode I)

Ground truth \ Classification accuracy [%]	<i>Balling</i>	<i>LoF pores</i>	<i>Conduction mode</i>	<i>Keyhole pores</i>
<i>Balling</i>	94.0	3.50	2.50	0
<i>LoF pores</i>	2.0	76.5	21.0	0.50
<i>Conduction mode</i>	3.0	17.75	75.75	4.0
<i>Keyhole pores</i>	0	1.5	5.0	93.5

b) 50% of the dataset (Mode II)

	<i>Balling</i>	<i>LoF pores</i>	<i>Conduction mode</i>	<i>Keyhole pores</i>
<i>Balling</i>	89	5.5	5.25	0.25
<i>LoF pores</i>	3.0	74.5	20.75	1.75
<i>Conduction mode</i>	2.5	21.25	72.0	4.25
<i>Keyhole pores</i>	0	1.75	7.25	91.0

5.5.2 Transfer learning using ResNet - 18 Architecture

Similar to the training of the VGG-16 network, the ResNet-18 architecture was also trained using the parameters listed in Table 13 on the spectrogram dataset from stainless-steel line track experiments. Figure 58 shows the accuracy and loss curves increasing and decreasing with every epoch, confirming that network weights adapt to classify the build quality. During the entire training process with a batch size of 40, about ≈ 11 million parameter weights of ResNet-18 architecture were updated using backpropagation. As indicated in the confusion matrix in

Table 16, the trained ResNet-18 model was able to classify with an overall accuracy of $\approx 94\%$ after 12 hours of training.

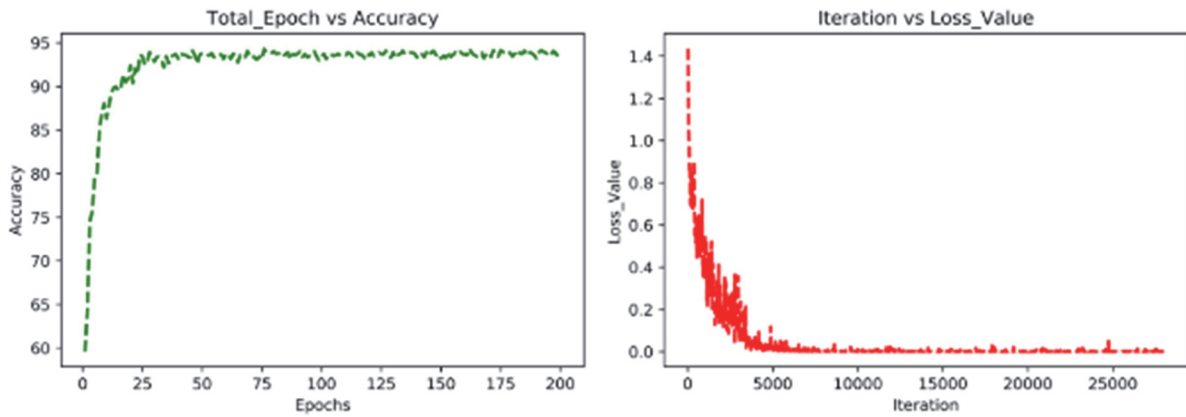


Figure 58. Accuracy and training loss plots during the training of ResNet-18 model on stainless-steel spectrogram dataset.

Table 16. Confusion matrix depicting the accuracy of trained ResNet-18 network on stainless-steel mechanisms.

Ground truth \ Classification accuracy [%]	<i>Balling</i>	<i>LoF pores</i>	<i>Conduction mode</i>	<i>Keyhole pores</i>
<i>Balling</i>	93.8	4.3	1.7	0.2
<i>LoF pores</i>	3.5	93.3	2.2	1.0
<i>Conduction mode</i>	0.7	0.3	93.3	5.7
<i>Keyhole pores</i>	0.4	0.8	5.4	93.4

For the transfer learning of the pre-trained ResNet-18 model, only the fifth bottleneck block layer and FC layer's weight is trainable, as shown in

Figure 59. The knowledge and patterns learned by the ResNet-18 network during the previous training on the stainless steel dataset are preserved as those weights are frozen. Out of ≈ 11 million parameter weights, only ≈ 8 million parameter weights are updated via backpropagation during transfer learning. The training parameters listed in Table 13 are used for transfer learning. Similar to VGG-16, the transfer learning on the Resnet - 18 architecture was also performed in two modes. Figure 60 shows the accuracy and loss curves during the transfer learning using the ResNet architecture on the full bronze dataset. Unlike VGG-16, the loss curves for the ResNet-18 during transfer learning and regular learning are stable. The transfer learned ResNet-18 model achieves an overall accuracy of $\approx 87\%$ in the first mode as shown in the confusion matrix in Table 17 (a). When training the network with the bronze dataset, which is 50% in size of the stainless steel data set, the frozen ResNet-18 model from the transfer learning still reaches an overall accuracy of $\approx 84\%$, and evidence of this is in Table 17 (b). The training times were considerably reduced by 6 hours in the first mode and 4 hours in the second mode during transfer learning of the ResNet-18 model.

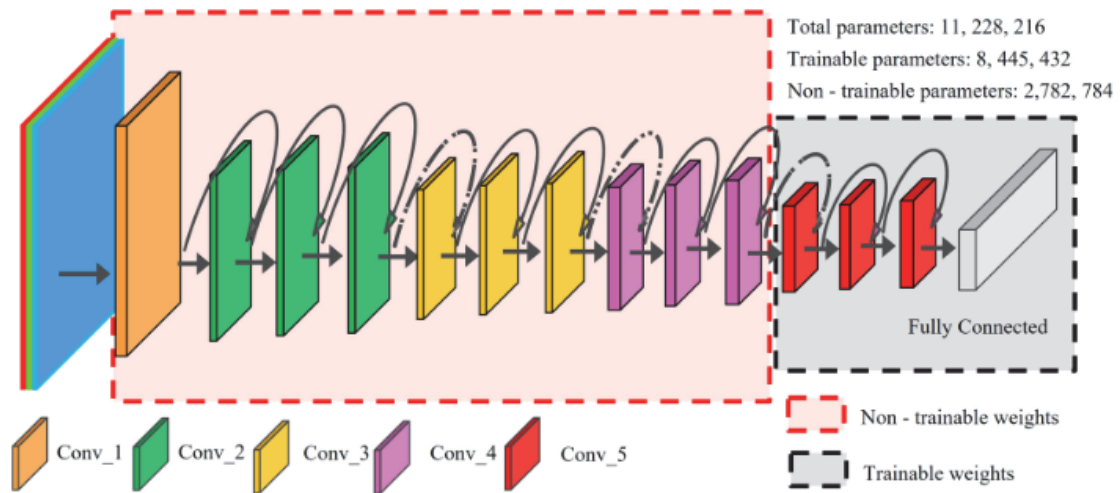


Figure 59. Freezing weights of pretrained ResNet-18 for transfer learning

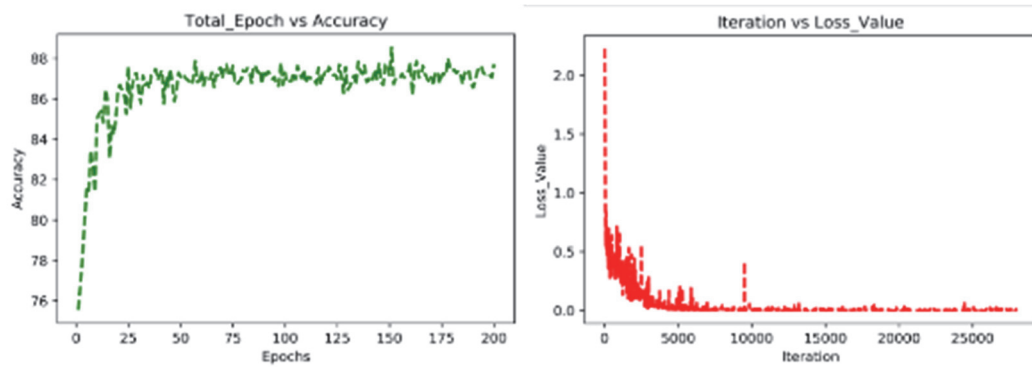


Figure 60. Accuracy and training loss plots during transfer learning of pretrained ResNet-18 model on bronze spectrogram dataset.

Table 17. Classification accuracy of the ResNet-18 model via transfer learning for mechanisms occurring during the LPBF process of bronze. a) Full dataset b) 50% of the dataset.

a) Full dataset (Mode I)

b) 50% of the dataset (Mode II)

Ground truth \ Classification accuracy [%]	<i>Balling</i>	<i>LoF pores</i>	<i>Conduction mode</i>	<i>Keyhole pores</i>
<i>Balling</i>	92	4.50	3.50	0
<i>LoF pores</i>	1.25	81.25	17	0.50
<i>Conduction mode</i>	0	16.50	80.25	3.25
<i>Keyhole pores</i>	0	1.25	4.50	94.25

<i>Balling</i>	<i>LoF pores</i>	<i>Conduction mode</i>	<i>Keyhole pores</i>
89	6.25	4.50	0.25
2.5	78.25	18.25	1.0
1.25	20.	76.25	2.50
0	1.5	5.0	93.5

Based on both CNN architectures' prediction results, we demonstrated that with spectrograms images as input, the material build qualities commonly occurring in additive manufacturing such as *balling*, *LoF pores*, *conduction mode* and *keyhole pores* could be classified on original materials. Secondly, with transfer learning, the qualities in another material could be predicted with the patterns and knowledge trained with build qualities in a first material. Comparing two CNN architectures used in this study, the ResNet-18 performs better in transfer learning with only ≈ 11 million parameter weights as compared to VGG-16 (≈ 134 million parameter weights) for the two transfer learning modes. Finally, we demonstrated that the transfer learning technique is very advantageous from an industrial perspective in terms of minimum training time and dataset collection when transferring the knowledge from one material to another in processing Functionally Graded Materials (FGM) or multi-materials. In this study, the training times were also considerably reduced by three-fold and two-fold in the two modes during transfer learning for Resnet-18 and VGG-16 models, respectively.

5.5.3 Comparison of VGG-16 and ResNet - 18 without transfer learning.

A comparative study was also performed to understand the performance of the models trained from scratch and using transfer learning on the bronze dataset. For training of the two models, namely VGG-16 and ResNet - 18, from scratch, the training parameters listed in Table 13 were used. As indicated in the confusion matrix in Table 18(a), the trained VGG-16 was able to classify with an overall accuracy of $\approx 91\%$ after 18 hours of training. For the case of the trained ResNet – 18, the classification accuracy was $\approx 89\%$ after 12 hours, and evidence of this is in the confusion matrix in Table 18(b). In terms of classification accuracy, the two models trained from scratch were higher on the full bronze dataset as compared to the one using transfer learning. However, in the case of training time, as previously known, models trained using transfer learning took only half of the time required to train the model from scratch.

Table 18. Classification accuracy of the VGG-16 and ResNet-18 model via normal learning for mechanisms occurring during the LPBF process of bronze.

a) VGG-16

Ground truth \ Classification accuracy [%]	<i>Balling</i>	<i>LoF pores</i>	<i>Conduction mode</i>	<i>Keyhole pores</i>
<i>Balling</i>	98.1	0.7	1.1	0
<i>LoF pores</i>	3.1	85.3	10.7	0.9
<i>Conduction mode</i>	1.7	14	82.3	2
<i>Keyhole pores</i>	0	0.4	0.4	99.1

b) ResNet - 18

	<i>Balling</i>	<i>LoF pores</i>	<i>Conduction mode</i>	<i>Keyhole pores</i>
<i>Balling</i>	98.2	0.9	0.9	0
<i>LoF pores</i>	3.1	80.6	15.6	0.7
<i>Conduction mode</i>	2.7	14.8	78.9	3.6
<i>Keyhole pores</i>	0	0.4	1.2	98.4

5.6 Conclusion

In this contribution, we have investigated a novel method for classifying four build qualities such as *balling*, *LoF pores*, *conduction mode* and *keyhole pores* occurring during the LPBF process across two materials. When processing line track experiments, the AE signals were recorded using a microphone that had an operating range of 0-100kHz. From the AE signals, spectrograms images were computed using wavelet transforms with Morlet as the mother wavelet for a window size of 2500 μ s. The spectrogram-based classification was performed in two different materials: stainless steel (316L) and bronze (CuSn8). Instead of training the network from scratch to classify the four qualities occurring in bronze, we have proposed a transfer learning technique using pretrained models from the stainless steel data as an alternate methodology. The methodology has been applied to state-of-the-art CNN architectures, namely VGG-16 and ResNet-18, to explore the interest of transfer learning on additive manufacturing. Moreover, transfer learning was applied to these two architectures in two modes: The bronze training dataset size was similar to the stainless steel original dataset in the first mode. The bronze training dataset size was 50% of the stainless steel original dataset size in the second mode. The following generalized conclusions can be drawn based on the experimental results:

- The VGG-16 network outperforms the ResNet-18 network slightly in terms of accuracy in classifying the build quality from line track stainless steel experiments. However, taking the size of the network into account, the improved performance of the ResNet-18 network with ≈ 11 million trainable parameters versus VGG-16 with ≈ 134 million trainable parameters is commendable.
- The ResNet-18 outperforms VGG-16 during the classifications of the build quality in the bronze during the transfer learning in both modes. For the two modes, the transfer learning of VGG-16 had an overall classification accuracy of 85% and 82%, respectively. In contrast, the Resnet-18 model had overall classification accuracy of 87% and 84%. Despite the ResNet-18 network's small size compared to VGG-16, it outperformed with a better classification accuracy, especially in the second mode of transfer learning.
- Apart from accuracy, the computational times were reduced twofold in the first mode and threefold in the second mode during transfer learning of Resnet-18 and VGG-16 models.

The proposed approach asserts that the knowledge of LPBF processes acquired from one material can be used and further augmented to assess other materials with minimum effort. This work proposes to work on 2D spectrogram image input on two native architectures; however, transfer learning can also be performed on simpler architectures with 1D convolutions. Only four build qualities resulting from LPBF processing are studied in this research work, using transfer learning. Transfer learning of mechanisms such as delamination, crack propagation, microstructure formation among various material combinations across machines is also under investigation. The direction towards optimizing hyperparameters for these networks will increase accuracy and optimize training, which is a part of future work. It is to be noted that appropriate sensing techniques

capable of capturing these mechanisms are also to be optimized and is a study in progress. Though the proposed strategy is promising for AM process monitoring, there is an inherent disadvantage of such a technique as they unlearn some of the previously gained knowledge acquired on one material when re-trained on another. In other words, these models are specific to the material composition and cannot be generalized. Also, the complexity of the CNN model required for monitoring may not be homogeneous when processing all the materials, therefore in some cases complex model may be applied on trivial tasks. The data and codes for this work are present in the following repo (<https://c4science.ch/diffusion/11778/>).

Acknowledgement

The author would like to acknowledge the financial support of the project MoCont from the program of the Strategic Focus Area Advanced Manufacturing (SFA-AM), a strategic initiative of the ETH Board. RDD and RL gratefully acknowledge the generous sponsoring of PX Group to their laboratory.

References

- Aboulkhair, N.T., Everitt, N.M., Ashcroft, I., Tuck, C., 2014. Reducing porosity in AlSi10Mg parts processed by selective laser melting. *Additive Manufacturing* 1, 77-86.
- Alippi, C., Disabato, S., Roveri, M., 2018. Moving convolutional neural networks to embedded systems: the alexnet and VGG-16 case, 2018 17th ACM/IEEE International Conference on Information Processing in Sensor Networks (IPSN). IEEE, pp. 212-223.
- Artzt, K., Siggel, M., Kleinert, J., Riccius, J., Requena, G., Haubrich, J., 2020. Pyrometric-Based Melt Pool Monitoring Study of CuCr1Zr Processed Using L-PBF. *Materials* 13, 4626.
- Berumen, S., Bechmann, F., Lindner, S., Kruth, J.-P., Craeghs, T., 2010. Quality control of laser-and powder bed-based Additive Manufacturing (AM) technologies. *Physics procedia* 5, 617-622.
- Brika, S.E., Letenneur, M., Dion, C.A., Brailovski, V., 2020. Influence of particle morphology and size distribution on the powder flowability and laser powder bed fusion manufacturability of Ti-6Al-4V alloy. *Additive Manufacturing* 31, 100929.
- Caggiano, A., Zhang, J., Alfieri, V., Caiazzo, F., Gao, R., Teti, R., 2019. Machine learning-based image processing for on-line defect recognition in additive manufacturing. *CIRP Annals* 68, 451-454.
- Canziani, A., Paszke, A., Culurciello, E., 2016. An analysis of deep neural network models for practical applications. *arXiv preprint arXiv:1605.07678*.
- Ch, S.R., Raja, A., Nadig, P., Jayaganthan, R., Vasa, N., 2019. Influence of working environment and built orientation on the tensile properties of selective laser melted AlSi10Mg alloy. *Materials Science and Engineering: A* 750, 141-151.
- Clijsters, S., Craeghs, T., Buls, S., Kempen, K., Kruth, J.-P., 2014. In situ quality control of the selective laser melting process using a high-speed, real-time melt pool monitoring system. *The International Journal of Advanced Manufacturing Technology* 75, 1089-1101.
- Craeghs, T., Bechmann, F., Berumen, S., Kruth, J.-P., 2010. Feedback control of Layerwise Laser Melting using optical sensors. *Physics Procedia* 5, 505-514.
- Craeghs, T., Clijsters, S., Kruth, J.-P., Bechmann, F., Ebert, M.-C., 2012. Detection of process failures in layerwise laser melting with optical process monitoring. *Physics Procedia* 39, 753-759.

- Eschner, N., Weiser, L., Häfner, B., Lanza, G., 2018. Development of an acoustic process monitoring system for selective laser melting (SLM), Proceedings of the 29th Annual International Solid Freeform Fabrication Symposium, Austin, TX, USA, pp. 13-15.
- Esmailizadeh, R., Keshavarzkermani, A., Ali, U., Mahmoodkhani, Y., Behraves, B., Jahed, H., Bonakdar, A., Toyserkani, E., 2020. Customizing mechanical properties of additively manufactured Hastelloy X parts by adjusting laser scanning speed. *Journal of Alloys and Compounds* 812, 152097.
- Everton, S.K., Hirsch, M., Stravroulakis, P., Leach, R.K., Clare, A.T., 2016. Review of in-situ process monitoring and in-situ metrology for metal additive manufacturing. *Materials & Design* 95, 431-445.
- Furumoto, T., Ueda, T., Alkahari, M.R., Hosokawa, A., 2013. Investigation of laser consolidation process for metal powder by two-color pyrometer and high-speed video camera. *CIRP Annals* 62, 223-226.
- Gerstgrasser, M., Cloots, M., Stirnimann, J., Wegener, K., 2021. Residual stress reduction of LPBF-processed CM247LC samples via multi laser beam strategies. *The International Journal of Advanced Manufacturing Technology*, 1-11.
- Ghasemi-Tabasi, H., Jhabvala, J., Boillat, E., Ivas, T., Drissi-Daoudi, R., Logé, R.E., 2020. An effective rule for translating optimal selective laser melting processing parameters from one material to another. *Additive Manufacturing* 36, 101496.
- Goh, G.D., Sing, S.L., Yeong, W.Y., 2021. A review on machine learning in 3D printing: applications, potential, and challenges. *Artificial Intelligence Review* 54, 63-94.
- Grasso, M., Demir, A., Previtali, B., Colosimo, B., 2018. In situ monitoring of selective laser melting of zinc powder via infrared imaging of the process plume. *Robotics and Computer-Integrated Manufacturing* 49, 229-239.
- Grm, K., Štruc, V., Artiges, A., Caron, M., Ekenel, H.K., 2018. Strengths and weaknesses of deep learning models for face recognition against image degradations. *Iet Biometrics* 7, 81-89.
- Gu, H., Gong, H., Pal, D., Rafi, K., Starr, T., Stucker, B., 2013. Influences of energy density on porosity and microstructure of selective laser melted 17-4PH stainless steel, 2013 Solid Freeform Fabrication Symposium.
- Gutknecht, K., Cloots, M., Sommerhuber, R., Wegener, K., 2021. Mutual comparison of acoustic, pyrometric and thermographic laser powder bed fusion monitoring. *Materials & Design* 210, 110036.
- He, K., Zhang, X., Ren, S., Sun, J., 2015. Deep residual learning for image recognition. *CoRR* abs/1512.03385 (2015).

- Huang, G., Sun, Y., Liu, Z., Sedra, D., Weinberger, K.Q., 2016. Deep networks with stochastic depth, European conference on computer vision. Springer, pp. 646-661.
- Ito, K., Kusano, M., Demura, M., Watanabe, M., 2021. Detection and location of microdefects during selective laser melting by wireless acoustic emission measurement. *Additive Manufacturing* 40, 101915.
- Kankar, P.K., Sharma, S.C., Harsha, S.P., 2011. Fault diagnosis of ball bearings using continuous wavelet transform. *Applied Soft Computing* 11, 2300-2312.
- Knieps, M.S., Reynolds, W.J., Dejaune, J., Clare, A.T., Evirgen, A., 2021. In-situ alloying in powder bed fusion: The role of powder morphology. *Materials Science and Engineering: A* 807, 140849.
- Kouprianoff, D., Yadroitsava, I., Du Plessis, A., Luwes, N., Yadroitsev, I., 2021. Monitoring of laser powder bed fusion by acoustic emission: investigation of single tracks and layers. *Frontiers in Mechanical Engineering* 7, 60.
- Li, R., Liu, J., Shi, Y., Wang, L., Jiang, W., 2012. Balling behavior of stainless steel and nickel powder during selective laser melting process. *The International Journal of Advanced Manufacturing Technology* 59, 1025-1035.
- Lin, J., Qu, L., 2000. Feature extraction based on Morlet wavelet and its application for mechanical fault diagnosis. *Journal of sound and vibration* 234, 135-148.
- Liu, J., Li, G., Sun, Q., Li, H., Sun, J., Wang, X., 2021. Understanding the effect of scanning strategies on the microstructure and crystallographic texture of Ti-6Al-4 V alloy manufactured by laser powder bed fusion. *Journal of Materials Processing Technology*, 117366.
- Long, J., Shelhamer, E., Darrell, T., 2015. Fully convolutional networks for semantic segmentation, *Proceedings of the IEEE conference on computer vision and pattern recognition*, pp. 3431-3440.
- Maskery, I., Aboulkhair, N., Corfield, M., Tuck, C., Clare, A., Leach, R.K., Wildman, R.D., Ashcroft, I., Hague, R.J., 2016. Quantification and characterization of porosity in selectively laser melted Al-Si10-Mg using X-ray computed tomography. *Materials Characterization* 111, 193-204.
- McLouth, T.D., Bean, G.E., Witkin, D.B., Sitzman, S.D., Adams, P.M., Patel, D.N., Park, W., Yang, J.-M., Zaldivar, R.J., 2018. The effect of laser focus shift on microstructural variation of Inconel 718 produced by selective laser melting. *Materials & Design* 149, 205-213.
- Meng, L., McWilliams, B., Jarosinski, W., Park, H.-Y., Jung, Y.-G., Lee, J., Zhang, J., 2020. Machine learning in additive manufacturing: A review. *Jom* 72, 2363-2377.

- Pandiyan, V., Drissi-Daoudi, R., Shevchik, S., Masinelli, G., Le-Quang, T., Logé, R., Wasmer, K., 2021. Semi-supervised Monitoring of Laser powder bed fusion process based on acoustic emissions. *Virtual and Physical Prototyping*, 1-17.
- Pandiyan, V., Drissi-Daoudi, R., Shevchik, S., Masinelli, G., Logé, R., Wasmer, K., 2020. Analysis of time, frequency and time-frequency domain features from acoustic emissions during Laser Powder-Bed fusion process. *Procedia CIRP* 94, 392-397.
- Pandiyan, V., Murugan, P., Tjahjowidodo, T., Caesarendra, W., Manyar, O.M., Then, D.J.H., 2019. In-process virtual verification of weld seam removal in robotic abrasive belt grinding process using deep learning. *Robotics and Computer-integrated Manufacturing* 57, 477-487.
- Parry, L., Ashcroft, I., Wildman, R.D., 2016. Understanding the effect of laser scan strategy on residual stress in selective laser melting through thermo-mechanical simulation. *Additive Manufacturing* 12, 1-15.
- Paszke, A., Gross, S., Massa, F., Lerer, A., Bradbury, J., Chanan, G., Killeen, T., Lin, Z., Gimelshein, N., Antiga, L., 2019. PyTorch: An imperative style, high-performance deep learning library, *Advances in Neural Information Processing Systems*, pp. 8024-8035.
- Qassim, H., Feinzimer, D., Verma, A., 2017. Residual squeeze vgg16. *arXiv preprint arXiv:1705.03004*.
- Rieder, H., Spies, M., Bamberg, J., Henkel, B., 2016. On-and off-line ultrasonic inspection of additively manufactured components, *19th World Conference on Non-Destructive Testing*, pp. 1-8.
- Scime, L., Beuth, J., 2018. Anomaly detection and classification in a laser powder bed additive manufacturing process using a trained computer vision algorithm. *Additive Manufacturing* 19, 114-126.
- Scime, L., Siddel, D., Baird, S., Paquit, V., 2020. Layer-wise anomaly detection and classification for powder bed additive manufacturing processes: A machine-agnostic algorithm for real-time pixel-wise semantic segmentation. *Additive Manufacturing* 36, 101453.
- Shevchik, S.A., Kenel, C., Leinenbach, C., Wasmer, K., 2018. Acoustic emission for in situ quality monitoring in additive manufacturing using spectral convolutional neural networks. *Additive Manufacturing* 21, 598-604.
- Shevchik, S.A., Masinelli, G., Kenel, C., Leinenbach, C., Wasmer, K., 2019. Deep learning for in situ and real-time quality monitoring in additive manufacturing using acoustic emission. *IEEE Transactions on Industrial Informatics* 15, 5194-5203.
- Simonyan, K., Zisserman, A., 2014. Very deep convolutional networks for large-scale image recognition. *arXiv preprint arXiv:1409.1556*.

- Simson, T., Emmel, A., Dwars, A., Böhm, J., 2017. Residual stress measurements on AISI 316L samples manufactured by selective laser melting. *Additive Manufacturing* 17, 183-189.
- Spears, T.G., Gold, S.A., 2016. In-process sensing in selective laser melting (SLM) additive manufacturing. *Integrating Materials and Manufacturing Innovation* 5, 16-40.
- Sun, C., Ma, M., Zhao, Z., Tian, S., Yan, R., Chen, X., 2018. Deep transfer learning based on sparse autoencoder for remaining useful life prediction of tool in manufacturing. *IEEE Transactions on Industrial Informatics* 15, 2416-2425.
- Tapia, G., Elwany, A., 2014. A review on process monitoring and control in metal-based additive manufacturing. *Journal of Manufacturing Science and Engineering* 136.
- Yang, B., Lei, Y., Jia, F., Xing, S., 2019. An intelligent fault diagnosis approach based on transfer learning from laboratory bearings to locomotive bearings. *Mechanical Systems and Signal Processing* 122, 692-706.
- Ye, D., Hong, G.S., Zhang, Y., Zhu, K., Fuh, J.Y.H., 2018. Defect detection in selective laser melting technology by acoustic signals with deep belief networks. *The International Journal of Advanced Manufacturing Technology* 96, 2791-2801.
- Yu, C., Jiang, J., 2020. A perspective on using machine learning in 3D bioprinting. *International Journal of Bioprinting* 6.

Chapter 6

Semi-Supervised Monitoring of Laser Powder Bed Fusion Process Based on Acoustic Emissions.

Vigneashwara Pandiyan ^a, Rita Drissi-Daoudi ^b, Sergey Shevchik ^a, Giulio Masinelli ^a, Tri Le-Quang ^a, Roland Logé ^b, Kilian Wasmer ^{a,*}

^a *Laboratory for Advanced Materials Processing (LAMP), Swiss Federal Laboratories for Materials Science and Technology (Empa)-CH-3602 Thun, Switzerland*

^b *Thermomechanical Metallurgy Laboratory – PX Group Chair, Ecole Polytechnique Fédérale de Lausanne (EPFL), CH-2002 Neuchâtel, Switzerland*

Vigneashwara Pandiyan, Rita Drissi-Daoudi, Sergey Shevchik, Giulio Masinelli, Tri Le-Quang, Roland Logé & Kilian Wasmer (2021), **Semi-supervised Monitoring of Laser powder bed fusion process based on acoustic emissions**, Virtual and Physical Prototyping, 16:4, 481-497, DOI: [10.1080/17452759.2021.1984444](https://doi.org/10.1080/17452759.2021.1984444)

Contribution: Rita Drissi-Daoudi developed the experimental plan and printed the samples. She reviewed the manuscript.

Abstract

Metal-based Laser Powder Bed Fusion (LPBF) suffers from a lack of repeatability and is challenging to model, making their quality monitoring essential and demanding. The reason lies in the high dynamics taking place during the interaction of the laser with metallic powders. To bring this technology to mass production, industries are only interested in the process regime where the built layer's quality meets their standards. All other process regimes leading to poor mechanical properties and/or defect formation such as *balling*, *Lack of Fusion (LoF) pores*, *keyhole pores*, delamination, and crack propagation irrespective of their different regimes are considered anomalies. Today, the common methodology for monitoring uses conventional/supervised Machine Learning (ML) algorithms for the classification task requires collecting a balanced dataset corresponding to each investigated regime from the sensors, which is very expensive and time-consuming. As an alternative, the article proposes a semi-supervised approach where the defect-free regime can be differentiated from the anomalies by familiarising the ML algorithms only with the distribution of acoustic signatures corresponding to the defect-free regime. This work presents two generative Convolutional Neural Network architectures based on Variational Auto-Encoder and General Adversarial Network. As a result, we could classify the anomaly regimes with 96 and 97% accuracy, respectively.

Keywords: Laser powder bed fusion; Monitoring; Laser processing; Convolutional Neural Network; Acoustic Emission.

6.1 Introduction

Laser Powder-Bed Fusion (LPBF) is one of the Additive Manufacturing (AM) techniques allowing the building of 3D complex geometries components from an alloy powder layer by layer (King et al. 2015). The main advantages of this technology are a considerable reduction of geometrical design constraints (Khairallah et al. 2016; Brandt 2016), lead-time optimization due to computer-aided design (CAD) (Guessasma et al. 2015), the possibility to use various powder materials, and last but not least revolutionize the production of spare parts in the supply chain (Khajavi, Partanen, and Holmström 2014). The major drawback of this technology is a deficiency in the process reproducibility and the lack of robust and economical process monitoring which impacts the mechanical properties (e.g., part density and grain structure) and quality (e.g., pore formation and delamination) of the built parts. The build quality is highly dependent on the process parameters such as laser energy density, the scanning speed and strategy, layer thickness, hatching spacing, environment, etc. (Chua, Ahn, and Moon 2017; Spears and Gold 2016; Gu et al. 2006). The parameter window dictates the complex physical phenomena and transients in the laser-material interaction zone and melt pool morphology, such as rapid heating, melting, cooling, evaporation of the materials and also potentially defect formation. For a desirable build quality in the LPBF process, a correct choice of parameter levels is primary (Chua, Ahn, and Moon 2017; Van Elsen 2007; Spears and Gold 2016). However, in practice, even though the process operates in a favourable

parameter window — owing to highly nonlinear dynamic transformations that arise in the laser interaction zone, especially in keyhole regime — the LPBF processes are prone to defects (Everton et al. 2016; Tapia and Elwany 2014).

Implementing sensors around the process zone and the correlation between the data and the process behaviour enable a better process real-time feedback and understanding. Several sensors have been used for defect monitoring in real-time during the LPBF process (Everton et al. 2016; Tapia and Elwany 2014; Grasso et al. 2018; Yan et al. 2018). Predominantly high-speed imaging and thermal-based vision system have been reported in the literature (Mani et al. 2017). Sensing and monitoring the temperature field around the process zone using pyrometers have been investigated for a decade (Pavlov, Doubenskaia, and Smurov 2010; Furumoto et al. 2013; Kruth et al. 2007). The major advantage of pyrometers is that the process zone's temperature can be measured without physical contact and can be converted to a digital signal for further analysis and correlation. However, the downside of the sensors is twofold. First, owing to the melt pools occurring in sizes of 10-250 microns (Cheng et al.; Gong et al. 2014), they often lack spatial resolution, except if these imaging techniques are combined with suitable optics to retrieve the spatial information from the melt pool morphology (Wang et al. 2017; Bayle and Doubenskaia 2008; Zhang et al. 2018; Clijsters et al. 2014). Second, only information about the surface can be detected, and understanding the mechanism beneath is unsolved at present. Though these imaging systems are a viable solution in AM monitoring, it is to be noted that they are not an economical solution in terms of cost, hardware and data management. Air and structure-borne acoustic emission (AE) based monitoring techniques for laser processing pose as an alternative and effective, low-cost solution for two main reasons (Shevchik et al. 2018; Masinelli, Shevchik, et al. 2020; Pandiyan et al. 2020). First, they are able to sense volumetric information of the process, e.g., melt pool fluctuation and keyhole instabilities leading to defect formation (Brandt 2016). Second, they have a high temporal resolution suitable to monitor melt pool events on a time scale between roughly 10 to 100 μ s (Khairallah et al. 2016; Fisher et al. 2018; Zhao et al. 2017). However, due to the 3D nature of acoustic waves, the sensors' installation in terms of location, distance, angle, and filtering must be crucially ensured. The AE sensing element's proximity and positioning are directly proportional to sensitivity and signal strength from the source, which will impact the decision making. The portability of AE sensing across the different configuration of LPBF requires these factors to be considered. From an industrialization and commercialization perspective, installing an AE monitoring system requires minimum alteration to the existing machines available in the market [29], which gives an edge over other sensing techniques.

Real-time monitoring, defect detection, and subsequent counteractive measures have been proven to be efficient for LPBF processes when the sensor data is analysed with Machine Learning (ML) algorithms. ML methods, indeed, are capable of recognizing patterns and correlations hidden in the sensors data. A comprehensive review of supervised, semi-supervised, unsupervised, and reinforcement learning techniques applied in monitoring the AM processes has been reported by Goh *et al.*, Meng *et al.* and Sing *et al.* (Goh, Sing, and

Yeong 2021; Meng et al. 2020; Sing, Kuo, et al. 2021). Gaussian Mixture Models (GMM) have also been proven to identify the build quality using randomized Singular Value Decomposition (SVD) features extracted from a photodiode sensor (Okaroa et al. 2018). Luke Scime and Jack Beuth proposed computer vision algorithms trained on the powder bed images to automatically detect and classify anomalies during the powder spreading process (Scime and Beuth 2018a, 2018b). Different Convolutional Neural Networks (CNN) architectures and ML algorithms have been successfully applied in classifying the quality of the build, melt states and melt-pool morphology using melt-pool imaging (Kwon et al. 2020; Tan et al. 2019; Ye, Fuh, et al. 2018a; Gobert et al. 2018). Deep Learning (DL) algorithms have been able to effectively detect flaws in each layer using digital camera images compared to algorithms such *K*-nearest neighbour (KNN), logistic regression, SVM, decision tree (DT), linear discriminant analysis (LDA), and boosted trees (BT) (Imani et al. 2019). Although, as mentioned, ML methods have implemented into AM processes in many ways in recent years, those methods have just started to be applied to bioprinting. Yu and Jiang (Yu and Jiang 2020) presented the perspective on the use of ML methods to improve 3D bioprinting whereas An *et al.* (An, Chua, and Mironov 2021) articulated the vision of future of 3D bioprinting via two missing links; big data and digital twin.

Several studies exist in a combination of ML algorithms with AE during the processing of metal-based materials with lasers for AM processes such as welding, direct energy deposition etc., to monitor and control the quality of the processes (Masinelli, Le-Quang, et al. 2020; Bastuck et al. 2015; Sumesh et al. 2015; Wasmer et al. 2018). With the feasibility of AE based monitoring proven in laser processing, there is a recent trend in the monitoring of the LPBF processes based on AE by exploiting state of the art ML algorithms. The linear SVM classifier was proven to be effective in classifying different processing regimes using statistical features computed on acoustic signals (Ye, Fuh, et al. 2018b). Shevchik *et al.* (Shevchik et al. 2019; Shevchik et al. 2018) successfully demonstrated that wavelet spectrograms computed on signals from optoacoustic fibre sensors corresponding to three porosity content could be classified with different CNN architectures Spectral CNN, Xception and ResNet. Deep belief networks have also been used to classify raw acoustic signals corresponding to defect patterns such as *balling*, normal and overheating (Ye, Hong, et al. 2018). Long short-term memory networks trained on AE have been able to detect process flaws such as keyhole porosity, lack of fusion, and bead up (Zhang et al.). Reinforcement learning approaches have also been combined with acoustic data for in situ quality monitoring (Wasmer et al. 2019). Structure-borne acoustic sensor data represented in the form of a spectrogram have been combined with neural networks to classify printed specimens' density in the LPBF process (Eschner et al. 2020). Most of the approaches discussed in material processing with lasers were based on a supervised learning paradigm. Semi-supervised CNN architectures for anomaly detection using AE signals in LPBF has been rarely reported in the literature (Goh, Sing, and Yeong 2021; Meng et al. 2020; Sing, Kuo, et al. 2021), which will be bridged in this work.

Conventional supervised ML classification problems involve collecting datasets corresponding to each investigated process regime (e.g., balling, lack of fusion, conduction, keyhole). It is also important to have each

dataset with equal weightage (a balanced database for each class) or otherwise requiring some compensation to be added during training to avoid biasing. Hence, developing and being aware of process maps for each class is a prerequisite before collecting the data. This is very time and material demanding and therefore expensive for industries. Also, supervised classification models would not be able to classify new regimes from the trained ones if they are unfamiliar. It will classify the new regime into the class, which is statistically the closest. This may have dramatic consequences if the new mechanism decreases either the mechanical properties or the lifetime of the parts but is statistically close to the best regime. Under such a situation, the model has to be retrained again with the inclusion of data from the new class, increasing the cost of the process maps. A solution to this problem is using semi-supervised anomaly detection models, which are helpful in two main circumstances. First, when it is difficult, if not possible, to have a balanced dataset between the investigated regimes. This is particularly the case, for example, for machines or parts subjected to tribological failures (Shevchik et al. 2021). Most of the time, the process runs in the "normal" condition until an abrupt failure takes place. Second, when out of all the classes that are to be identified, only one is the most important or of interest. The semi-supervised models are trained only from the data distribution corresponding to the desired class, enabling the model to differentiate the data from which it was not trained. Works on monitoring the LPBF process using AE signatures reported so far have been more focused on discriminative models that are supervisedly trained. The novelty of the present work is on exploiting the generative models such as Variational autoencoder (VAE's) and General adversarial network (GAN's) trained semi-supervisedly to monitor the metal-based AM process. In this work, AE signals were acquired by a low-cost microphone during the process of the LPBF of a nickel-based super-alloy (Inconel 718) powder. The laser processes parameters were selected to produce parts of different qualities; a defect-free regime and three regimes containing defects. The main goals were to train two generative CNN models based on VAE and GAN with AE signals of the defect-free regime to detect anomalies (defects) such as *balling*, *LoF pores*, and *keyhole pores*.

The paper is organized into 4 Sections. Section 6.1 presents a succinct literature review of the LPBF process regimes, sensing techniques, and machine learning algorithms used for real-time process monitoring. Section 5.2 gives a brief overview of autoencoders and GAN. Section 5.3 describes the LPBF experimental setup, processing parameters, and data acquisition setup than presents and discusses the anomaly prediction results using the AE signals emitted during LPBF by the two generative CNN architectures, such as VAE and GANomaly. Finally, Section 6.4 summarizes this investigation's findings and the future works on in situ monitoring for the LPBF process.

6.2 Theoretical basis

6.2.1 Variational Auto Encoder

Autoencoders and their variants find their applications predominant in image denoising (Gondara 2016), dimensionality reduction (Mahmud, Huang, and Fu 2020), feature extraction (Nishizaki 2017), image generation

(Pandiyani et al. 2019; Cai, Gao, and Ji 2019), machine translation (Pagnoni, Liu, and Li 2018), and anomaly detection (Sakurada and Yairi 2014; Hahn and Mechefske 2021; Pandiyani et al. 2021). An autoencoder architecture generally consists of a pair of networks, namely an encoder and a decoder whose purpose is to learn the identity function for the data distribution they had been trained on. The encoder-decoder combination learns the data representation efficiently in a dense manner and reconstructs the original input. The encoder network maps the original data $x \in X$, to z belonging to low dimensional latent space z using a function Φ . Subsequently, the decoder network recreates $x' \in X$ similar to the original data from z by a function Ψ , as depicted in Equations (4) and (5):

$$\Phi: X \rightarrow z, \quad z = f(x, \Phi) \quad (4)$$

$$\Psi: z \rightarrow X, \quad x' = f'(z, \Phi') \quad (5)$$

During training, the model learns to retain the minimal information to encode the original data X so that it can be regenerated as the output on the other side by back-propagating the reconstruction loss as presented in Equation (6), which is the difference between the input and output.

$$\mathcal{L}(x, x') = \|x - x'\|^2 = \|x - f'(f(x, \Phi), \Phi')\|^2 \quad (6)$$

Once the autoencoder has been trained, we both have an encoder and a decoder to reconstruct the input. However, still, there are chances of overfitting as the latent space is not regularised, as illustrated in Figure 61(a). Variational autoencoder (VAE) is one of the types of autoencoders where latent space distribution is regularised during the training. The VAE provides a probabilistic manner for describing an observation in latent space. Thus, instead of building an encoder that outputs a single value to describe each latent state attribute, we will make our encoder define a probability distribution for each latent feature. In other words, the encoder does not directly map to the latent space as depicted in Figure 61(a), instead it generates two quantities, mean (μ) and variance (σ^2) describing the distribution as shown in Figure 61(b).

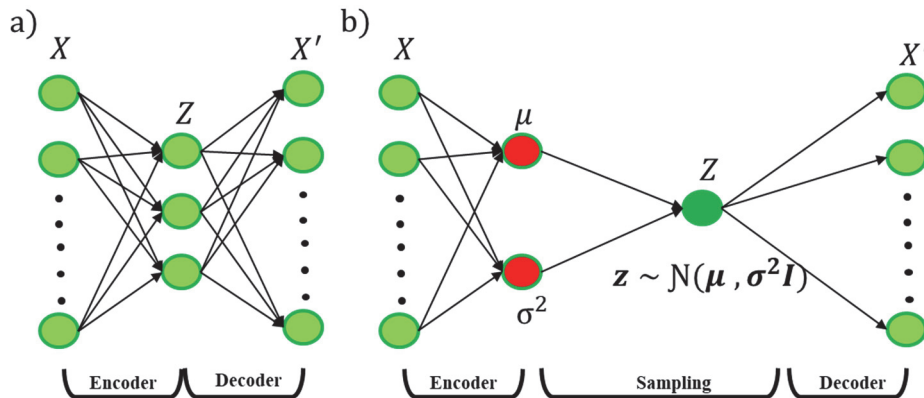


Figure 61. Illustration of (a) an autoencoder and (b) variational autoencoder architecture depicting latent space with and without regularisation.

Unlike vanilla autoencoders (An and Cho 2015), the loss function of the VAE network consists of two terms. The first term maximizes the reconstruction likelihood similar to Equation (6). The second term, also known as the Kullback–Leibler (KL) divergence, encourages the learned distribution $q(z|x)$ to be identical to the true prior distribution $p(z)$, for each dimension j of the latent space as depicted in Equation (7). The KL divergence score ensures that the distribution learned q is similar to the true existing distribution p .

$$\mathcal{L}(x, x') = \|x - x'\|^2 + \sum_j KL(q_j(z|x) \| p(z)) \quad (7)$$

6.2.2 Generative Adversarial Network

A Generative Adversarial Network (GAN) is based on the idea that two adversarial networks, as shown in Figure 62, a generative network G and a discriminative network D that are set against one another during model training. The goal of the generative network's is to create new distribution samples that are different but still reminiscent enough from the training data. The goal of the discriminator network is to differentiate the synthetic distribution created by the generator network from the original training set.

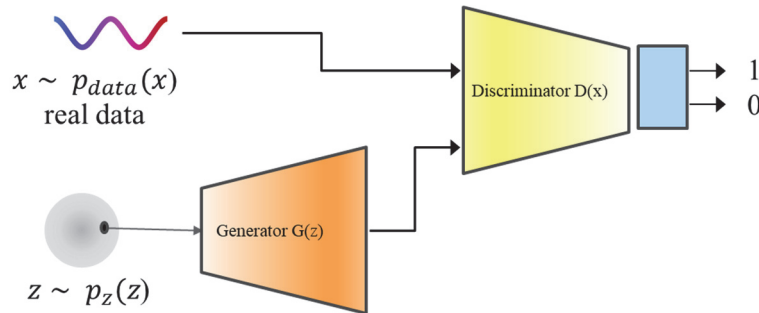


Figure 62. Illustration of a GAN architecture with generator network G and a discriminator network D .

Based on the set objective, the two networks iteratively improve during training such that the generator network is capable of creating synthetic data resembling the actual distribution. An example is presented in Figure 63.

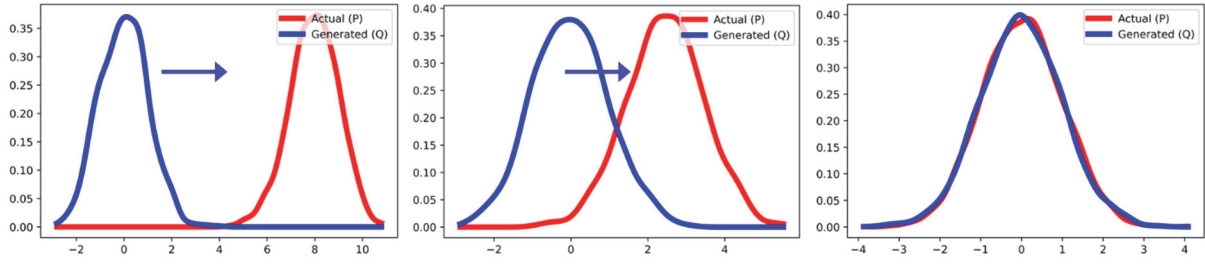


Figure 63. Comparisons of the distribution generated by the generator with training iteration with the actual distribution.

The training of the two networks requires a loss function, which primarily depends on the second network. The update of the weights does not occur simultaneously in the networks. The loss function for the vanilla GANs are of the form shown in Equation (8), where D is the discriminator, G is the generator, $p_z(z)$ is the input noise distribution, $p_{data}(x)$ is the original data distribution, and $p_g(x)$ is the generated distribution. The objective of the architecture is to maximize the discriminator (D) and minimize the generator (G). V is the sum of the Expected log-likelihoods for real and generated data. The loss function aims to move $p_g(x)$ towards $p_{data}(x)$ for an optimal D .

$$\frac{\min_G \max_D}{G} V(D, G) = \mathbb{E}_{x \sim p_{data}(x)} [\log D(x)] + \mathbb{E}_{z \sim p_z(z)} [\log(1 - D(G(z)))] \quad (8)$$

GANomalies are recent variants of the GAN network architectures where — based on known input — the network would generate a manifold representation of the input. However, when unusual input is encoded, its reconstruction can be poor, which can be used for anomaly detection. GANomaly (Akçay, Atapour-Abarghouei, and Breckon 2018), AnoGan (Schlegl et al. 2019), and Efficient-GAN-Anomaly (Zenati et al. 2018) are the adversarial networks based on GAN architecture for identifying anomalies and outliers.

6.3 Experimental setup

6.3.1 Experimental setup and materials

The experimental setup, presented in Figure 64, consists of an enclosed chamber hosting a base plate, a recoater, and a laser. The laser operates in continuous mode at a 1070 ± 10 nm wavelength and has a spot size of $82 \mu\text{m}$ ($1/e^2$) with a beam quality with an $M^2 < 1.1$. The experiments were a series of overlapping lines track to build on a defect-free cube of the same material. The chosen scanning strategy was one-directional parallel lines with a hatch distance of 0.1 mm. The scanning speed and laser power were altered simultaneously to induce the four main process regimes (*balling*, *Lack of Fusion pores (LoF pores)*, *conduction mode*, *keyhole*

pores). The material used for the experiments was a nickel-based super-alloy known as Inconel 718. The powder was acquired from Oerlikon Metco, and its chemical composition is listed in Table 19. The size of the Inconel 718 powder particles used in this study varied between 15 and 45 μm and followed a normal distribution. The combination of laser power and scanning velocity for the investigated process regimes *balling*, *LoF pores*, *conduction mode*, and *keyhole pores* is listed in Table 20. The occurrence of the four process regimes was confirmed by cross-section analysis. The samples were sectioned perpendicular to the scan direction and polished. The melt pool was revealed by etching with Kalling's No.2 Reagent (5 g CuCl, HCl 100 mL, C₂H₆O 100 mL, H₂O 100 mL) for 10 to 20 seconds. The cross-sections were inspected with a Leica DM6000M light optical microscope in bright field mode. The optical pictures acquired for the four regimes are shown in Figure 65. Based on the picture "no pores", the porosity of the built layer on the defect free cube was less than 0.01% in conduction regime.

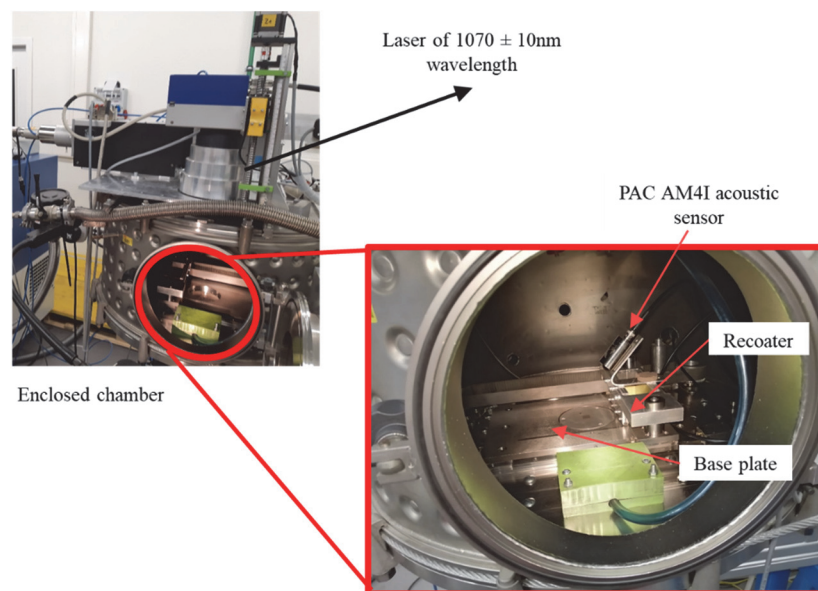


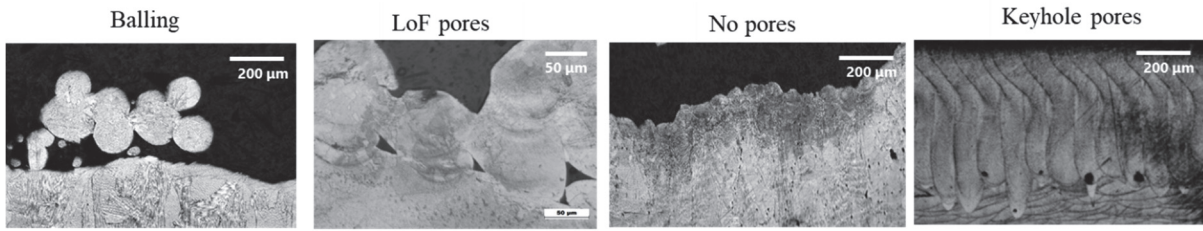
Figure 64. Customized LPBF experimental setup with the embedded acoustic sensor setup for anomaly detection.

Table 19. Chemical composition of the Inconel 718.

Ni	Ti	Cr	Mo	Nb+Ta	Fe	Al	Other
Balance	1	18	3	5	18	0.60	< 0.5

Table 20. Energy densities for line track experimental trials to induce the four regimes.

Categories	Laser power [W]	Scan speed [mm/s]	Normalized enthalpy (Ghasemi-Tabasi et al. 2020)
<i>Balling</i>	30	300	8.9
<i>LoF pores</i>	50	300	14.9
<i>Conduction mode</i>	120	300	35
<i>Keyhole pores</i>	450	200	164



Different mechanisms occurring during processing of Inconel (718) powder in LPBF process.

Figure 65. Optical pictures of different regimes such as *balling*, *LoF pores*, *conduction mode*, and *keyhole pores* occurring during LPBF of Inconel 718.

6.3.2 Data acquisition and dataset preparation

In this work, the airborne AE of the process zone was acquired with a PAC AM4I (Physical Instruments, US) airborne resonant acoustic sensor with an operating range of 0-100 kHz and Advantech Data Acquisition (DAQ) card. The AE sensor was fixed at a distance of more or less 5 cm from the process zone, as shown in Figure 64. The data acquisition rate of 1 MHz was chosen to ensure that the Nyquist Shannon theorem (Jerri 1977) is satisfied. The data acquisition was automatically triggered with a photodiode, and a schematic of the sensor setup is given in Figure 66. Owing to the 0-100 kHz sensor sensitivity range, an offline low-pass Butterworth filter with a cut-off frequency of 100 kHz is applied on the raw signal to omit noises. The raw signal corresponding to the four different process regimes is chopped into windows of 5ms (Pandiyani et al. 2020). Figure 67 presents the moving average plot of the normalized raw signals corresponding to all four process regimes. In building up an ML pipeline, emphasis should be made on the pre-processing of the signal based on the nature of the sensor used and the process environment. The data and codes for this work are present in the following repo (<https://c4science.ch/diffusion/11519/>).

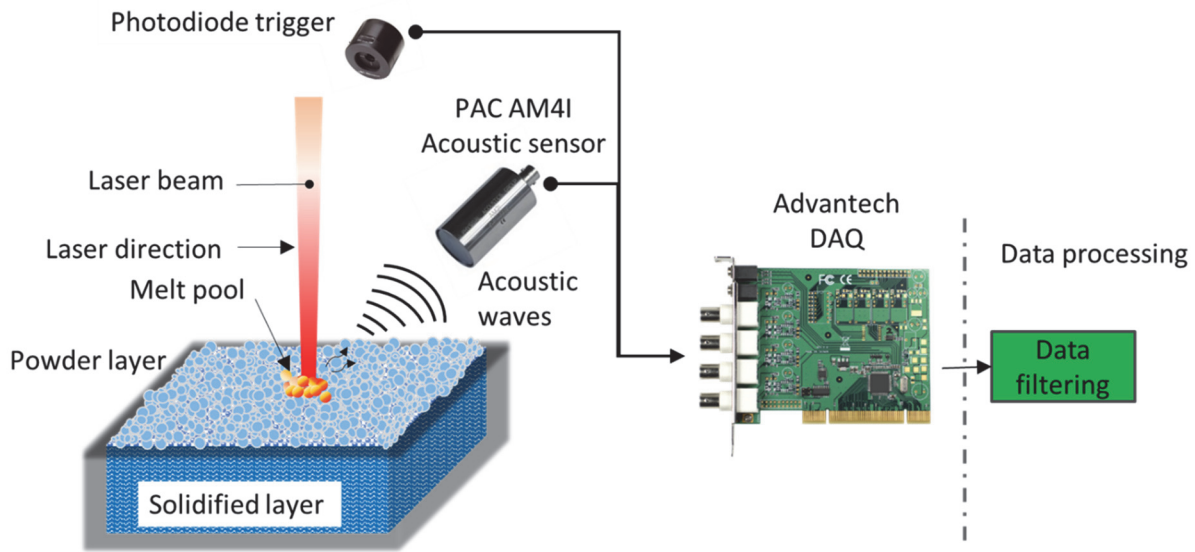


Figure 66. Schematic of the data acquisition pipeline with PAC AM4I acoustic sensor and photodiode trigger.

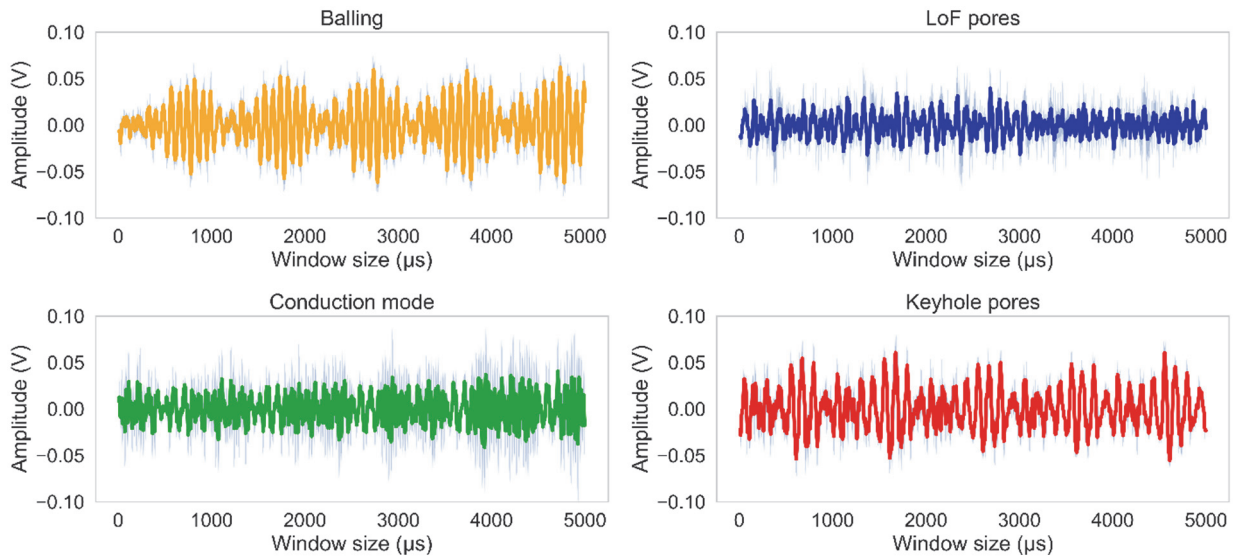


Figure 67. Normalized AE signals acquired of the four investigated process regimes, namely *balling*, *LoF pores*, *conduction mode*, and *keyhole pores*.

6.3.3 Anomaly detection

The primary idea of this work is to predict outliers or anomalies in the LPBF process based on acoustic emissions. The parts printed in the *conduction mode* regime are considered ideal conditions for the best mechanical properties. In contrast, each regime (*balling*, *LoF pores* and *keyhole pores*) is considered as process anomaly. Consequently, the acoustic signals from these regimes are grouped as anomalies, whereas the signals corresponding to *conduction mode* are used for training the neural networks. The anomaly detection accuracy depends on understanding the "normal" data (AE signature from *conduction mode* in our case) so that abnormal

data (AE signature from *balling*, *LoF pores*, and *keyhole pores* in our case) can be easily differentiated. Table 21 shows the dataset to train the two CNN architectures. The parameter inputs for training the two architectures, namely VAE and GANomaly, for identifying the anomalies, are listed in Table 22.

Table 21. Acoustic signal datasets for training and testing.

Class	AM process regime	Samples of window size (5ms)	Training model	Testing model
Normal	<i>Conduction mode</i>	2700	75% of the total sample	25% of the total sample
Anomaly / Outlier	<i>Balling, LoF pores and keyhole pores</i>	13680 (2730- <i>balling</i> , 2750- <i>keyhole pores</i> , 8200- <i>LoF pores</i>)	-	100% of the total sample

Table 22. Parameters used in VGG and ResNet Architectures for training.

Training parameters	VAE	GANomaly
Type of analysis	Anomaly detection	Anomaly detection
Solver name	'adam'	'adam'
Learn rate	0.001	0.001
Architecture	Encoder / Decoder architecture with 5 layers	Generator / Discriminator architecture with 5 layers
Momentum	0.9	0.9
Total Epochs	300	300
BatchSize	100	100
Shuffle	Every-epoch	Every-epoch
Batch normalization	True	True
Training set (<i>Conduction mode</i>)	AE signal corresponding to <i>conduction mode</i> with a window size of 5ms	AE signal corresponding to <i>conduction mode</i> with a window size of 5000 μ s
Anomaly set	AE signal corresponding to <i>balling</i> , <i>LoF pores</i> and <i>keyhole pores</i> with a window size of 5ms	AE signal corresponding to <i>balling</i> , <i>LoF pores</i> and <i>keyhole pores</i> with a window size of 5 ms
Input tensor size	1 x 1 x 5000	1 x 1 x 5000
Loss function	Mean squared error (MSE) with KL divergence loss	Customized loss functions
GPU training	GeForce RTX 2080 Ti	GeForce RTX 2080 Ti
Dropout	0.2	0.2
Library	Pytorch	Pytorch
Training parameters	786736	892691

6.3.4 VAE based anomaly detection

The variational autoencoder architecture selected in this research consists of 10 layers with 5 layers corresponding to the encoder (E) and 5 layers corresponding to the decoder (D), as illustrated by Figure 68. The choice of the VAE design was to have good accuracy with a minimum number of parameters to train. The input to the network is a tensor of size $1 \times 1 \times 5000$, which is the windowed acoustic signal of 5 ms corresponding to the *conduction mode* regime. The five-layer architecture of the encoder (E) compresses the raw acoustic signal into a latent space of the size of $1 \times 256 \times 10$, sampled randomly from the training distribution via 1-Dimensional convolution, batch normalization, and \tanh activation. The compressed latent space representation of the signal is then reconstructed to its original form by the decoder (D), whose architecture consisting of 5 layers. The decoder (D) architecture is an inverse of the encoder architecture with 1-Dimensional convolution replaced by the 1-Dimensional transpose convolution for upsampling. The overall architecture of the VAE is symmetrical, and evidence of this is in Figure 68. The VAE is trained with the combination of Adam as its optimizer with a batch size of 100, a dropout rate of 0.5, and a learning rate of 0.001 for 300 epochs. The training parameters were selected based on trial and error. At each epoch of the model training, the normal dataset is passed into the network. The reconstruction loss is back-propagated to alter the weights of the network for better performance. The variational autoencoder's loss function is the sum of the reconstruction loss, given by Mean Squared Error (MSE) with the KL divergence loss.

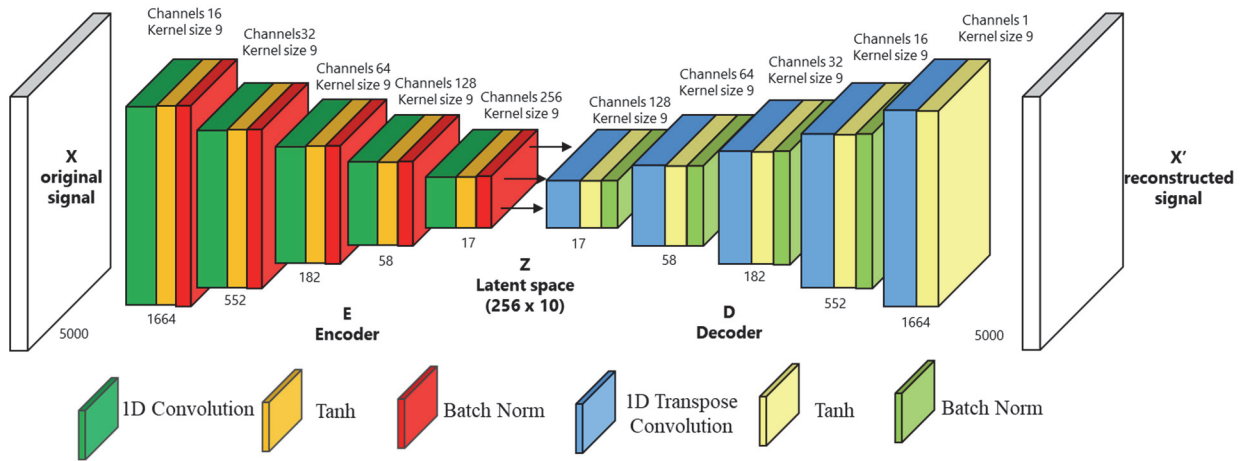


Figure 68. The architecture of the proposed variational autoencoder network.

Figure 69 represents the loss curves of the VAE model trained on raw acoustics signals corresponding to the *conduction mode* regime. From this figure, it is observed that the loss decreases with every epoch, confirming that the network learns the "normal" dataset patterns (*conduction mode*) and can reconstruct them efficiently. The saturation of the training loss with epochs suggests that the VAE network is trained.

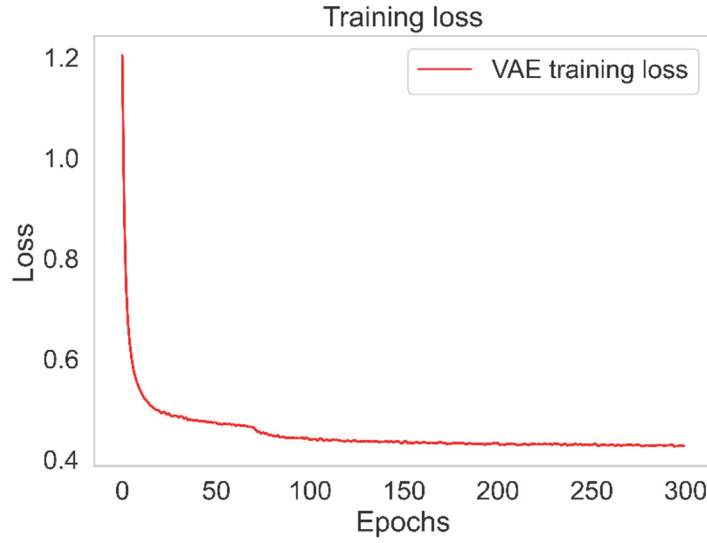


Figure 69. Training loss plot of VAE model on acoustic signals corresponding to *conduction mode* regime.

With the trained VAE network, the next step is to identify the reconstruction loss distribution on the "normal" dataset (*conduction mode* regime). Examining Figure 70(a), the maximum area of the reconstruction loss distribution lies in the range of 0 to 0.35 with a confidence of $\approx 95\%$. The threshold loss is calculated from the reconstruction distribution shown in Equation (6). We can define that any reconstruction loss corresponding to a signal more than the threshold value is classified as an anomaly.

$$\text{Threshold} = \text{mean } (\mu) + 3 \cdot \text{standard deviations } (\sigma) \quad (9)$$

Based on Equation (9), the threshold for anomaly detection for the trained VAE model has a value of 0.35, which is also synonymous with the visual examination. The VAE network's predictability is evaluated by comparing the reconstruction loss for each acoustic signal window in the anomaly dataset (*balling*, *LoF pores*, and *keyhole pores*) to the threshold value. The acoustic signals with reconstruction loss greater than threshold values are flagged as an anomaly. The reconstruction loss distribution of the *balling*, *LoF pores* and *keyhole pores* anomaly regimes are also plotted in Figure 70(b)-(d), respectively. It can be seen in Figure 70(b)-(d) that the reconstruction loss distribution density for the anomaly regimes are higher than 0.35. We can conclude that our proposed VAE architecture will differentiate normal conditions from other undesirable events for the selected time window from the reconstruction losses.

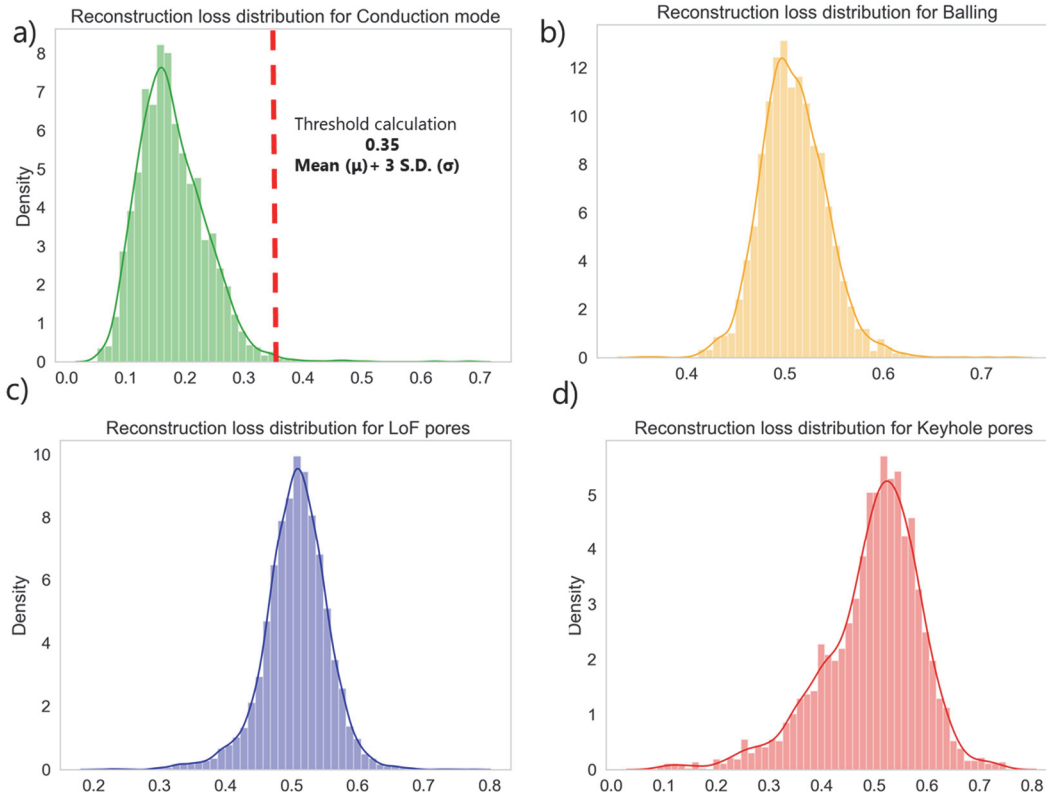


Figure 70. Distribution plots of reconstruction losses for normal and abnormal conditions.

The reconstructions of the VAE model on the acoustic signals corresponding to the "normal" conditions (the *conduction mode* regime) are presented in Figure 71(a). In this figure, the VAE model can recreate the true signal envelopes and patterns for the *conduction mode* regime. However, the reconstruction is pretty poor for the acoustic signals corresponding to the anomalies, and evidence of this is by the reconstruction losses in Figure 71(b). To achieve a statistically sound conclusion, we tested our approach on a total of 2100 windows (each 5 ms) corresponding to anomalies (700 each of *balling*, *LoF pores* and *keyhole pores*) and 700 windows (each 5 ms) corresponding to the normal regime. The trained VAE model correctly classified 2690 signal windows out of the 2800 windows giving an accuracy rate higher than 96% compared with the ground-truth labels.

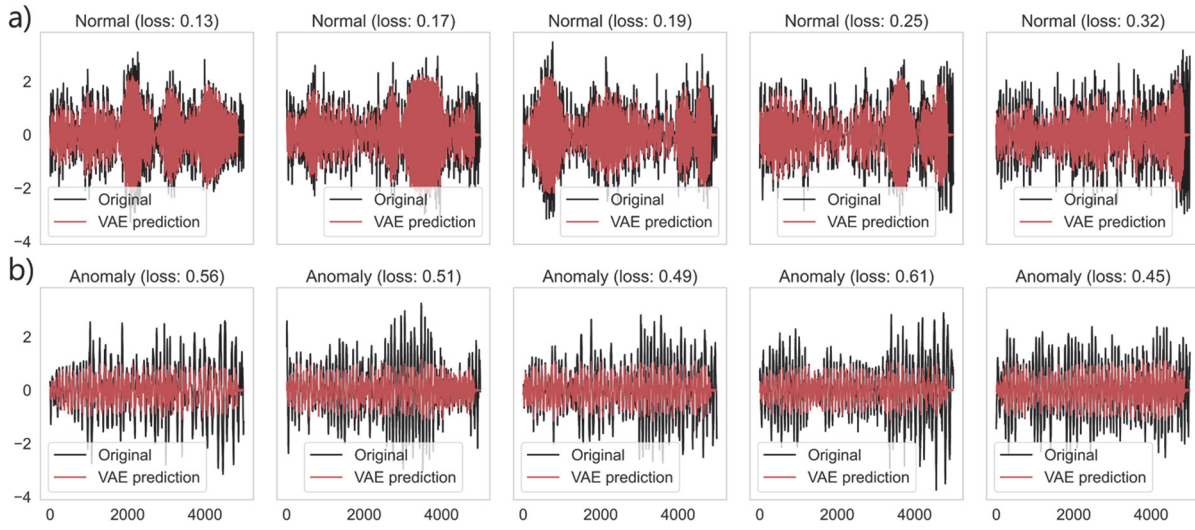


Figure 71. Reconstructions of the VAE model on (a) the "normal" and (b) the anomaly conditions.

6.3.5 GANomaly based anomaly detection

The signal analysis procedure for the GANomaly network is identical to VAE, and so only a summary is given here. The GANomaly network is trained on the acoustic signals corresponding to the *conduction mode* regime during training. Once trained, its parametrization is not suitable for generating distributions different from the trained samples. As a result, anomalies can be identified. The GANomaly architecture used in this work is inspired by the work of Akcay *et al.* (Akcay, Atapour-Abarghouei, and Breckon 2018).

Figure 72 is a schematic of the GANomaly architecture for time-series anomaly detection. The GANomaly model contains two encoders (G_{E1} , G_{E2}), a decoder (G_D), which forms the generator (G) and discriminator (D) network. The generator (G) learns the input data representation of the "normal" time-series signal distribution and reconstructs the signal via the use of an encoder (G_{E1}) and a decoder (G_D) network combination. Owing to the symmetrical VAE encoder-decoder architecture performance discussed in Section 6.3.4, the same layers and kernel filters are exploited to build the generator part. The second encoder (G_{E2}) design, a part of the generator, is a replica of the first encoder (G_{E1}). The encoder (G_{E1}) network downsamples the raw acoustic signal into a latent representation of size $1 \times 256 \times 10$, and the decoder (G_D) network reconstructs the original signal from the latent space. The second encoder (G_{E2}) of the generator part compresses the reconstructed time-series signal into a latent size of $1 \times 256 \times 10$. The discriminator (D) network plays the role of identifying fake and real signals like vanilla GANs. The GANomaly architecture is trained with adam optimizer with a batch size of 100, a drop out rate of 0.2, and a learning rate of 0.01 for 300 epochs similar to VAE training parameters. At each epoch of the model training, the *conduction mode* dataset is passed into the network, and the computed loss is back-propagated to alter the network's weights for better performance. The loss function used for the training is a cumulative sum of three losses function as given in Equation (1).

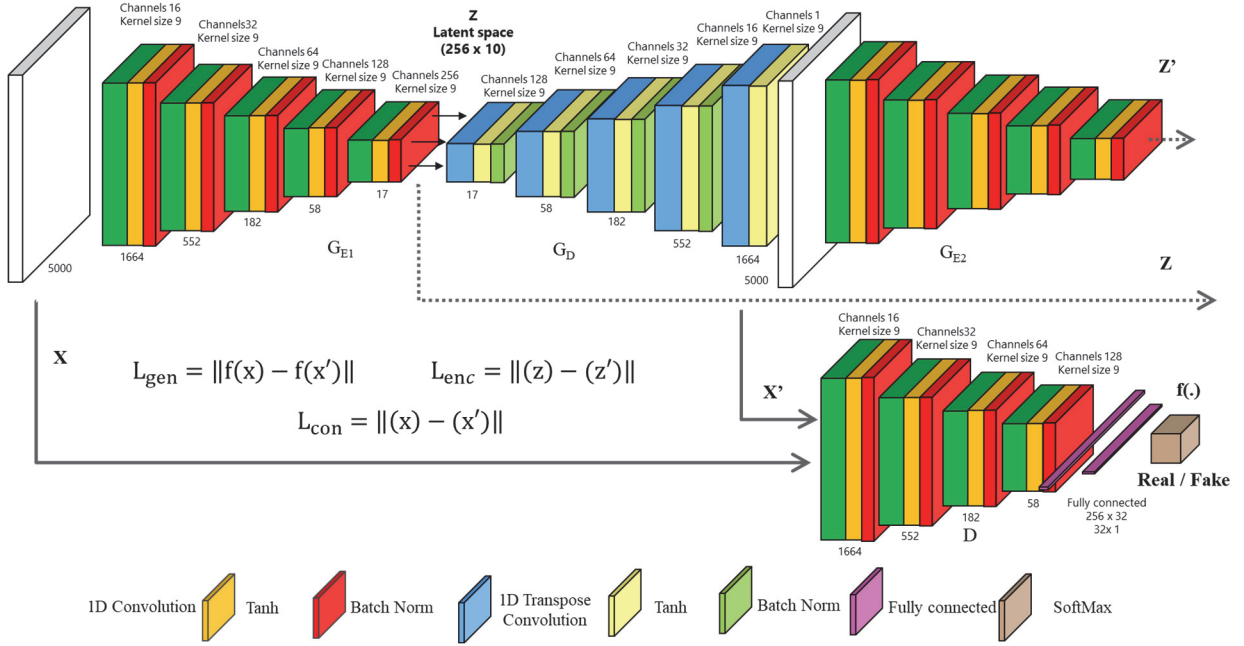


Figure 72. The architecture of the proposed GANomaly network comprising the generator and discriminator.

$$\text{Loss} = \omega_{con} \cdot L_{con} + \omega_{enc} \cdot L_{enc} + \omega_{gen} \cdot L_{gen} \quad (10)$$

Where, $L_{gen} = \|f(x) - f(x')\|$, $L_{enc} = \|(z) - (z')\|$ and $L_{con} = \|(x) - (x')\|$

The construction loss (L_{con}) penalizes the generator as it is the MSE between the original sample x and the reconstructed one ($x' = G(x)$). The encoder loss (L_{enc}) is an additional loss minimizing the distance between the bottleneck features of the input ($z = G_E(x)$) and the encoded features of the generated image ($z' = E(G(x))$). Finally, the discriminator loss (L_{gen}) is the distance between the feature representation of the original acoustic signal and the generated signal. Unlike traditional vanilla GANs, where the generator (G) is not updated by back-propagating the output of discriminator (D) (real/fake), in this case, we update the generator (G) based on the internal representation of discriminator (D). Apart from the losses, there are weights (ω_{con} , ω_{enc} , ω_{gen}) that can be tuned to the loss terms, which gives flexibility for the training. The weight values used for ω_{con} , ω_{enc} and ω_{gen} during training are 20, 5 and 1, which were down-selected based on exhaustive search. Figure 73 shows the three training loss curves for the GANomaly model trained on the raw acoustics signals. The plots indicate that all three losses decrease with every epoch, confirming that the network is learning the training dataset's representation.

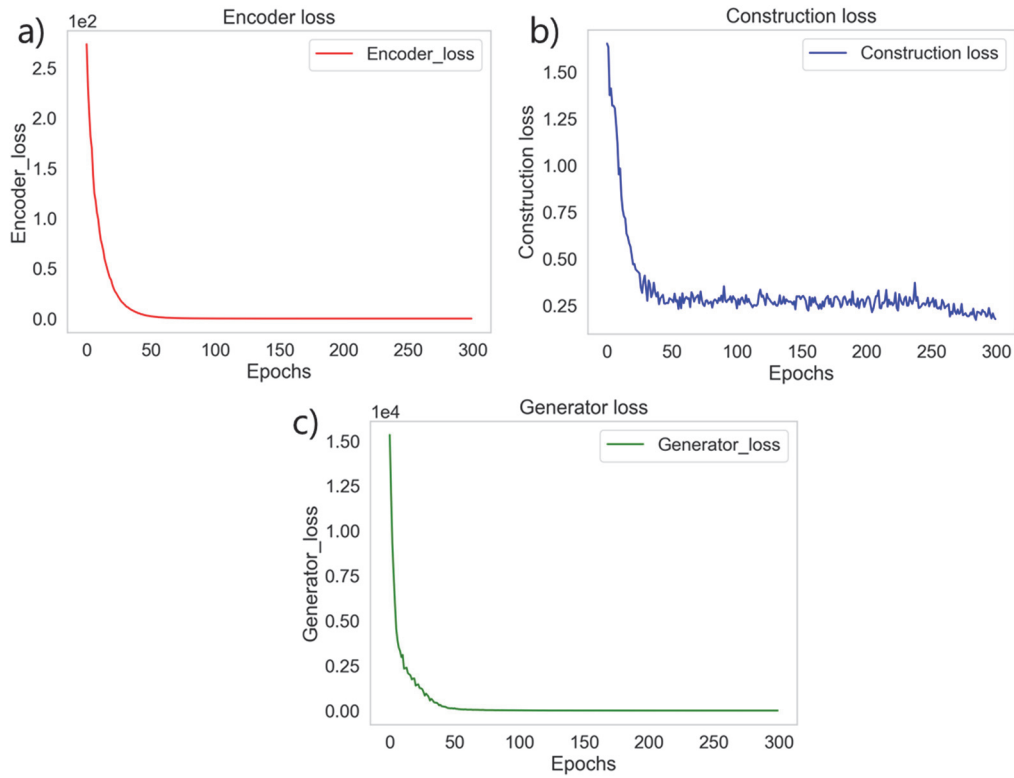


Figure 73. Training loss plot (a) Encoder loss, (b) Generator loss and (c) Construction loss of GANomaly model on acoustic signals corresponding to *conduction mode* regime.

After training the GANomaly, the next step is to identify the distribution of the reconstruction loss on the conduction mode dataset, similar to VAE, and the threshold value to flag the anomaly is calculated. Figure 74(a) is the distribution of the reconstruction loss for the *conduction mode* regime, and it is seen that it lies in the range of 0.0 to 0.22. With Equation (9), the threshold for anomaly detection is found to be 0.40. In other words, the reconstruction losses greater than the threshold value of 0.22 will be flagged as an anomaly. Figure 74(b) – (d) shows the reconstruction loss for each acoustic signal window in the anomaly datasets *balling*, *LoF pores* and *keyhole pores*, respectively. From these figures, it is seen that the reconstruction loss distribution of the anomaly regimes is higher than the threshold value of 0.22. Consequently, inferring from the reconstruction losses, we can conclude that the proposed GANomaly architecture will differentiate normal conditions from other undesirable events.

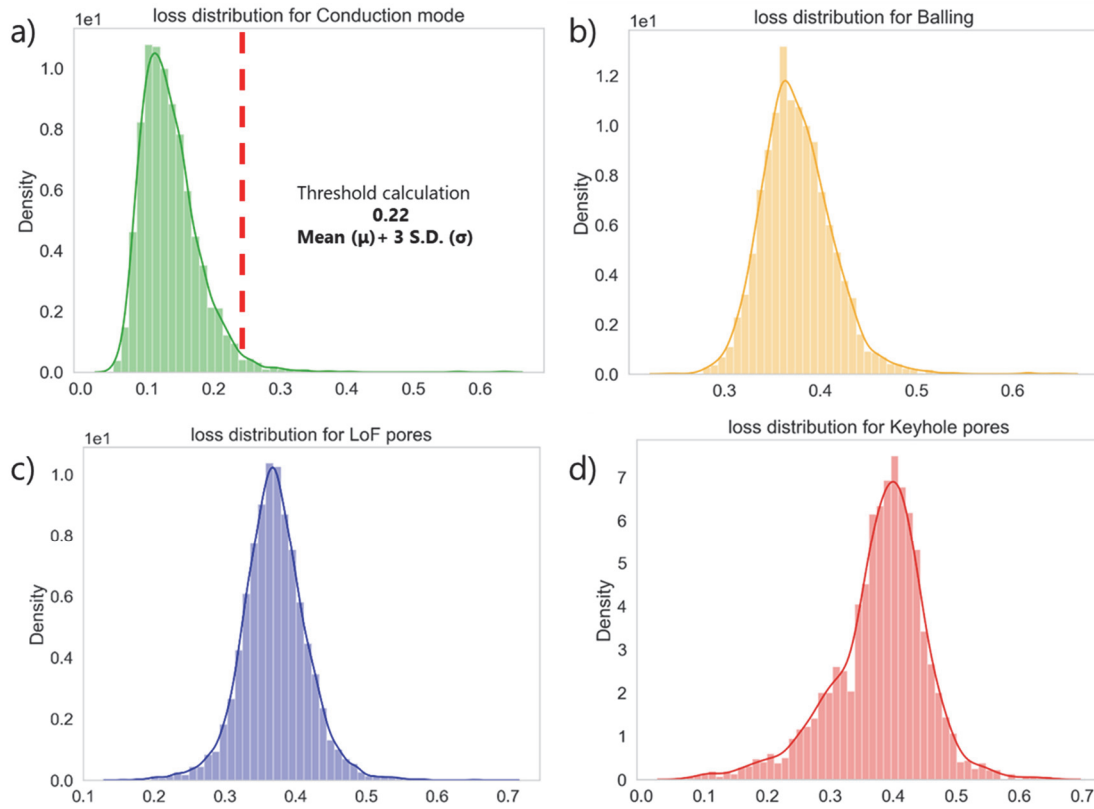


Figure 74. Distribution plots of reconstruction losses for normal and abnormal conditions.

Figure 75 presents the boxplot distribution of the losses predicted by the GANomaly model on the acoustic signals corresponding to the "normal" regime (*conduction mode* regime) and abnormal conditions (*balling*, *LoF pores* and *keyhole pores*). The plot shows that the losses for the trained *conduction mode* dataset are below the threshold of 0.22 as the parameterization are biased towards the distribution corresponding to the *conduction mode* dataset. A total of 2100 windows (each 5 ms) corresponding to anomalies (700 each of *balling*, *LoF pores* and *keyhole pores*) and 700 windows (each 5 ms) corresponding to the normal regime were tested. The trained GANomaly model correctly classified 2720 signal windows out of the 2800 windows giving an accuracy rate higher than 97% compared with the ground-truth labels.

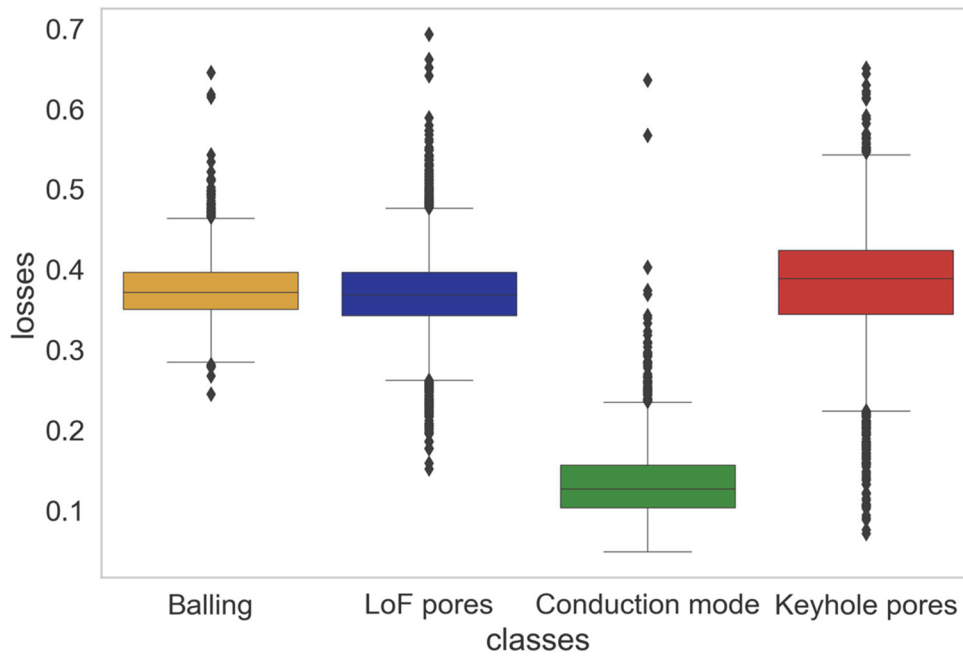


Figure 75. Box plots of reconstruction losses for normal and abnormal conditions confirm that the AE signal corresponding to anomaly regimes is greater than the threshold of 0.22.

6.3.6 Summary of the main results

Based on both the VAE and GANomaly models' prediction results, we demonstrated that the raw acoustic signals could be used as an input dataset to detect with high accuracy abnormal regimes such as *balling*, *LoF pores*, and *keyhole pores* occurring during LPBF processing of Inconel 718. VAE and GANomaly models distinguished the anomaly regimes such *balling*, *LoF pores*, and *keyhole pores* from the normal regime, i.e. *conduction mode*, with 96 and 97% accuracy. Comparing the two CNN architectures used in this study, it is found that the VAE performs slightly better in anomaly detection compared to GANomaly when the size of the network, trainable parameter, computational resource, and training time is taken as benchmarks and vice-versa if accuracy is taken into account.

6.4 Conclusions

We have demonstrated an approach based on semi-supervised methods to detect deviations from chosen qualities during the LPBF processes. In particular, based on the airborne acoustic signals from the process, the undesirable regimes, namely, *balling*, *LoF pores*, and *keyhole pores* could be differentiated from the reference regime *conduction mode*. Two CNN architectures, VAE and GANomaly, were tested. The two models were trained on acoustic signals divided into windows of 5 ms corresponding to the *conduction mode* regime. These acoustic signals were captured during line track experiments on Inconel 718 in a customized LPBF setup. The sensor used in the study was an airborne resonant microphone with an operating range of 0–100 kHz. The data

acquisition was made with an Advantech DAQ board at 1MHz. Based on the experimental results, the following generalized conclusions are drawn:

- Both the VAE and GANomaly models with symmetrical encoder-decoder architecture were able to detect undesirable regimes with ease. The GANomaly architecture with three losses and larger weights had better detection accuracy compared to VAE. Though GANomaly is a reasonably large network compared to the VAE architecture used in this work, it comes with a loss function that can be optimized during training to similar tasks on time-series signals.
- The two models' accuracy suggests that the reference regime's sensor signatures, i.e., defect regimes, can be differentiated from the too many ambiguous unfavourable regimes involved in the LPBF process with minimum effort spent on data collection and labelling.

The proposed approach establishes that the knowledge of LPBF processes on one regime in a material can be used to assess other regimes with minimum effort. The size of the Inconel 718 powder particles used in this study varied between 15 and 45 μm and followed a normal distribution. The laser-material interaction is affected by the powder characteristics, machine parameters and surface topography (Vock et al. 2019; Han et al. 2020; Sing, Huang, et al. 2021). Therefore trained GAN and VAE models cannot be generalized across different powder distributions, process parameters and alloying compositions. Though the models cannot be generalized, the VAE and GAN framework can be applied to process different powders with process map knowledge in Industrial LPBF setups to identify the abnormal regimes in a production environment. We have presented our work based on a window size of 5 ms, and the performance of the network in smaller window sizes is also a study in progress. The methodologies robustness in a more demanding situation where there are soft boundaries between anomaly and normal regimes is the planned research direction. As a final word, the optimization and fine-tuning of weights by adding skip connections in VAE architectures and performing a grid search to identify suitable weights for the loss function in GANomaly architecture will further optimize training and is also a part of future work. The data and codes for this work are present in the following repo (<https://c4science.ch/diffusion/11519/>).

References

- Akçay, Samet, Amir Atapour-Abarghouei, and Toby P Breckon. 2018. Ganomaly: Semi-supervised anomaly detection via adversarial training. Paper presented at the Asian conference on computer vision.
- An, Jia, Chee Kai Chua, and Vladimir Mironov. 2021. "Application of Machine Learning in 3D Bioprinting: Focus on Development of Big Data and Digital Twin." *International Journal of Bioprinting* 7 (1).
- An, Jinwon, and Sungzoon Cho. 2015. "Variational autoencoder based anomaly detection using reconstruction probability." *Special Lecture on IE* 2 (1):1-18.
- Bastuck, Matthias, Hans-Georg Herrmann, Bernd Wolter, Peter-Christian Zinn, and Ralf-Kilian Zaeh. 2015. Acoustic in-process monitoring of laser welding. Paper presented at the International Congress on Applications of Lasers & Electro-Optics.
- Bayle, F, and M Doubenskaia. 2008. Selective laser melting process monitoring with high speed infra-red camera and pyrometer. Paper presented at the Fundamentals of laser assisted micro-and nanotechnologies.
- Brandt, Milan. 2016. "Laser additive manufacturing: materials, design, technologies, and applications."
- Cai, Lei, Hongyang Gao, and Shuiwang Ji. 2019. Multi-stage variational auto-encoders for coarse-to-fine image generation. Paper presented at the Proceedings of the 2019 SIAM International Conference on Data Mining.
- Cheng, Bo, James Lydon, Kenneth Cooper, Vernon Cole, Paul Northrop, and Kevin Chou. "Melt Pool Dimension Measurement In Selective Laser Melting Using Thermal Imaging Bo Cheng¹, James Lydon², Kenneth Cooper², Vernon Cole³, Paul Northrop³, Kevin Chou¹."
- Chua, Zhong Yang, Il Hyuk Ahn, and Seung Ki Moon. 2017. "Process monitoring and inspection systems in metal additive manufacturing: Status and applications." *International Journal of Precision Engineering and Manufacturing-Green Technology* 4 (2):235-45.
- Clijsters, Stijn, Tom Craeghs, Sam Buls, Karolien Kempen, and J-P Kruth. 2014. "In situ quality control of the selective laser melting process using a high-speed, real-time melt pool monitoring system." *The International Journal of Advanced Manufacturing Technology* 75 (5-8):1089-101.
- Eschner, N, L Weiser, B Häfner, and G Lanza. 2020. "Classification of specimen density in Laser Powder Bed Fusion (L-PBF) using in-process structure-borne acoustic process emissions." *Additive Manufacturing* 34:101324.

- Everton, Sarah K, Matthias Hirsch, Petros Stravroulakis, Richard K Leach, and Adam T Clare. 2016. "Review of in-situ process monitoring and in-situ metrology for metal additive manufacturing." *Materials & Design* 95:431-45.
- Fisher, Brian A, Brandon Lane, Ho Yeung, and Jack Beuth. 2018. "Toward determining melt pool quality metrics via coaxial monitoring in laser powder bed fusion." *Manufacturing letters* 15:119-21.
- Furumoto, Tatsuaki, Takashi Ueda, Mohd Rizal Alkahari, and Akira Hosokawa. 2013. "Investigation of laser consolidation process for metal powder by two-color pyrometer and high-speed video camera." *CIRP annals* 62 (1):223-6.
- Ghasemi-Tabasi, Hossein, Jamasp Jhabvala, Eric Boillat, Toni Ivas, Rita Drissi-Daoudi, and Roland E Logé. 2020. "An effective rule for translating optimal selective laser melting processing parameters from one material to another." *Additive Manufacturing* 36:101496.
- Gobert, Christian, Edward W Reutzel, Jan Petrich, Abdalla R Nassar, and Shashi Phoha. 2018. "Application of supervised machine learning for defect detection during metallic powder bed fusion additive manufacturing using high resolution imaging." *Additive Manufacturing* 21:517-28.
- Goh, GD, SL Sing, and WY Yeong. 2021. "A review on machine learning in 3D printing: Applications, potential, and challenges." *Artificial Intelligence Review* 54 (1):63-94.
- Gondara, Lovedeep. 2016. Medical image denoising using convolutional denoising autoencoders. Paper presented at the 2016 IEEE 16th International Conference on Data Mining Workshops (ICDMW).
- Gong, Haijun, Hengfeng Gu, Kai Zeng, JJS Dilip, Deepankar Pal, Brent Stucker, Daniel Christiansen, Jack Beuth, and John J Lewandowski. 2014. Melt pool characterization for selective laser melting of Ti-6Al-4V pre-alloyed powder. Paper presented at the Solid freeform fabrication symposium.
- Grasso, M, AG Demir, B Previtali, and BM Colosimo. 2018. "In situ monitoring of selective laser melting of zinc powder via infrared imaging of the process plume." *Robotics and Computer-Integrated Manufacturing* 49:229-39.
- Gu, DD, YF Shen, JL Yang, and Y Wang. 2006. "Effects of processing parameters on direct laser sintering of multicomponent Cu based metal powder." *Materials science and technology* 22 (12):1449-55.
- Guessasma, Sofiane, Weihong Zhang, Jihong Zhu, Sofiane Belhabib, and Hedi Nouri. 2015. "Challenges of additive manufacturing technologies from an optimisation perspective." *International Journal for Simulation and Multidisciplinary Design Optimization* 6:A9.

- Hahn, Tim Von, and Chris K Mechefske. 2021. "Self-supervised learning for tool wear monitoring with a disentangled-variational-autoencoder." *International Journal of Hydromechatronics* 4 (1):69-98.
- Han, Changjun, Qihong Fang, Yusheng Shi, Shu Beng Tor, Chee Kai Chua, and Kun Zhou. 2020. "Recent advances on high-entropy alloys for 3D printing." *Advanced Materials* 32 (26):1903855.
- Imani, Farhad, Ruimin Chen, Evan Diewald, Edward Reutzel, and Hui Yang. 2019. "Deep learning of variant geometry in layerwise imaging profiles for additive manufacturing quality control." *Journal of Manufacturing Science and Engineering* 141 (11).
- Jerri, A. J. 1977. "The Shannon sampling theorem—Its various extensions and applications: A tutorial review." *Proceedings of the IEEE* 65 (11):1565-96. doi: 10.1109/PROC.1977.10771.
- Khairallah, Saad A, Andrew T Anderson, Alexander Rubenchik, and Wayne E King. 2016. "Laser powder-bed fusion additive manufacturing: Physics of complex melt flow and formation mechanisms of pores, spatter, and denudation zones." *Acta Materialia* 108:36-45.
- Khajavi, Siavash H, Jouni Partanen, and Jan Holmström. 2014. "Additive manufacturing in the spare parts supply chain." *Computers in Industry* 65 (1):50-63.
- King, Wayne E, Andrew T Anderson, Robert M Ferencz, Neil E Hodge, Chandrika Kamath, Saad A Khairallah, and Alexander M Rubenchik. 2015. "Laser powder bed fusion additive manufacturing of metals; physics, computational, and materials challenges." *Applied Physics Reviews* 2 (4):041304.
- Kruth, Jean-Pierre, Peter Mercelis, Jonas Van Vaerenbergh, and Tom Craeghs. 2007. Feedback control of selective laser melting. Paper presented at the Proceedings of the 3rd international conference on advanced research in virtual and rapid prototyping.
- Kwon, Ohjung, Hyung Giun Kim, Min Ji Ham, Wonrae Kim, Gun-Hee Kim, Jae-Hyung Cho, Nam Il Kim, and Kangil Kim. 2020. "A deep neural network for classification of melt-pool images in metal additive manufacturing." *Journal of intelligent Manufacturing* 31 (2):375-86.
- Mahmud, Mohammad Sultan, Joshua Zhexue Huang, and Xianghua Fu. 2020. "Variational Autoencoder-Based Dimensionality Reduction for High-Dimensional Small-Sample Data Classification." *International Journal of Computational Intelligence and Applications* 19 (01):2050002.
- Mani, Mahesh, Brandon M Lane, M Alkan Donmez, Shaw C Feng, and Shawn P Moylan. 2017. "A review on measurement science needs for real-time control of additive manufacturing metal powder bed fusion processes." *International Journal of Production Research* 55 (5):1400-18.

- Masinelli, Giulio, Tri Le-Quang, Silvio Zanolì, Kilian Wasmer, and Sergey A Shevchik. 2020. "Adaptive Laser Welding Control: A Reinforcement Learning Approach." *IEEE Access* 8:103803-14.
- Masinelli, Giulio, Sergey A Shevchik, Vigneashwara Pandiyan, Tri Quang-Le, and Kilian Wasmer. 2020. Artificial Intelligence for Monitoring and Control of Metal Additive Manufacturing. Paper presented at the International Conference on Additive Manufacturing in Products and Applications.
- Meng, Lingbin, Brandon McWilliams, William Jarosinski, Hye-Yeong Park, Yeon-Gil Jung, Jehyun Lee, and Jing Zhang. 2020. "Machine learning in additive manufacturing: A review." *JOM* 72 (6):2363-77.
- Nishizaki, Hiromitsu. 2017. Data augmentation and feature extraction using variational autoencoder for acoustic modeling. Paper presented at the 2017 Asia-Pacific Signal and Information Processing Association Annual Summit and Conference (APSIPA ASC).
- Okaroa, Ikenna A, Sarini Jayasingheb, Chris Sutcliffeb, Kate Blackb, Paolo Paolettia, and Peter L Greena. 2018. "Automatic Fault Detection for Selective Laser Melting using Semi-Supervised Machine Learning."
- Pagnoni, Artidoro, Kevin Liu, and Shangyan Li. 2018. "Conditional variational autoencoder for neural machine translation." *arXiv preprint arXiv:1812.04405*.
- Pandiyan, Vigneashwara, Rita Drissi-Daoudi, Sergey Shevchik, Giulio Masinelli, Roland Logé, and Kilian Wasmer. 2020. "Analysis of time, frequency and time-frequency domain features from acoustic emissions during Laser Powder-Bed fusion process." *Procedia CIRP* 94:392-7.
- Pandiyan, Vigneashwara, Pushparaja Murugan, Tegoeh Tjahjowidodo, Wahyu Caesarendra, Omey Mohan Manyar, and David Jin Hong Then. 2019. "In-process virtual verification of weld seam removal in robotic abrasive belt grinding process using deep learning." *Robotics and Computer-Integrated Manufacturing* 57:477-87.
- Pandiyan, Vigneashwara, Josef Prost, Georg Vorlaufer, Markus Varga, and Kilian Wasmer. 2021. "Identification of abnormal tribological regimes using a microphone and semi-supervised machine-learning algorithm." *Friction*:1-14.
- Pavlov, M, M Doubenskaia, and I Smurov. 2010. "Pyrometric analysis of thermal processes in SLM technology." *Physics Procedia* 5:523-31.
- Sakurada, Mayu, and Takehisa Yairi. 2014. Anomaly detection using autoencoders with nonlinear dimensionality reduction. Paper presented at the Proceedings of the MLSDA 2014 2nd Workshop on Machine Learning for Sensory Data Analysis.

- Schlegl, Thomas, Philipp Seeböck, Sebastian M Waldstein, Georg Langs, and Ursula Schmidt-Erfurth. 2019. "f-anogan: Fast unsupervised anomaly detection with generative adversarial networks." *Medical image analysis* 54:30-44.
- Scime, Luke, and Jack Beuth. 2018a. "Anomaly detection and classification in a laser powder bed additive manufacturing process using a trained computer vision algorithm." *Additive Manufacturing* 19:114-26.
- . 2018b. "A multi-scale convolutional neural network for autonomous anomaly detection and classification in a laser powder bed fusion additive manufacturing process." *Additive Manufacturing* 24:273-86.
- Shevchik, SA, S Zanolli, F Saeidi, B Meylan, G Flück, and K Wasmer. 2021. "Monitoring of friction-related failures using diffusion maps of acoustic time series." *Mechanical Systems and Signal Processing* 148:107172.
- Shevchik, Sergey A, Christoph Kenel, Christian Leinenbach, and Kilian Wasmer. 2018. "Acoustic emission for in situ quality monitoring in additive manufacturing using spectral convolutional neural networks." *Additive Manufacturing* 21:598-604.
- Shevchik, Sergey A, Giulio Masinelli, Christoph Kenel, Christian Leinenbach, and Kilian Wasmer. 2019. "Deep learning for in situ and real-time quality monitoring in additive manufacturing using acoustic emission." *IEEE Transactions on Industrial Informatics* 15 (9):5194-203.
- Sing, SL, S Huang, GD Goh, GL Goh, CF Tey, JHK Tan, and WY Yeong. 2021. "Emerging metallic systems for additive manufacturing: In-situ alloying and multi-metal processing in laser powder bed fusion." *Progress in Materials Science*:100795.
- Sing, SL, CN Kuo, CT Shih, CC Ho, and CK Chua. 2021. "Perspectives of using machine learning in laser powder bed fusion for metal additive manufacturing." *Virtual and physical prototyping*:1-15.
- Spears, Thomas G, and Scott A Gold. 2016. "In-process sensing in selective laser melting (SLM) additive manufacturing." *Integrating Materials and Manufacturing Innovation* 5 (1):16-40.
- Sumesh, A, Dinu Thomas Thekkuden, Binoy B Nair, K Rameshkumar, and K Mohandas. 2015. Acoustic signature based weld quality monitoring for SMAW process using data mining algorithms. Paper presented at the Applied Mechanics and Materials.
- Tan, Yingshui, Baihong Jin, Alexander Nettekoven, Yuxin Chen, Yisong Yue, Ufuk Topcu, and Alberto Sangiovanni-Vincentelli. 2019. An encoder-decoder based approach for anomaly detection with application in additive manufacturing. Paper presented at the 2019 18th IEEE International Conference On Machine Learning And Applications (ICMLA).

- Tapia, Gustavo, and Alaa Elwany. 2014. "A review on process monitoring and control in metal-based additive manufacturing." *Journal of Manufacturing Science and Engineering* 136 (6).
- Van Elsen, Maarten. 2007. "Complexity of Selective Laser Melting: a new optimisation approach."
- Vock, Silvia, Burghardt Klöden, Alexander Kirchner, Thomas Weißgärber, and Bernd Kieback. 2019. "Powders for powder bed fusion: a review." *Progress in Additive Manufacturing* 4 (4):383-97.
- Wang, Di, Shibiao Wu, Fan Fu, Shuzhen Mai, Yongqiang Yang, Yang Liu, and Changhui Song. 2017. "Mechanisms and characteristics of spatter generation in SLM processing and its effect on the properties." *Materials & Design* 117:121-30.
- Wasmer, K, T Le-Quang, B Meylan, and SA Shevchik. 2019. "In situ quality monitoring in AM using acoustic emission: A reinforcement learning approach." *Journal of Materials Engineering and Performance* 28 (2):666-72.
- Wasmer, K, T Le-Quang, B Meylan, F Vakili-Farahani, MP Olbinado, A Rack, and SA Shevchik. 2018. "Laser processing quality monitoring by combining acoustic emission and machine learning: a high-speed X-ray imaging approach." *Procedia CIRP* 74:654-8.
- Yan, Zhaorui, Weiwei Liu, Zijue Tang, Xuyang Liu, Nan Zhang, Mingzheng Li, and Hongchao Zhang. 2018. "Review on thermal analysis in laser-based additive manufacturing." *Optics & Laser Technology* 106:427-41.
- Ye, Dongsan, Jerry Ying Hsi Fuh, Yingjie Zhang, Geok Soon Hong, and Kunpeng Zhu. 2018a. "In situ monitoring of selective laser melting using plume and spatter signatures by deep belief networks." *ISA transactions* 81:96-104.
- Ye, Dongsan, Geok Soon Hong, Yingjie Zhang, Kunpeng Zhu, and Jerry Ying Hsi Fuh. 2018. "Defect detection in selective laser melting technology by acoustic signals with deep belief networks." *The International Journal of Advanced Manufacturing Technology* 96 (5-8):2791-801.
- Ye, DS, YHJ Fuh, YJ Zhang, GS Hong, and KP Zhu. 2018b. "Defects Recognition in Selective Laser Melting with Acoustic Signals by SVM Based on Feature Reduction." *MS&E* 436 (1):012020.
- Yu, Chunling, and Jingchao Jiang. 2020. "A perspective on using machine learning in 3D bioprinting." *International Journal of Bioprinting* 6 (1).
- Zenati, Houssam, Chuan Sheng Foo, Bruno Lecouat, Gaurav Manek, and Vijay Ramaseshan Chandrasekhar. 2018. "Efficient gan-based anomaly detection." *arXiv preprint arXiv:1802.06222*.

Zhang, Wentai, Brandon Abranovic, Jacob Hanson-Regalado, Can Koz, Bhavya Duvvuri, Kenji Shimada, Jack Beuth, and Levent Burak Kara. "Flaw Detection in Metal Additive Manufacturing Using Deep Learned Acoustic Features."

Zhang, Yingjie, Geok Soon Hong, Dongsun Ye, Kunpeng Zhu, and Jerry YH Fuh. 2018. "Extraction and evaluation of melt pool, plume and spatter information for powder-bed fusion AM process monitoring." *Materials & Design* 156:458-69.

Zhao, Cang, Kamel Fezzaa, Ross W Cunningham, Haidan Wen, Francesco De Carlo, Lianyi Chen, Anthony D Rollett, and Tao Sun. 2017. "Real-time monitoring of laser powder bed fusion process using high-speed X-ray imaging and diffraction." *Scientific reports* 7 (1):1-11.

Learnings and following work:

Two last chapters proved the possibility of using DL to transfer knowledge from one alloy to another avoiding retraining from scratch. They also proved the possibility to have a semi-supervised AE monitoring.

The two following chapters 7 and 8 are now investigating the change of used microphone. The analysis in chapters 4-6 were conducted on the AE acquired with a narrow wide frequency response microphone. A second microphone, with a flat frequency response and acquiring in the same frequency range, is chosen to highlight the importance of the frequencies for in-situ AE monitoring. The following chapter 7 will compare the two microphones. A CNN is chosen for this comparison. The chapters 4-6 have proven its great efficiency for AE classification. Moreover, it is not feature based and it allows the computation of saliency maps. Saliency maps are performed to highlight the frequencies that have the most influence on the outcome of the CNN for four categories: *keyhole pores*, *conduction mode*, *LoF pores* and *noise*. To reach a robust monitoring it is essential to evaluate the quality of the CNN model used. A methodology based on the saliency map computation is developed. The noise category is added in the chapter 7 analysis to help evaluate the quality of the models. Indeed the saliency map highlighting the most influent frequencies should not be highlighted specific ones for the *noise* category. The *noise* being the AE signal acquired when the laser is off, no laser matter interaction is recorded.

For the following analysis of the chapter 7 and 8, the design of experience is extended for stainless steel 316L to 13 samples with different parameters sets for each process regimes. To develop an accurate processing map, independent from the thermal history, one second delay is applied between each laser line track.

A reliable CNN model with the appropriate microphone can then be chosen in order to study the generalization to unseen conditions. The prediction of the processing regime based on AE produced during the LPBF process for parameters sets that are unseen by the training database is studied in chapter 8. The choice of processing conditions used in the training database (training sets) is then discussed, looking at the influence of their number, relative normalized distance, and position in the processing map on the classification accuracy.

Chapter 7

On the importance of acoustic emission frequencies for in-situ monitoring of Laser Powder Bed Fusion

Rita Drissi-Daoudi¹, Giulio Masinelli², Charlotte de Formanoir¹, Sergey Shevchik², Kilian Wasmer², Jamasp Jhabvala¹, Roland Logé¹

¹Thermomechanical Metallurgy Laboratory – PX Group Chair, Ecole Polytechnique Fédérale de Lausanne (EPFL), Neuchâtel, Switzerland

²Laboratory for Advanced Materials Processing (LAMP), Swiss Federal Laboratories for Materials Science and Technology (Empa), Thun

This manuscript is submitted to Journal of Materials Processing Technology

Contribution: Rita Drissi-Daoudi developed the experimental plan and printed the samples. She optimized the CNN models and performed the different classification and saliency maps investigations. She wrote the manuscript.

Abstract

Acoustic emission analysis gains an increasing interest in the context of Laser powder bed fusion (LPBF) quality monitoring. In this work, different Convolution Neural Networks are used to classify acoustic spectrograms based on the acoustic emissions of four categories in stainless steel 316L: three LPBF process regimes (keyhole pores, conduction mode, and LoF pores) and the machine background noise. Saliency maps are computed to estimate the distinct frequencies that provide efficient classification of each category. Here, we compare classification results and corresponding saliency maps from two microphones with different frequency responses. Classification accuracy for both microphones is above 91 %. However, the quality of the learning of a Convolution Neural Network can be evaluated through the inspection of the saliency maps. The microphone with narrow-wide frequency response, use frequencies that lie outside of the microphone's high sensitivity frequencies. A better model could be trained with the flat response microphone. The frequencies responsible for the classification of the three processing regimes were found to be below 30 kHz. The methodology presented here contributes to the development of robust acoustic monitoring of the LPBF process and offers perspectives for wider generalization of Convolution Neural Network models, e.g. to process conditions outside of the trained conditions, and to other machines or alloys.

Keywords: Laser powder bed fusion, acoustic monitoring, convolution neural networks, saliency maps, frequencies

7.1 Introduction

Laser powder bed fusion is the most studied additive manufacturing method for metals and alloys. It fabricates metallic parts layer-by-layer, by laser consolidation of a given alloy powder [1]. Recent progress allows reaching near-full density and mechanical properties competing with (or even exceeding) those obtained by conventional processing routes [2]. Furthermore, complex geometries can be manufactured with minimal feed-stock waste as all the non-used matter is recycled. Hence, this technology is of great interest to various industries such as medical [3]–[6], automotive [7] or aerospace [8], [9]. However, the range of process parameters to achieve such high material and mechanical properties is limited to a narrow window, called the keyhole threshold [10]. Identifying the optimal processing window often requires a trial-and-error approach, sometimes coupled with numerical simulations [11], [12]. It is tremendously time-consuming and expensive [13], [14]. Moreover, the laser-material interaction is known to be highly non-reproducible [15]–[19].

Porosity is one of the main defects in LPBF process. Two types of pores are distinguished. Lack of fusion (LoF) pores originate from insufficient bonding between two layers or adjacent line tracks, resulting from an insufficient energy input [20]–[23]. Keyhole pores are formed on the contrary when an excess of energy is

provided to the system. A characteristic keyhole depression is created when the metal reaches an evaporation state. The keyhole is filled with metal vapor exercising a recoil pressure whose instability results in the collapse of the wall and possible entrapment of a gas bubble [24]–[28]. The process parameters can be optimized to reach the conduction mode, which can be predicted using equations that combine the most relevant process parameters (power, speed, hatching distance and layer thickness). The Volumetric Energy Density (VED) is widely used [29]–[31] but raises debate due to significant drawbacks [32]. The concept of normalized enthalpy introduced by Hann et al [33] takes into account key material properties, in addition to the process parameters employed in the VED, and provides a more accurate prediction of the melt pool geometry. As recently demonstrated [10], optimal process parameters can be translated from one material to another, based on a rule derived from the normalized enthalpy.

However, even when the parameters are optimized, spatter generation [34]–[38], denudation [39], and powder pollution [18] make it difficult to have a reproducible and predictive process. One of the solutions to detect the occurrence of pores is in-situ monitoring. Two types of monitoring, either based on optical (OE) or on acoustic (AE) emissions, are distinguished. OE monitoring can be classified as follows: spatially resolved (e.g. camera), spatially integrated (e.g. photodiode, pyrometers) and spectrally resolved (e.g. spectrometers) [40]. The spatially resolved methods either measure the melt-pool size and temperature with an IR camera or monitor the powder bed/laser interaction with a high-speed camera [37][40]–[51]. However, these methods are costly and the 2D data management heavy. Spatially integrated methods, including photodiodes [49][50][52]–[55] and pyrometers [51][56]–[58], can convert the light input emission (LE) into a single voltage value, which decreases the amount of data but also the possible monitoring output. These sensors collect data relative only to the surface temperature. Spectrometers measure and filter the intensity of Light Emission (LE) as a function of wavelength or frequency. The deflection of light is produced either by refraction in a prism or diffraction gratings. Spectrometers cover a wide frequency range from gamma rays to microwaves [60], [61]. The information gathered by all these methods are restricted to surface information.

Acoustic Emission (AE) sensors acquire one-dimension data, which is easier to manage, and offer high sensitivity, and temporal resolution while being relatively cheap. A key advantage of this approach is the possibility to detect features not only at the surface but also in the bulk, during LPBF processing. Two types of acoustics sensors can be distinguished: air-borne acoustics emission (ABAE) and structure-borne acoustics emission (SBAE) [62], [63].

Acoustic monitoring was first widely investigated for other laser-based processes, particularly laser welding. In most cases, signal analysis is performed in the frequency domain by applying a Fast Fourier Transform or a wavelet transform. SBAE, with piezoceramic transducers, have a higher frequency spectrum that can go up to 1850 kHz [64]–[66]. The correlation between the acoustics emission signals and the penetration depth of the weld was studied by Shevchik et al. [64], Le Quang et al. [65] as well as Bastuck et al. [62]. Shevchik et al. [64] and Le Quang et al. [65] used SBAE sensors to detect keyhole porosity. In a following study, Wasmer et

al. [67] used a gradient booster ML algorithm to classify with good accuracy (from 74% to 95%) among stable keyhole weld, unstable keyhole weld, conduction welding and spatter generation. Saifi et al. [68] as well as Lee et al. [69] also used SBAE sensors to differentiate different qualities of weld. Lee et al. [69] employed artificial neural network (ANN) to classify three qualities of the weld (good weld, unsuccessful, and with defect). They claimed that the frequencies of interest range from 100 kHz to 500 kHz and that the low frequencies (<100 kHz) result from the fluctuation of the inner gas rather than from the welding process.

However, SBAE sensors do not acquire the same information as ABAE even though both can provide relevant guidance regarding the weld depth or quality [62]. The use of SBAE is more limited due to the difficulty and lack of reproducibility of the coupling to the workpiece. Most studies using ABAE correlate the AE signals with the weld penetration depth and they all agree to say that the differentiation between a good weld, a defective one or an insufficient penetration one comes from the evaporation dynamics and temperature gradients. In most cases, condenser microphones – with a frequency range of up to 50 kHz – are studied [70]–[77]. Some have a higher frequency ranging up to 100 kHz [78], 500 kHz [79] or 1200 kHz [62]. Based on the frequency analysis, the different studies establish ranges of frequencies correlated with defect formation or good welding. However, there is not a definitive consensus on which band of frequencies contains the information that can determine the quality of the welding. For Li et al. [80] the information lies between 0 and 50 kHz. Luo et al. [75] claim that a good weld can be detected from 10 to 20 kHz, while a weld having defect has a lower amplitude between 781 Hz and 1562 Hz. Mao et al. detected keyhole welding between 3 kHz and 9 kHz. Farson et al. [72], [81], Lee et al. [77], and Huang et al. [76] reported that the information of interest lies in frequencies ranging from 500 to 2000 Hz. Finally, Nava-Rüdiger et al. [73] studied the frequencies around 400-600 Hz where they correlate the increase in the amplitude of these frequencies to an increase of laser power leading to a larger penetration depth. Mao et al. [70], [78] and Gu et al. [71] used flat response microphones but the frequency responses of the other microphones was not specified. Gu et al. [71] and Bordatchev et al. [79] employed pattern recognition to differentiate weld classes and Luo et al. [75] and Huang et al. [76] used a designed ANN with a classification accuracy of up to 85%. However, it has to be noted that the presented studies investigate different alloys with or without coating, which could lead to a difference in the frequencies of interest.

In additive manufacturing processes, less research has been done so far on AE monitoring. Due to the presence of powder and gas flow, the laser-matter interactions are more complex and the processes are noisier. However, combined with machine learning (ML) solutions, this approach is gaining more and more interest and showing increasing capabilities for in-situ monitoring of regime changes and defects formation.

Two main studies of AE for monitoring of the LPBF process were performed without the use of ML. Ito et al. [82] used a SBAE sensor, a wireless piezoelectric with a flat response and a high sensitivity between 150 and 600 kHz, except at the resonance frequency of 250 kHz. They used the acquired signal to localize, with an error of few millimeters, keyholes and cracks in a nickel LPBF piece, based on the changes of amplitude in the time domain. Gutknecht et al. [83] investigated the use of a very sensitive ABAE, a XARION Eta250 Ultra

membrane-free microphone. Its sensitivity is 40 times higher than a camera and 15 times higher than a pyrometer. Its operating principle differs from that of a condenser microphone, as it consists in an optical microphone that utilizes the principle of interferometry to measure sound in a frequency range of 10 Hz to 1 MHz. They investigated the influence of the inclination of the sensor and the effect of its distance to the melt pool. Both factors induce a frequency-dependent dissipation. They consider that the frequencies below 40 kHz are noise and machine-related and filtered these frequencies with a butterwoth high-pass filter. This microphone has a high temporal resolution but is applicable only from 100 kHz because of reverberation in the build chamber. They detect millisecond phenomena at the higher frequency bands.

Taheri et al. [84], [85] as well as Eschner et al. [63] used SBAE monitoring sensors coupled with ML solutions to classify different regimes. Taheri et al. [84], for the monitoring of DED of Ti64, employed four piezoceramic transducers attached below the build plate, with a frequency range from 100-2000 kHz. They chose a K-means algorithms clustering for the classification of three conditions (optimal, low laser power and low powder feed). They obtained an 87% accuracy with a higher classification confidence in the higher frequency band (>800 kHz). Eschner et al. [63] monitored LPBF of stainless steel using a mass-less piezoceramic sensor with a frequency of up to 2 MHz. They used STFT spectrograms extracted from the acquired AE signals to train a designed ANN algorithm and classify three density classes with an averaged classification accuracy of 83%.

Shevchik et al. [86] used a Fiber Bragg Grating (FBG) for recording AE signals during LPBF of stainless steel CL20ES. The FBG sensor is an interferometric structure, imprinted inside the core of an optical fiber with unique spectral characteristics of reflectivity. The AE waves result in periodical extension/compression of the optical fiber core. These deformations affect the reflectivity properties of the FBG. Based on this principle, the variations in intensity of the reflected light encode the deformation states of the fiber core. These sensors can have a linear response in a frequency range of 0–60 GHz. They have a behavior similar to a piezoelectric sensor but are not placed in contact with the build plate and record the information from the waves propagation in the controlled atmosphere, as in the case of an ABAE sensor. In this study, the spectrogram from wavelet transform goes until 200 kHz and the information seems to be scattered below 100 kHz. They compared a classic Convolution Neural Network (CNN) and a Spectral NN and successfully classified with more than 85% confidence three classes: poor quality (LoF porosity), medium quality (keyhole pores) and high quality (conduction mode).

Ye et al. [87], [88] employed a microphone with a frequency response from 0 to 100 kHz to acquire AE from single lines scanned with a pulsed laser on a stainless steel 304 powder bed. Using a FFT analysis, they narrowed the range of frequencies below 65 kHz and managed to classify five categories – balling, slight balling, normal, slight overheating, overheating – with high confidence (above 90%). A deep-belief networks was chosen for the classification tasks.

Tempelman et al.[89] used as well a low-frequency-range microphone but the authors did not specify the frequency range of sensitivity. They studied the frequency distribution of the “no pores” and “keyhole” categories from 10 to 40 kHz. Support Vector Machine (SVM) with a window size down to 2.5 ms was used to detect keyhole and no-pores segments using process parameters scattered in the 2D processing map and with.

Drissi-Daoudi et al. [90] and Pandiyan et al. [91] employed a low-cost condenser microphone with a frequency range from 0 to 100 kHz but with a non-flat frequency response. The sensitivity of the acquisition was mainly around 10 kHz, 20 kHz, 40 kHz, and 80 kHz. With a feature analysis in the frequency domain, they could highlight that the frequencies of interest are below 60 kHz. Four ML algorithms were compared (Logistic Regression, Random Forest, Support Vector Machine and a CNN) for the classification of three process regimes (LoF pores, Conduction mode, and Keyhole pores) for three different alloys (stainless steel 316L, bronze, and Inconel). All algorithms classified the regimes with high accuracy (around 90%) for the three alloys. The authors selected two process parameters per regimes with specific normalized enthalpy to prove that the AE features extracted and used as inputs for training algorithms are related to the laser-material interaction and not to the difference of parameters. However, they proved that with this microphone the generalization of the classification from one alloy to the other was not possible. Finally, they designed a CNN capable of simultaneously classifying the alloy and the process regime.

CNN has become a common algorithm for classification tasks, demonstrating great efficiency and enabling the possibility of suppressing stationary noise [86], [90]. Drissi Daoudi et al. [92] proved that a CNN model trained with at least eight different processing conditions is able to predict the process regime for any unseen laser parameters within the processing map. They also proved that with a robust model, a decrease in the classification accuracy can help identify the boundaries between different processing regimes in the 2D processing map.

All presented works used frequency features analysis to identify the frequencies with higher intensity. However, the frequencies responsible for the classification of different categories by a ML algorithm are not investigated. In this work, we propose the use of saliency maps to perform this task. Saliency maps are often used for controlling the quality of a CNN model for image classification [93]. They have been employed for spectrograms from AE data, in the context of end milling for example [94], but never to determine if a model has learned the physical characteristics of a given regime or how to distinguish the different types of defect formation in LPBF (or other laser processes).

This work compares the classification accuracy of CNN models as well as the saliency maps, based on acoustic data obtained with two microphones with different frequency responses. We highlight the importance of frequency information in acoustic-emission-based monitoring and show how the analysis of saliency maps of a trained CNN can be an effective tool in determining the frequency footprints associated with three LPBF regimes (keyhole pores, conduction mode and LoF pores), as well as the quality of the CNN model.

7.2 Methodology and experimental plan

The experiments were performed on an in-house LPBF system, shown in Figure 76. The machine uses a continuous wave modulated Ytterbium laser (1070 nm wavelength) with a maximum power of 500 W and a Ray-lase triaxial scan-fiber scanning head. The process can reach scanning speeds of up to 20 m.s⁻¹. The beam has a measured diameter of 42 µm (1/e²) at the focal plane. For this work, the build chamber is equipped with two microphones, as shown in Figure 76: a PAC AM41 (Physical Instrument, Germany) airborne acoustic sensor (used in previous studies [90]) and a CM16/CMPA40-5V ultrasound microphone (Avisoft Bioacoustics). Both are placed on the top of the build chamber, with the recording face directed to the process zone in order not to disturb the deposition system and to be protected from powder, spatters and fumes. AE sensors are placed at approximate distance of 23 cm from the center of the substrate. An Advantech Data Acquisition (DAQ) card (Advantech, Taiwan) acquires the output from the microphones. The acquisition rate of DAQ is set to 0.6 MHz, ensuring the satisfaction of Nyquist Shannon theorem [95]. Data acquisition is triggered by the laser start, providing synchronization of LPBF and recorded AE.

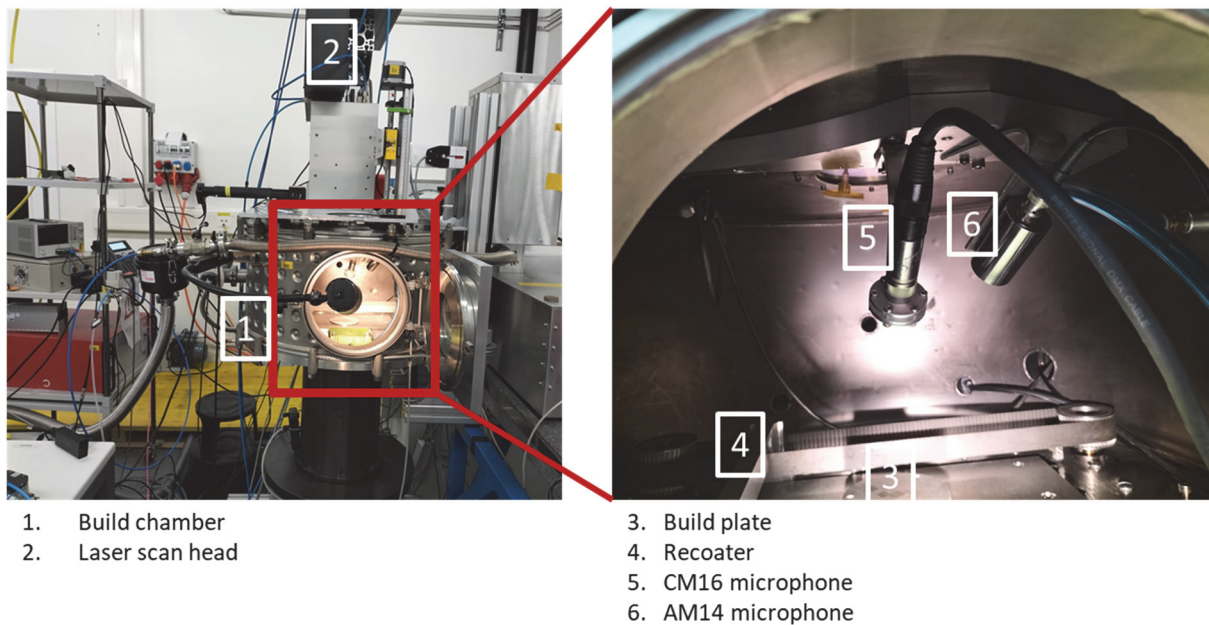


Figure 76. Experimental set-up of the custom-built LPBF with the CM16 and the AM41 microphones

The printed alloy is stainless steel MetcoAdd 316L micro powder (Oerlikon) with a particle size between 15 µm and 45 µm (composition in Table 23).

Table 23. Chemical composition of stainless steel 316L powder

Fe	Cr	Ni	Mo	Other	C
Balance	18	12	2	<1.00	<0.03

The metallurgical states of the printed material are distinguished by 3 categories or regimes: *keyhole pores*, *conduction mode*, and *LoF pores*. In addition, a fourth category is defined as the noise of the process when the laser is off. Thirteen cubes of 13x13x3 mm with thirteen different processing parameters, reported in Table 24, were printed for each category. This design of experiment is also presented and detailed in [92]. An example of the microstructure of each category is shown in Figure 77.

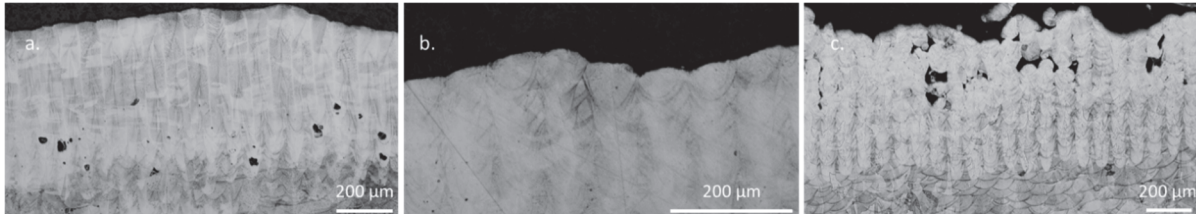


Figure 77. Typical example of microstructure of the three regimes, a. Keyhole pores, b. Conduction mode, c. LoF pores.

For a better visualization, the parameters used for the building of each sample are represented in the 2D processing map in Figure 78. The black point (parameter set n°13) in each domain is called the central point and corresponds to the unseen parameter set, while the 12 other points (n°1 to 12) compose the training databases for ML algorithms built from AE recorded with both microphones.

Table 24. Process parameters (laser power and speed) used for the experimental plan for the three categories (keyhole pores, conduction mode, and LoF pores). The sample 13 in bold is the central point, unseen by the training of the ML algorithm (in black in Figure 78).

N°	Keyhole pores		Conduction mode		LoF pores	
	Power [W]	Speed [mm/s]	Power [W]	Speed [mm/s]	Power [W]	Speed [mm/s]
1	282	350	107	450	68	450
2	267	350	96	450	64	450
3	235	350	82	450	57	450
4	220	350	71	450	51	450
5	251	276	89	350	61	358
6	251	310	89	400	61	400
7	251	398	89	500	61	500
8	251	457	89	550	61	550
9	240	320	85	410	59	430
10	245	333	87	432	60	443
11	256	364	91	466	61	457
12	261	378	93	490	62	470
13	251	350	89	450	61	450

For each cube, a 1 mm support structure is printed on top of which a 2 mm thickness is built, with a low porosity content. Then, 10 layers of 110 overlapping line tracks were processed with the parameters listed in Table 24, and the acoustic signals of these lines were recorded with both microphones simultaneously. A total of 1100 acoustic signals were acquired per sample. Twelve parameter sets (samples 1 to 12) are taken in the ML training set, resulting in 13'200 signals in each category. The scanning strategy was unidirectional and parallel with a hatching distance of 0.1 mm and a layer thickness of 40 μ m.

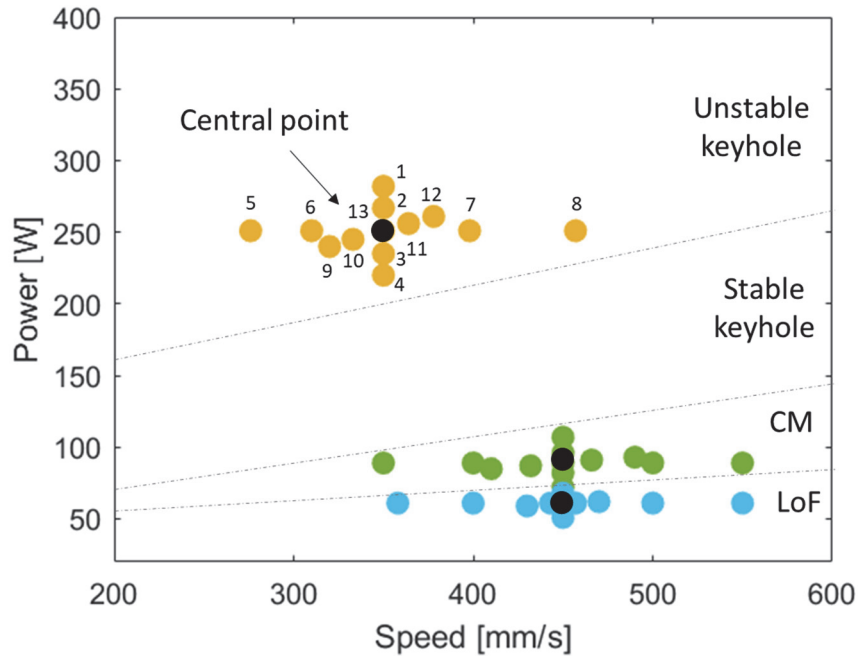


Figure 78. Process parameter map with thirteen parameter sets for each category, in yellow for the keyhole domain, in green for the conduction mode, and in blue for LoF pores. The parameter sets are numbered from 1 to thirteen for the keyhole pores domain. The same numbering strategy can be transferred to the two other domains. The “central point” (i.e. the set unseen by the ML training) is depicted in black. The dotted line represents the limits of each process regime domain.

Between each recorded line, a one-second delay is applied to ensure that all lines are independent of the thermal history. A pre-delay of 0.03 ms is applied to guarantee that the AE signal is recorded over the complete line. 27'000 data points are acquired for the *keyhole* category, 21'000 for the *conduction mode* and 18'000 for the *LoF pores* category. The first 3'000 points were removed from all AE signals and only the 10'000 following points were kept, so that the non-steady state conditions (when the laser has not yet reached the required velocity and speed) are removed from the analysis. An example of a keyhole line recording is given in Figure 79. It presents the signals recorded with both microphones as well as the triggering laser signal. The analyzed signals have the same duration and number of acquisition points. It can be seen that the CM16 is more sensitive than the AM41 microphone.

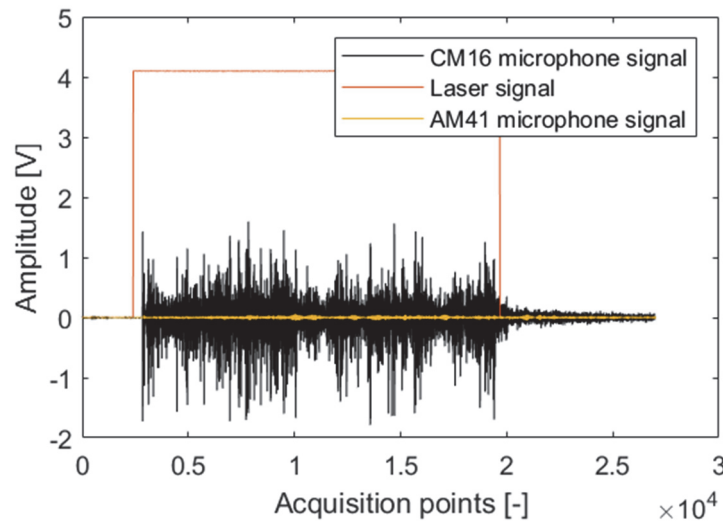


Figure 79. Signal of an LPBF scan line with keyhole pores generation parameters. In black the signal recorded with the CM16 microphone, in yellow with the AM41 microphone and in orange the laser voltage signal used as trigger for data acquisition.

The CNN models were developed with pyTorch library (Meta, USA). For all signals, the spectrograms were extracted from acoustic signals using the span of 16 ms. The training of the optimized CNN was performed on 80% of the 13'200 signals per category, which were randomly chosen, while the validation of the model performance was done on the remaining 20%. The model was then tested on 1100 signals of the central black point in Figure 78, corresponding to completely unseen conditions by the trained algorithm. The labeling of each category was done by metallographic analysis of each sample's cross section (Figure 77). To reveal the melt pool morphology, the samples were etched with diluted Aqua regia (100 mL HNO₃, 100 mL HCl, 100 mL H₂O) for 30 s.

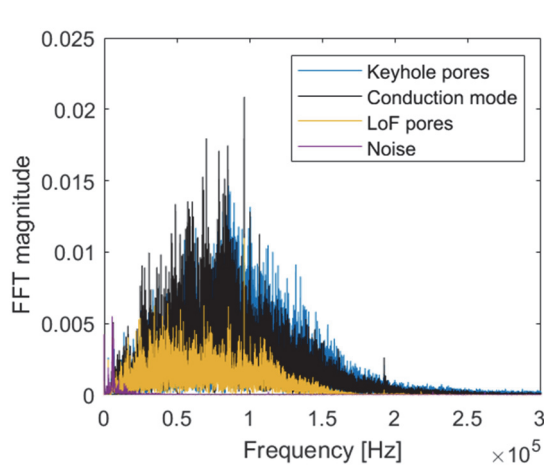


Figure 80. FFT responses of the averaged AE signals for each category, recorded by the CM16 flat frequency response microphone

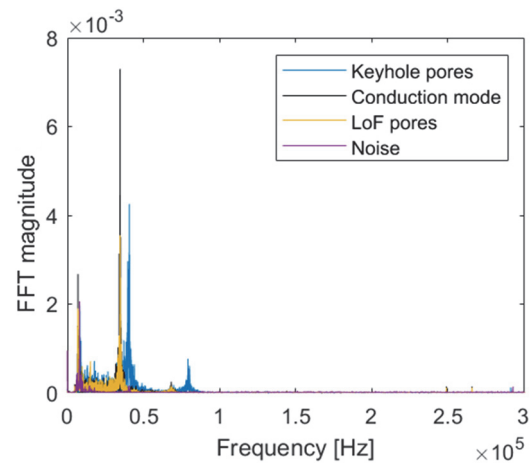


Figure 81. FFT responses of the averaged AE signals for each category, recorded by the AM41 microphone.

Figure 80 and Figure 81 represent the Fast Fourier Transforms (FFT) of signals from the four categories, either using the CM16 or the AM14 microphone. The CM16 microphone has a flat response from 0 to 200 kHz. It is however polarized for the higher frequencies. The AM41 microphone acquires information principally from 0 to 20 kHz, and around 40 kHz and 80 kHz.

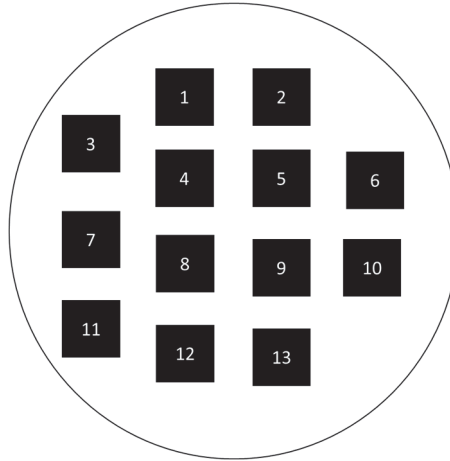


Figure 82. The position in the base plate of the 13 samples (see Table 24 for the corresponding process parameters). The positions are the same for the three printed metallurgical regimes (keyhole pores, conduction mode and LoF pores).

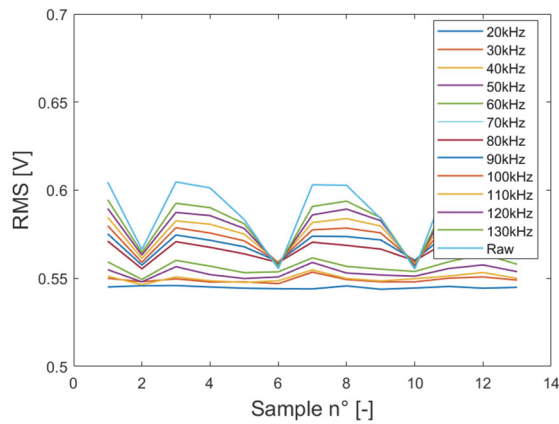


Figure 83. RMS for different low pass filter frequencies (from 20 kHz to 130 kHz), for the keyhole pores category.

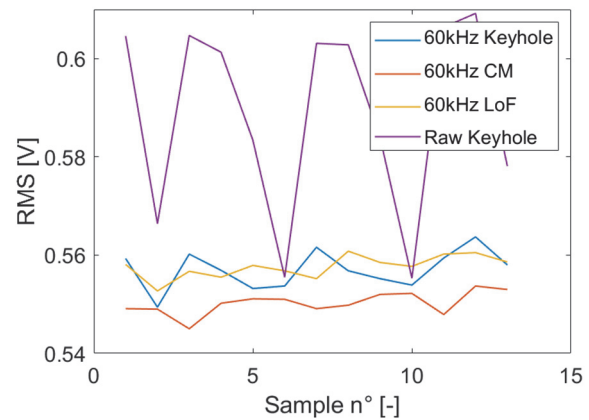


Figure 84. RMS for the three regimes categories (keyhole pores, conduction mode and LoF pores) when all the samples are filtered with a low pass filter at 60 kHz, compared to the raw signal of the keyhole pores category

The Root Mean Square (RMS) of signals for each sample is calculated for different low pass filter frequencies (from 20 kHz to 130 kHz) for the keyhole pores category, and represented in Figure 83. The influence of the position of the samples on the substrate on the quality of the acquired signals is highlighted. Each process regime or category (thirteen cubes) was printed on a different substrate. The position of the samples on the substrate are shown in Figure 82. For the cubes 2, 6 and 10, when no filter is applied, the RMS is significantly lower than for the other cubes. When the filter threshold is around 60 kHz, the RMS becomes stable enough

across all samples for the three categories (Figure 83 and Figure 84). In light of this analysis, two post-processing approaches of the signal for the CM16 microphone are studied. In the first case, the CM16 signals are only normalized (between 0 and 1). The result is then compared with an algorithm trained with signals filtered with a low pass filter at 60 kHz, downsampled 4 times, and normalized. In these conditions, the database associated to the CM16 microphone is position-independent. The AE signals of the AM41 microphone are filtered with a low pass filter at 90 kHz (as no data is recorded above this frequency), then downsampled three times, and finally normalized.

An additional experiment was conducted by printing two adjacent lines with different parameters, and recording the AE signals as one single line on the top layer of a cube. The first line is built with the parameters of the central black point of the keyhole pores category (251 W and 350 mm/s) while the second line is built with the parameters of the central black point of the conduction mode (89 W and 450 mm/s). Figure 85 shows the recording of one of these double lines, with a time delay of 1.6 ms when the laser stops between the two lines. The micrographs of the cross-section of each part of this double-line are presented as well in Figure 85. A total of 546 of such double-lines were recorded. The aim of this experiment was to validate the quality of the trained model. If the AE features associated to the formation of pores are successfully learned by the model, the regimes of these lines should be predicted with a high confidence as belonging to the keyhole regime. Indeed, in keyhole regime the characteristics of the conduction mode are present as well, so the classifier should recognize the characteristic features of the keyhole mode in the first half of the signal and classify the whole as keyhole accordingly. It can be noted that no evident differences can be noticed between the two half of the signal.

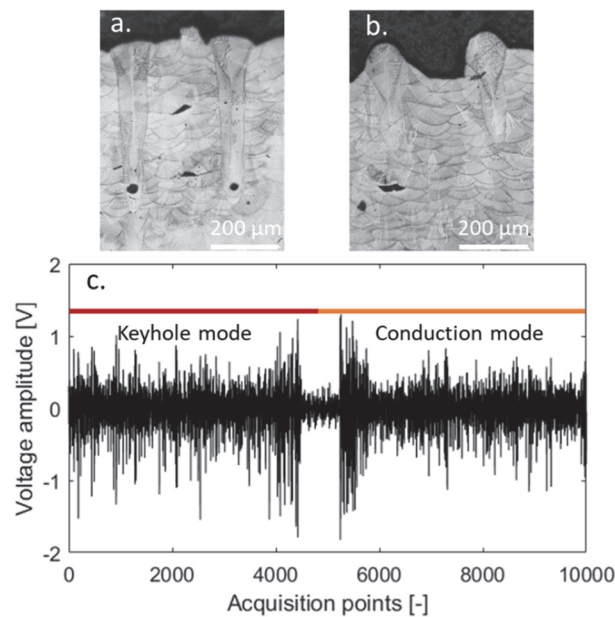


Figure 85. Scheme of the double line experiments. Two adjacent LPBF lines with different laser parameters are recorded as one line. The first line in red in c. is built with the parameters of the central black point, in Figure 78, of the keyhole pores category (251 W and 350mm/s). The second line in orange in c. is built with the parameters of the central black point of the conduction mode (89 W and 450 mm/s). a. Micrograph of the keyhole part of the line, b. micrograph of the

conduction mode part of the same line and c. raw acoustic signal acquired with the CM16 microphone for one of these double-lines. No evident differences can be noticed between the two half of the signal.

Saliency maps are used to determine the distinct frequencies that provide efficient classification, and to evaluate the quality of the trained model. A saliency map is defined as the partial derivative of the network output S_c with respect to the input x (Equation 1). In other words, the saliency of every input data point is defined as how big the influence of the data point on the outcome of the classifier. The bigger the saliency of a data point, the bigger the change the output undergoes if the data point is changed. Hence, the results of the saliency is a possible explanation for the model decision. [96], [97]

$$M_c(x) = \frac{\delta S_c}{\delta x} |_{x=x} = \nabla_x \max(out_{units}(x)) \quad (1)$$

where S_c is the saliency score function for each label candidate. The derivative is computed for the maximally excited output unit $out_{units}(x)$.

To highlight the frequencies that consistently remain in the saliency map even by adding noise, we calculated the average gradients of signals resulting from the addition of Gaussian noise to the input..

$$\hat{M}_c(x) = \frac{1}{n} \sum_{k=1}^n M_c(x + \epsilon_k), \epsilon \sim \mathcal{N}(0, \sigma^2). \quad (2)$$

For $k \leq n$, the k -th noise is denoted by ϵ_k , σ being the noise level.

The average gradient of 200 iterations with a Gaussian noise level of 0.001 is used to remove the noise of all saliency maps presented in the rest of this work.

Four criteria were considered to determine the quality of a CNN model:

- An accuracy of classification in validation and in test higher than 80%;
- Stabilization of the loss function;
- Saliency maps highlighting specific frequencies for the three process regimes while being undetermined for the noise category;
- Classification of the double line experiment as keyhole, with saliency results distinguishing the conduction mode zone from the keyhole mode zone.

7.3 Results

The analysis of recorded AE signals is reported below, considering two microphones with two different frequency responses (Figure 80 and Figure 81) and technology. The AM41 is a transducer microphone with an enclosed diaphragm and the CM16 microphone is a condenser microphone with an externally polarized film diaphragm.

7.3.1 AM41 microphone

The CNN architecture is illustrated in Figure 86. It includes two 2D convolution layers max pooled by 2x2 followed by one 2D convolution layer. The Rectified Linear Units (ReLU) activation function is applied for three convolution layers. Two fully connected layers follow these layers. The model is trained for 200 epochs with a batch size of 1000, a learning rate of 5e-4 and an Adam optimizer [98].

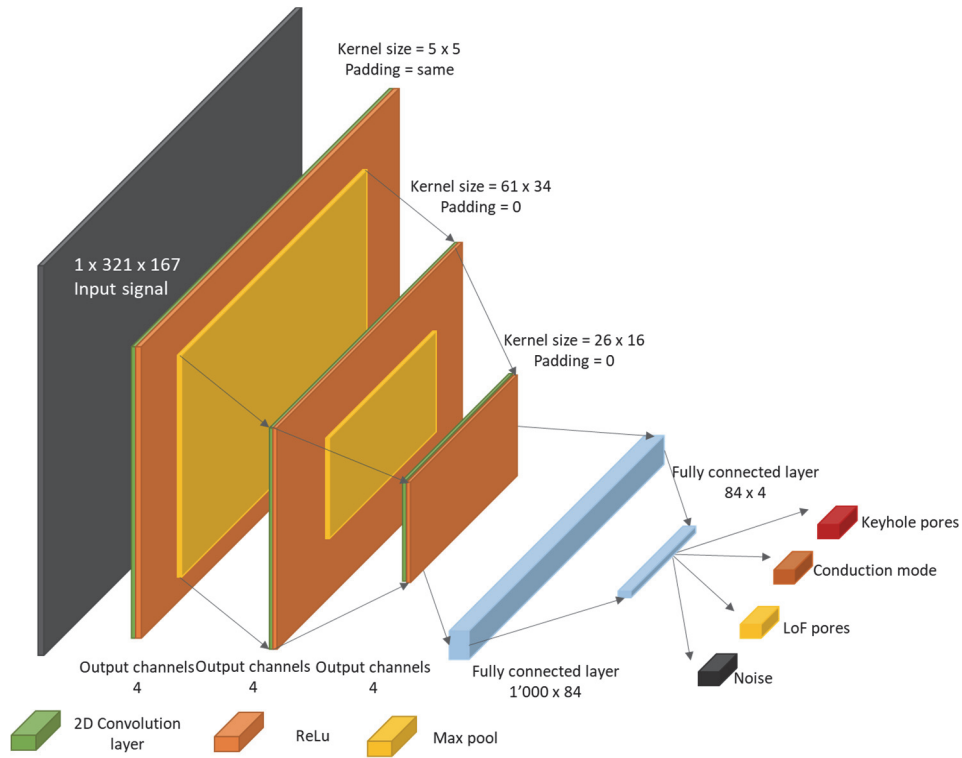


Figure 86. Scheme of the CNN architecture with two max pooled convolution layers, followed with one convolution layer and 2 fully connected layers.

Figure 87 presents the losses of the training and validation over the training epochs. It can be seen that they stabilize after 150 epochs. The losses are of the same order magnitude, implying that the model does not seem to be overfitting.

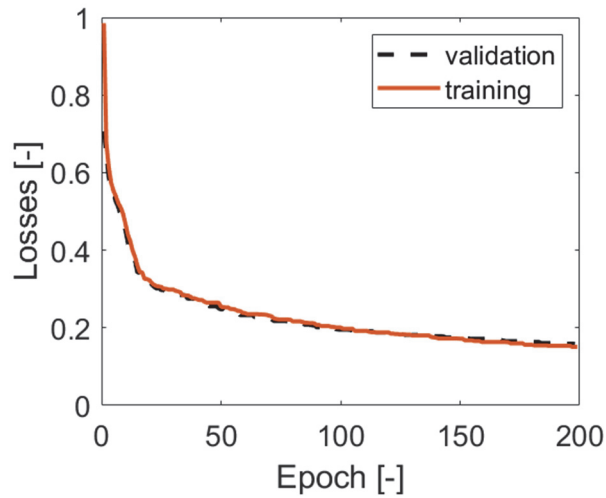


Figure 87. Validation and training losses in function of the epochs for the model Figure 86 trained for 200 epochs.

Table 25 presents the confusion matrix of the classification of the four categories (*keyhole pores*, *conduction mode*, *LoF pores*, and *noise*) on the 13th sample (central black point in Figure 78) of each category, unseen by the training. The accuracy, in %, (diagonal values, in bold in Table 25) is defined as the number of true positives divided by the total number of tests in each category. The misclassifications are the false positives and false negatives divided by the total number of tests in each category. The classification accuracy is very high (> 91%) for all categories.

Table 25. Confusion matrix of the CNN model (Figure 86) applied to the prediction of the process regime of the central black point in Figure 78, with the AM41 signals

Classification accuracy [%]	Ground truth			
	Keyhole pores	Conduction mode	LoF pores	Noise
Keyhole pores	92	8	1	0
Conduction mode	6	91	0	0
LoF pores	2	1	99	0
Noise	0	0	0	100

Figure 88 provides a typical spectrogram of one signal of each category of the tested set, the unseen parameter set (n°13, Table 24). Figure 88 also presents the average as well as the standard deviation of the saliencies of the 1100 signals in each category of the tested unseen parameter set.

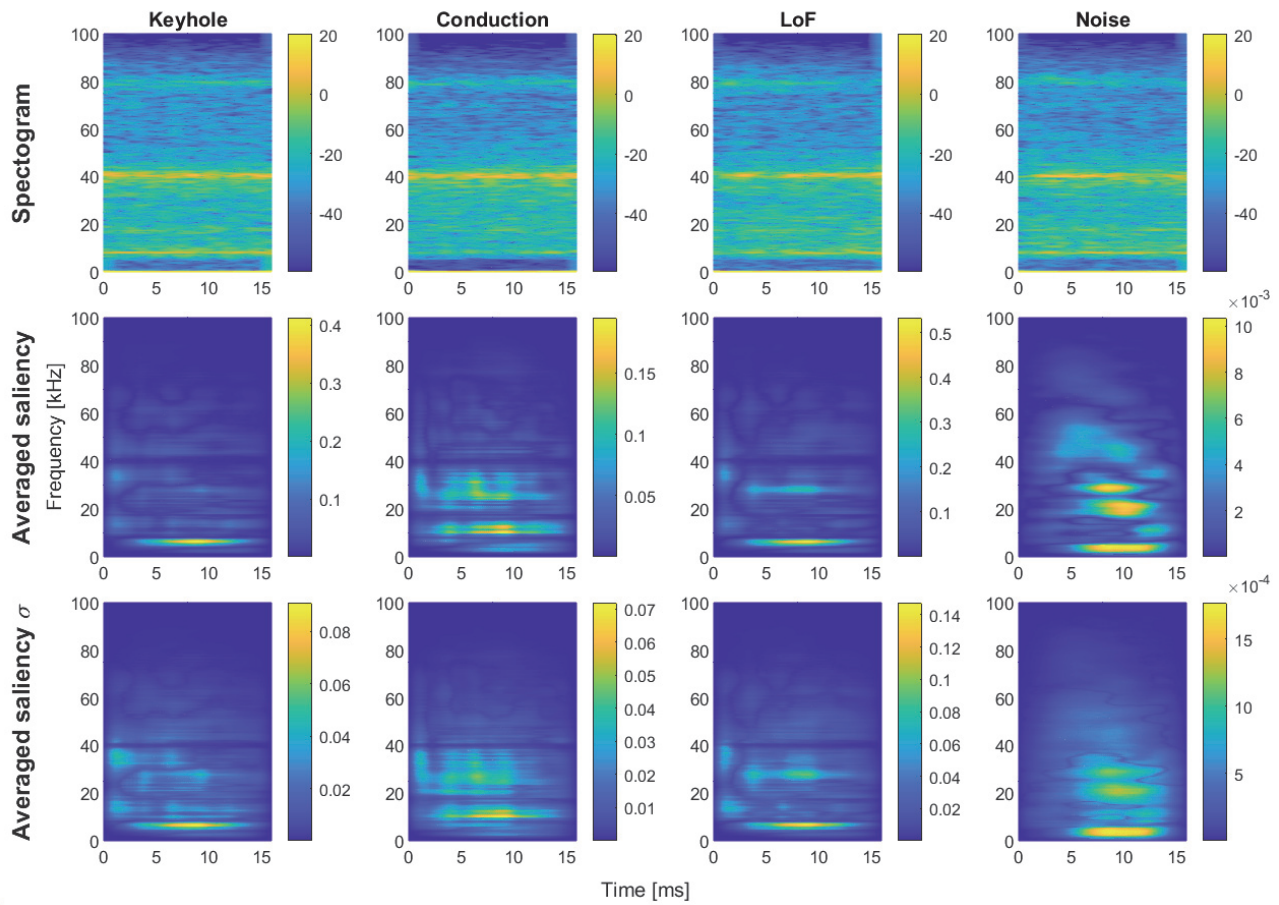


Figure 88. Example of a spectrogram of one signal of each category (keyhole pores, conduction mode, and LoF pores) of the unseen parameter tested set with averaged the saliencies of the 1100 signals in each category of the unseen parameter tested set (central black point) as well as its standard deviation σ for the CNN model (Figure 86) trained with the AM41 signals.

As expected from the frequency response of the AM41 microphone, the spectrograms show that the signals are mostly recorded around 80 kHz, 40 kHz, 18 kHz, and 9 kHz. In the saliency maps, it can be seen that for all categories, the frequencies that seem to provide efficient classification lie below 40 kHz. The saliency of the keyhole pores indicates that the important frequencies range between 6 and 8 kHz. In the case of the conduction mode, the relevant frequencies are around 10 kHz, 12 kHz, and in the [21-35] kHz range. The frequencies of high importance for the formation of the LoF pores are a bit below those observed for the keyhole regime, namely in the range of 5 to 7 kHz and around 30 kHz. For the background noise, as expected, the saliency maps display all frequencies scattered below 40 kHz. The saliency standard deviations confirm that similar frequency ranges hold for the majority of the 1100 signals of each category. However, it can be observed that, for the three metallurgical regimes, the frequencies of higher importance for the classification are not in the ranges of sensitivity of the AM41 [90], [91]. Several CNN models have been trained and none performed the classification – according to the saliency maps – based on frequencies inside the high sensitivity range of the microphone. In addition to the information gathered on these frequencies, the algorithm also for other frequencies to highlight differences between the classes.

The trained model was tested on 547 double-lines described in Figure 85, and 87% (Table 26) of those lines were successfully classified as keyhole, when compared to the same conduction and LoF experiments considered in Table 26. Only 5% of accuracy was lost (87 versus 92%). Figure 89 presents the average saliency maps of these double-lines, assuming the conduction mode. It appears to be consistent with the experiments and with the frequencies highlighted in Figure 88. In particular, the high saliency values are, as expected, in the second line.

Table 26. Confusion matrix equivalent to Table 25, but replacing the keyhole pores tested category by the double-lines experiments presented in Figure 85

Classification accuracy [%]	Ground truth			
	Keyhole pores	Conduction mode	LoF pores	Noise
Keyhole pores	87	8	1	0
Conduction mode	9	91	0	0
LoF pores	4	1	99	0
Noise	0	0	0	100

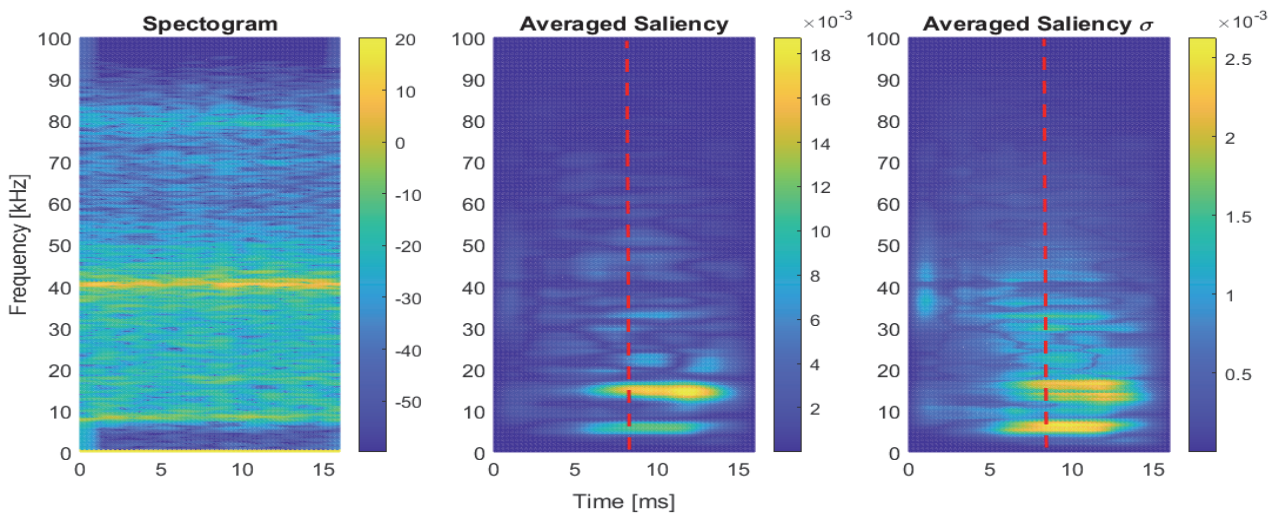


Figure 89. An example of the spectrogram of one double-line AE signal, the averaged saliency maps of the 547 recorded double-lines assuming the conduction mode, and their standard deviation σ .

7.3.2 CM16 microphone

i. Raw data model

The results presented in the previous section motivate the use of a flat response microphone. The frequencies that have the most influence in the model trained with the narrow wide frequency response microphone for the classification were in regions of least sensibility of the microphone. The use of flat response microphone will avoid to the classifier to be biased and to discard frequencies present in all categories. As a first study of the acquisition signals obtained with the CM16 microphone, a CNN model trained and tested on the spectrograms

extracted from the raw signals is presented schematically in Figure 90. It includes two first 2D convolution layers with the first layer max pooled by 2x2. Three fully connected layers are following these layers. The Rectified Linear Units (ReLU) activation function is applied for the two convolution layers and the first fully connected one. The model is trained for 50 epochs with a batch size of 1000, a learning rate of 5e-4 and an Adam optimizer. The losses of the training and validation classification are presented in Figure 91, and it can be seen that they stabilize and that the model does not overfit.

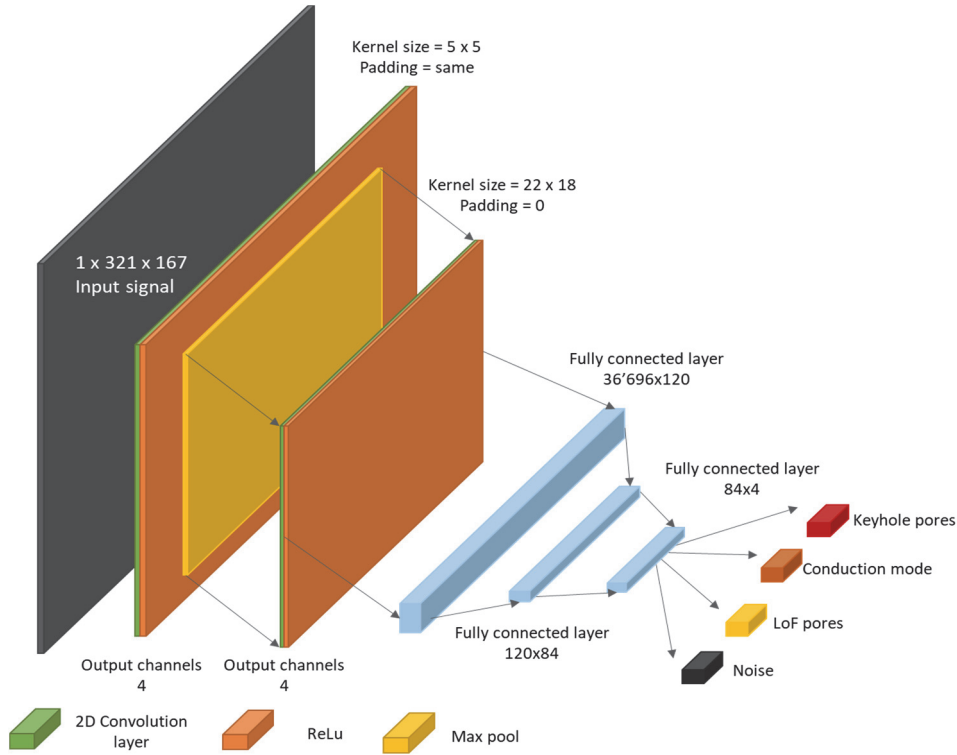


Figure 90. Scheme of the CNN architecture with one max pooled convolution layer, followed with one convolution layer and 3 fully connected layers.

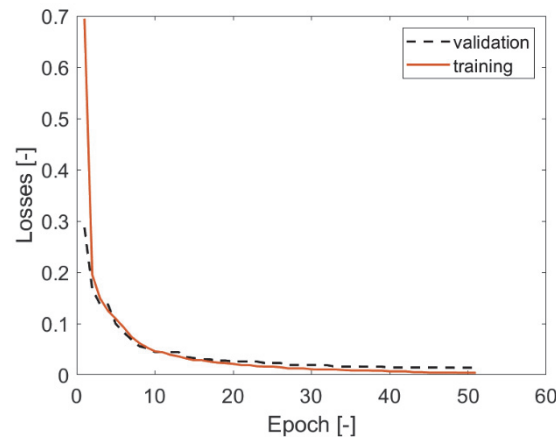


Figure 91. Validation and training losses in function of the epochs for the model Figure 90 trained for 50 epochs.

Table 27 presents the confusion matrix of the classification accuracies when trying to predict the process regime of the central black point (Figure 78) for each category, unseen by the training. The classification accuracy is very high ($>97\%$).

Table 27. Confusion matrix of the CNN model (Figure 90) for the prediction of the process regime of the unseen central black point (Figure 78), with the CM16 raw signals

Classification accuracy [%]	Ground truth			
	Keyhole pores	Conduction mode	LoF pores	Noise
Keyhole pores	97	0	0	0
Conduction mode	3	100	0	0
LoF pores	0	0	100	0
Noise	0	0	0	100

Figure 92, as did Figure 88 for the other microphone, presents a typical spectrogram as well as the average and standard deviation of the saliency maps, for each category of the model trained, tested on the unseen parameter set (black central point Figure 78).

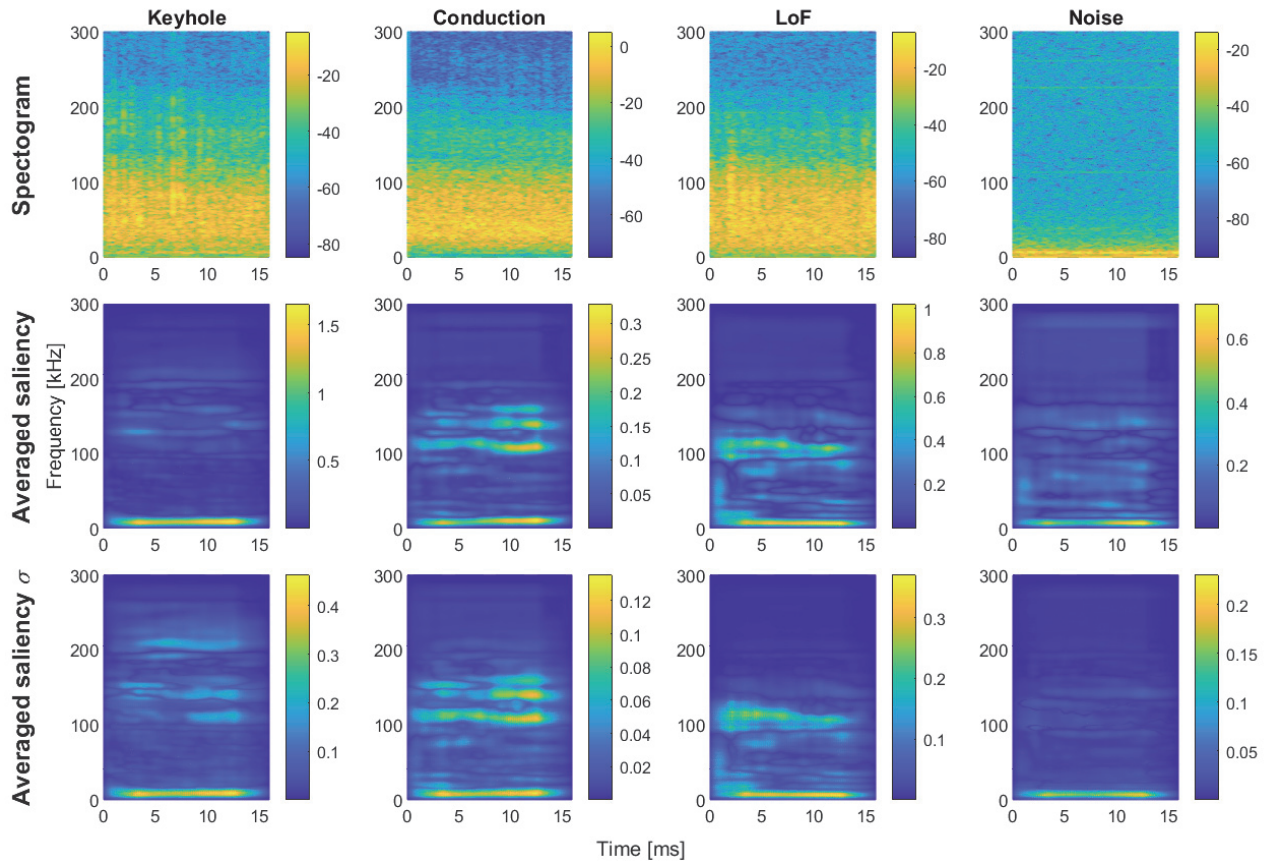


Figure 92. Example of a spectrogram of one signal of each category (keyhole pores, conduction mode, and LoF pores) of the unseen parameter tested se (black central point Figure 78) with the averaged saliency values of the 1100 signals in

each category of the unseen parameter tested set (black central point Figure 78), as well as their standard deviation σ , for the CNN model in Figure 90 trained with the CM16 raw signals.

The spectrograms of the conduction mode and the keyhole pores regime seem closer to each other than that of the LoF category. Indeed, the information present in the conduction mode is also present in the keyhole mode. It can be seen that the frequencies highlighted by the saliency maps are mostly from 5 to 12 kHz for the four categories, with some intensity changes. Higher frequencies are highlighted around 110 kHz and 140 kHz for the conduction mode classification, these frequencies are as well underlined for the keyhole pores but at lower intensity compared to the 12 kHz range. For the LoF pores category, frequencies around 112 kHz are emphasized. The noise category saliency maps highlight only the frequencies from 5 kHz to 12 kHz, which can be an indication of a bad model quality despite the high classification accuracy. In fact, no specific frequency should be highlighted by the saliency map for the noise category because there is laser-matter interaction present in this category.

A low-pass filter with threshold at 60 kHz was applied to the spectrograms of the tested signals. The trained model was then tested on the resulting spectrograms. Table 28 displays the confusion matrix of the test performed on the central black point (Figure 78), unseen in the training. The classification accuracies are high, above 89%, indicating that the interval of frequency below 60 kHz contains enough features to classify with high confidence the four categories.

Table 28. Confusion matrix of the CNN model presented in Figure 90 on the tested central point, when the data is treated with a low pass filter at 60 kHz.

Classification accuracy [%]	Ground truth			
	Keyhole pores	Conduction mode	LoF pores	Noise
Keyhole pores	89	0	0	0
Conduction mode	9	99	0	0
LoF pores	1	1	100	0
Noise	0	0	0	100

Figure 93 presents the averaged saliency maps for the four categories when the trained CNN model of Figure 90 is tested on the unseen sets with the 60 kHz low-pass filter. The saliency maps are very similar to the ones presented Figure 92. Even the high frequencies highlighted for the conduction mode occurrence in Figure 92 are also highlighted in Figure 93, despite the filtering.

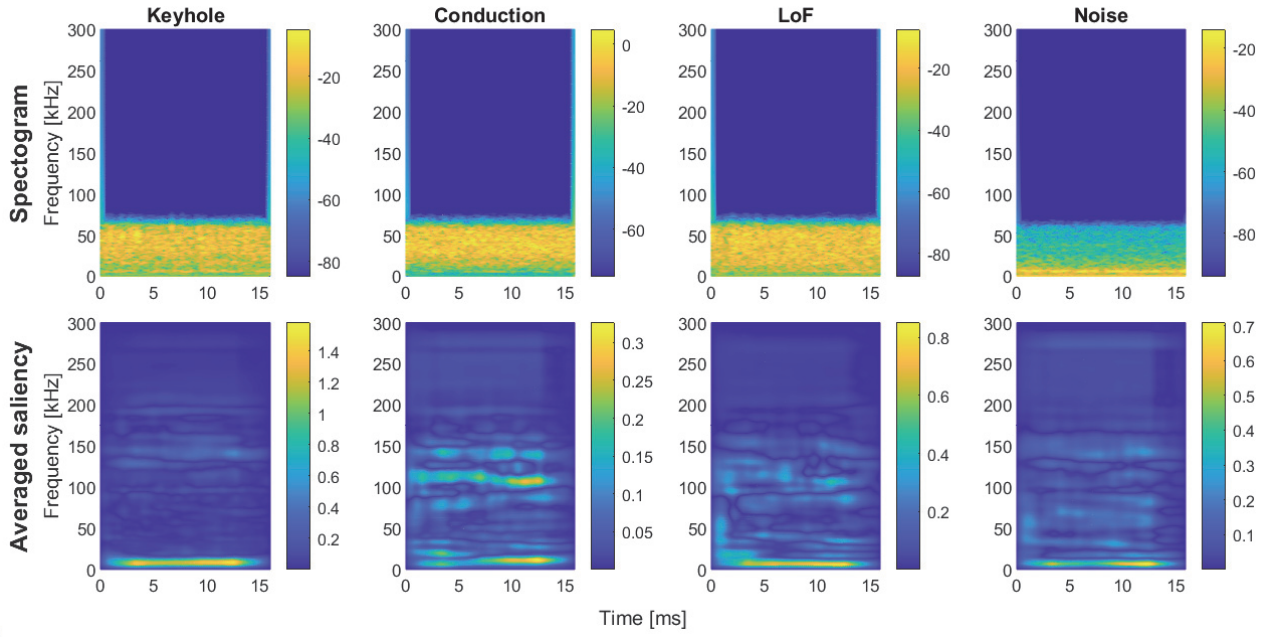


Figure 93. aA example of a spectrogram of AE signal filtered with a low pass filter at 60 kHz of the tested set. The average saliency maps of the tested category keyhole pores, The average saliency maps of the tested category conduction mode, The average saliency maps of the tested category LoF pores, The average saliency maps of the tested category noise.

ii. Filtered at 60kHz, four times downsampled, and normalized model

Another CNN model is trained with all the data filtered with a low pass filter at 60kHz, down-sampled four times to avoid aliasing, and normalized between 0 and 1. As the microphone is polarized above 60 kHz, the aforementioned signal post-processing was chosen to lead to signals for all samples in the substrate to be position independent. This signal processing ensures that the data is sample-position-independent and allows the frequency resolution to be increased. Moreover, the normalization ensures that the model classifies on the basis of the features responsible for the formation of a given metallurgical state rather than on the difference in process parameters between different categories (especially the power variations, which are known to induce differences in signal amplitude).

The architecture of a bigger model is presented in Figure 94. Five 2D convolutions layers with ReLU function activated and batch normalized are present in this model. They are followed with three fully connected layers. The losses stabilize after 15 epochs (Figure 95). The confusion matrix in Table 29 shows high classification accuracy for each category.

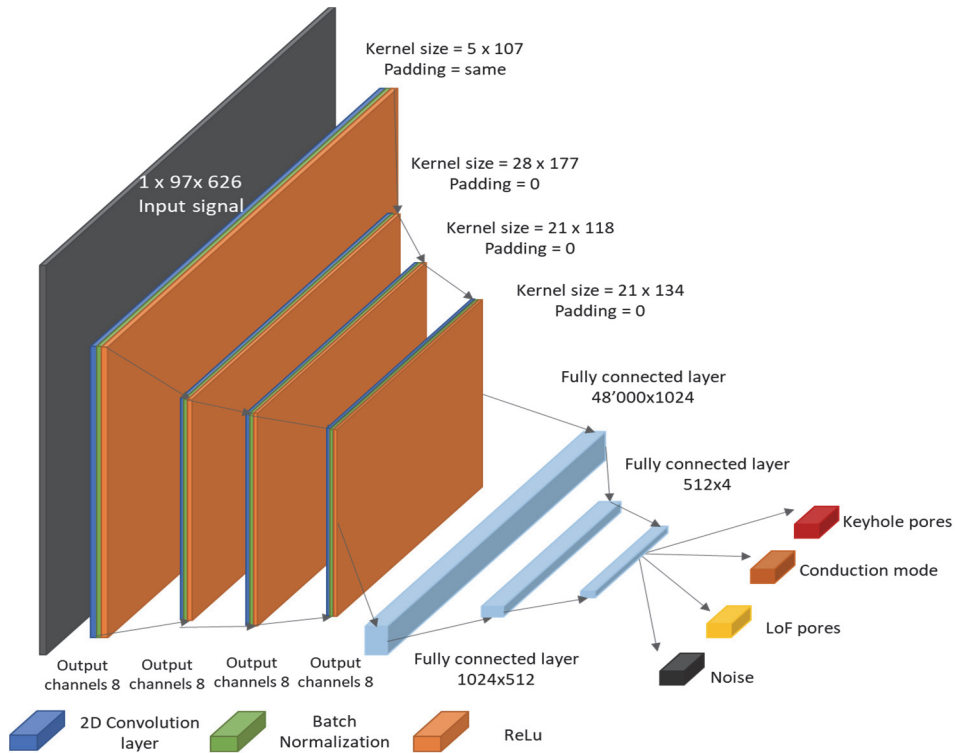


Figure 94. Scheme of the CNN architecture with four convolution layer folowed by 3 fully connected layers.

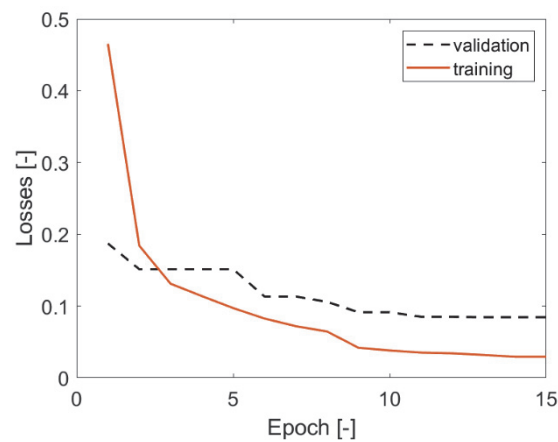


Figure 95. Validation and training losses in function of the epochs for the model of Figure 94 trained for 15 epochs.

Table 29. Confusion matrix of the CNN model Figure 94 on the tested central sample with the CM16 signals, filtered with a low pass filtered at 60 kHz, downsampled 4 times and normalized.

Classification accuracy [%]	Ground truth			
	Keyhole pores	Conduction mode	LoF pores	Noise
Keyhole pores	98	2	1	0
Conduction mode	1	98	2	0
LoF pores	1	0	97	0
Noise	0	0	0	100

Figure 96 presents a spectrogram of each category of the central black point conditions (Figure 78), as well as the average saliency maps and their standard deviation. It can be observed that no specific frequencies are highlighted in the noise category. For the three other regimes, the main frequency ranges responsible for classification lie below 30 kHz. For the keyhole pores, the main frequency is around 5 kHz, although the frequencies around 13 kHz and 20 kHz seem to be decisive as well. For the conduction mode, the frequencies emphasized for the classification are around 9-10 kHz. In the case of the LoF pores classification, the saliency maps underline mainly two frequencies, namely 4 and 8 kHz. The standard deviations confirm that the emphasized frequencies are common to all signals in the tested conditions.

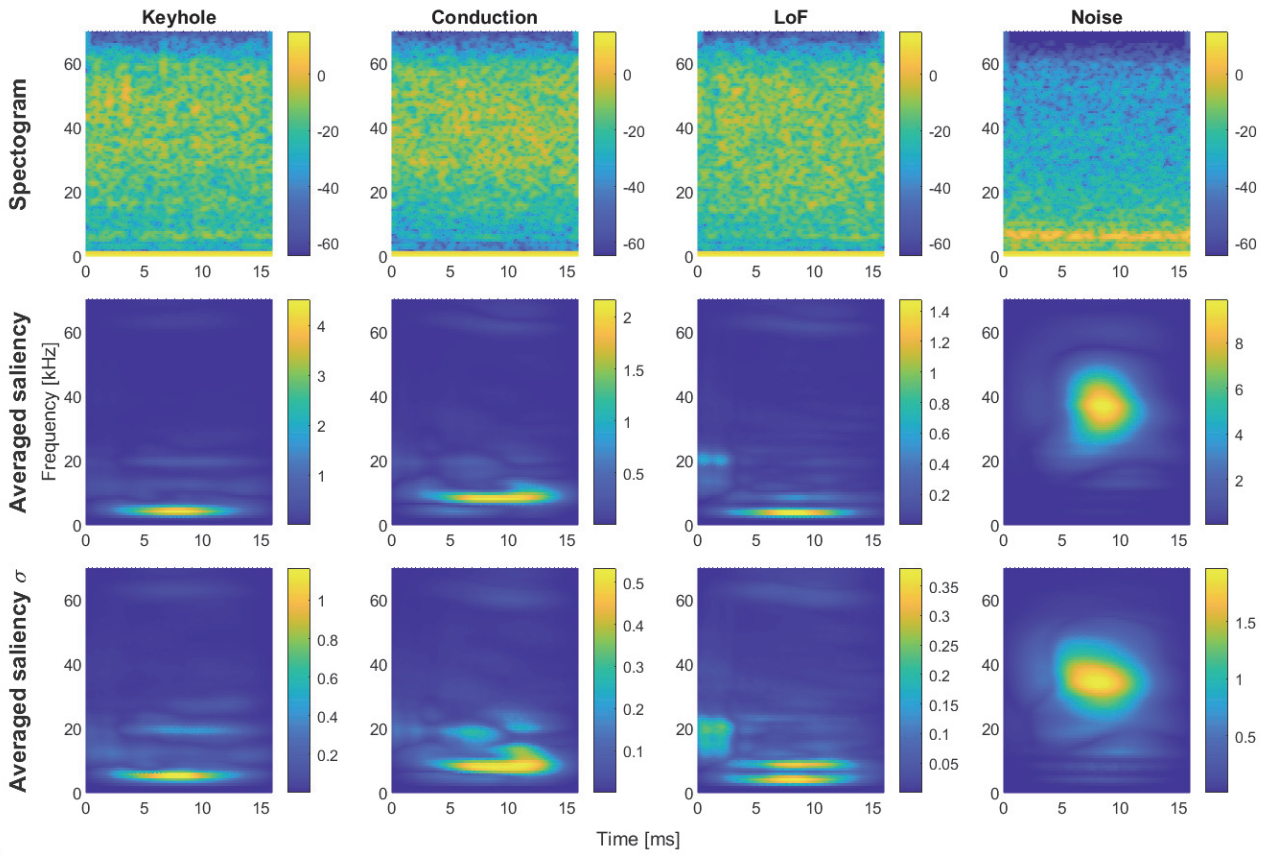


Figure 96. Example of a spectrogram of one signal of each category (keyhole pores, conduction mode, and LoF pores) of the unseen parameter tested set (black central point Figure 78 with saliencies averaged over the 1100 signals in each category, and the corresponding standard deviations σ for the CNN model described in Figure 94, trained with the CM16 signals, filtered with a low-pass filter at 60 kHz, downsampled 4 times and normalized.

This model is tested on the spectrograms extracted from the signals of the 2 lines experiments (Figure 85), as was done in Table 26. In Table 30 it can be seen that these lines are classified with a good accuracy of 92%, compared to the other conduction mode and LoF experiments. The accuracy is 5% better than with the other microphone (Table 26). Figure 97 displays an example of a spectrogram of one double-line recorded with the CM16 microphone with the same AE signal post-processing as for the training data, along with the average and standard deviation of the saliency maps when assuming the conduction mode. The saliency maps show

higher values on the second half of the line where the conduction mode was processed. The frequencies are scattered between 5 and 30 kHz. While the model has learned correctly how to differentiate the conduction mode zone from the keyhole zone, it still classifies the whole scan line as keyhole pores due to the first half processing conditions.

Table 30. Confusion matrix of the CNN presented in Figure 94, for the prediction of the process regime between double-lines experiments and conduction and LoF experiments (corresponding to the black central point in Figure 78).

Classification accuracy [%]	Ground truth			
	Keyhole pores	Conduction mode	LoF pores	Noise
Keyhole pores	92	2	1	0
Conduction mode	5	98	2	0
LoF pores	3	0	97	0
Noise	0	0	0	100

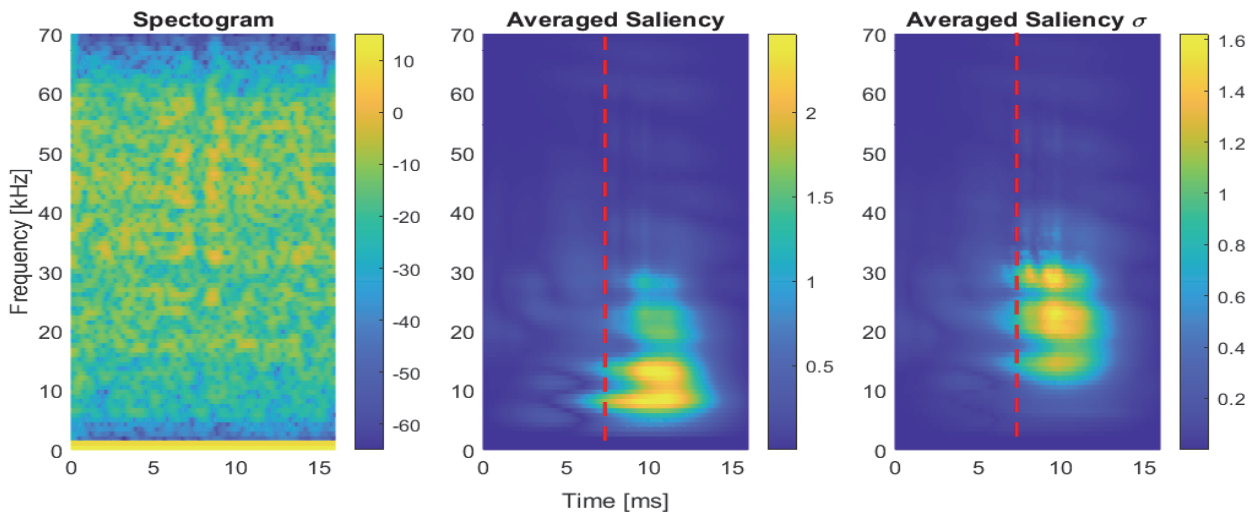


Figure 97. An example of the spectrogram of one double-line AE signal, the averaged saliency maps of the 547 recorded double-lines assuming the conduction mode, and their standard deviation σ .

7.4 Discussion

Four criteria to assess the quality of a model were defined earlier. A model should have a classification accuracy of at least 80%, its loss function should have stabilized, it should classify the double-line data set as keyhole category with an accuracy of at least 80%, and its saliency map should highlight specific frequencies for each category, but not for the noise category. The hypothesis underlining the last criterion is that the CNN model should train on events characteristic of a specific LPBF regime, happening at specific frequencies. If this criteria is not met, it would mean the model is relying on noise not necessarily related to specific laser-material interactions, and it would therefore not be reliable. Moreover, the saliency maps investigation of the

background noise can help ascertain the quality of a model. Indeed if no information is recorded, no specific frequency should be highlighted by the saliency map.

The model with the microphone AM41 with a non-flat response has a general classification accuracy of over 92% and a classification accuracy of the double-line data set over 87%, while its loss function is stabilized. It could be considered as a good CNN model. However, the analysis of its saliency map shows the model does not use much the frequencies around 10 kHz, 20 kHz, 40 kHz for the classification. As those frequencies are the ones for which the microphone is the most sensitive, it means the model is not using the principal information that the microphone provides. It could also mean that the information is not in the frequency range for which the microphone AM41 is the most sensitive. The microphone CM16, that has a flat frequency response, was used for the next models, to avoid this issue. Moreover, it can be seen in Figure 79 that the CM16 is more sensitive than the AM41.

The first model trained with the microphone CM16 also had a good general classification accuracy (over 97%). The investigation of the saliency maps emphasized mainly frequencies below 20 kHz but the information is also scattered until 120 kHz. The analysis of the saliency map of the category noise highlights specific frequencies in the low frequency range. It is an indication of learning of unphysical features.

As this microphone is polarized at high frequencies, the tested signals are treated with a low pass filter at 60 kHz and the trained model is applied on these treated signals. The classification accuracy reached above 89%. This seems to indicate that the information below 60 kHz is relevant enough for the classification decisions. However, the saliency maps show that the model also considers frequencies above 60 kHz, despite the fact that they have been filtered.

A third model with the microphone CM16 with input data filtered under 60 kHz, down-sampled four times and normalized, was therefore trained. The data from all the samples can be included in the database without bias, as the response is flat below 60 kHz regardless of the sample position. Moreover, normalizing the data ensures that model will more easily learn on the features and frequencies responsible of the regime formation, rather than on the differences in laser parameters (e.g. the amplitude is higher with a higher power). This model fulfills the four defined criteria. The accuracy classification is above 97%. The losses stabilize after 15 epochs. The analysis of the saliency maps highlights that the three LPBF regimes are classified based on signal frequencies from 5 kHz to 30 kHz. And the noise category saliency maps do not underline any specific frequency. The frequencies of interest are in accordance with other LPBF studies using ABAE microphones with a low frequency spectrum[88], [89]. However, exceptions exist, e.g. Gutknecht et al.[83] filtered all frequencies below 40 kHz, considering them as the noise of the machine. Moreover, they highlighted a reverberation in the build chamber of frequencies below 100 kHz. However, their very sensitive Xarion ABAE does not use the same technology compared to condenser membrane microphones. As for SBAE sensors, the critical frequencies of each process regime can vary depending on the type of sensor.

7.5 Conclusions

This study presents the results of different CNN models trained with spectrograms extracted from the acoustic signal acquired by two air-borne sensors, for classifying three LPBF processing regimes (keyhole pores, conduction mode, and LoF pores). The two microphones are placed inside a custom-design LPBF machine simultaneously recording the AE of thirteen laser parameter sets per regime. The first microphone AM41 has a frequency response limited to distinct spectral peaks centered at around 10 kHz, 20 kHz, 40 kHz, and 80 kHz. The second microphone CM16 has a flat response from 2 Hz to 200 kHz. The two microphones are able to classify with high confidence (>91%) a tested set with parameters that is not present in the training database, regardless of the CNN architecture and signals post-processing. All model losses of the training and validation stabilize, and the models do not seem to be overfitting. The information for classifications of the four categories (keyhole pores, conduction mode, LoF pores and, noise) are scattered in the studied frequencies. For both microphones, the frequencies mainly responsible for the classification lie below 40 kHz.

It is also proposed in this work to evaluate the quality of a CNN model with saliency maps. These can for example demonstrate how a model can learn unphysical features and still classify with high accuracy. The first trained CNN model with the AE from the AM41 microphone did not learn on its high sensitivity frequency range. To avoid a model to discard frequency ranges, a flat response microphone is better suited for the monitoring of a complex and noisy process such as LPBF. However, it is important to optimize the CNN model correctly, and to post-process the data according to the selected sensor. The CM16 being polarized at high frequencies, a better model is trained on data filtered below 60 kHz, down-sampled 4 times, and normalized. With this model, the frequencies responsible for the classification of the three regimes are found to be below 30 kHz, for 316L stainless steel.

The methodology developed here is of utmost importance for the possible generalization of monitoring methods to other alloys or machines. The comparison of the frequencies responsible for the classification of the three process regimes with those of other alloys is part of the future work.

In this work, we emphasize the frequencies associated with process regimes, resulting in a relatively poor time resolution. However, if a model is trained only in the time domain, such as to have the highest resolution in time, localization of defects could be implemented with saliency maps applied to raw acoustic data.

References

- [1] T. DebRoy *et al.*, “Additive manufacturing of metallic components – Process, structure and properties,” *Progress in Materials Science*, vol. 92, pp. 112–224, Mar. 2018, doi: 10.1016/j.pmatsci.2017.10.001.
- [2] C. Y. Yap *et al.*, “Review of selective laser melting: Materials and applications,” *Applied Physics Reviews*, vol. 2, no. 4, p. 041101, Dec. 2015, doi: 10.1063/1.4935926.
- [3] C. L. Ventola, “Medical Applications for 3D Printing: Current and Projected Uses,” *P T*, vol. 39, no. 10, pp. 704–711, Oct. 2014.
- [4] B. Vandenbroucke and J. Kruth, “Selective laser melting of biocompatible metals for rapid manufacturing of medical parts,” *Rapid Prototyping Journal*, vol. 13, no. 4, pp. 196–203, Jan. 2007, doi: 10.1108/13552540710776142.
- [5] J. M. Williams *et al.*, “Bone tissue engineering using polycaprolactone scaffolds fabricated via selective laser sintering,” *Biomaterials*, vol. 26, no. 23, pp. 4817–4827, Aug. 2005, doi: 10.1016/j.biomaterials.2004.11.057.
- [6] F. Rengier *et al.*, “3D printing based on imaging data: review of medical applications,” *Int J Comput Assist Radiol Surg*, vol. 5, no. 4, pp. 335–341, Jul. 2010, doi: 10.1007/s11548-010-0476-x.
- [7] S. N. Reddy, V. Maranan, T. W. Simpson, T. Palmer, and C. J. Dickman, “Application of topology optimization and design for additive manufacturing guidelines on an automotive component: ASME 2016 International Design Engineering Technical Conferences and Computers and Information in Engineering Conference, IDETC/CIE 2016,” *42nd Design Automation Conference*, 2016, doi: 10.1115/DETC2016-59719.
- [8] R. Liu, Z. Wang, T. Sparks, F. Liou, and J. Newkirk, “Aerospace Applications of Laser Additive Manufacturing,” *Laser Additive Manufacturing: Materials, Design, Technologies, and Applications*, pp. 351–371, Sep. 2016, doi: 10.1016/B978-0-08-100433-3.00013-0.
- [9] N. K. Dey, “Additive manufacturing laser deposition of Ti-6Al-4V for aerospace repair application,” p. 70.
- [10] H. Ghasemi-Tabasi, J. Jhabvala, E. Boillat, T. Ivas, R. Drissi-Daoudi, and R. E. Logé, “An effective rule for translating optimal selective laser melting processing parameters from one material to another,” *Additive Manufacturing*, vol. 36, p. 101496, Dec. 2020, doi: 10.1016/j.addma.2020.101496.
- [11] C. Körner, A. Bauereiß, and E. Attar, “Fundamental consolidation mechanisms during selective beam melting of powders,” *Modelling Simul. Mater. Sci. Eng.*, vol. 21, p. 5011, Dec. 2013, doi: 10.1088/0965-0393/21/8/085011.
- [12] T. Heeling, M. Cloots, and K. Wegener, “Melt pool simulation for the evaluation of process parameters in selective laser melting,” *Additive Manufacturing*, vol. 14, pp. 116–125, Mar. 2017, doi: 10.1016/j.addma.2017.02.003.
- [13] W. M. Tucho, V. H. Lysne, H. Austbø, A. Sjolyst-Kverneland, and V. Hansen, “Investigation of effects of process parameters on microstructure and hardness of SLM manufactured SS316L,” *Journal of Alloys and Compounds*, vol. 740, pp. 910–925, Apr. 2018, doi: 10.1016/j.jallcom.2018.01.098.

- [14] I. Koutiri, E. Pessard, P. Peyre, O. Amlou, and T. De Terris, "Influence of SLM process parameters on the surface finish, porosity rate and fatigue behavior of as-built Inconel 625 parts," *Journal of Materials Processing Technology*, vol. 255, pp. 536–546, May 2018, doi: 10.1016/j.jmatprotec.2017.12.043.
- [15] A. Mostafaei *et al.*, "Defects and anomalies in powder bed fusion metal additive manufacturing," *Current Opinion in Solid State and Materials Science*, vol. 26, no. 2, Jan. 2022, doi: 10.1016/j.cossms.2021.100974.
- [16] M. Montazeri, R. Yavari, P. Rao, and P. Boulware, "In-Process Monitoring of Material Cross-Contamination Defects in Laser Powder Bed Fusion," *Journal of Manufacturing Science and Engineering*, vol. 140, no. 11, Jul. 2018, doi: 10.1115/1.4040543.
- [17] P. Hanzl, M. Zetek, T. Bakša, and T. Kroupa, "The Influence of Processing Parameters on the Mechanical Properties of SLM Parts," *Procedia Engineering*, vol. 100, pp. 1405–1413, Jan. 2015, doi: 10.1016/j.proeng.2015.01.510.
- [18] A. Ramalho, T. G. Santos, B. Bevans, Z. Smoqi, P. Rao, and J. P. Oliveira, "Effect of contaminations on the acoustic emissions during wire and arc additive manufacturing of 316L stainless steel," *Additive Manufacturing*, vol. 51, p. 102585, Mar. 2022, doi: 10.1016/j.addma.2021.102585.
- [19] W. King *et al.*, "Laser powder bed fusion additive manufacturing of metals; physics, computational, and materials challenges," *Applied Physics Reviews*, vol. 2, p. 041304, Dec. 2015, doi: 10.1063/1.4937809.
- [20] T. Mukherjee and T. DebRoy, "Mitigation of lack of fusion defects in powder bed fusion additive manufacturing," *Journal of Manufacturing Processes*, vol. 36, pp. 442–449, Dec. 2018, doi: 10.1016/j.jmapro.2018.10.028.
- [21] M. Tang, P. C. Pistorius, and J. L. Beuth, "Prediction of lack-of-fusion porosity for powder bed fusion," *Additive Manufacturing*, vol. 14, pp. 39–48, Mar. 2017, doi: 10.1016/j.addma.2016.12.001.
- [22] K. Darvish, Z. W. Chen, and T. Pasang, "Reducing lack of fusion during selective laser melting of CoCrMo alloy: Effect of laser power on geometrical features of tracks," *Materials & Design*, vol. 112, pp. 357–366, Dec. 2016, doi: 10.1016/j.matdes.2016.09.086.
- [23] M. Laleh *et al.*, "Two and three-dimensional characterisation of localised corrosion affected by lack-of-fusion pores in 316L stainless steel produced by selective laser melting," *Corrosion Science*, vol. 165, p. 108394, Apr. 2020, doi: 10.1016/j.corsci.2019.108394.
- [24] C. Zhao *et al.*, "Critical instability at moving keyhole tip generates porosity in laser melting," *Science*, vol. 370, no. 6520, pp. 1080–1086, Nov. 2020, doi: 10.1126/science.abd1587.
- [25] A. A. Martin *et al.*, "Dynamics of pore formation during laser powder bed fusion additive manufacturing," *Nat Commun*, vol. 10, no. 1, p. 1987, Apr. 2019, doi: 10.1038/s41467-019-10009-2.
- [26] F. Lu, X. Li, Z. Li, X. Tang, and H. Cui, "Formation and influence mechanism of keyhole-induced porosity in deep-penetration laser welding based on 3D transient modeling," *International Journal of Heat and Mass Transfer*, vol. 90, pp. 1143–1152, Nov. 2015, doi: 10.1016/j.ijheatmasstransfer.2015.07.041.
- [27] W. E. King *et al.*, "Observation of keyhole-mode laser melting in laser powder-bed fusion additive manufacturing," *Journal of Materials Processing Technology*, vol. 214, no. 12, Art. no. LLNL-JRNL-642426; LLNL-JRNL-650285, Jun. 2014, doi: 10.1016/j.jmatprotec.2014.06.005.

- [28] T. Qi, H. Zhu, H. Zhang, J. Yin, L. Ke, and X. Zeng, “Selective laser melting of Al7050 powder: Melting mode transition and comparison of the characteristics between the keyhole and conduction mode,” *Materials & Design*, vol. 135, Sep. 2017, doi: 10.1016/j.matdes.2017.09.014.
- [29] F. Caiazzo, V. Alfieri, and G. Casalino, “On the Relevance of Volumetric Energy Density in the Investigation of Inconel 718 Laser Powder Bed Fusion,” *Materials*, vol. 13, p. 538, Jan. 2020, doi: 10.3390/ma13030538.
- [30] Y. H. Zhou *et al.*, “Selective laser melting of typical metallic materials: An effective process prediction model developed by energy absorption and consumption analysis,” *Additive Manufacturing*, vol. 25, pp. 204–217, Jan. 2019, doi: 10.1016/j.addma.2018.10.046.
- [31] I. Koutiri, E. Pessard, P. Peyre, O. Amlou, and T. De Terris, “Influence of SLM process parameters on the surface finish, porosity rate and fatigue behavior of as-built Inconel 625 parts,” *Journal of Materials Processing Technology*, vol. 255, pp. 536–546, May 2018, doi: 10.1016/j.jmatprotec.2017.12.043.
- [32] U. Scipioni Bertoli, A. J. Wolfer, M. J. Matthews, J.-P. R. Delplanque, and J. M. Schoenung, “On the limitations of Volumetric Energy Density as a design parameter for Selective Laser Melting,” *Materials & Design*, vol. 113, pp. 331–340, Jan. 2017, doi: 10.1016/j.matdes.2016.10.037.
- [33] D. B. Hann, J. Iammi, and J. Folkes, “A simple methodology for predicting laser-weld properties from material and laser parameters,” *J. Phys. D: Appl. Phys.*, vol. 44, no. 44, p. 445401, Oct. 2011, doi: 10.1088/0022-3727/44/44/445401.
- [34] V. Gunenthiram, P. Peyre, M. Schneider, M. Dal, C. Frederic, and R. Fabbro, “Analysis of laser–melt pool–powder bed interaction during the selective laser melting of a stainless steel,” *Journal of Laser Applications*, vol. 29, p. 022303, May 2017, doi: 10.2351/1.4983259.
- [35] V. Gunenthiram *et al.*, “Experimental analysis of spatter generation and melt-pool behavior during the powder bed laser beam melting process,” *Journal of Materials Processing Technology*, vol. 251, pp. 376–386, Jan. 2018, doi: 10.1016/j.jmatprotec.2017.08.012.
- [36] D. Wang *et al.*, “Mechanisms and characteristics of spatter generation in SLM processing and its effect on the properties,” *Materials & Design*, vol. 117, pp. 121–130, Mar. 2017, doi: 10.1016/j.matdes.2016.12.060.
- [37] S. A. Khairallah, A. T. Anderson, A. Rubenchik, and W. E. King, “Laser powder-bed fusion additive manufacturing: Physics of complex melt flow and formation mechanisms of pores, spatter, and denudation zones,” *Acta Materialia*, vol. 108, pp. 36–45, Apr. 2016, doi: 10.1016/j.actamat.2016.02.014.
- [38] P. Bidare, I. Bitharas, R. M. Ward, M. M. Attallah, and A. J. Moore, “Fluid and particle dynamics in laser powder bed fusion,” *Acta Materialia*, vol. 142, pp. 107–120, Jan. 2018, doi: 10.1016/j.actamat.2017.09.051.
- [39] M. J. Matthews, G. Guss, S. A. Khairallah, A. M. Rubenchik, P. J. Depond, and W. E. King, “Denudation of metal powder layers in laser powder bed fusion processes,” *Acta Materialia*, vol. 114, pp. 33–42, Aug. 2016, doi: 10.1016/j.actamat.2016.05.017.
- [40] T. Purtonen, A. Kalliosaari, and A. Salminen, “Monitoring and Adaptive Control of Laser Processes,” *Physics Procedia*, vol. 56, pp. 1218–1231, Jan. 2014, doi: 10.1016/j.phpro.2014.08.038.

- [41] T. Furumoto, K. Egashira, K. Munekage, and S. Abe, "Experimental investigation of melt pool behaviour during selective laser melting by high speed imaging," *CIRP Annals*, vol. 67, no. 1, pp. 253–256, Jan. 2018, doi: 10.1016/j.cirp.2018.04.097.
- [42] P. Lott, H. Schleifenbaum, W. Meiners, K. Wissenbach, C. Hinke, and J. Bültmann, "Design of an Optical system for the In Situ Process Monitoring of Selective Laser Melting (SLM)," *Physics Procedia*, vol. 12, pp. 683–690, Jan. 2011, doi: 10.1016/j.phpro.2011.03.085.
- [43] C. Bruna-Rosso, A. G. Demir, and B. Previtali, "Selective laser melting finite element modeling: Validation with high-speed imaging and lack of fusion defects prediction," *Materials & Design*, vol. 156, pp. 143–153, Oct. 2018, doi: 10.1016/j.matdes.2018.06.037.
- [44] F. Caltanissetta, M. Grasso, S. Petró, and B. M. Colosimo, "Characterization of in-situ measurements based on layerwise imaging in laser powder bed fusion," *Additive Manufacturing*, vol. 24, pp. 183–199, Dec. 2018, doi: 10.1016/j.addma.2018.09.017.
- [45] Y. Zhang, J. Y. H. Fuh, D. Ye, and G. S. Hong, "In-situ monitoring of laser-based PBF via off-axis vision and image processing approaches," *Additive Manufacturing*, vol. 25, pp. 263–274, Jan. 2019, doi: 10.1016/j.addma.2018.10.020.
- [46] U. Scipioni Bertoli, G. Guss, S. Wu, M. J. Matthews, and J. M. Schoenung, "In-situ characterization of laser-powder interaction and cooling rates through high-speed imaging of powder bed fusion additive manufacturing," *Materials & Design*, vol. 135, no. C, Art. no. LLNL-JRNL-738525, Sep. 2017, doi: 10.1016/j.matdes.2017.09.044.
- [47] J. L. Bartlett, F. M. Heim, Y. V. Murty, and X. Li, "In situ defect detection in selective laser melting via full-field infrared thermography," *Additive Manufacturing*, vol. 24, pp. 595–605, Dec. 2018, doi: 10.1016/j.addma.2018.10.045.
- [48] M. Khanzadeh, W. Tian, A. Yadollahi, H. R. Doude, M. A. Tschopp, and L. Bian, "Dual process monitoring of metal-based additive manufacturing using tensor decomposition of thermal image streams," *Additive Manufacturing*, vol. 23, pp. 443–456, Oct. 2018, doi: 10.1016/j.addma.2018.08.014.
- [49] H. Krauss, T. Zeugner, and M. F. Zaeh, "Layerwise Monitoring of the Selective Laser Melting Process by Thermography," *Physics Procedia*, vol. 56, pp. 64–71, Jan. 2014, doi: 10.1016/j.phpro.2014.08.097.
- [50] S. Berumen, F. Bechmann, S. Lindner, J.-P. Kruth, and T. Craeghs, "Quality control of laser- and powder bed-based Additive Manufacturing (AM) technologies," *Physics Procedia*, vol. 5, pp. 617–622, Jan. 2010, doi: 10.1016/j.phpro.2010.08.089.
- [51] S. Clijsters, T. Craeghs, S. Bults, K. Kempen, and J.-P. Kruth, "In situ quality control of the selective laser melting process using a high-speed, real-time melt pool monitoring system," *Int J Adv Manuf Technol*, vol. 75, no. 5, pp. 1089–1101, Nov. 2014, doi: 10.1007/s00170-014-6214-8.
- [52] T. Furumoto, T. Ueda, M. R. Alkahari, and A. Hosokawa, "Investigation of laser consolidation process for metal powder by two-color pyrometer and high-speed video camera," *CIRP Annals*, vol. 62, no. 1, pp. 223–226, Jan. 2013, doi: 10.1016/j.cirp.2013.03.032.
- [53] S. Coeck, M. Bisht, J. Plas, and F. Verbist, "Prediction of lack of fusion porosity in selective laser melting based on melt pool monitoring data," *Additive Manufacturing*, vol. 25, pp. 347–356, Jan. 2019, doi: 10.1016/j.addma.2018.11.015.

- [54] T. Craeghs, F. Bechmann, S. Berumen, and J.-P. Kruth, “Feedback control of Layerwise Laser Melting using optical sensors,” *Physics Procedia*, vol. 5, pp. 505–514, Jan. 2010, doi: 10.1016/j.phpro.2010.08.078.
- [55] F. Vakili-Farahani, J. Lungershausen, and K. Wasmer, “Wavelet analysis of light emission signals in laser beam welding,” *Journal of Laser Applications*, p. 022424 (7 pp.), 2017, doi: 10.2351/1.4983507.
- [56] S. Shevchik *et al.*, “Supervised deep learning for real-time quality monitoring of laser welding with X-ray radiographic guidance,” *Sci Rep*, vol. 10, no. 1, Art. no. 1, Feb. 2020, doi: 10.1038/s41598-020-60294-x.
- [57] M. Pavlov, M. Doubenskaia, and I. Smurov, “Pyrometric analysis of thermal processes in SLM technology,” *Physics Procedia*, vol. 5, pp. 523–531, Jan. 2010, doi: 10.1016/j.phpro.2010.08.080.
- [58] J.-B. Forien, P. J. DePond, G. M. Guss, B. H. Jared, J. D. Madison, and M. J. Matthews, “Effect of laser power on roughness and porosity in laser powder bed fusion of stainless steel 316L alloys measured by X-ray tomography: Paper presented at the Symposium ‘Tomographic and Radiographic Imaging with Synchrotron X-rays and Neutrons’ of the MSE 2018, 26–28 September 2018, Darmstadt, Germany,” *International Journal of Materials Research*, vol. 111, no. 1, pp. 47–54, Jan. 2020, doi: 10.3139/146.111816.
- [59] A. Gaikwad, B. Giera, G. M. Guss, J.-B. Forien, M. J. Matthews, and P. Rao, “Heterogeneous sensing and scientific machine learning for quality assurance in laser powder bed fusion – A single-track study,” *Additive Manufacturing*, vol. 36, p. 101659, Dec. 2020, doi: 10.1016/j.addma.2020.101659.
- [60] J. Trapp, A. M. Rubenchik, G. Guss, and M. J. Matthews, “In situ absorptivity measurements of metallic powders during laser powder-bed fusion additive manufacturing,” *Applied Materials Today*, vol. 9, pp. 341–349, Dec. 2017, doi: 10.1016/j.apmt.2017.08.006.
- [61] V. N. Lednev *et al.*, “In situ multi-elemental analysis by laser induced breakdown spectroscopy in additive manufacturing,” *Additive Manufacturing*, vol. 25, pp. 64–70, Jan. 2019, doi: 10.1016/j.addma.2018.10.043.
- [62] M. Bastuck, H.-G. Herrmann, B. Wolter, D. Böttger, and P.-C. Zinn, “AkuProLas: Acoustic Inline Process Monitoring for Laser Welding Applications,” p. 10.
- [63] N. Eschner, L. Weiser, B. Häfner, and G. Lanza, “Classification of specimen density in Laser Powder Bed Fusion (L-PBF) using in-process structure-borne acoustic process emissions,” *Additive Manufacturing*, vol. 34, p. 101324, Aug. 2020, doi: 10.1016/j.addma.2020.101324.
- [64] S. Shevchik, “Acoustic emission for in situ monitoring of laser processing,” p. 9.
- [65] T. Le-Quang *et al.*, “Why is in situ quality control of laser keyhole welding a real challenge?,” *Procedia CIRP*, vol. 74, pp. 649–653, Jan. 2018, doi: 10.1016/j.procir.2018.08.055.
- [66] K. Wasmer *et al.*, “Laser processing quality monitoring by combining acoustic emission and machine learning: a high-speed X-ray imaging approach,” *Procedia CIRP*, vol. 74, pp. 654–658, Jan. 2018, doi: 10.1016/j.procir.2018.08.054.
- [67] K. Wasmer *et al.*, “Laser processing quality monitoring by combining acoustic emission and machine learning: a high-speed X-ray imaging approach,” *Procedia CIRP*, vol. 74, pp. 654–658, Jan. 2018, doi: 10.1016/j.procir.2018.08.054.

- [68] M. Saifi and S. Vahaviolos, "Laser spot welding and real-time evaluation," *IEEE Journal of Quantum Electronics*, vol. 12, no. 2, pp. 129–136, Feb. 1976, doi: 10.1109/JQE.1976.1069104.
- [69] S. Lee, S. Ahn, and C. Park, "Analysis of Acoustic Emission Signals During Laser Spot Welding of SS304 Stainless Steel," *J. of Materi Eng and Perform*, vol. 23, no. 3, pp. 700–707, Mar. 2014, doi: 10.1007/s11665-013-0791-9.
- [70] W. W. Duley and Y. L. Mao, "The effect of surface condition on acoustic emission during welding of aluminium with CO₂ laser radiation," *J. Phys. D: Appl. Phys.*, vol. 27, no. 7, pp. 1379–1383, Jul. 1994, doi: 10.1088/0022-3727/27/7/007.
- [71] H. Gu and W. W. Duley, "A statistical approach to acoustic monitoring of laser welding," *J. Phys. D: Appl. Phys.*, vol. 29, no. 3, pp. 556–560, Mar. 1996, doi: 10.1088/0022-3727/29/3/011.
- [72] D. Farson, Y. Sang, and A. Ali, "Relationship between airborne acoustic and optical emissions during laser welding," *Journal of Laser Applications*, vol. 9, no. 2, pp. 87–94, Apr. 1997, doi: 10.2351/1.4745448.
- [73] E. Nava-Rüdiger and M. Houlot, "Integration of real time quality control systems in a welding process," *Journal of Laser Applications*, vol. 9, no. 2, pp. 95–102, Apr. 1997, doi: 10.2351/1.4745449.
- [74] H. Zeng, Z. Zhou, Y. Chen, H. Luo, and L. Hu, "Wavelet analysis of acoustic emission signals and quality control in laser welding," *Journal of Laser Applications*, vol. 13, no. 4, pp. 167–173, Aug. 2001, doi: 10.2351/1.1386799.
- [75] H. Luo, H. Zeng, L. Hu, X. Hu, and Z. Zhou, "Application of artificial neural network in laser welding defect diagnosis," *Journal of Materials Processing Technology*, vol. 170, no. 1, pp. 403–411, Dec. 2005, doi: 10.1016/j.jmatprotec.2005.06.008.
- [76] W. Huang and R. Kovacevic, "A neural network and multiple regression method for the characterization of the depth of weld penetration in laser welding based on acoustic signatures," *J Intell Manuf*, vol. 22, no. 2, pp. 131–143, Apr. 2011, doi: 10.1007/s10845-009-0267-9.
- [77] C.-J. Lee, J.-D. Kim, and Y.-C. Kim, "Study on monitoring of plasma emission signal in lap welding of Zn coated steel sheet using CO₂ laser," *Int. J. Precis. Eng. Manuf.*, vol. 16, no. 3, pp. 495–500, Mar. 2015, doi: 10.1007/s12541-015-0067-4.
- [78] Y. Mao, G. Kinsman, and W. W. Duley, "Real-Time Fast Fourier Transform Analysis of Acoustic Emission during CO₂ Laser Welding of Materials," *Journal of Laser Applications*, vol. 5, no. 2, pp. 17–22, Oct. 1993, doi: 10.2351/1.4745326.
- [79] E. V. Bordatchev and S. K. Nikumb, "Effect of focus position on informational properties of acoustic emission generated by laser–material interactions," *Applied Surface Science*, vol. 253, no. 3, pp. 1122–1129, Nov. 2006, doi: 10.1016/j.apsusc.2006.01.047.
- [80] L. Li and W. M. Steen, "Non-contact acoustic emission monitoring during laser processing," *ICALEO*, vol. 1992, no. 1, pp. 719–728, Oct. 1992, doi: 10.2351/1.5058543.
- [81] D. Farson, K. Hillsley, J. Sames, and R. Young, "Frequency-time characteristics of air-borne signals from laser welds," *ICALEO*, vol. 1994, no. 1, pp. 86–94, Oct. 1994, doi: 10.2351/1.5058875.

- [82] K. Ito, M. Kusano, M. Demura, and M. Watanabe, "Detection and location of microdefects during selective laser melting by wireless acoustic emission measurement," *Additive Manufacturing*, vol. 40, p. 101915, Apr. 2021, doi: 10.1016/j.addma.2021.101915.
- [83] K. Gutknecht, M. Cloots, R. Sommerhuber, and K. Wegener, "Mutual comparison of acoustic, pyrometric and thermographic laser powder bed fusion monitoring," *Materials & Design*, vol. 210, p. 110036, Nov. 2021, doi: 10.1016/j.matdes.2021.110036.
- [84] H. Taheri, L. W. Koester, T. A. Bigelow, E. J. Faierson, and L. J. Bond, "In Situ Additive Manufacturing Process Monitoring With an Acoustic Technique: Clustering Performance Evaluation Using K-Means Algorithm," *Journal of Manufacturing Science and Engineering*, vol. 141, no. 4, Feb. 2019, doi: 10.1115/1.4042786.
- [85] L. W. Koester, H. Taheri, L. J. Bond, and E. J. Faierson, "Acoustic monitoring of additive manufacturing for damage and process condition determination," *AIP Conference Proceedings*, vol. 2102, no. 1, p. 020005, May 2019, doi: 10.1063/1.5099709.
- [86] S. A. Shevchik, C. Kenel, C. Leinenbach, and K. Wasmer, "Acoustic emission for in situ quality monitoring in additive manufacturing using spectral convolutional neural networks," *Additive Manufacturing*, vol. 21, pp. 598–604, May 2018, doi: 10.1016/j.addma.2017.11.012.
- [87] D. Ye, J. Y. Hsi Fuh, Y. Zhang, G. S. Hong, and K. Zhu, "In situ monitoring of selective laser melting using plume and spatter signatures by deep belief networks," *ISA Transactions*, vol. 81, pp. 96–104, Oct. 2018, doi: 10.1016/j.isatra.2018.07.021.
- [88] D. Ye, G. S. Hong, Y. Zhang, K. Zhu, and J. Y. H. Fuh, "Defect detection in selective laser melting technology by acoustic signals with deep belief networks," *Int J Adv Manuf Technol*, vol. 96, no. 5, pp. 2791–2801, May 2018, doi: 10.1007/s00170-018-1728-0.
- [89] J. R. Tempelman *et al.*, "Detection of keyhole pore formations in laser powder-bed fusion using acoustic process monitoring measurements," *Additive Manufacturing*, vol. 55, p. 102735, Jul. 2022, doi: 10.1016/j.addma.2022.102735.
- [90] R. Drissi-Daoudi *et al.*, "Differentiation of materials and laser powder bed fusion processing regimes from airborne acoustic emission combined with machine learning," *Virtual and Physical Prototyping*, vol. 17, no. 2, pp. 181–204, Apr. 2022, doi: 10.1080/17452759.2022.2028380.
- [91] V. Pandiyan, R. Drissi-Daoudi, S. Shevchik, G. Masinelli, R. Logé, and K. Wasmer, "Analysis of time, frequency and time-frequency domain features from acoustic emissions during Laser Powder-Bed fusion process," *Procedia CIRP*, vol. 94, pp. 392–397, Jan. 2020, doi: 10.1016/j.procir.2020.09.152.
- [92] R. Drissi Daoudi *et al.*, "Acoustic Emission for the Prediction of Processing Regimes in Laser Powder Bed Fusion, and the Generation of Processing Maps," *SSRN Journal*, 2022, doi: 10.2139/ssrn.4267682.
- [93] J. Seo, J. Choe, J. Koo, S. Jeon, B. Kim, and T. Jeon, "Noise-adding Methods of Saliency Map as Series of Higher Order Partial Derivative," Jun. 2018. Accessed: Sep. 10, 2022. [Online]. Available: <https://ui.adsabs.harvard.edu/abs/2018arXiv180603000S>
- [94] A. Kothuru, S. P. Nooka, and R. Liu, "Application of deep visualization in CNN-based tool condition monitoring for end milling," *Procedia Manufacturing*, vol. 34, pp. 995–1004, Jan. 2019, doi: 10.1016/j.promfg.2019.06.096.

- [95] A. J. Jerri, "The Shannon sampling theorem - Its various extensions and applications: A tutorial review," *IEEE Proceedings*, vol. 65, pp. 1565–1596, Nov. 1977.
- [96] J. Seo, J. Choe, J. Koo, S. Jeon, B. Kim, and T. Jeon, "Noise-adding Methods of Saliency Map as Series of Higher Order Partial Derivative." arXiv, Jun. 08, 2018. Accessed: Sep. 10, 2022. [Online]. Available: <http://arxiv.org/abs/1806.03000>
- [97] V. Pandiyan *et al.*, "Deep learning-based monitoring of laser powder bed fusion process on variable time-scales using heterogeneous sensing and operando X-ray radiography guidance," *Additive Manufacturing*, vol. 58, p. 103007, Oct. 2022, doi: 10.1016/j.addma.2022.103007.
- [98] S. Albawi, T. A. Mohammed, and S. Al-Zawi, "Understanding of a convolutional neural network," in *2017 International Conference on Engineering and Technology (ICET)*, Aug. 2017, pp. 1–6. doi: 10.1109/ICEngTechnol.2017.8308186.

Chapter 8

Acoustic emission for the prediction of processing regimes in Laser Powder Bed Fusion, and the generation of processing maps

Rita Drissi-Daoudi¹, Giulio Masinelli², Charlotte de Formanoir¹, Kilian Wasmer², Jamasp Jhabvala¹, Roland Logé¹

¹Thermomechanical Metallurgy Laboratory – PX Group Chair, Ecole Polytechnique Fédérale de Lausanne (EPFL), Neuchâtel, Switzerland

²Laboratory for Advanced Materials Processing (LAMP), Swiss Federal Laboratories for Materials Science and Technology (Empa), Thun

This manuscript is under review in Additive Manufacturing

Contribution: Rita Drissi-Daoudi developped the experimental plan and printed the samples. She optimized the CNN model and performed the different classification. She wrote the manuscript.

Abstract

The Laser Powder Bed Fusion (LPBF) process is of high interest to many industries, such as motors and vehicles, robotics, biomedical applications, aerospace, and others. LPBF workpieces can indeed achieve near full density and high resistance. However, a large amount of pore formation, in conjunction with the probabilistic nature of defect formation, results in a lack of process repeatability and reproducibility. This limits the range of industrial applications requiring high quality and defect free workpieces. To overcome this issue, we developed an acoustic monitoring system able to classify with high confidence three processing regimes (*lack of fusion pores, conduction mode, keyhole pores*) using a Convolution Neural Network (CNN). For the first time, we infer the processing regime based on AE waves produced during the LPBF process for conditions that are new and not part of the training database (>96%). The choice of processing conditions used in the database (training sets) is discussed in details, looking at the influence of their number, relative normalized distance, and position in the processing map on the classification accuracy. We found that the higher the number of processing conditions in the database, the higher the classification accuracies. Moreover, the higher the relative normalized “distance” between training and testing sets (measured in terms of laser speed and power), the lower the classification accuracies. Finally, the threshold defining the minimum number of training processing conditions is identified as eight to obtain a robust model able to identify the processing regimes for new laser parameters within the processing map. This number can be lowered to six if the training sets are in the surrounding region of the testing set. When one process parameter (speed, power, or normalized enthalpy) is constant between all the training and the testing sets, only four parameter sets allow a high classification accuracy (>88%). These results demonstrate the potential of in situ acoustic emission for monitoring the additive manufacturing process, in particular when the process conditions may deviate from the conduction mode. Finally, for a well-chosen set of training conditions, the model is able to construct a full processing map without additional experiments.

Keywords: Laser powder bed fusion, acoustic monitoring, convolution neural networks, generalization, robustness, processing maps.

8.1 Introduction

In the past years, additive manufacturing (AM) has brought a new paradigm in the production of metallic parts, allowing the design of complex and intricate geometries while minimizing both lead time and buy-to-fly ratios [1]. Among the various categories of AM processes, Laser Powder Bed Fusion (LPBF), also known as Selective Laser Melting (SLM), consists in building up successive layers of pre-alloyed metallic powder according to a predefined 3D CAD model by selectively melting each layer of powder with a high-power laser beam [5–8]. Although this technology has gained significant interest from many industries [2–8] due to its versatility and accuracy, a number of drawbacks still limit its range of applications and impede a wider industrial use [9]–[13].

In particular, LPBF suffers from a frequent and sometimes hard-to-predict formation of defects, such as pores, which impedes certification processes. Porosity in as-built LPBF parts can originate from multiple causes, including the quality of the powder feedstock and the laser-material interactions. This latter source includes lack-of-fusion and keyhole pores. Lack-of-fusion pores result from an insufficient energy input, inducing incomplete melting of the powder during laser processing [14]–[17]. On the other hand, keyhole pores are caused by an excessive heat input: vaporization of the metal creates a deep keyhole-shaped depression zone whose collapse can generate a void in the lower region of the melt pool [18]–[23]. Optimal conditions for minimal porosity content are encountered in the conduction mode, a transition regime between lack-of-fusion and keyhole [23], [24].

Different tools have been developed in order to determine and thus mitigate the occurrence of pores. For a given material, processing maps based on parameters such as laser power and speed can be built to find the optimum conditions for high-density parts [24]–[28]. However, establishing such 2D-processing maps is a laborious procedure, requiring extensive printing of specimens using a variety of process parameters followed by a very time-consuming metallurgical characterization of the as-built parts. Furthermore, this trial-and-error process optimization needs to be reiterated when transitioning from either one alloy [29], or one LPBF machine, to another.

In most laser processes dealing with powders, the laser-material interaction is highly non-linear and always exhibits a non-negligible stochastic component. This leads to non-reproducibility of microstructures and properties, and non-homogeneity of the printed parts. Moreover, the generation of unpredictable spatter [30]–[35] and contamination leads to irregular defect formation [12]. In order to detect the formation of defects during the LPBF process, and identify the melting regime (lack-of-fusion, conduction, or keyhole), real-time process monitoring is a promising solution/approach. In the past 10 years, various optical techniques have been investigated, including spatially integrated sensors such as photodiodes [36]–[38], pyrometers [39]–[43], infrared

and high speed cameras [36], [37], [41], [43], [44]. Complementary to these optical techniques, acoustic emission (AE) has been reported as a high sensitivity, low-cost and robust technique for monitoring laser processes.

The analysis of AE was first identified as a valid technique for monitoring laser welding [45]–[48]. One drawback of the AE sensors is that they record any AE waves produced during the laser processes, including the undesired noise from the machine or the environment [38], [49], [50]. Consequently, it is not a trivial task to isolate the AE information coming from the laser-material interactions [51]. To address this issue, state-of-the-art machine learning algorithms were able to classify welds of various regimes and quality based AE signals [50], [52]–[55]. More recently, the potential of AE as a monitoring tool has been extended to the field of laser-based additive manufacturing. Several papers have demonstrated the ability to differentiate lack-of-fusion, conduction, and keyhole regimes with high confidence, based on AE signal analysis [29], [49], [56]–[67].

To be specific, over the past few years, Convolutional Neural Networks (CNN) have become a common algorithm for acoustic classification tasks [29], [56], demonstrating great effectiveness and enabling the possibility of suppressing stationary noise. For example, Shevchik et al. [56] used a Fiber Bragg Grating (FBG) as AE sensor, and combined two types of CNN (a Spectral one and a conventional one). They have successfully classified the quality of LPBF with a classification accuracy around 80%. In a following work, Shevchik et al. [62] used two running windows with various time span as input to several types of CNNs, to address the localization of defects. The classification accuracies varied between 73 and 91%, depending on the time span of the running window and the process quality. Similarly, Ye et al. [63] used a deep belief network to classify acoustic data of five category – balling, slight balling, normal, slight overheating, overheating –with high accuracy (95%) in the LPBF process. Eschner et al. [61] have designed a Neural Network to classify three density classes of laser operation with 90% accuracy. Drissi-Daoudi et al. [29] have compared four ML algorithms (Logistic Regression, Random Forest, Support Vector Machine and a CNN) for the classification of three process regimes (LoF pores, Conduction mode, and Keyhole pores) for three different alloys (stainless steel, bronze, and Inconel), using a low cost airborne AE sensor. All algorithms had comparable and high classification accuracies (around 90%), for all alloys. The authors selected two process parameters per regimes, with specific normalized enthalpy, to prove that the extracted AE features used for training the ML algorithms relate to the laser-material interaction. Finally, they designed a CNN capable of simultaneously classifying the alloy and the process regime.

Tempelman et al. [64] used a Support Vector Machine (SVM) to detect keyhole and non-pore segments of single lines using process parameters scattered in the 2D processing map. The data segmentation and labeling were obtained by X-ray tomography. Their approach confirmed the previous works from Shevchik et al. [29], [62] that keyhole pore formation can be detected using airborne AE sensors combined with ML algorithms. However, in all AE-based studies for LPBF, the techniques' performance was evaluated on random AE signals that are, obviously, not part of the training database but coming from the collected database using the same

parameters set; which raises two questions. First, does the ML algorithm classify the process parameters or the laser-material interaction? Clearly, the main goal is to monitor the laser-material interaction leading to the different process regimes (LoF, conduction, and keyhole) and not the process parameters themselves; otherwise, we would just extract this information from the machine directly. The second question is the ability of the ML algorithm to classify AE signals from trained process regimes but from new (unseen) parameter sets. This generalization of the ML predictability is a critical step towards AE based process monitoring. Finally, significant factors and exhaustive details for constructing a robust database are overall lacking in the literature. Consequently, the novelty of this contribution is twofold. First, it focuses on the ability of ML algorithms to classify AE data outside the parameters sets they were trained on. Second, the present study provides all the necessary tools to help building an otherwise time-consuming processing map for a given alloy.

The present work studies the classification of AE signals recorded by a microphone during LPBF of a 316L stainless steel alloy. The occurrence of three process regimes (lack-of-fusion (LoF), keyhole, and conduction mode) is identified through metallurgical characterization. The CNN algorithms are trained with three categories representing the three different process regimes; as well as with the background noise as the fourth category, i.e., the noise of the machine and process when the laser is off. A CNN is selected for the classification tasks of these four categories.

The paper is organized into 4 Sections. Section 2 details the method and experimental plan, while Section 3 presents the results and discussion. The generalization of the CNN model, trained with twelve parameter sets, is tested on an unseen thirteenth parameter set. We check in what extent the accuracy of the classification relates to: (i) the position (in the 2D space) and number of the parameter sets used in the training database with respect to the tested set, (ii) the influence of key process parameters – normalized enthalpy, laser power and speed, (iii) the relative normalized “distance” in terms of power, speed and normalized enthalpy between the training and the tested set. The results provide insights into the collection of a robust model for classification of LPBF processing regimes based on AE, which are summarized in the conclusion.

8.2 LPBF Experiments

8.2.1 Experimental setup and data acquisition

All experiments of this work were performed on an in-house LPBF system shown in Figure 98. The customized LPBF contains a hopper filled with powder that deposits each layer by gravity when the piston below the substrate moves down by the required layer thickness. A continuous-wave (CW) modulated Ytterbium fiber laser is used for melting the powder. The fiber laser operates in a continuous mode with a 1070 ± 10 nm wavelength and a maximum power of 500 W. The beam diameter is around $42 \mu\text{m}$ ($1/e^2$) at the focal plane with $M^2 < 1.1$. The laser scan speed is up to $20 \text{ m}\cdot\text{s}^{-1}$. The chamber’s atmosphere is controlled under a laminar flow of argon and a monitored oxygen level of maximum 200 ppm.

Acoustics emission for the prediction of processing regimes in Laser Powder Bed Fusion, and the generation of processing maps

The build chamber is equipped with a CM16/CMPA40-5V ultrasound microphone (Avisoft Bioacoustics), as shown in Figure 98 (6). This main advantage of this microphone is that it has a flat response up to 200 kHz. It is positioned on the top of the build chamber so that the recording face points to the process zone while not disturbing the deposition system and being protected from powder, spatters, and fumes. It is placed at a distance of approximately 23 cm from the center of the substrate. An Advantech Data Acquisition (DAQ) card (Advantech, Taiwan) records the output from the microphone. The AE signals are acquired at a rate of 0.6 MHz and stored locally for processing with a custom-built C# code that interacts with the Advantech DAQ card. The data acquisition rate was chosen to ensure that the Nyquist Shannon theorem [68] is satisfied. The data acquisition is triggered by the laser head signal. This ensures synchronization between the LPBF process and the obtained data.

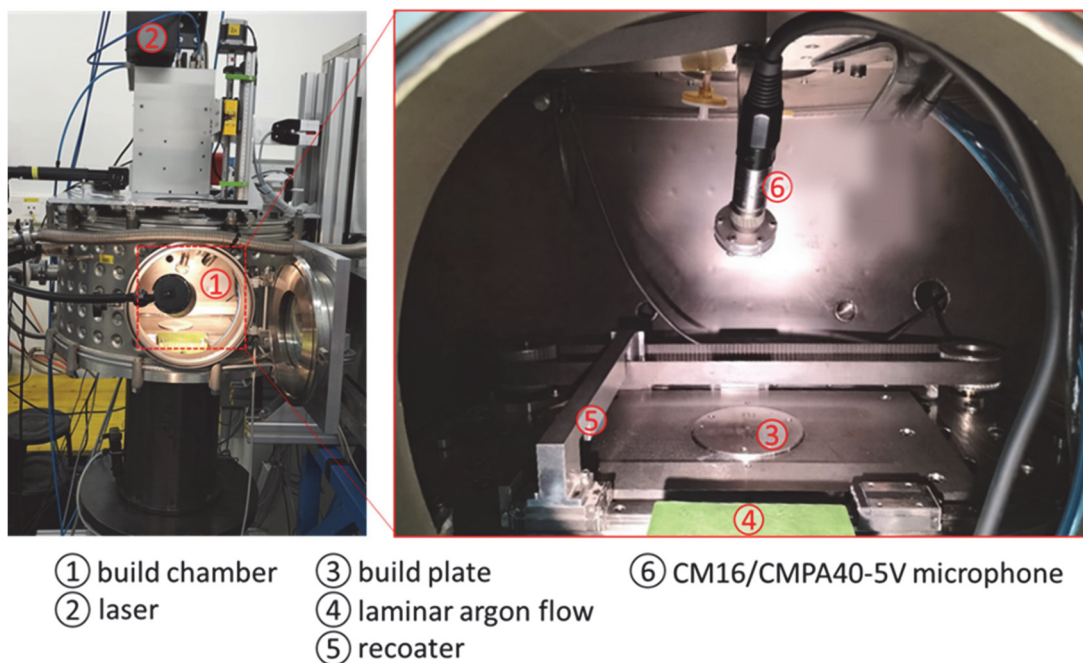


Figure 98. Experimental set-up of the custom-built LPBF with the CM16 microphone

All experiments were performed with a stainless steel MetcoAdd 316L micro powder (Oerlikon Metco) with a particle size distribution between 15 and 45 μm . Its composition is presented in Table 31 and the corresponding physical and optical properties are given in Table 32.

Table 31. Chemical composition of stainless steel (316L) powder

Fe	Cr	Ni	Mo	Other	C
Balance	18	12	2	<1.00	<0.03

8.2.2 Experimental plan

We considered three distinct process regimes: *LoF pores*, *conduction mode*, and *keyhole pores*. For each regime, thirteen cubes of 13x13x3 mm³ with thirteen different parameter sets were printed. The thirteen process parameters are given in Table 33 and plotted in Figure 99. 1-mm-thick porous structures were built on top of the base plate as support for the samples in order to ensure that the experiments would have the same heat flow as when processing bulk material. On top of these support structures, high-density layers were built over 2 mm to guarantee similar initial conditions for all experiments. Finally, for each of the three above-mentioned process regimes, 10 layers (above the red line in Figure 99) of 110 overlapping line tracks were produced, during which the AE signals were recorded with the microphone. The scanning strategy was unidirectional and parallel, with a hatch distance of 0.1 mm and a layer thickness of 40 μm. For all 39 cubes, the data labeling of the process regime was identified via cross-section analysis. Typical examples of the microstructure for each process regime are presented in Figure 99. The samples were etched with diluted Aqua regia (100 mL HNO₃, 100 mL HCl, 100 mL H₂O) for 30 s to reveal the microstructure and melt pool morphology. Micrographs were taken with a Leica DM6000M light optical microscope in bright field mode.

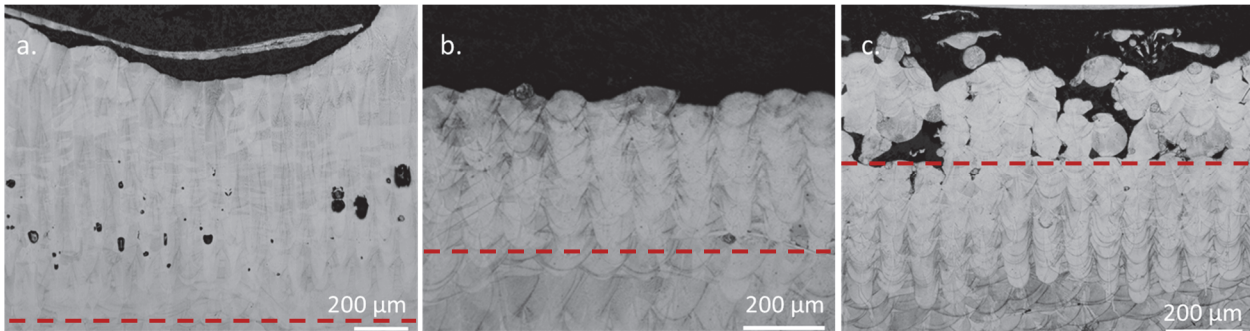


Figure 99. Typical example of microstructure of the three regimes, a. Keyhole pores, b. Conduction mode, c. LoF pores. The dotted red line delimits the recorded lines from the printed cube.

As illustrated in Figure 100, the process parameters were chosen to have, for each process regime, five sets of parameters with iso-power ($P=61$ W, $P=89$ W and $P=251$ W), five with iso-speed ($v=350$ mm/s or $v=450$ mm/s), and five with iso-normalized enthalpy ($\Delta H=17$, $\Delta H=25$ or $\Delta H=80$).

The normalized enthalpy ΔH is defined as [24], [69]:

$$\overline{\Delta H} = \frac{\alpha P}{\rho(C\Delta T + L_m)\sqrt{\pi\omega^3 v D}} \quad (1)$$

Where α is the absorptivity of the bulk material, P is the laser power (W), ρ the density (kg/m^3), C the specific heat ($\text{J}/\text{kg}\cdot\text{K}$), ΔT the difference between the melting and initial temperature (K), L_m the latent heat of melting (kJ/kg), ω the laser spot radius (m), v the laser speed (m/s), D the thermal diffusivity (m^2/s).

Table 32. Physical and optical properties of stainless steel 316L
Parameters values

Absorptivity α [-]	0.52
Density ρ [kg/m ³]	7900
Specific heat C [J/kg.K]	490
Melting point [K]	1640
Latent heat of melting L_m [kJ/kg]	260
Laser spot diameter [μ m]	42
Thermal diffusivity [m ² /s]	$3.5 \cdot 10^{-6}$

All three iso-conditions share a common central point (in black in Figure 100) corresponding to line n°13 in Table 33, which leads to a total of thirteen experiments for each regime. The enumeration in Figure 100, given for the keyhole regime, is transferable to the two other process regimes (Table 33).

The DOE is designed such as to allow predicting the process regime with an unseen parameter set (central point, n° 13) with the training performed on a database composed of 12 parameter sets surrounding it. It also allows predicting the process regimes related to parameter sets that are off-centered (n° 1, 4, 5 and 8) with 12 parameter sets that are further away in the processing map. The influence of the “distance” (in the processing map) between the data points used for the training and the prediction will be studied, by comparing the results of the classification when the database is formed with the 6 closest points (full markers in Figure 100, n° 2, 3, 6, 7, 10, 11) to the results when the training is based on the 6 other more distant points (empty markers in Figure 100, n°1, 4, 5, 8, 9, 12). Moreover, the prediction of the central point process regime will be tested with three databases trained with the 4 parameter sets in iso-power, iso-speed, or iso-normalized enthalpy, respectively, in order to highlight the influence of the choice of process parameters on the training. Finally, the influence of the relative normalized “distance” in terms of normalized enthalpy, power, and speed as well as the number of parameter sets needed for a high-confidence prediction of an unseen point will be determined. The relative normalized “distance” in terms of normalized power is defined in equation (2).

$$d_P = \frac{\sum_1^n (P_{training} - P_{unseen})}{\sum_1^n P_{training}} \cdot 100 [\%] \quad , \quad (2)$$

where n is the number of parameter sets in the training database, $P_{training}$ the power [W] of each set in the training database, and P_{unseen} the power [W] of the unseen parameter set. The same definition can be applied to d_S and $d_{\Delta E}$, by considering the laser speed values and the normalized enthalpy values, respectively.

Acoustics emission for the prediction of processing regimes in Laser Powder Bed Fusion, and the generation of processing maps

Table 33. Process parameters (power, speed, and normalized enthalpy) used for the experimental plan for the three categories, keyhole pores, conduction mode, and LoF pores. The values in bold are iso-speed, iso-power, and iso-normalized enthalpy for each category. The sample n°13 in **Italics Bold** is the black central point in Figure 100, common for the three iso-parameters.

Keyhole pores				Conduction mode			LoF pores		
N°	Power [W]	Speed [mm/s]	Normalized enthalpy [-]	Power [W]	Speed [mm/s]	Normalized enthalpy [-]	Power [W]	Speed [mm/s]	Normalized enthalpy [-]
1	282	350	89.9	107	450	30.1	68	450	19.1
2	267	350	85.1	96	450	27.0	64	450	18.0
3	235	350	74.9	82	450	23.1	57	450	16.0
4	220	350	70.1	71	450	19.9	51	450	14.3
5	251	276	90.1	89	350	28.4	61	358	19.2
6	251	310	85.0	89	400	26.5	61	400	18.2
7	251	398	75.1	89	500	23.7	61	500	16.3
8	251	457	70.0	89	550	22.7	61	550	15.5
9	240	320	80.0	85	410	25.0	59	430	17.0
10	245	333	80.1	87	432	25.0	60	443	17.0
11	256	364	80.0	91	466	25.1	61	457	17.0
12	261	378	80.1	93	490	25.0	62	470	17.1
13	251	350	80.0	89	450	25.0	61	450	17.1

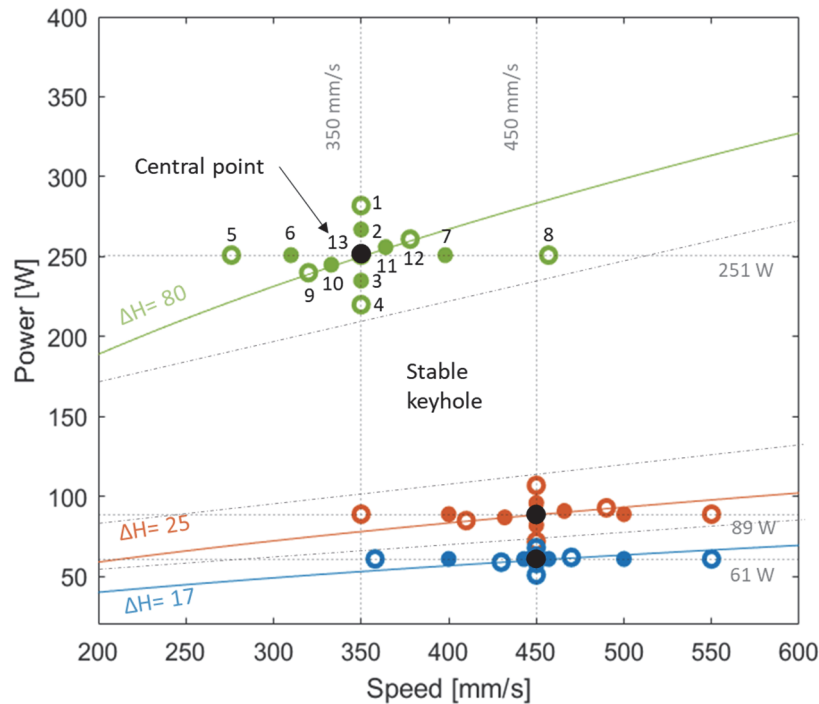


Figure 100. Process parameter map with the thirteen parameter sets for each category, in green for the keyhole domain, in orange for the conduction mode, and in blue for Lof pores. The parameter sets are numbered from 1 to 13 for the keyhole pores domain. The same numbering strategy can be transferred to the two other domains. The “central point” is depicted in black. Three iso-normalized enthalpies at 80, 25 and 17 are plotted. The full markers are the six parameter sets closest to each central points, and the six empty markers are the six parameter sets the furthest away from the central points.

A one-second delay was applied between each line track to ensure that the recording of each line is done under the same thermal conditions. Moreover, this delay guarantees that the reverberation of the sound inside the build chamber, which can last ~ 100 ms after the laser stops, is completely attenuated. Again, this guarantees that the recording of a new line always starts under the same conditions [70]. However, as compared to the processing maps reported by Tucho et al. [25], the one-second delaying time reduces the size of the conduction regime domain, and even more significantly, the one of the LoF regime. In contrast, the stable keyhole regime domain (i.e., with no porosity formation) becomes larger.

8.3 Data processing

A pre-delay of 0.5 ms is implemented to make certain that the acoustic signal is recorded from the beginning of the laser process. To ensure having recorded the signal over the entire line, 27'000 data points were acquired for the *keyhole pores* process regimes, 21'000 for the *conduction mode* and 18'000 for the *LoF pores*. All acoustics signals were then extracted as follows: the first 3'000 points were removed, the next 10'000 points were kept, and the remaining points were also removed. With this procedure, all analyzed signals have the same length, and the non-steady state conditions (when the laser has not yet reached the required speed) are excluded from the analysis.

A CNN is chosen for the classification tasks. CNN have been proven to be effective for noisy signal [29], [62] and they avoid the feature extraction step. It is implemented using a PyTorch library is chosen for the classification tasks. The AE signals have been filtered with a low pass filter at 60 kHz, as the microphone is polarized for higher frequencies and because [29] showed that the information responsible for the three regimes formation were mostly below 40 kHz. The signals were then downsampled by a factor of four, and finally normalized between 0 and 1.

For all signals, spectrograms, after the post-processing, were extracted from the acoustics signals. A short window increases the time and spatial resolution of defect detection, but could be more affected by noise. The time span must also be large enough for at least one defect to form. A good compromise was obtained with a window of 16 ms (10'000 data points). In order to have the best tradeoff between the resolution in time and in frequency, a spectrogram of size 97x626 was selected after an exhaustive search. A typical spectrogram for each process regime is presented in Figure 101.

1,100 acoustics signals were taken per sample. As a result, if twelve parameters sets (samples) are included in the training set, then 13,200 signals (and thus the same amount of spectrograms) are considered per category.

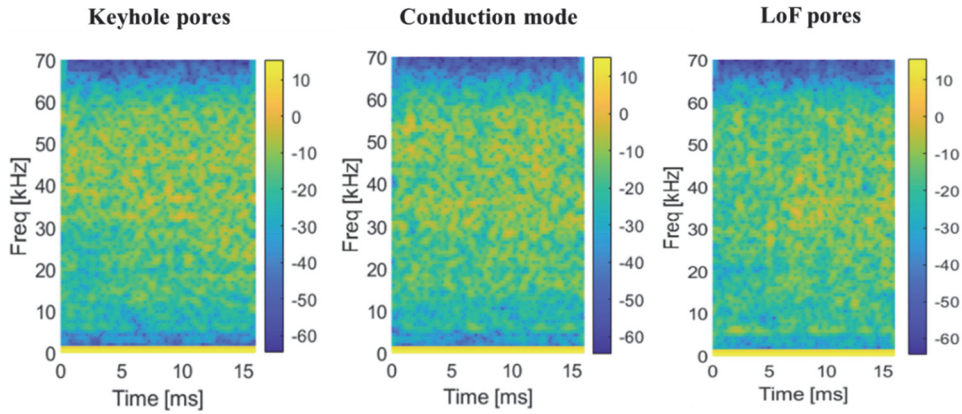


Figure 101. Example of a spectrogram for the three regime related categories.

The training of the CNN is performed on 80% of the signals (randomly picked), and the remaining 20% of the signals are kept for the validation of the model's performance. The model is then tested on 1,100 signals from the same process regime or category but with another parameter set unseen by the algorithm. The CNN architecture is illustrated in Figure 102. It includes two 2D convolution layers max pooled by 2x2, each batch-normalized to reduce overfitting. The Rectified Linear Units (ReLU) activation function is applied to both layers. Two fully connected layers are following these layers. The model is trained for 50 epochs with a batch size of 1,000, a learning rate of 5e-4, and the Adam optimizer. The same architecture is kept unaltered for all the classifications in this work, for comparison purpose. The use of the background noise in the training is only to help the algorithm. The classification accuracy for the background noise was always 100 %. Hence, it will not be further mentioned in the description of this work.

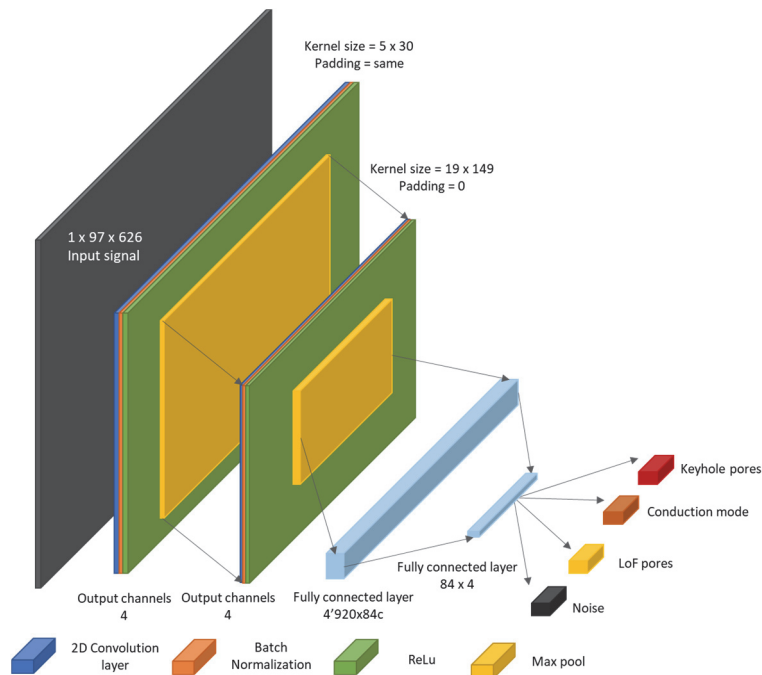


Figure 102. Scheme of the CNN architecture with two convolutional layers and two fully connected layers

8.4 Results and discussion

8.4.1 Toward the generalization of the ML model over the entire processing map

One important objective of this paper is to investigate to what extent the proposed ML algorithm can predict the process regime of an unseen parameter set (i.e. not part of the training) from its recorded AE signals.

As already described in section 2.2, the airborne AE signals from a chosen number of parameter sets are used for training the ML, which is then tested on a new parameter set. In this work, the CNN architecture in Figure 102 has been trained first with twelve parameter sets (experiments n°1 to 12 in Figure 100 and Table 33) for each process regime (*LoF pores*, *conduction mode*, and *keyhole pores*). Then, the model was tested by classifying the process regime on an unseen parameter set (black point in Figure 100, n°13 in Table 33). As shown in Figure 100, the unseen parameter is surrounded by the ones used for training the ML model.

The results of the classification accuracies for the three process regimes (*LoF pores*, *conduction mode*, and *keyhole pores*) are given in the confusion matrix in Table 34. The accuracy, in % (diagonal values in Table 34) is defined as the number of true positives divided by the total number of tests in each category. The misclassifications are the false positives and false negatives divided by the total number of tests in each category as well. For example, the conduction mode was classified with a very high accuracy rate of 96%. The classification distributed equally between the *conduction mode* and *keyhole pores* with 2% each. From this table, it is observed that classification results are higher than 96% for all three categories. We can therefore conclude that the model can be generalized to predict, with high confidence, the regime of a new, unseen parameter set, if it is surrounded (in the processing map) by parameters sets used to train the algorithm. The generalization here can be thought as a type of interpolation.

Table 34. Confusion matrix for a CNN model trained on 12 parameter sets and tested on an unseen 13th parameter set

Classification accuracy [%]	Ground truth		
	Keyhole pores	Conduction mode	LoF pores
Keyhole pores	96	2	0
Conduction mode	2	96	0
LoF pores	2	2	100

8.4.2 Influence of the position, number of parameter sets and choice of process parameters on the classification accuracy

While the previous sub-section demonstrated the interpolation abilities of our CNN algorithm, the present section investigates the influence of different factors on the classification accuracy of the tested parameter sets to establish the conditions required to construct a robust model.

For each process regime, the factors considered to influence the classification accuracy are:

- The position (in the processing map) of the parameter sets chosen for the training database as compared to the tested (unseen) parameter set.
- The number of sets in the training database
- The influence of the chosen process parameters: laser power, laser speed, and normalized enthalpy.
- The relative normalized “distance”, in terms of laser power, laser speed, and normalized enthalpy (d_p , d_s and $d_{\Delta E}$) between the average values of the parameter sets considered in the training, and the tested (unseen) parameter set.

The same CNN architecture (Figure 101) is used.

iii. Influence of the position of the parameter sets in the training database with respect to the tested (unseen) parameter set

To study the influence of the position of the training parameter sets with respect to the unseen parameter set, the four extreme parameter sets (n° 1, 4, 5, and 8 in Figure 100 and Table 33), in terms of laser power and speed, are successively chosen as the unseen parameter set. The remaining 12 other parameter sets are, each time, used for training the ML. Table 35 shows the corresponding 3-by-3 confusion matrices for the classification of the three regimes. The unseen parameter set has either the highest speed (n°8, **Bold** font in Table 35), the lowest speed (n°5, Normal font in Table 35), the highest power (n° 1, **Bold Italics** font in Table 35), or the lowest power (n°4, *Italics* font in Table 35).

Overall, it can be seen that the classification accuracy remains high, although slightly lower values are obtained in keyhole and conduction modes for the “**highest speed**” unseen parameter set, when compared to the earlier case for which the unseen parameter was the central black point (Table 34). However, the classification accuracy in conduction mode for the “*lowest power*” unseen parameter set, sample n°4, is significantly lower (75%). This decrease can be correlated to the fact that this set is located near the boundary between the conduction mode domain and the LoF domain (see Figure 100). The micrographs of the sample n°4 of the conduction mode and of the sample n°1 of the LoF mode are displayed in Figure 103.a. and in Figure 103.b., respectively. Although scattered LoF pores can be observed in Figure 103.b., it can be seen that the microstructures are similar in terms of melt pool dimensions. The average melt pool depth and length for the conduction mode sample are equal to 63 μm and 87 μm , respectively. In the case of the LoF sample, they are of 57 μm and 82 μm , respectively. In Ghasemi et al. [24], the minimal ratio between the melt pool depth and the layer thickness that guarantees the conduction mode state was reported around 1.5-1.6. This ratio is here equal to 1.57 and 1.43 in sample 4 (conduction mode) and sample 1 (LoF mode), respectively. It is possible that a low amount

of LoF pores is present in sample 4 (conduction mode) while not visible in the analyzed cross sections. The proximity between these microstructures could explain the decrease in classification accuracy for this sample set, as the AE signals are expected to have many similar features. This means that for a reliable and robust model, a local decrease in accuracy could be indicative of a parameter set located at the border between two processing regimes. In other words, it could help identifying the frontiers of the processing regime domains when constructing a processing map.

Table 35. Confusion matrices for CNN models trained with twelve parameter sets and tested on the highest speed set (**Bold**), on the lowest speed set (Normal), highest power set (**Italic Bold**), and lowest power set (Italic).

Classification accuracy [%]	Ground truth		
	Keyhole pores	Conduction mode	LoF pores
Keyhole pores	83	15	4
	96	1	3
	97	9	3
	98	17	4
Conduction mode	6	84	1
	3	99	2
	2	90	1
	2	75	2
LoF pores	1	1	95
	1	0	95
	0	1	96
	0	8	95

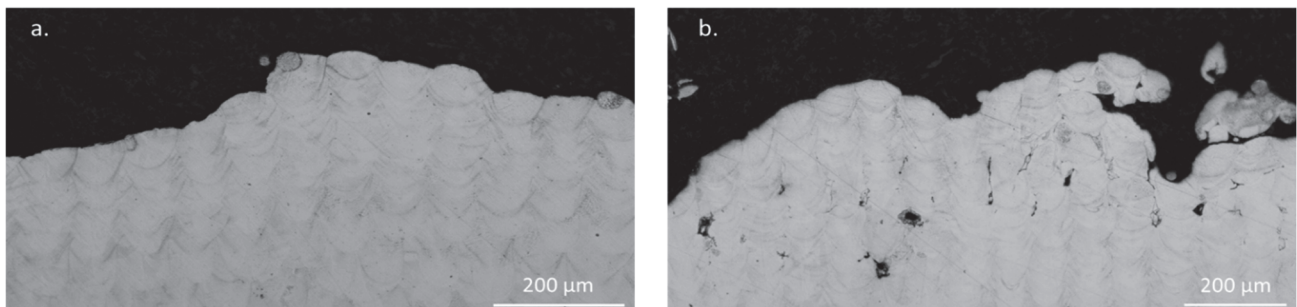


Figure 103. Micrograph of a cross section of the sample. a) n°4 in the conduction mode domain and b) of the n°1 in the LoF pores domain. The parameter sets used for these samples are at the boundary between the conduction and LoF domains.

iv. The number of parameter sets

The influence of the number of sets in the training database was also evaluated. In addition to the 12 sets previously used (Table 33), training databases with six, eight, and ten different process parameter sets were employed. Once again, the trained CNN algorithm was used to predict the process regime of an unseen parameter set, chosen among the four most extreme points in the processing map (n°1, 4, 5, and 8 in Figure 100).

Acoustics emission for the prediction of processing regimes in Laser Powder Bed Fusion, and the generation of processing maps

The parameter sets present in each training database were selected in order to maximize d_s and d_p . Similar to Table 35, Table 36 presents the 3-by-3 confusion matrices for the three categories (process regimes) on the four tested unseen conditions when ten, eight, and six parameter sets are included in the training database. The classification accuracies with ten parameter sets in the training database are similar to the ones obtained with twelve parameter sets (Table 35). The accuracies are high, except for the prediction of the unseen parameter set n°4, located at the border of the conduction mode domain. The lower accuracy can again be explained by this particular location, as discussed above when using 12 parameter sets. The average classification accuracy for the models trained with 8 parameter sets is remarkably high for all tested unseen parameter sets. However, when six parameter sets are included in the training, the classification accuracies on unseen parameter sets are, on average, lower and more scattered, depending on the considered tested point. Six parameter sets do not seem to be sufficient to obtain a robust model able to perform accurate predictions in other unseen locations of the processing map.

Table 36. Confusion matrices for CNN models trained with ten, eight, and six parameter sets and tested on the highest speed set (**Blod**), lowest speed set (Normal), highest power set (**Italic Bold**), and lowest power set (Italic).

10 sets				8 sets			6 sets		
Ground truth Classification accuracy [%]	Keyhole pores	Conduction mode	LoF pores	Keyhole pores	Conduction mode	LoF pores	Keyhole pores	Conduction mode	LoF pores
Keyhole pores	88	17	4	100	3	1	78	16	3
	93	1	3	93	0	3	83	2	16
	91	9	4	94	11	2	91	13	7
	95	14	3	94	5	0	92	7	4
Conduction mode	2	83	1	0	97	0	8	82	1
	6	99	5	7	100	4	15	98	15
	8	91	5	4	88	0	6	80	3
	4	74	2	3	93	0	6	71	2
LoF pores	10	0	95	0	0	99	14	2	96
	1	0	91	0	0	93	2	0	70
	1	0	91	1	1	98	3	7	90
	1	12	95	3	2	100	2	22	94

In addition to the number of parameter sets in the training database, the position of the sets with respect to the unseen parameter set was also considered. In the first case, the six sets with full markers (n° 2, 3, 6, 7, 10, 11) in Figure 100 constitute the training database, and the model is applied for predicting the processing regime of the central point, n°13 (in black in Figure 100). The accuracy results are compared with those obtained in the second case, i.e., when the six sets with empty markers (n°1, 4, 5, 8, 9, 12) in Figure 100 are in the training database, and the model is also applied on the unseen central point, n°13. In both cases, the average value of the process parameters considered in the training database are the same as for the unseen parameter set (both in terms of laser power and speed); however, the full marker sets are closer to the central point than the empty

markers. It can be seen in Table 38 that all classification accuracies are very high (>91 %), and that no significant difference between the two configurations can be noted.

From these results, it can be highlighted that the number of parameter sets in the training base can be lowered down to six if the points are surrounding the unseen parameter set. The average RMS “distance” in power (d_{p_RMS}) and in speed (d_{s_RMS}) between the training sets and the unseen parameter set is given in Table 37, considering either the closest or the most distant sets.

$$d_{P_RMS} = \sqrt{\frac{1}{n} \sum_1^n (P_{training} - P_{unseen})^2} \quad (3)$$

The RMS distances (d_{p_RMS} , d_{s_RMS}) give us an evaluation of how far the training set is from the testing set. Where the normalized relative distances (d_s , d_p) give us an indication on how the training sets are distributed around the tested set.

The model has a good classification accuracy both when the sets are close to the unseen set (small d_{p_RMS} and d_{s_RMS} values as shown in Table 37) as when the sets are more distant from the tested set. Therefore, the parameters that seems to have a higher importance are the relative normalized distances.

Table 37. The RMS “distance” values d_{p_RMS} (considering laser power) and d_{s_RMS} (considering laser speed) between the training parameter sets and the central unseen parameter set. The close parameter sets and distant ones are distinguished.

	d_{p_RMS} (W)	d_{s_RMS} (mm/s)
Distant training sets to the unseen set	12	61
Closest training sets to the unseen set	5	16

Table 38. Confusion matrices for CNN models trained with the six closest parameter sets to the unseen central parameter set, and the six more distant points, for each regime.

Ground truth \ Classification accuracy [%]	Closest (i.e. full markers)			Furthest (i.e. empty markers)		
	Keyhole pores	Conduction mode	LoF pores	Keyhole pores	Conduction mode	LoF pores
Keyhole pores	97	1	0	91	1	1
Conduction mode	2	98	1	7	98	2
LoF pores	1	1	99	2	1	97

v. The process parameters: speed, power, normalized enthalpy

The influence of the choice of process parameters in the training set was also studied. The processing map is expressed in terms of laser speed and power. The normalized enthalpy (equation 1) is a function of these two process parameters. In each process regime, the four-parameter sets with the same speed (i.e., “iso-speed” parameter sets, n°1, 2, 3, 4 in Figure 100) were chosen to compose the training database, and the trained CNN was used for predicting the process regime of the central unseen parameter set (n° 13). The same strategy was used with the four “iso-power” (n° 5, 6, 7, 8 in Figure 100) and four “iso-normalized enthalpy” (n° 9, 10, 11, 12 in Figure 100) parameter sets. The aim was to determine how the algorithm behaves if one parameter (speed, power, or normalized enthalpy) is constant for all parameter sets in the training database, and remains the same for the unseen parameter set. The confidence matrices in Table 39 show that for the three considered training sets, the classification accuracies are high (> 88%), despite the fact that only four parameter sets were used for the training.

Table 39. Confusion matrices for CNN models predicting the process regime of an unseen ‘central’ parameter set, with one of the parameters being the same as the one in the training set. Three training databases made of 4 parameter sets were considered with iso-speed, iso-power, and iso-enthalpy.

		Iso-speed			Iso-power			Iso-enthalpy		
Ground truth \ Classification accuracy [%]		Keyhole pores	Conduction mode	LoF pores	Keyhole pores	Conduction mode	LoF pores	Keyhole pores	Conduction mode	LoF pores
Keyhole pores		88	3	2	96	4	0	93	1	0
Conduction mode		11	97	6	2	93	1	5	97	0
LoF pores		1	0	92	2	3	99	2	2	100

Additionally, for each process regime (*LoF pores*, *conduction mode*, and *keyhole pores*), the set with the highest power (n°1) was selected as the unseen parameter set, and the two sets with the lowest power values (n° 3 and 4) were used for the training database. The resulting classification accuracy was then compared with the one obtained with a training database made of the two sets with the smallest d_p to the unseen parameter set n°1 (i.e., n°2 and 13). The same procedure was applied considering the laser speed or the normalized enthalpy, instead of the power. In the former case, the unseen parameter was chosen as n°8, and the CNN was either trained with the parameter sets n°5 & 6 or with the n°13 & 7. In the latter case, the unseen parameter was chosen as n°12, and the CNN was either trained with the parameter sets n°9 & 10 or with the n°11 & 13. The results are presented in Table 40.

One can observe that the average classification accuracy is 18% higher when the training parameter sets are closer to the unseen parameter set in terms of laser speed (smaller d_s), and 5% higher when they are closer in

Acoustics emission for the prediction of processing regimes in Laser Powder Bed Fusion, and the generation of processing maps

terms of laser power (smaller d_p). The difference can be explained by the fact that, in the present DOE, the power range is smaller than the speed range. It can still be concluded that the smaller d_s and d_p , the higher would be the classification accuracies for the unseen parameter set. However, when comparing the influence of $d_{\Delta E}$, it can be seen that the accuracies are similar for both conditions (in average 75% for a smaller $d_{\Delta E}$, and 78% for a higher $d_{\Delta E}$). Table 41 presents the values of $d_{\Delta E}$ along with the corresponding values of d_s and d_p , for the predictions where the difference in $d_{\Delta E}$ is considered. While $d_{\Delta E}$ is higher for the sample in conduction mode, the corresponding d_s is equal to zero, which could explain that a higher classification accuracy (94% compared to 64%) is achieved, even though $d_{\Delta E}$ is higher. It can be presumed from these observations that the relative normalized distance in terms of normalized enthalpy is not a very relevant parameter.

Table 40. Confusion matrices for CNN models trained on two parameter sets and used for predicting the process regime on an unseen condition with the highest power, speed or enthalpy values compared to the training parameter sets, distinguishing training databases with the smallest and highest d_s , d_p , and $d_{\Delta E}$ values.

Closest		Distance in speed			Distance in power			Distance in enthalpy		
Ground truth	Classification accuracy [%]	Keyhole pores	Conduction mode	LoF pores	Keyhole pores	Conduction mode	LoF pores	Keyhole pores	Conduction mode	LoF pores
		Keyhole pores	Conduction mode	LoF pores	Keyhole pores	Conduction mode	LoF pores	Keyhole pores	Conduction mode	LoF pores
Keyhole pores		88	21	18	85	9	10	80	25	15
Conduction mode		3	78	15	13	90	4	18	64	4
LoF pores		9	1	67	2	1	86	2	11	81
Average		78			87			75		
Most distant		Distance in speed			Distance in power			Distance in enthalpy		
Ground truth	Classification accuracy [%]	Keyhole pores	Conduction mode	LoF pores	Keyhole pores	Conduction mode	LoF pores	Keyhole pores	Conduction mode	LoF pores
		Keyhole pores	Conduction mode	LoF pores	Keyhole pores	Conduction mode	LoF pores	Keyhole pores	Conduction mode	LoF pores
Keyhole pores		61	46	30	88	13	14	85	6	25
Conduction mode		9	52	3	10	87	13	14	94	18
LoF pores		30	1	67	2	0	73	1	2	56
Average		60			82			78		

Table 41. Values of d_s , d_p , and $d_{\Delta E}$ when predicting the process regime of an unseen condition with the lowest and the highest $d_{\Delta E}$.

	d_s [%]		d_p [%]		$d_{\Delta E}$ [%]	
	Closest	Most distant	Closest	Most distant	Closest	Most distant
Keyhole pores	21	31.6	8.6	6.6	3	28.6
Conduction mode	6	0	15.7	39.8	12.5	40
LoF pores	6	5.3	8.5	18	5.5	22

vi. Relative normalized distance in terms of power and speed

All the aforementioned CNN prediction results motivate an in-depth investigation of the influence of the number of parameter sets and the relative normalized distance in terms of power and speed (d_p and d_s) on the robustness of the models performance. Several models were trained with various numbers of parameter sets (from two to twelve), with different relative positions of the training sets with respect to the unseen parameter set, and with different values of d_p and d_s . The resulting classification accuracies were averaged between the three process regimes (*LoF pores*, *conduction mode* and *keyhole pores*). Figure 104 and Figure 105 present the average classification accuracy for the unseen parameter sets, as a function of the relative normalized distance in terms of speed (d_s) and power (d_p), respectively, for the different numbers of training sets used in the CNN database. The linear regressions of accuracies, obtained with a common number of training sets, are plotted in dotted lines (Figure 104 and Figure 105) in order to highlight tendencies.

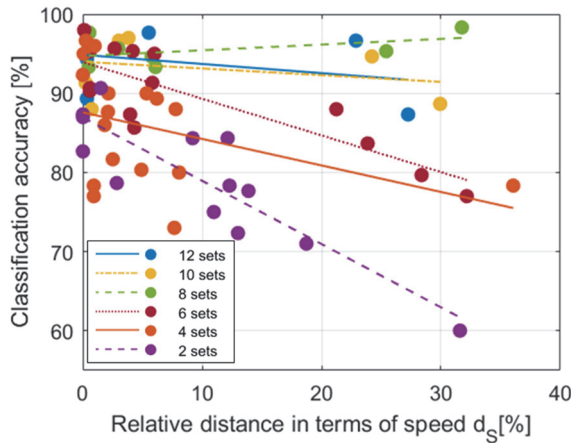


Figure 104. Average classification accuracy of the processing regime of the unseen parameter set, as a function of the relative normalized distance in terms of speed d_s for different numbers of parameter sets included in the training database (from 2 to 12).

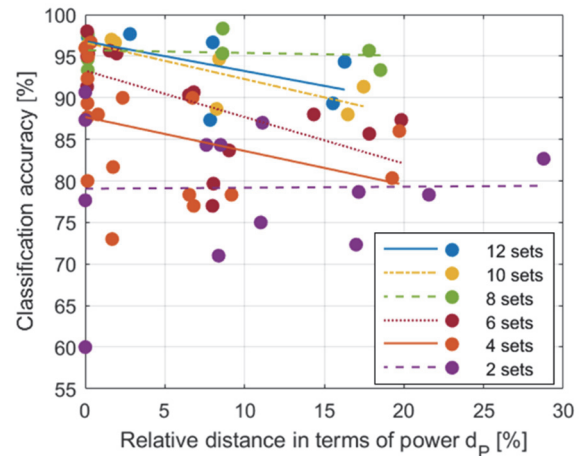


Figure 105. Average classification accuracy of the processing regime of the unseen parameter set, as a function of the relative normalized distance in terms of power d_p for different numbers of parameter sets included in the training database (from 2 to 12).

It can be first observed that the higher the number of parameter sets included in the training database, the higher the average classification accuracy. Additionally, a general trend can be highlighted: the higher the

relative normalized distance (for both d_p and d_s), the lower the classification accuracies. One outlier is the prediction of the sample n°4 regime (conduction mode), when using 10 and 12 training sets. The processing conditions refer, as aforementioned, to the intersection between the *conduction mode* domain and the *LoF* domain. In the context of predicting processing maps, and as already noted, this feature is interesting, as it indicates a transition zone between 2 process regimes. When eight parameters are included in the database, the prediction for this condition n°4 has a higher accuracy (93%), which explains the excellent average results with 8 training sets, even better than those with 10 or 12 training sets. The relatively scattered nature of the results can be explained by the statistical behavior of the CNN.

Nevertheless, if at least eight parameter sets compose the training database, the resulting model seems to be robust and able to predict with high confidence ($>88\%$) the entire studied processing map, regardless of the distance in term of speed and power (up to a difference of approximatively 30%). When training with only two parameter sets, the results are very scattered and seem more related to the process parameters differences (power and speed) than to the laser-material interaction. In other words, using only two training sets is not enough to have a reliable model.

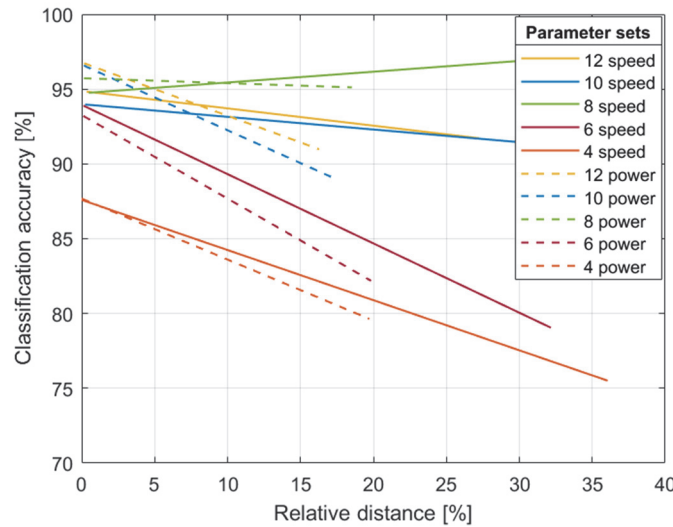


Figure 106. Linear regressions of the average classification accuracy when predicting the process regime of an unseen parameter set, as a function of the distance d_s (speed) and d_p (power).

In order to compare the influence of the relative normalized distance in power and the relative normalized distance in speed, Figure 106 presents the linear regressions of all results displayed in Figure 104 and Figure 105, when at least four parameter sets were included in the training database, and distinguishing between the two types of distance. The systematically larger slopes of accuracies as a function of d_p point towards a bigger influence of the relative normalized distance in power.

The difference in slope between the two considered linear regressions (as a function of d_s and d_p) varies significantly depending on the number of training parameter sets (from 17% with 4 and 6 parameter sets, up to 80% with 10 parameter sets).

Although the influence of d_p appears somehow larger, both d_s and d_p should be minimized to guarantee high classification accuracies.

8.5 Conclusions

This work presents the results of a CNN model applied to spectrograms extracted from measurements of an airborne acoustic sensor for the classification of LPBF processing regimes. The microphone placed inside a custom-design LPBF machined recorded the acoustic signals of the process for 39 different process parameters, i.e., thirteen parameter sets per process regime (*keyhole pores*, *conduction mode*, or *LoF pores*). The labeling of the categories for each process condition was verified by cross-section analysis. A CNN model was optimized for spectrograms extracted from the acoustic signals filtered with a low pass filter at 60 kHz, downsampled 4 times and normalized.

The aim of this contribution was to establish a methodology for the construction of a robust training database, leading to a CNN able to predict the processing regime in conditions unseen in the database, covering the entire LPBF processing map of 316L steel. The three considered regimes are *LoF pores*, *conduction mode*, and *keyhole pores*. The CNN model is trained on a given number of laser parameter sets, and used for predicting the process regime of an unseen parameter set. The resulting classification accuracy is very high (>97%), proving that it is possible to construct a model general enough for identifying the features related to specific laser-material interactions and leading to specific metallurgical states. Three main parameters are found to influence the classification accuracy. The first one is the relative normalized distance in terms of power and speed between the average laser parameters used in the training sets, and those of the unseen parameter set (d_s , d_p). The second is the number of parameter sets included in the training database, and the third is the position (in the processing map) of the training sets relative to that of the unseen parameter set. These three parameters have been proven to be interdependent. Results highlight that higher d_s and d_p values lower the classification accuracies. The influence of the relative normalized distance in terms of normalized enthalpy $d_{\Delta E}$ does not seem to be relevant. However, the influence of d_p seems to be higher than that of d_s . Moreover, it has been concluded that on average, the higher the number of parameter sets in the training database, the higher the classification accuracy. Two parameter sets are not enough to allow a model to generalize. A minimum number of eight training sets is identified, leading to high classification accuracies (>88 %) for all relative normalized distances and position considered in the present DOE. This number can be lowered to six if the training sets surrounding the unseen parameter set have a d_s and d_p lower than 5 %. If one process parameter (speed, power, or normalized enthalpy) is constant among all sets in the training database, and common to the unseen parameter set,

then four training sets are enough for predicting the process regime with a high accuracy, regardless of the particular choice of process parameters.

In summary, one model trained with eight distinct laser parameter sets randomly distributed in each process regime domain would be sufficient to classify the entire processing map. Once a robust model is obtained, a decrease in the classification accuracy can help identifying the boundaries between different domains in the 2D processing map. This can significantly facilitate the time-consuming building of an LPBF processing map for a given alloy. In the context of in-situ acoustic monitoring for the control of the LPBF process, we demonstrate here that unexpected processing conditions happening during the fabrication of a 3D part could be detected, for example, by predicting from the AE signals a regime different from the conduction mode. In future work, the understanding of the features and frequencies responsible for specific laser material interactions, in each process regime, will be investigated based on the present results. The same methodology could be applied to the detection of other various critical events, such as crack propagation or microstructure changes.

References

- [1] T. DebRoy et al., “Additive manufacturing of metallic components – Process, structure and properties,” *Prog. Mater. Sci.*, vol. 92, pp. 112–224, Mar. 2018, doi: 10.1016/j.pmatsci.2017.10.001.
- [2] N. K. Dey, “Additive manufacturing laser deposition of Ti-6Al-4V for aerospace repair application,” p. 70.
- [3] K. Zeng, D. Pal, and B. Stucker, “A review of thermal analysis methods in Laser Sintering and Selective Laser Melting,” p. 19.
- [4] R. Liu, Z. Wang, T. Sparks, F. Liou, and J. Newkirk, “Aerospace Applications of Laser Additive Manufacturing,” *Laser Addit. Manuf. Mater. Des. Technol. Appl.*, pp. 351–371, Sep. 2016, doi: 10.1016/B978-0-08-100433-3.00013-0.
- [5] J. M. Williams et al., “Bone tissue engineering using polycaprolactone scaffolds fabricated via selective laser sintering,” *Biomaterials*, vol. 26, no. 23, pp. 4817–4827, Aug. 2005, doi: 10.1016/j.biomaterials.2004.11.057.
- [6] J. Gao, J. Folkes, O. Yilmaz, and N. Gindy, “Investigation of a 3D non-contact measurement based blade repair integration system,” *Aircr. Eng. Aerosp. Technol.*, vol. 77, pp. 34–41, Feb. 2005, doi: 10.1108/00022660510576028.
- [7] C. L. Ventola, “Medical Applications for 3D Printing: Current and Projected Uses,” *P T Peer-Rev. J. Formul. Manag.*, vol. 39, no. 10, pp. 704–711, Oct. 2014.
- [8] B. Vandenbroucke and J. Kruth, “Selective laser melting of biocompatible metals for rapid manufacturing of medical parts,” *Rapid Prototyp. J.*, vol. 13, no. 4, pp. 196–203, Jan. 2007, doi: 10.1108/13552540710776142.
- [9] A. Mostafaei et al., “Defects and anomalies in powder bed fusion metal additive manufacturing,” *Curr. Opin. Solid State Mater. Sci.*, vol. 26, no. 2, Jan. 2022, doi: 10.1016/j.cossms.2021.100974.
- [10] M. Montazeri, R. Yavari, P. Rao, and P. Boulware, “In-Process Monitoring of Material Cross-Contamination Defects in Laser Powder Bed Fusion,” *J. Manuf. Sci. Eng.*, vol. 140, no. 11, Jul. 2018, doi: 10.1115/1.4040543.
- [11] P. Hanzl, M. Zetek, T. Bakša, and T. Kroupa, “The Influence of Processing Parameters on the Mechanical Properties of SLM Parts,” *Procedia Eng.*, vol. 100, pp. 1405–1413, Jan. 2015, doi: 10.1016/j.pro-eng.2015.01.510.

- [12] A. Ramalho, T. G. Santos, B. Bevans, Z. Smoqi, P. Rao, and J. P. Oliveira, “Effect of contaminations on the acoustic emissions during wire and arc additive manufacturing of 316L stainless steel,” *Addit. Manuf.*, vol. 51, p. 102585, Mar. 2022, doi: 10.1016/j.addma.2021.102585.
- [13] W. King et al., “Laser powder bed fusion additive manufacturing of metals; physics, computational, and materials challenges,” *Appl. Phys. Rev.*, vol. 2, p. 041304, Dec. 2015, doi: 10.1063/1.4937809.
- [14] T. Mukherjee and T. DebRoy, “Mitigation of lack of fusion defects in powder bed fusion additive manufacturing,” *J. Manuf. Process.*, vol. 36, pp. 442–449, Dec. 2018, doi: 10.1016/j.jmapro.2018.10.028.
- [15] M. Tang, P. C. Pistorius, and J. L. Beuth, “Prediction of lack-of-fusion porosity for powder bed fusion,” *Addit. Manuf.*, vol. 14, pp. 39–48, Mar. 2017, doi: 10.1016/j.addma.2016.12.001.
- [16] K. Darvish, Z. W. Chen, and T. Pasang, “Reducing lack of fusion during selective laser melting of CoCrMo alloy: Effect of laser power on geometrical features of tracks,” *Mater. Des.*, vol. 112, pp. 357–366, Dec. 2016, doi: 10.1016/j.matdes.2016.09.086.
- [17] M. Laleh et al., “Two and three-dimensional characterisation of localised corrosion affected by lack-of-fusion pores in 316L stainless steel produced by selective laser melting,” *Corros. Sci.*, vol. 165, p. 108394, Apr. 2020, doi: 10.1016/j.corsci.2019.108394.
- [18] C. Zhao et al., “Critical instability at moving keyhole tip generates porosity in laser melting,” *Science*, vol. 370, no. 6520, pp. 1080–1086, Nov. 2020, doi: 10.1126/science.abd1587.
- [19] A. A. Martin et al., “Dynamics of pore formation during laser powder bed fusion additive manufacturing,” *Nat. Commun.*, vol. 10, no. 1, p. 1987, Apr. 2019, doi: 10.1038/s41467-019-10009-2.
- [20] F. Lu, X. Li, Z. Li, X. Tang, and H. Cui, “Formation and influence mechanism of keyhole-induced porosity in deep-penetration laser welding based on 3D transient modeling,” *Int. J. Heat Mass Transf.*, vol. 90, pp. 1143–1152, Nov. 2015, doi: 10.1016/j.ijheatmasstransfer.2015.07.041.
- [21] W. E. King et al., “Observation of keyhole-mode laser melting in laser powder-bed fusion additive manufacturing,” *J. Mater. Process. Technol.*, vol. 214, no. 12, Art. no. LLNL-JRNL-642426; LLNL-JRNL-650285, Jun. 2014, doi: 10.1016/j.jmatprotec.2014.06.005.
- [22] T. Klein, M. Vicanek, J. Kroos, I. Decker, and G. Simon, “Oscillations of the keyhole in penetration laser beam welding,” *J. Phys. Appl. Phys.*, vol. 27, no. 10, pp. 2023–2030, Oct. 1994, doi: 10.1088/0022-3727/27/10/006.

- [23] T. Qi, H. Zhu, H. Zhang, J. Yin, L. Ke, and X. Zeng, "Selective laser melting of Al7050 powder: Melting mode transition and comparison of the characteristics between the keyhole and conduction mode," *Mater. Des.*, vol. 135, Sep. 2017, doi: 10.1016/j.matdes.2017.09.014.
- [24] H. Ghasemi-Tabasi, J. Jhabvala, E. Boillat, T. Ivas, R. Drissi-Daoudi, and R. E. Logé, "An effective rule for translating optimal selective laser melting processing parameters from one material to another," *Addit. Manuf.*, vol. 36, p. 101496, Dec. 2020, doi: 10.1016/j.addma.2020.101496.
- [25] W. M. Tucho, V. H. Lysne, H. Austbø, A. Sjolyst-Kverneland, and V. Hansen, "Investigation of effects of process parameters on microstructure and hardness of SLM manufactured SS316L," *J. Alloys Compd.*, vol. 740, pp. 910–925, Apr. 2018, doi: 10.1016/j.jallcom.2018.01.098.
- [26] I. Koutiri, E. Pessard, P. Peyre, O. Amlou, and T. De Terris, "Influence of SLM process parameters on the surface finish, porosity rate and fatigue behavior of as-built Inconel 625 parts," *J. Mater. Process. Technol.*, vol. 255, pp. 536–546, May 2018, doi: 10.1016/j.jmatprotec.2017.12.043.
- [27] T. Mishurova, K. Artzt, J. Haubrich, G. Requena, and G. Bruno, "New aspects about the search for the most relevant parameters optimizing SLM materials," *Addit. Manuf.*, vol. 25, pp. 325–334, Jan. 2019, doi: 10.1016/j.addma.2018.11.023.
- [28] Y. H. Zhou et al., "Selective laser melting of typical metallic materials: An effective process prediction model developed by energy absorption and consumption analysis," *Addit. Manuf.*, vol. 25, pp. 204–217, Jan. 2019, doi: 10.1016/j.addma.2018.10.046.
- [29] R. Drissi-Daoudi et al., "Differentiation of materials and laser powder bed fusion processing regimes from airborne acoustic emission combined with machine learning," *Virtual Phys. Prototyp.*, vol. 17, no. 2, pp. 181–204, Apr. 2022, doi: 10.1080/17452759.2022.2028380.
- [30] V. Gunenthiram, P. Peyre, M. Schneider, M. Dal, C. Frederic, and R. Fabbro, "Analysis of laser–melt pool–powder bed interaction during the selective laser melting of a stainless steel," *J. Laser Appl.*, vol. 29, p. 022303, May 2017, doi: 10.2351/1.4983259.
- [31] M. J. Matthews, G. Guss, S. A. Khairallah, A. M. Rubenchik, P. J. Depond, and W. E. King, "Denuation of metal powder layers in laser powder bed fusion processes," *Acta Mater.*, vol. 114, pp. 33–42, Aug. 2016, doi: 10.1016/j.actamat.2016.05.017.
- [32] V. Gunenthiram et al., "Experimental analysis of spatter generation and melt-pool behavior during the powder bed laser beam melting process," *J. Mater. Process. Technol.*, vol. 251, pp. 376–386, Jan. 2018, doi: 10.1016/j.jmatprotec.2017.08.012.

- [33] P. Bidare, I. Bitharas, R. M. Ward, M. M. Attallah, and A. J. Moore, “Fluid and particle dynamics in laser powder bed fusion,” *Acta Mater.*, vol. 142, pp. 107–120, Jan. 2018, doi: 10.1016/j.actamat.2017.09.051.
- [34] S. A. Khairallah, A. T. Anderson, A. Rubenchik, and W. E. King, “Laser powder-bed fusion additive manufacturing: Physics of complex melt flow and formation mechanisms of pores, spatter, and denudation zones,” *Acta Mater.*, vol. 108, pp. 36–45, Apr. 2016, doi: 10.1016/j.actamat.2016.02.014.
- [35] D. Wang et al., “Mechanisms and characteristics of spatter generation in SLM processing and its effect on the properties,” *Mater. Des.*, vol. 117, pp. 121–130, Mar. 2017, doi: 10.1016/j.matdes.2016.12.060.
- [36] S. Berumen, F. Bechmann, S. Lindner, J. P. Kruth, and T. Craeghs, “Quality control of laser- and powder bed-based Additive Manufacturing (AM) technologies,” *Phys. Procedia*, vol. 5, no. PART 2, pp. 617–622, 2010, doi: 10.1016/j.phpro.2010.08.089.
- [37] S. Clijsters, T. Craeghs, S. Buls, K. Kempen, and J. P. Kruth, “In situ quality control of the selective laser melting process using a high-speed, real-time melt pool monitoring system,” *Int. J. Adv. Manuf. Technol.*, vol. 75, no. 5–8, pp. 1089–1101, 2014, doi: 10.1007/s00170-014-6214-8.
- [38] S. Shevchik et al., “Supervised deep learning for real-time quality monitoring of laser welding with X-ray radiographic guidance,” *Sci. Rep.*, vol. 10, no. 1, p. 3389, Feb. 2020, doi: 10.1038/s41598-020-60294-x.
- [39] M. Pavlov, M. Doubenskaia, and I. Smurov, “Pyrometric analysis of thermal processes in SLM technology,” *Phys. Procedia*, vol. 5, no. PART 2, pp. 523–531, Jan. 2010, doi: 10.1016/J.PHPRO.2010.08.080.
- [40] M. Doubenskaia, M. Pavlov, and Y. Chivel, “Optical System for On-Line Monitoring and Temperature Control in Selective Laser Melting Technology,” *Key Eng. Mater.*, vol. 437, pp. 458–461, 2010, doi: 10.4028/www.scientific.net/KEM.437.458.
- [41] T. Furumoto, T. Ueda, M. R. Alkahari, and A. Hosokawa, “Investigation of laser consolidation process for metal powder by two-color pyrometer and high-speed video camera,” *CIRP Ann.*, vol. 62, no. 1, pp. 223–226, Jan. 2013, doi: 10.1016/J.CIRP.2013.03.032.
- [42] J.-B. Forien, N. P. Calta, P. J. Depond, G. M. Guss, T. T. Roehling, and M. J. Matthews, “Detecting keyhole pore defects and monitoring process signatures during laser powder bed fusion: A correlation between in situ pyrometry and ex situ X-ray radiography,” *Addit. Manuf.*, vol. 101336, 2020.
- [43] A. Gaikwad, B. Giera, G. M. Guss, J. B. Forien, M. J. Matthews, and P. Rao, “Heterogeneous sensing and scientific machine learning for quality assurance in laser powder bed fusion – A single-track study,” *Addit. Manuf.*, vol. 36, p. 101659, 2020, doi: 10.1016/j.addma.2020.101659.

- [44] T. Furumoto, M. R. Alkahari, T. Ueda, M. S. A. Aziz, and A. Hosokawa, "Monitoring of Laser Consolidation Process of Metal Powder with High Speed Video Camera," *Phys. Procedia*, vol. 39, pp. 760–766, Jan. 2012, doi: 10.1016/J.PHPRO.2012.10.098.
- [45] L. Li and W. M. Steen, "Non-contact acoustic emission monitoring during laser processing," *LIA Laser Inst. Am.*, vol. 75, pp. 719–728, 1993, doi: 10.2351/1.5058543.
- [46] Y. Mao, G. Kinsman, and W. W. Duley, "Real-Time Fast Fourier Transform Analysis of Acoustic Emission during CO₂ Laser Welding of Materials," *J. Laser Appl.*, vol. 5, no. 2, pp. 17–22, 1993, doi: 10.2351/1.4745326.
- [47] W. W. Duley and Y. L. Mao, "The effect of surface condition on acoustic emission during welding of aluminium with CO₂ laser radiation," *J. Phys. Appl. Phys.*, vol. 27, no. 7, pp. 1379–1383, 1994, doi: 10.1088/0022-3727/27/7/007.
- [48] D. Farson, K. Hillsley, and J. Sames, "Frequency–time characteristics of air-borne signals from laser welds," *J Laser Appl*, vol. 8, pp. 33–42, 1996.
- [49] K. Wasmer, C. Kenel, C. Leinenbach, and S. A. Shevchik, "In Situ and Real-Time Monitoring of Powder-Bed AM by Combining Acoustic Emission and Artificial Intelligence," in *Industrializing Additive Manufacturing - Proceedings of Additive Manufacturing in Products and Applications - AMPA2017*, Cham, 2018, pp. 200–209. doi: 10.1007/978-3-319-66866-6_20.
- [50] S. A. Shevchik et al., "Laser Welding Quality Monitoring via Graph Support Vector Machine With Data Adaptive Kernel," *IEEE Access*, vol. 7, pp. 93108–93122, 2019, doi: 10.1109/ACCESS.2019.2927661.
- [51] T. Le-Quang et al., "Why is in situ quality control of laser keyhole welding a real challenge?," *Procedia CIRP*, vol. 74, pp. 649–653, Jan. 2018, doi: 10.1016/j.procir.2018.08.055.
- [52] K. Wasmer et al., "Laser processing quality monitoring by combining acoustic emission and machine learning: a high-speed X-ray imaging approach," *Procedia CIRP*, vol. 74, pp. 654–658, Jan. 2018, doi: 10.1016/j.procir.2018.08.054.
- [53] W. Huang and R. Kovacevic, "A neural network and multiple regression method for the characterization of the depth of weld penetration in laser welding based on acoustic signatures," *J. Intell. Manuf.*, vol. 22, no. 2, pp. 131–143, Apr. 2011, doi: 10.1007/s10845-009-0267-9.
- [54] H. Gu and W. W. Duley, "A statistical approach to acoustic monitoring of laser welding," *J. Phys. Appl. Phys.*, vol. 29, no. 3, pp. 556–560, Mar. 1996, doi: 10.1088/0022-3727/29/3/011.

- [55] S. Lee, S. Ahn, and C. Park, “Analysis of Acoustic Emission Signals During Laser Spot Welding of SS304 Stainless Steel,” *J. Mater. Eng. Perform.*, vol. 23, no. 3, pp. 700–707, Mar. 2014, doi: 10.1007/s11665-013-0791-9.
- [56] S. A. Shevchik, C. Kenel, C. Leinenbach, and K. Wasmer, “Acoustic emission for in situ quality monitoring in additive manufacturing using spectral convolutional neural networks,” *Addit. Manuf.*, vol. 21, pp. 598–604, May 2018, doi: 10.1016/j.addma.2017.11.012.
- [57] L. W. Koester, H. Taheri, L. J. Bond, and E. J. Faierson, “Acoustic monitoring of additive manufacturing for damage and process condition determination,” *AIP Conf. Proc.*, vol. 2102, no. 1, p. 020005, May 2019, doi: 10.1063/1.5099709.
- [58] K. Ito, M. Kusano, M. Demura, and M. Watanabe, “Detection and location of microdefects during selective laser melting by wireless acoustic emission measurement,” *Addit. Manuf.*, vol. 40, p. 101915, Apr. 2021, doi: 10.1016/j.addma.2021.101915.
- [59] H. Taheri, L. W. Koester, T. A. Bigelow, E. J. Faierson, and L. J. Bond, “In Situ Additive Manufacturing Process Monitoring With an Acoustic Technique: Clustering Performance Evaluation Using K-Means Algorithm,” *J. Manuf. Sci. Eng.*, vol. 141, no. 4, Feb. 2019, doi: 10.1115/1.4042786.
- [60] G. Masinelli, S. A. Shevchik, V. Pandiyan, T. Quang-Le, and K. Wasmer, “Artificial Intelligence for Monitoring and Control of Metal Additive Manufacturing,” in *Industrializing Additive Manufacturing*, Cham, 2021, pp. 205–220. doi: 10.1007/978-3-030-54334-1_15.
- [61] N. Eschner, L. Weiser, B. Häfner, and G. Lanza, “Classification of specimen density in Laser Powder Bed Fusion (L-PBF) using in-process structure-borne acoustic process emissions,” *Addit. Manuf.*, vol. 34, p. 101324, Aug. 2020, doi: 10.1016/j.addma.2020.101324.
- [62] S. A. Shevchik, G. Masinelli, C. Kenel, C. Leinenbach, and K. Wasmer, “Deep Learning for In Situ and Real-Time Quality Monitoring in Additive Manufacturing Using Acoustic Emission,” *IEEE Trans. Ind. Inform.*, vol. 15, no. 9, pp. 5194–5203, Sep. 2019, doi: 10.1109/TII.2019.2910524.
- [63] D. Ye, G. S. Hong, Y. Zhang, K. Zhu, and J. Y. H. Fuh, “Defect detection in selective laser melting technology by acoustic signals with deep belief networks,” *Int. J. Adv. Manuf. Technol.*, vol. 96, no. 5, pp. 2791–2801, May 2018, doi: 10.1007/s00170-018-1728-0.
- [64] J. R. Tempelman et al., “Detection of keyhole pore formations in laser powder-bed fusion using acoustic process monitoring measurements,” *Addit. Manuf.*, vol. 55, p. 102735, Jul. 2022, doi: 10.1016/j.addma.2022.102735.

- [65] K. Wasmer, T. Le-Quang, B. Meylan, and S. A. Shevchik, "In Situ Quality Monitoring in AM Using Acoustic Emission: A Reinforcement Learning Approach," *J. Mater. Eng. Perform.*, vol. 28, no. 2, pp. 666–672, Feb. 2019, doi: 10.1007/s11665-018-3690-2.
- [66] V. Pandiyan et al., "Semi-supervised Monitoring of Laser powder bed fusion process based on acoustic emissions," *Virtual Phys. Prototyp.*, vol. 16, no. 4, pp. 481–497, Jul. 2021, doi: 10.1080/17452759.2021.1966166.
- [67] V. Pandiyan et al., "Deep transfer learning of additive manufacturing mechanisms across materials in metal-based laser powder bed fusion process," *J. Mater. Process. Technol.*, vol. 303, p. 117531, May 2022, doi: 10.1016/j.jmatprotec.2022.117531.
- [68] A. J. Jerri, "The Shannon sampling theorem - Its various extensions and applications: A tutorial review," *IEEE Proc.*, vol. 65, pp. 1565–1596, Nov. 1977.
- [69] D. B. Hann, J. Iammi, and J. Folkes, "A simple methodology for predicting laser-weld properties from material and laser parameters," *J. Phys. Appl. Phys.*, vol. 44, no. 44, p. 445401, Oct. 2011, doi: 10.1088/0022-3727/44/44/445401.
- [70] K. Gutknecht, M. Cloots, R. Sommerhuber, and K. Wegener, "Mutual comparison of acoustic, pyrometric and thermographic laser powder bed fusion monitoring," *Mater. Des.*, vol. 210, p. 110036, Nov. 2021, doi: 10.1016/j.matdes.2021.110036.

Chapter 9 Conclusions and future work

9.1 Conclusions

Throughout the present PhD thesis, the acoustic monitoring of laser powder-bed fusion (LPBF) with the help of machine learning algorithms was investigated. AE signals were acquired during LPBF processing of three metallic alloys: stainless steel (316L), bronze (CuSn_8), and Inconel (Inconel 718). Processing maps are developed to produce three principal LPBF regimes: *LoF pores*, *conduction mode*, and *keyhole pores*. This contribution focuses on the correlation of the three regimes with their corresponding AE signals. The main conclusions are summarised below.

Airborne sensors are proven to be efficient for real-time monitoring of processing regimes, for different alloys. With the first low-cost microphone investigated, the AM41, the frequency distribution of AE signals for the three materials three process regimes is positioned between 1 and 60 kHz. The peaks were principally around 10 and 40 kHz, as the AM41 acoustic sensor's sensitivity is higher in this region. The wavelet transform plot presents discrete peaks asserting that the regimes are distinct, and the selection of the window size for the classification task is essential for real-time defect localization. The clustered feature space visualization proves that the LPBF process is highly dynamic, and algorithms capable of classifying data in non-linear spaces are necessary.

Four ML algorithms, LR, RF, SVM, and a CNN, were trained to classify the three process regimes individually for each alloy, but also with all materials mixed. Very high classification accuracy was obtained from all algorithms (at least 86%) on the individual alloys. A multi-label CNN was designed and shown capable of simultaneously classifying the alloy and the process regime, with high confidence (>91%). This is of great interest for the LPBF processing of multi-materials.

Two process parameters per regime with specific normalized enthalpy and with the same laser parameters for the keyhole pores and LoF pores formation across materials proved that the AE features extracted and used as inputs for training algorithms are strongly related to the laser-material interaction. The generalization of the classification of LPBF defects to new alloys (not considered in the training) has been proven most of the time not possible with the chosen microphone.

To reach a more robust monitoring approach, two methodologies are investigated. The first one consists in developing ML solutions based on semi-supervised or transfer learning algorithms, and the second one is to optimize the choice of the microphone, considering a flat frequency response.

The first methodology investigated a semi-supervised approach where the defect categories are differentiated from the conduction mode regime. This method reduced the amount of data needed for the classification as well as computational needs and the requirement of a balanced dataset. As a result, we could classify the anomaly regimes with 96% accuracy for the Inconel 718. A Deep Learning (DL) network has also been proven to be effective in transferring knowledge from stainless steel (316L) to bronze (CuSn8), considering four LPBF process regimes such as *balling*, *LoF pores*, *conduction mode*, and *keyhole pores* in . The classification accuracy was above 80%.

The second methodology compared the classification results as well as saliency maps of the microphone AM41 (with a high sensitivity around specific frequencies) to the ones of a second microphone CM16 (a flat response from 2 Hz to 200 kHz). The two microphones' AE signals recorded from stainless steel 316L, considering three regimes, led to models able to classify with high confidence (>91%) a tested set of parameters not present in the training database, regardless of the CNN architecture and signals post-processing. However, a better CNN could be trained as the CNN models trained with the AM41 discarded information in the band of high sensitivity of the microphone. With this model, the frequencies responsible for the classification of the three regimes are found to be below 30 kHz. A methodology is determined to evaluate the quality of a CNN model using saliency maps.

With a good CNN model, we finally determined the important criteria leading to a robust model able to predict the process regime in conditions unseen by the trained database. The minimum number of training processing conditions is identified as eight, in order to predict the process regime for any (unseen) laser parameters within the processing map. This number can be lowered to six if the training set is in the surrounding of the unseen parameters set. When one laser parameter (speed, power, or normalized enthalpy) is constant between all training and unseen parameter sets, only four training parameter sets allow a high classification accuracy. Once a robust model is obtained, a decrease in the classification accuracy can help identify the boundaries between different processing regimes in the 2D processing map.

Overall, the thesis demonstrates that ML algorithm can effectively learn enough about laser-material interaction, with adequate choice of training conditions, such that a robust real-time acoustic emission control of the LPBF process becomes possible. It also provides the means to numerically construct an entire processing map.

9.2 Future work

The results of this thesis open new avenues toward robust acoustic emission-based monitoring for additive manufacturing. However, there are still some challenges that require in-depth investigations.

First, the use of the CM16 flat response microphone should be tested with other alloys and other LPBF machines. The comparison of the frequencies involved with the saliency map investigation for the three regimes

studied for other alloys and other machines can deepen the understanding of the phenomena that lead to the differentiation of acoustic footprints in relation to defect formation mechanisms.

This knowledge could lead to the understanding of the next steps to reach a universal model for process monitoring. In the same spirit, the study should be reiterated with a SBAE sensor and the saliency maps analyzed. The involved frequencies as well as the conditions to reach a robust training database that provide a model able to predict regimes in unseen conditions could be different. The combination of ABAE and SBAE should as well be investigated.

The combination with optical and acoustics monitoring is rare and deserves further investigation. With the developed methodology, it can lead to a more reliable monitoring system able to better capture the complex process dynamics.

Moreover, to reach a fully robust monitoring, the methodology developed in this thesis can be applied to various other critical events, such as crack propagation or microstructure changes.

ML models used in this thesis are discriminative models, they draw boundaries in the data space. As the data space changes, they are susceptible to error. To reach a universal and robust modeling, the development of generative ML models, for example using domain adaptation, could also be investigated. The presented transfer learning method can also be tried from one machine to the other.

Finally, some preliminary analysis during this thesis led to promising results towards the localization of pores with saliency maps. A robust CNN trained with the raw data in the time domain (to have the best time resolution) should be developed. Another method could be the use of several ABAE sensors, such as to implement localization through signal triangulation.

Curriculum Vitae



RITA DRISSI DAOUDI

+41 79 841 77 37

Rue des Chavannes 3

2000 Neuchâtel – Switzerland

rita.drissidaoudi@gmail.com

29.09.1994

B Permit

Moroccan



WORK EXPERIENCE



Ph.D. in the Thermomechanical Metallurgy Laboratory in Additive Manufacturing - EPFL, Neuchâtel

April 2018- September 2022

- Autonomous theoretical and applied research
- Multidisciplinary project management and collaboration with different Swiss research centers
- 3D printing, Laser-Powder-Bed-Fusion
- Various characterization and process knowledge for steel, nickel, and copper alloys
- Pores and cracks formations
- 3D imaging: Neutrons and X-raytomography
- Acoustic Emission Monitoring
- Machine learning-Saliency Maps



Master Thesis - Alpes Lasers SA, Neuchâtel

September 2017 – Mars 2018

- FEA development to simulate the response of the packaged of a Quantum Cascade Lasers under environmental conditions and propose design improvements to reach aerospace specifications



R&D internship - Rolex, Geneva

February 2016-July 2016

- Fragile material mechanical characterization



Production internship - Bosch Packaging, Ecublens

July 2015-August 2015

- Development of a robotic tray separator system

EDUCATION











Ph.D. Student in the Laboratory of Thermomechanical Metallurgy (LMTM) in Advance Manufacturing – **EPFL 2018-2022**



Master in Mechanical Engineering, specialization in Mechanics of Solids and Structures – Minor in Material Sciences – **EPFL 2015-2018**

Bachelor in Mechanical Engineering – **EPFL 2012-2015**

LANGUAGE

	French Native language	
	English Fluent- C1	
	Arabic B1	
	Spanish B1	
	German Ongoing courses-A2	

SOME +

Teaching Assistant - EPFL Lausanne

- Help for the exercises of the courses Introduction to material sciences, Deformation of materials, Analyse, Chemistry and Simulation and modeling by finite element
- Master student project supervision

2^e price My Thesis in 180 seconds - EPFL:

<https://www.youtube.com/watch?v=kOxKMD209Ag>

EXPERIMENTAL AND COMPUTATIONAL SKILLS

Mechanical characterization: Gleeble machine/ traction test / 3-4 pts bending tests/ hardness measurement

Samples preparation for different metallic alloys as well as for different ceramics (polishing, etching)

3D imaging: X rays and neutron tomography reconstructions

Microscopy analysis: Optic and SEM.

Curriculum Vitae

Differential calorimetry (DSC measurement)

Microsoft Office, Latex

FE simulation: Abaqus, AnsysMechanical, Fluent, Comsol

Conception : Catia, Solidworks

Programming: C++, Matlab, Fortran,Python

3D printing : Magics, Autodesk Netfabb

HOBBIES

Theatrical improvisation

Literature

Board games